Strong light-mediated coupling between a membrane oscillator and an atomic spin ensemble

Inauguraldissertation

zur
Erlangung der Würde eines Doktors der Philosophie
vorgelegt der
Philosophisch-Naturwissenschaftlichen Fakultät
der Universität Basel

von

Thomas Michael Karg
aus München, Deutschland

Basel, 2020

Genehmigt von der Philosophisch-Naturwissenschaftlichen Fakultät
auf Antrag von
Prof. Dr. Philipp Treutlein
Prof. Dr. Simon Gröblacher

Basel, den 18. Februar 2020

Prof. Dr. Martin Spiess
Dekan

Creative Commons License Deed

Attribution-NonCommercial-NoDerivatives 4.0 International

This is a human-readable summary of (and not a substitute for) the license.

You are free to:

Share — copy and redistribute the material in any medium or format

The licensor cannot revoke these freedoms as long as you follow the license terms.

Under the following terms:

Attribution — You must give appropriate credit, provide a link to the license, and indicate if changes were made. You may do so in any reasonable manner, but not in any way that suggests the licensor endorses you or your use.

NonCommercial — You may not use the material for commercial purposes.

NoDerivatives — If you remix, transform, or build upon the material, you may not distribute the modified material.

No additional restrictions — You may not apply legal terms or technological measures that legally restrict others from doing anything the license permits.

Notices:

You do not have to comply with the license for elements of the material in the public domain or where your use is permitted by an applicable exception or limitation.

No warranties are given. The license may not give you all of the permissions necessary for your intended use. For example, other rights such as publicity, privacy, or moral rights may limit how you use the material.

Abstract

This thesis presents theoretical and experimental work on light-mediated coupling between a collective atomic spin and a micromechanical membrane oscillator. With our work we address a fundamental question of quantum optics: Can a beam of light mediate coherent Hamiltonian interactions between two distant quantum systems? This is an intriguing question whose answer is not *a priori* clear, since the light carries away information about the systems and might be subject to losses, giving rise to intrinsic decoherence channels associated with the coupling. Our answer is affirmative and we derive a particularly simple sufficient condition for the interactions to be Hamiltonian: The light field needs to interact twice with the systems and the second interaction has to be the time reversal of the first. We demonstrate theoretically that, even in the presence of significant optical loss, coherent interactions can be realized and generate substantial amounts of entanglement between the systems.

In our experiments, we employ this approach to strongly couple a spin-polarized atomic ensemble and a micromechanical oscillator via a free-space laser beam across a distance of one meter in a room-temperature environment. The atomic ensemble consists of about ten million laser-cooled Rubidium atoms in an optical dipole trap that interact with the coupling laser via an off-resonant Faraday interaction. The mechanical oscillator is a silicon nitride membrane which is mounted in a single-sided optical cavity and couples to the laser field via radiation-pressure forces. In order to mediate a bidirectional Hamiltonian interaction between spin and membrane, the coupling beam is arranged in a loop such that it couples twice to the spin. This looped geometry enables destructive interference of quantum back-action by the light field on the spin.

Using this setup, we experimentally demonstrate for the first time strong Hamiltonian coupling between remote quantum systems and explore different dynamical regimes of cascaded light-mediated interactions: With the spin initialized in its ground state we observe normal-mode splitting and coherent energy exchange oscillations, both hallmarks of strong coupling. If we invert the spin to its highest energy state, we observe parametric-gain interactions, resulting in two-mode thermal noise squeezing. Furthermore, by shifting the phase of the light field between spin and membrane we can switch to non-Hamiltonian coupled dynamics, allowing us to observe level attraction and exceptional points. This high level of control in a strongly coupled modular system gives access to a unique toolbox for designing hybrid quantum systems and coherent optical feedback loops. Our approach to engineer coherent long-distance interactions with light makes it possible to couple very different systems in a modular way, opening up a range of new opportunities for quantum control.

Contents

Abstract **i**

Introduction **1**

1 Remote Hamiltonian interactions mediated by light **7**
- 1.1 Introduction . . . 7
- 1.2 General Description . . . 10
- 1.3 Specific geometries . . . 16
- 1.4 Coherent dynamics in the looped geometries . . . 21
- 1.5 Conclusion . . . 29

2 Membrane optomechanical system **31**
- 2.1 Cavity optomechanics . . . 31
- 2.2 Membrane optomechanical cavity . . . 37
- 2.3 Silicon-nitride membranes . . . 43
- 2.4 Cavity assembly . . . 47
- 2.5 Experimental setup . . . 52
- 2.6 Basic optomechanical characterisation . . . 61
- 2.7 Measurement of the optomechanical response . . . 66
- 2.8 Conclusion . . . 74

3 Atomic Ensemble **75**
- 3.1 Theory of the atom-light interface . . . 75
- 3.2 Experimental setup . . . 91
- 3.3 Preparation of the atomic ensemble . . . 94
- 3.4 Spin-state preparation and readout . . . 102
- 3.5 Characterization of the spin-light interface . . . 112
- 3.6 Collective effects . . . 118
- 3.7 Conclusion . . . 123

4 Spin-optomechanical interface **125**
- 4.1 Optical interface between an optomechanical and an atomic spin ensemble 125
- 4.2 Double-pass spin-light interface . . . 131
- 4.3 Details of the experimental setup . . . 142

4.4 Coupled spin-membrane dynamics . . . 145
4.5 Conclusion . . . 154

5 Light-mediated strong coupling between a mechanical oscillator and atomic spins one meter apart 155
5.1 Introduction . . . 155
5.2 Description of the coupling scheme . . . 156
5.3 Results . . . 159
5.4 Conclusion . . . 166

6 Outlook 167

Appendix A Cascaded quantum systems 171
A.1 Proof that Λ_{eff} is positive semidefinite . . . 171
A.2 Master equation . . . 172
A.3 Time delays . . . 172
A.4 Gaussian Dynamics . . . 174
A.5 Gaussian state entanglement criteria . . . 176
A.6 Master equation with delay . . . 176
A.7 Adiabatic elimination of the cavity . . . 179

Bibliography 183

Acknowledgements 199

Introduction

Two physical objects can strongly interact if they are in close proximity to each other. In the classical world, it seems natural that billiard balls only collide upon contact and two pendula show coupled oscillations when they are connected by a short spring. In a similar way, this is also true for most implementations of strongly coupled quantum systems. For example, trapped ions [1] or solid-state spins [2] couple via short-range electrostatic or magnetic forces, superconducting quantum bits (qubits) via capacitive or inductive coupling [3] and Rydberg atoms interact via dipole-dipole interactions [4]. These systems are routinely operated in the strong-coupling regime, where energy can be exchanged between them much faster than the decoherence time of the individual systems [5, 6]. To achieve this, it is important that the systems are in close proximity to each other, to both achieve a large coupling strength and to avoid parasitic coupling to the environment that would add unwanted dissipation. By this argument, increasing the distance between two quantum systems would weaken their interaction strength such that at some point dissipative processes take over and the coherent character of the interaction is lost [7].

In order to overcome this limitation and realize entanglement of quantum systems in large-scale quantum networks, the spatially separated systems can be interfaced via propagating photons [8, 9, 10]. This principle is universal and works for all quantum systems with strong light-matter interactions, like atoms [11, 12] solid-state spins [13], or optomechanical systems [14]. By mapping the state of a quantum system onto a photon which propagates along a low-loss, one-dimensional waveguide, quantum information is preserved in a well defined photonic mode. This can be used either to implement an efficient, unidirectional state-transfer by absorbing the photon in another system [15, 16], or to herald entanglement between two systems conditioned on the detection of a single photon emitted by both of them in an indistinguishable way [8]. Despite their proven usefulness for long-distance quantum networks, these quantum communication protocols do not implement coherent Hamiltonian interactions like the short-range couplings mentioned in the beginning. In one case the coupling is unidirectional, and in the other it is probabilistic and must be made deterministic by a single-photon detection event and feedback on the systems. These protocols are thus relatively limited compared to the variety of quantum operations available with short-range Hamiltonian couplings [17].

A related approach to generate long-distance light-mediated couplings between quantum systems is the framework of cascaded quantum systems [18, 19], which recently attracted great interest in the context of chiral quantum optics [20, 21] and waveguide quantum-electrodynamics [22, 23]. Here, multiple quantum systems couple to the same waveguide, over which they continuously exchange photons and thus interact. A fundamental challenge in this approach is, however, that the same photons that generate the coupling eventually leak out of the open waveguide. Hence, light carries away information about the systems which inherently gives rise to decoherence channels that must be equally strong as the light-mediated coupling. For this reason, cascaded quantum systems are mainly regarded as a means for generating entanglement by collective dissipation [24, 25, 26, 27] or, again, conditioning on a collective measurement [28].

A natural way to counter decoherence by photon loss is to terminate the waveguide with mirrors such that it forms a high quality resonator. This has enabled coherent coupling of superconducting qubits [29], atoms [30], or atomic mechanical oscillators [31] in mesoscopic setups. In another intriguing experiment, an ensemble of superconducting qubits in a collective dark state has been turned into a cavity that strongly couples to another qubit [32]. However, stability constraints and bandwidth limitations make it difficult to extend such resonator-based approaches to larger distances. Despite recent advances with coupled cavity arrays [33, 34], strong bi-directional Hamiltonian coupling mediated by light over a truly macroscopic distance remains a challenge.

In this thesis, we address this open problem by asking: *Can a beam of light mediate coherent Hamiltonian interactions between two distant quantum systems?* The answer to this question must provide a method to suppress the leakage of quantum information from the systems, while preserving the light-mediated coupling. In essence, all information about the systems must be erased before the light leaks out [35]. This seems to be at odds with the goal that the systems interact strongly via the waveguide. Our solution to this problem (cf. chapter 1 and reference [36]) relies on engineering the cascaded light-matter interactions in a loop, such that every system couples twice to the waveguide and with opposite phase. In this way, the light scattered by the systems into the waveguide interferes destructively such that decoherence is suppressed. Interaction between the systems is still possible when their coupling points to the waveguide are interleaved such that they can exchange photons with each other. In this way, the coupled systems are effectively closed to the environment, even though the light field mediates strong interactions between them. This finding is also striking from the perspective that light fundamentally carries vacuum noise [37], which would be imparted onto the light-coupled systems and result in quantum back-action [31]. However, destructive interference of the light field that leaks out from the systems also implies that noise entering the systems via the waveguide interferes destructively. Consequently, the light-mediated coupling can be seen in analogy to an ideal spring which couples the systems without introducing any noise. Of course, the above discussion has referred to an idealized scenario, where no light is lost between the systems. In reality this is never the case, but we can show that even in the presence of significant optical loss, coherent interactions can be realized and generate substantial amounts of entanglement between the systems. In parallel to our own work which was published in [36], a related article focusing on superconducting qubits has proposed a similar method to generate Hamiltonian interactions mediated by an open waveguide [38]. This shows that our results are relevant for a wide variety of physical systems.

In parallel with this theoretical work, we designed and realized an experiment that directly implements such a light-mediated interaction between a spin-polarized atomic

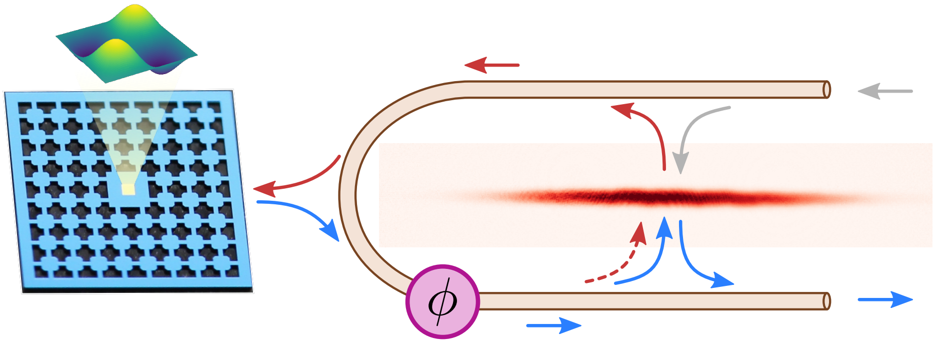

Figure 0.1: Sketch of the long-distance coupling scheme. Light couples an atomic ensemble to a micromechanical membrane oscillator and vice versa. The optical field takes a path in the form of a loop that couples twice to the spin, thus enabling destructive interference of the quantum back-action for phase shift $\phi = \pi$. The images show a side-view absorption image of the atomic cloud on the right and on the left a photograph of the silicon nitride membrane (yellow square) suspended from a silicon chip (blue) with phononic bandgap structure [41]. The inset on top left shows the mode profile of the membrane's 2,2 vibrational mode.

ensemble [39] and a micromechanical membrane oscillator [40]. A sketch of the setup is shown in Fig. 0.1. Here, the waveguide is actually a free-space laser beam that connects the two devices, which are held in independent vacuum systems, over a macroscopic distance of one meter in a room temperature environment. The arrows in the sketch symbolize the signals that propagate from the atomic ensemble (red) to the membrane and from the membrane (blue) back to the atoms. At the input, the light contains only vacuum noise (gray). An optical phase shift (ϕ) which is applied to the fields going from the membrane back to the atoms allows to control whether the spin signal on the output interferes constructively ($\phi = 0$) or destructively ($\phi = \pi$). This allows us to modify the character of the effective interaction between the spin and the membrane without having to modify the systems themselves. For $\phi = 0$ the interaction is dissipative and the spin is subject to enhanced quantum back-action, while for $\phi = \pi$ the interaction is Hamiltonian and quantum back-action onto the spin is suppressed. In order to also cancel back-action induced decoherence of the membrane, an additional optomechanical coupling would have to be realized. However, our theoretical work shows that this is not required to observe quantum coherent dynamics between the two systems, as long as the atoms couple more strongly to the light than the membrane.

The spin-membrane coupling experiment, which is the topic of this thesis, follows a tradition of experiments investigating the light-mediated interaction between atoms and optomechanical systems in the research group of P. Treutlein. The coupling of atoms with solid-state optomechanical systems [42] holds great potential for future applications in quantum metrology [43, 44] and for hybrid quantum devices [45]. First experiments used the motional states of atoms trapped in an optical lattice that was retro-reflected from the membrane in free-space to dampen the membrane by dynamical back-action [46]. By enhancing the membrane-light interaction using an optical cavity, it was possible to observe significant sympathetic cooling of the membrane by the laser-cooled atoms from room temperature to below 1 K [47]. In an attempt to increase the atom-membrane coupling even further by loading more atoms into the lattice and reducing the laser detuning from the atomic transition, the system was observed to become dynamically unstable due to light-mediated collective atomic motion [48]. At this point, a proposal for instead using the atomic spin degree of freedom had already been developed [49], which would allow a much higher level of control over the atomic system. However, in this proposal, the importance of quantum back-action cancellation for coherent light-mediated dynamics and how it can be controlled were not yet understood in general terms. This triggered us to design an experimental setup which grants full flexibility in designing cascaded interactions between the systems and inspired the development of a fully general theoretical framework, which is part of this thesis [36]. One of the key achievements of this new theory is, that its comprehensive language enables the design of such cascaded Hamiltonian couplings between any quantum systems with strong light-matter interactions. Recently, two other groups have also implemented hybrid mechanical-atomic systems, demonstrating sympathetic cooling of a membrane in a cryogenic setup [50] and quantum back-action evading measurement using an atomic spin ensemble in a vapour-cell [51], respectively.

Atomic ensembles are currently one of the major platforms for quantum optics research [39]. In particular, they are investigated for quantum communication as quantum memories [52] and quantum repeaters [53], and for quantum metrology [44], optical atomic clocks [54] and quantum simulation [55]. Laser-cooled atomic ensembles at ultracold temperatures offer exquisite control over collective atomic spin states, which has enabled the preparation and detection of highly non-classical states [44]. Recently, novel light-matter interfaces between atoms and nanophotonics have been realized [20, 21] which enable new paradigms of light-matter coupling, i.e. chiral quantum optics, which seem perfectly tailored towards applications in quantum networks [10].

Optomechanical systems [56] have seen tremendous progress over the past years. With the large mechanical quality factors that have recently been achieved [57, 58, 59, 60], cavity optomechanical systems have entered a regime where thermal decoherence can be strongly suppressed and give way to quantum motion. Cavity optomechanics uses laser light to detect and manipulate mechanical motion in the quantum regime and has enabled ground-state cooling [61, 62, 63] and measurement-based quantum control [64, 65]. Moreover, cavity optomechanics also provides a means for efficient conversion between the microwave and optical domain [66, 67]. This offers exciting prospects for connecting different superconducting quantum processors in an optical room-temperature network. Finally, optomechanical devices have also been used to generate non-classical correlations between phonons and photons [68] in the spirit of the quantum communication protocols originally proposed for atomic ensembles [8]. This has been taken one step further by creating entanglement between two mechanical devices [14].

To emphasize the similarity between collective spins and optomechanical systems, we show sketches of these light-matter interfaces in Fig. 0.2. In cavity optomechanics, the vibrations of a mechanical oscillator couple to an optical cavity field via radiation pressure [56] (see Fig. 0.2a). This interaction can be understood in terms of optical Raman transitions between different mechanical Fock states. If the cavity bandwidth

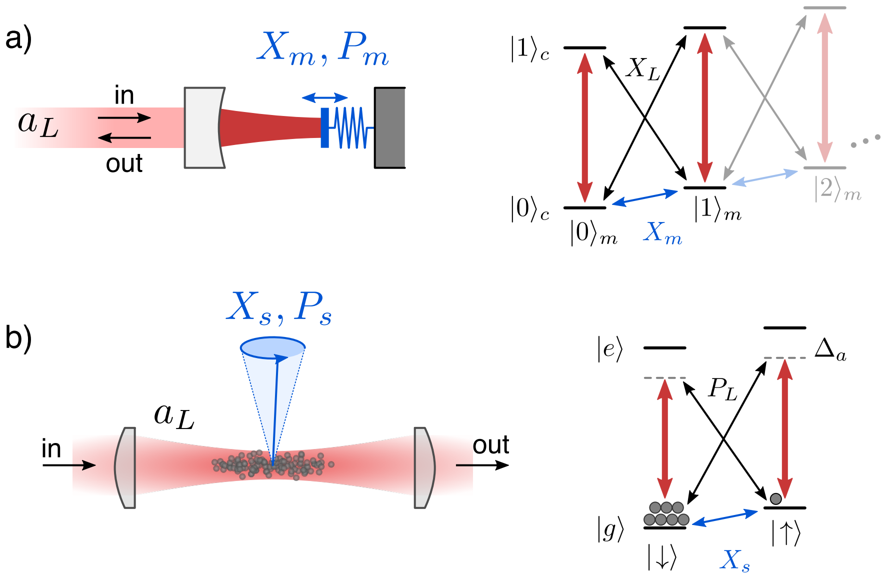

Figure 0.2: Sketch of light-matter interfaces. a) Optomechanical interface with level diagram. b) Atom-light interface with level diagram.

is much larger than the mechanical resonance frequency (non-resolved sideband regime) this interaction effectively reduces to a coupling between the mechanical oscillator and the external field to which the cavity decays. The optomechanical interaction Hamiltonian is then given by $H_m \propto X_m X_L$, where X_m is the mechanical displacement and X_L is the amplitude quadrature of the light field.

The interface between an atomic ensemble and a free-space laser beam is sketched in Fig. 0.2b. Here, a laser field that is detuned from the atomic $|g\rangle \rightarrow |e\rangle$ dipole transition drives Raman transitions between different spin sublevels $|\downarrow\rangle$ and $|\uparrow\rangle$ of the ground state $|g\rangle$. Since the light field couples equally to all atoms, a single photon creates a single spin excitation that is a symmetric superposition of one out of all spins being flipped. Hence, the coupling strength of an ensemble with N atoms is enhanced by $\sqrt{N}$ [8]. The atomic spin ensemble can then be described in terms of collective variables X_s, P_s that resemble quadratures of a harmonic oscillator [39]. The spin-light interaction Hamiltonian has the form $H_s \propto X_s P_L$, where P_L is the phase quadrature of the light field.

With this striking similarity between the optomechanical interaction and the spin-light interaction, it seems natural to couple these two systems. Mechanical oscillators offer ultra-high mechanical quality factors but suffer from thermal decoherence due to their support. Contrarily, spin oscillators in cold atomic ensembles are very well decoupled from any thermal noise and can be prepared in the ground state (all atoms in $|\downarrow\rangle$) by means of optical pumping. Moreover, the spin resonance frequency is given by the energy splitting between the two ground states, which can readily be tuned into resonance with the mechanical oscillator by means of an external magnetic field. Using the light-mediated coupling, this configuration allows us to realize energy exchange oscillations and normal-mode splitting between the membrane oscillator and the collective atomic spin oscillator (cf. chapter 5).

On top of that, a collective spin can also mimick an oscillator with effective negative mass [28, 69] if it is optically pumped into the upper spin state $|\uparrow\rangle$. This realizes an inverted configuration where every excitation actually reduces the spin's energy. This feature has enabled quantum back-action evading measurement in a hybrid spin-membrane experiment [51] and the observation of a parametric instability between the spin and motion of a cold atomic gas [70]. In this work, we use the negative-mass spin configuration to create a resonant parametric-gain interaction between the spin and the membrane that leads to two-mode thermal noise squeezing (cf. chapter 5). In principle, this interaction enables remote spin-membrane entanglement if thermal noise on the mechanical oscillator can be reduced. The experimental results of this thesis were published as a research article in [71].

This thesis is organized as follows:

Chapter 1 provides the general theoretical framework for cascaded quantum systems with loops which allows us to design long-distance Hamiltonian interactions between quantum systems.

Chapter 2 introduces the membrane optomechanical system and its characterization in the fast-cavity regime.

Chapter 3 introduces the atomic ensemble and a characterization of the Faraday interaction between light and the collective atomic spin.

Chapter 4 presents the experimental setup that we have built to create light-mediated interactions between the collective spin and the membrane. It also includes a detailed theoretical analysis of the various dynamical regimes that can be accessed by the coupling.

Chapter 5 presents the observation of strong light-mediated coupling between the atomic spins and the membrane.

Chapter 6 concludes this thesis and gives an outlook on future experiments in the quantum regime.

CHAPTER 1

Remote Hamiltonian interactions mediated by light

We address a fundamental question of quantum optics: Can a beam of light mediate coherent Hamiltonian interactions between two distant quantum systems? This is an intriguing question whose answer is not *a priori* clear, since the light carries away information about the systems and might be subject to losses, giving rise to intrinsic decoherence channels associated with the coupling. Our answer is affirmative and we derive a particularly simple sufficient condition for the interactions to be Hamiltonian: The light field needs to interact twice with the systems and the second interaction has to be the time reversal of the first. We demonstrate that, even in the presence of significant optical loss, coherent interactions can be realized and generate substantial amounts of entanglement between the systems. Our method is directly applicable for building hybrid quantum systems, with relevant applications in the fields of optomechanics and atomic ensembles.

The content of this chapter has been published in [36].

1.1 Introduction

Light is an excellent carrier of information over a distance. It not only has become an essential tool of modern communication technologies, but is also the most realistic quantum information carrier for large scale quantum communication networks [9]. On the other hand, coherent Hamiltonian coupling between quantum objects is typically observed on a local scale and mediated by short-range interactions, e.g. ions interacting via the Coulomb force [1] or superconducting qubits via capacitive or inductive coupling [3].

Instead of carrying information from one point to another, light can also be used to mediate a remote Hamiltonian interaction between two distant objects and thus create an "effective spring" between them. We present here a formalism to describe such light-mediated interactions, discuss their properties, and in particular derive conditions for them to be Hamiltonian.

Light-mediated interactions not only allow one to remotely couple two similar objects, but any set of different objects, as soon as a proper light-matter interface exists for each of them. This may open up new possibilities for quantum technologies, allowing one to combine the strengths of disparate devices in order to meet the requirements of quantum technologies in a modular setup [72].

We consider a quite general scenario where quantum systems couple sequentially, and possibly repeatedly, to a one-dimensional (1D) waveguide. Such a setup is described theoretically in the framework of cascaded quantum systems [18, 19, 73] and generically results in Hamiltonian interactions among the quantum systems along with collective decay at a comparable level. This conceptual framework was applied fruitfully in the description of cascaded optical cavities [74], atomic ensembles interacting with light in free space [75], superconducting systems [23] and optomechanical devices [76]. It also received renewed interest in recent years in the context of chiral quantum optics where near-field effects in nanophotonics are exploited in order to realize unidirectional coupling of quantum emitters to waveguides [27]. Our work contributes to the theory of cascaded quantum systems by demonstrating that it is possible to exploit the light-induced interaction for coherent dynamics among the quantum systems by efficiently suppressing the relative strength of light-induced decoherence. The main idea is to use

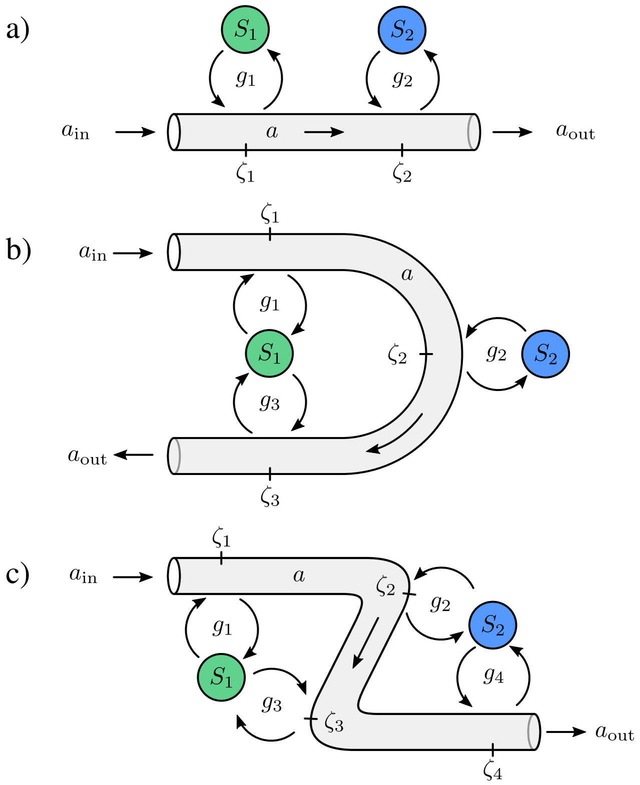

Figure 1.1: Coupling schemes considered in this chapter. (a) Standard cascaded setup where two systems S_1 and S_2 interact sequentially with a 1D optical mode a and realize a unidirectional interaction $1 \to 2$. (b) Looped cascaded setup where system 1 couples to the light field twice, once before system 2 and once after, thus realizing the interaction $1 \to 2 \to 1$. (c) Setup with double passes through both systems, realizing the interaction $1 \to 2 \to 1 \to 2$.

a looped geometry where one or several of the cascaded quantum systems interact with the beam of light twice, effectively reducing or removing decoherence via destructive interference of quantum noise. For the specific case of superconducting systems such an effect has been studied theoretically in Ref. [38]. Here we aim to develop a general framework for the engineering of remote Hamiltonian interactions mediated by light which is applicable to a large variety of cascaded quantum systems.

We focus on simple geometries involving multiple passes of light through two quantum systems S_1 and S_2 which are sketched in Fig. 1.1. In geometry (a), because light carries information in a single direction, the effective dynamics cannot be reduced to a Hamiltonian. In (b) however, where light travels back and forth, the effective interaction can be Hamiltonian and we derive a simple condition for this: The second interaction of light with S_1 must be the time reversal of the first. Light necessarily exits the optical mode with some information about the two systems which leads to a diffusive noise process associated with measurement back-action. In configuration (a), the strength of this noise process will always be stronger than the mediated coherent interaction. In case (b), however, engineering a time reversal in the two light-matter interactions with S_1 cancels the back-action noise and erases the measurement done by the light field. This allows us to increase the coherent coupling strength without adding excess noise and we show that, in principle, the coherent coupling strength can be made arbitrarily stronger than the light-induced diffusion rate on S_2. To go one step further, the remaining back-action noise on S_2 can also be removed by extending the simple looped geometry by another time-reversed light-matter interaction with S_2 as depicted in Fig. 1.1(c). In the absence of any back-action noise, this scheme realizes a perfect Hamiltonian interaction between two quantum systems.

Previously, the same formalism has been used to treat hybrid mechanical-atomic systems [82, 83, 84, 49], lacking, however, precise and general statements about the role of optical losses, optical back-action noise, and the time-reversal condition required to achieve Hamiltonian dynamics. Here, we address all of these open questions in a unified framework, thus greatly facilitating the design of future experiments.

Our scheme readily applies to a variety of quantum systems that interact coherently

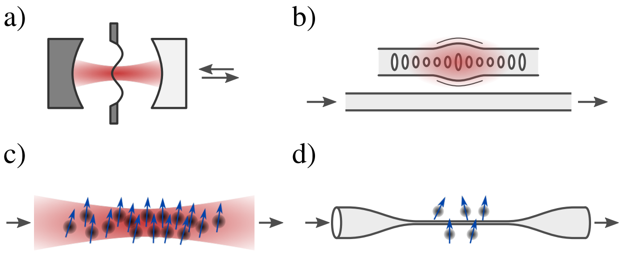

Figure 1.2: Overview of suitable experimental systems to build cascaded systems as shown in Fig. 1.1. (a) Membrane-in-the-middle optomechanical cavity coupled to a free-space laser beam [77, 78], (b) integrated optomechanical crystal device coupled to an optical waveguide [79, 14], (c) collective atomic spin ensemble probed by a free-space laser beam [28], and (d) atoms coupled to a nano-fiber [80, 81].

with free-space or guided light (for examples, see Fig. 1.2), in particular optomechanical systems [56], atomic ensembles [39], nanophotonic devices [20, 21], and hybrid quantum systems thereof [42, 45]. These systems exhibit large cooperativity for the coupling to the waveguide mode as compared to all other modes.

A number of related works that are close to but beyond the scope of this work also exist and can be discussed and interpreted with the insight presented here. This includes single-pass entanglement schemes with conditioning on a measurement of the output field [25, 75, 51, 85], or experiments involving cavity-mediated effective interactions [86, 31]. We remark that the results presented here could be generalized to describe light-mediated dynamics in optical ring cavities. We emphasize, however, that the free-space character of our scheme is particularly appealing for high-bandwidth and long-distance networks, and allows local operations on the optical field between nodes which can be used to modify the character of the interaction on the timescale of the mediated dynamics.

This chapter is organized as follows. In Sec. 1.2, we consider the general problem of a set of isolated quantum objects interacting locally and possibly repeatedly with a traveling light field. The field carries information between the different objects, creating an effective interaction, before exiting the system. The local light-matter interactions are assumed to be Hamiltonian and linear in the field quadratures. Propagation delays are neglected relative to the local and effective interaction dynamics. For this problem, we derive a general Markovian master equation that captures the effective dynamics.

In Sec. 1.3, we apply the results of the general theory to the different geometries of Fig. 1.1 and discuss the resulting dynamics. Based on a decomposition of the master equation into Hamiltonian and dissipative evolution, we identify conditions such that the effective dynamics is dominated by the Hamiltonian term. We find that in these cases light-induced dissipation can in principle be made arbitrarily small such that the effective coupling becomes fully coherent.

Section 1.4 discusses the cooperativity as a figure of merit for coherent dynamics and analyzes different applications relevant for hybrid quantum systems. Straightforward results also arise for a scenario with multiple passes of light through the same object. This leads, for example, to an apparent cancellation of radiation-pressure noise in an optomechanical system or deterministic squeezing in a spin ensemble.

1.2 General Description

We consider N quantum systems that sequentially interact with a common traveling electromagnetic field mode $a(\zeta)$, whose path is parametrized by a position coordinate ζ. Using a Fourier transform, we can decompose a into its different frequency components [37]

$$a(\zeta) = \int \frac{\mathrm{d}\omega}{\sqrt{2\pi}} a(\omega) e^{\mathrm{i}\omega\zeta/c}, \tag{1.1}$$

where c is the speed of light and it is implicitly assumed that the mode frequencies ω are limited to a small bandwidth, i.e. sidebands around the carrier frequency of a laser. The (equal-time) commutation relations of a read $[a(\zeta), a^\dagger(\zeta')] = c\delta(\zeta - \zeta')$ and $[a(\omega), a^\dagger(\omega')] = \delta(\omega - \omega')$ in the position and frequency domains, respectively. The dimensions of a are such that $a^\dagger(\zeta)a(\zeta)$ is the photon flux (unit s^{-1}) at position ζ and $a^\dagger(\omega)a(\omega)$ is the photon number at frequency ω per unit bandwidth (unit $\mathrm{Hz}^{-1} = \mathrm{s}$).

Each of the light-matter interactions happens at a distinct spatial coordinate ζ_j along the optical path and couples a system operator B_j to the local field $a(\zeta_j)$ with real-valued coupling strength g_j (see Fig. 1.3). A total of $n \geq N$ interactions are allowed such that any system can interact with the field more than once. We work in a rotating frame for the optical mode where the full Hamiltonian reads

$$\begin{aligned} H &= H_0 + H_{\text{int}}, && (1.2)\\ H_0 &= \sum_{i=1}^{N} H_i + \int \mathrm{d}\omega \hbar\omega \; a^\dagger(\omega) a(\omega), && (1.3)\\ H_{\text{int}} &= \sum_{j=1}^{n} \hbar g_j \left(B_j^\dagger a(\zeta_j) + a^\dagger(\zeta_j) B_j \right). && (1.4) \end{aligned}$$

The coordinates ζ_j are chosen in increasing order such that they can be associated with propagation times $\tau_j = \zeta_j / c$. Delays between interactions j and k are denoted $\tau_{jk} = \tau_j - \tau_k$.

The system operators B_j can be arbitrary operators acting on a single system. However, their typical form for harmonic oscillators or spin systems as considered in this work is $B_j = e^{\mathrm{i}\phi_j}(\mu_j b_{s_j} + \nu_j b_{s_j}^\dagger)$. Here, b_{s_j} and $b_{s_j}^\dagger$ are annihilation and creation operators, respectively, of an oscillator or ladder operators of a spin [44] satisfying the commutation relation $[b_j, b_k^\dagger] = \delta_{jk}$. We use the label s_j for the system that is involved in light-matter interaction j. The phase ϕ_j selects a specific optical quadrature and the coefficients $\mu_j = \cos(\theta_j)$ and $\nu_j = \sin(\theta_j)$ correspond to different amplitudes for Stokes and anti-Stokes scattering, respectively, realizing beam-splitter and parametric gain interactions with the light field [87, 88]. The parameters ϕ_j and θ_j can be tuned experimentally. For light-matter interactions based on two-photon transitions involving a classical drive, ϕ_j is the relative phase between the quantum and classical fields. It is adjustable via polarization optics or interferometry. In cavity-optomechanical systems, tuning the scattering amplitudes μ_j, ν_j is commonly achieved via the detuning of the pump laser relative to the cavity resonance [56]. For atomic spin ensembles it requires adjusting the pump laser's polarization and detuning relative to the atomic transition [39]. Note that we assume B_j to be dimensionless such that g_j^2 has dimension Hz and can be interpreted as the measurement rate with which information about B_j is read out by the light field [89]. The local Hamiltonians considered here are those for harmonic oscillators, i.e. $H_i = \hbar\Omega_i b_i^\dagger b_i$ with oscillation frequency Ω_i.

We remark that for linearized light-matter interactions, as typically encountered in cavity optomechanics or quantum optics with atomic ensembles, the coupling strengths g_j are proportional to the field amplitude of a pump laser co-propagating with the quantum field. In fact, it is the pump laser that enhances the coupling to a single mode of the waveguide over that to all other modes. In chiral quantum optics, such uni-directional light-matter interactions can also be engineered without the need of a pump laser.

In the following we derive equations for the effective coupled dynamics of the N quantum systems by eliminating the light field in a Born-Markov approximation. In 1.2.1 we write the Heisenberg-Langevin equations of motion in the spirit of the input-output formalism [90] commonly used in quantum optics, cavity optomechanics and

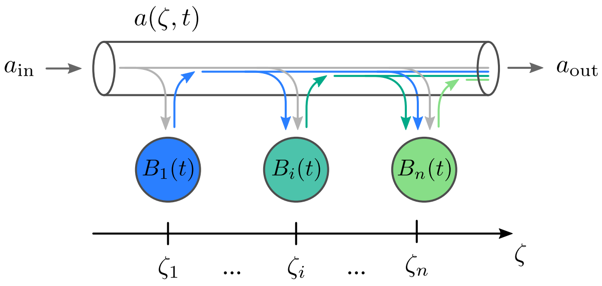

Figure 1.3: Sketch of the cascaded light-matter interactions.

cavity quantum electrodynamics. They provide insight on how one system drives another via the light field and can be used to obtain a master equation with stochastic differential calculus [73]. In Sec. 1.2.2 we directly derive such a master equation by tracing out the light field within the density matrix formalism. Losses are then included and the resulting coupled dynamics are later discussed for the different geometries of Fig. 1.1.

1.2.1 Heisenberg-Langevin equations

In the Heisenberg picture, the equation of motion of the optical field is

$$\dot{a}(\omega,t) = -\mathrm{i}\omega a(\omega,t) - \mathrm{i}\sum_{j=1}^{n} \frac{g_j}{\sqrt{2\pi}} B_j(t) e^{-\mathrm{i}\omega\tau_j}. \tag{1.5}$$

This equation of motion is subject to the initial condition $a(\omega, t = 0) = a_0(\omega)$. Formal integration to a time t larger than all propagation delays τ_{jk} and a Fourier transform yields [90, 18]

$$a(\zeta,t) = a_{\mathrm{in}}(\zeta,t) - \mathrm{i}\sum_{j=1}^{n} g_j B_j(t-(\zeta-\zeta_j)/c)\Theta(\zeta-\zeta_j). \tag{1.6}$$

Here, $a_{\mathrm{in}}(\zeta)$ is the Fourier transform of $a_0(\omega)$ according to Eq. (1.1) which is the input field driving the system. In practice, $a(\zeta,t) = a_{\mathrm{in}}(\zeta,t)$ for $\zeta < \zeta_1$. The Heaviside step function is defined by $\Theta(x) = 1$ for $x > 0$, $\Theta(x) = 0$ for $x < 0$ and $\Theta(0) = 1/2$. Evaluating the above expression (1.6) at positions $\zeta > \zeta_n$ yields the output field

$$a_{\mathrm{out}}(t) = a_{\mathrm{in}}(t) - \mathrm{i}\sum_{j=1}^{n} g_j B_j(t+\tau_j), \tag{1.7}$$

which we have defined as $a_{\mathrm{out}}(t) = a(\zeta, t+\zeta/c)$ and the input field via $a_{\mathrm{in}}(t) = a_{\mathrm{in}}(\zeta, t+\zeta/c) = a_{\mathrm{in}}(0,t)$.

The time evolution of the operator b_i of system i interacting with the optical mode via Eq. (1.4) is

$$\dot{b}_i = \mathcal{L}_i b_i - \mathrm{i}\sum_{j=1}^{n} g_j \left([b_i, B_j^\dagger] a(\zeta_j) + a^\dagger(\zeta_j)[b_i, B_j]\right), \tag{1.8}$$

with local dynamics captured by a Liouvillian $\mathcal{L}_i$ that includes dynamics due to H_0. Inserting expression (1.6) gives

$$\begin{aligned}\dot{b}_i &= \mathcal{L}_i b_i - \mathrm{i}\sum_{j=1}^{n} g_j \Big([b_i, B_j^\dagger]a_{\mathrm{in}}(\zeta_j) + a_{\mathrm{in}}^\dagger(\zeta_j)[b_i, B_j]\Big) \\ &\quad - \sum_{j=1}^{n}\sum_{k\leq j} g_j g_k \Theta(\zeta_j - \zeta_k)\Big([b_i, B_j^\dagger(t)]B_k(t-\tau_{jk}) \\ &\qquad - B_k^\dagger(t-\tau_{jk})[b_i, B_j(t)]\Big). \qquad (1.9)\end{aligned}$$

This expression is one of our main results. It can be divided into three parts, (i) internal dynamics, (ii) source terms of the input field driving the systems and (iii) interactions between systems. The fact that the optical input field drives all systems in a similar way means that the resulting noise processes are correlated between all systems. It has been demonstrated that these noise channels can be made to destructively interfere in the collective measurement of two oscillators with equal and opposite linear responses [51]. If the quantum noise correlations induced by the input field are stronger than intrinsic system noise processes the collective measurement can establish entanglement or even Einstein-Podolsky-Rosen (EPR) correlations [91]. In this paper we focus on the direct system-system interactions that can be harnessed to generate coherent quantum dynamics and unconditional quantum correlations. A particular aim of this paper is to explore the conditions under which the coherent mediated interaction can compete against the quantum noise added by the light field. To gain further insight into the interactions achievable within this framework we must make assumptions on the topology of the optical path and the form of the local interactions.

1.2.2 Master equation

Derivation Following Gardiner and Zoller [73] an alternative description of the effective dynamics can be obtained in the framework of a quantum optical master equation. We take the perspective that the optical mode is a vacuum bath to which all systems couple in a time-ordered fashion. To derive the master equation we work in an interaction frame with respect to the Hamiltonian H_0. Operators in the interaction frame are marked with a tilde symbol. The time evolution of the reduced density operator $\rho = \mathrm{Tr}_L\{\rho_{\mathrm{tot}}\}$ of the systems 1 to N is obtained by tracing out the light field L. This gives

$$\dot{\tilde{\rho}}(t) = -\frac{1}{\hbar^2}\int_0^t \mathrm{Tr}_L\left\{[\tilde{H}_{\mathrm{int}}(t), [\tilde{H}_{\mathrm{int}}(t'), \tilde{\rho}_{\mathrm{tot}}(t')]]\right\} \mathrm{d}t'. \qquad (1.10)$$

We then make a weak-coupling and Markov approximation [73]. This replaces the full density matrix $\rho_{\mathrm{tot}}(t')$ in Eq. (1.10) by $\rho(t)\otimes\rho_{L,0}$ and extends the lower limit of the integral to $-\infty$. The state $\rho_{L,0}$ of the optical mode is the vacuum state such that the only non-vanishing optical correlation function is $\mathrm{Tr}_L\left\{a(\omega)a^\dagger(\omega')\rho_{L,0}\right\} = \delta(\omega-\omega')$. Physically, we assume that light exits the cascaded systems on a timescale that is fast when compared to the system dynamics and is only weakly perturbed by the light-matter interaction. By virtue of these approximations we can derive a master equation of the form

$$\dot{\tilde{\rho}} = -A\tilde{\rho} - \tilde{\rho}A^\dagger + \mathcal{J}\tilde{\rho}, \tag{1.11}$$

where

$$\begin{aligned} A &= \sum_j \sum_{k<j} g_j g_k \tilde{B}_j^\dagger(t)\tilde{B}_k(t-\tau_{jk}) && (1.12)\\ &\quad + \sum_j \frac{g_j^2}{2}\tilde{B}_j^\dagger(t)\tilde{B}_j(t), && (1.13)\end{aligned}$$

and

$$\begin{aligned} \mathcal{J}\tilde{\rho} &= \sum_j \sum_{k<j} g_j g_k \tilde{B}_k(t-\tau_{jk})\tilde{\rho}(t)\tilde{B}_j^\dagger(t) + \text{ h.c.} && (1.14)\\ &\quad + \sum_j g_j^2 \tilde{B}_j(t)\tilde{\rho}(t)\tilde{B}_j^\dagger(t). && (1.15)\end{aligned}$$

We remark that this result also holds in the case where the coupling constants g_i or the phase factors ϕ_i or θ_i determining the local interactions are time dependent. In this case these parameters are evaluated at the same times as their parent system operators B_i.

The structure of the general master equation derived above demands some explanation. Looking at the expression for the operators A and $\mathcal{J}$, we distinguish between two types of contributions: (i) lines (1.12) and (1.14) describe correlated dynamics mediated by the light field. Any system s_j is driven by other systems s_k with $k < j$ that were probed by the light field at earlier times. Causality is preserved because interactions with systems probed in the future ($k > j$) are not present. The coupling constants for these interactions are the products $g_j g_k$ of the coupling strengths of the individual light-matter interactions. We note that these correlated dynamics can be of either dissipative or unitary character, i.e., collective damping and amplification or Hamiltonian interaction. (ii) Lines (1.13) and (1.15) contain purely non-unitary time evolution acting on the individual systems with corresponding dissipation rates g_j^2. This results in radiative decay as in spontaneous emission or decay of an optical cavity [90] and associated diffusion due to quantum noise from the input field. Since these noise processes are uncorrelated, they destroy quantum coherence between the systems.

In order to harness the mediated interactions for inter-system entanglement and coherent dynamics, they have to be made stronger than the uncorrelated quantum noise. At first sight this task appears impossible because the coherent coupling strengths $g_j g_k$ can never exceed both dissipation rates g_j^2 and g_k^2. However, as we will show in the following section, one can engineer the system-reservoir interaction in order to suppress quantum noise while preserving the effective light-mediated interaction.

Effective interaction To interpret the general master equation (1.11), we compare it with the Lindblad form

$$\dot{\rho} = -\frac{\mathrm{i}}{\hbar}[H_{\text{eff}}, \rho] + \sum_k \mathcal{D}[j_k]\rho, \tag{1.16}$$

with effective Hamiltonian H_{eff} and jump operators j_k. The Lindblad terms read $\mathcal{D}[j]\rho = j\rho j^\dagger - \frac{1}{2}\{j^\dagger j, \rho\}$. Here and in what follows we neglect the time delays τ_j in accordance with the Markov approximation. We also transform back to the laboratory frame and drop the tilde on top of interaction frame operators. The effective Hamiltonian is then

$$H_{\text{eff}} \quad = \quad \frac{\hbar}{2\mathrm{i}}(A - A^\dagger), \tag{1.17}$$

and the dissipative part can be written as

$$\sum_k j_k^\dagger j_k = A + A^\dagger =: \Lambda_{\text{eff}}. \tag{1.18}$$

As shown in Appendix A.2, the form of $\mathcal{J}\rho = \sum_k j_k \rho j_k^\dagger$ is closely linked to that of Λ_{eff} and it is sufficient to know A or Λ_{eff} in order to write down the equations of motion. In the model presented so far, the effective Hamiltonian is

$$H_{\text{eff}} \quad = \quad \sum_j \sum_{k<j} \hbar g_j g_k \frac{1}{2\mathrm{i}} \left(B_j^\dagger B_k - B_k^\dagger B_j \right), \tag{1.19}$$

and the dissipative dynamics are governed by a single collective jump process $\Lambda_{\text{eff}} = j_+^\dagger j_+$ with jump operator

$$j_+ \quad = \quad \sum_j g_j B_j, \tag{1.20}$$

which is a superposition of all subsystem operators. More diverse dissipative dynamics are observed when optical losses are included.

Master equation including losses It is essential to take into account optical losses in our model, as they will contribute significantly to decoherence by introducing uncorrelated vacuum noise. To describe losses we insert beam splitters with (amplitude) transmission coefficient η_j between every pair of interactions j and $j+1$. The beam-splitter relations

$$a(\zeta_j) \;\rightarrow\; \eta_j a(\zeta_j) + \sqrt{1-\eta_j^2}\, h_j(\zeta_j), \tag{1.21}$$

mix the optical mode with an uncorrelated mode h_j in the vacuum state. With losses the new time evolution operator becomes

$$A = \sum_j \sum_{k<j} \eta_{jk} g_j g_k B_j^\dagger B_k + \sum_j \frac{g_j^2}{2} B_j^\dagger B_j, \tag{1.22}$$

where $\eta_{jk} = \eta_k \cdot \ldots \cdot \eta_{j-1}$ is the transmittance from system k to system j. The sandwich term changes accordingly:

$$\mathcal{J}\rho = \sum_j \sum_{k<j} \eta_{jk} g_j g_k (B_k \rho B_j^\dagger + B_j \rho B_k^\dagger) + \sum_j g_j^2 B_j \rho B_j^\dagger. \tag{1.23}$$

If the coupling constants g_j depend on the amplitude of a co-propagating pump field, they also need to be rescaled with the total transmission until system j, i.e. $\eta_{j1} = \eta_1 \cdot \ldots \cdot \eta_{j-1}$. This renormalizes the coupling constants and only becomes important in the case when a system interacts multiple times with the optical mode.

From the two equations (1.22) and (1.23), we see that losses between two systems only affect the cross-coupling terms, but leave the noise terms unchanged. Put another way, the effective interaction mediated by light is weakened relative to the quantum noise added by the light. The Lindblad jump operators in this new setting can be derived by diagonalizing the Hermitian matrix Λ_{eff} in the basis of the B_j operators. The eigenvalues of Λ_{eff} are the corresponding damping rates. In the presence of losses there is more than one jump operator with non-zero eigenvalue. In Appendix A.1, we provide a proof that Λ_{eff} is always positive semidefinite for the master equation derived above, which ensures that it can be written in Lindblad form with positive rates and that the dynamics are completely positive [92].

1.3 Specific geometries

Having established a general theoretical framework for cascaded quantum systems with looped interactions we now analyze this model for the specific geometries displayed in Fig. 1.1.

1.3.1 Two objects: Single pass

In the case of two cascaded systems like in Figs. 1.1(a) and1.4, the effective Hamiltonian is

$$H_{\text{eff}} = \hbar\eta_1 g_1 g_2 \frac{1}{2\mathrm{i}} \left(B_2^\dagger B_1 - B_1^\dagger B_2 \right), \tag{1.24}$$

and the effective dissipation reads

$$\Lambda_{\text{eff}} = g_1^2\, B_1^\dagger B_1 + g_2^2 B_2^\dagger B_2 + \eta_1 g_1 g_2 \left(B_2^\dagger B_1 + B_1^\dagger B_2 \right). \tag{1.25}$$

We note that the interaction terms in Hamiltonian and collective dissipation are out of phase. In the master equation, both terms partially cancel such that only an interaction term proportional to $B_2^\dagger B_1$ remains. This is a causality statement which reflects the unidirectional nature of the setup. It means that only system 1 can drive system 2, but not vice versa. The jump operators for this cascaded system are $j_\pm = \sqrt{1 \pm \eta_1}(g_1 B_1 \pm g_2 B_2)$ representing dark (j_-) and bright modes (j_+) of the cascaded system. The effective Hamiltonian mixes these modes as $H_{\text{eff}} \propto \mathrm{i}(j_+^\dagger j_- - j_-^\dagger j_+)$.

There is an extensive amount of work on exploiting the mediated interaction between two cascaded quantum systems for a state transfer from system 1 to system 2 [15, 76].

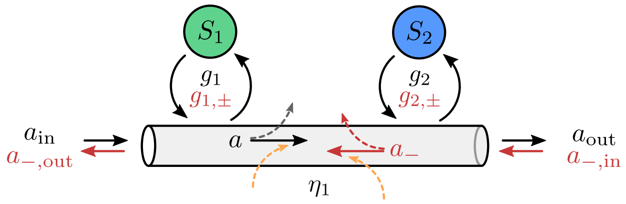

Figure 1.4: Detailed schematic of the single-pass and double-pass coupling schemes. The counter-propagating mode a_- is relevant only for the double-pass scheme.

These proposals make use of the effective interaction to transfer an excitation from system 1 to system 2 via a dark state of the cascaded system. By ensuring that the system always stays in the dark mode j_-, for which the collective decay rate is suppressed by a factor $1-\eta_1$, unity transfer efficiency can be achieved in principle.

1.3.2 Two objects: Double pass

In order to make the interaction bidirectional, one could exploit a counter-propagating optical mode as sketched in Fig. 1.4 to achieve coupling from system 2 to system 1. For simplicity, we neglect standing wave effects here and assume the counter-propagating mode a_- to be independent of the forward-propagating mode $a_+ = a$. Since the two modes are uncorrelated one can simply add up the two resulting effective Hamiltonian and dissipative terms. Because of the antisymmetry of Hamiltonian (1.24) under permutation of the systems 1 and 2 we get

$$H_{\text{eff}} = \hbar\eta_1(g_+ - g_-)\frac{1}{2\text{i}}\left(B_2^\dagger B_1 - B_1^\dagger B_2\right), \tag{1.26}$$

where $g_\pm = g_{1,\pm}g_{2,\pm}$ are the coupling strengths of the light-mediated coupling in forward (+) and backward (−) directions with coupling strengths of the individual systems to the two modes denoted by $g_{i,\pm}$. The effective dissipation (1.25) is symmetric under permutation of systems 1 and 2 such that with two passes

$$\begin{aligned}\Lambda_{\text{eff}} &= \sum_i (g_{i,+}^2 + g_{i,-}^2)B_i^\dagger B_i \\ &\quad + \eta_1(g_+ + g_-)\left(B_2^\dagger B_1 + B_1^\dagger B_2\right).\end{aligned}$$

Consequently, if one naively sets the backward interaction to be of equal strength and phase as the forward interaction, one is left with $H_{\text{eff}} = 0$ and Λ_{eff} being twice that of the single-pass scheme, rendering the interaction completely dissipative. In order to still get non-vanishing coupling, one has to implement a coupling that inverts the sign of the backward interaction relative to the forward interaction, e.g., by setting $g_{1,-} = -g_{1,+}$ but $g_{2,-} = g_{2,+}$. This means that the backward interaction is the time reversal of the forward interaction. We remark that this can be achieved naturally if system 1 couples to the photon momentum which is inverted under reflection. In general, as outlined in the beginning of Sec. 1.2, this sign reversal requires appropriate phase shifts to be applied to the optical field between the two systems.

However, because there are now two independent optical noise inputs the single system decay terms $\sim 2g_1^2B_1^\dagger B_1 + 2g_2^2B_2^\dagger B_2$ still remain at twice the original strength. Consequently, the coherent coupling with strength $g = 2g_1g_2$ will never exceed both back-action rates $\Gamma_1 = 2g_1^2$ and $\Gamma_2 = 2g_2^2$ as outlined before. The only way to suppress quantum noise from the inputs is by recycling the output of the forward propagating optical field as the input for the backward propagating field by placing a mirror after system 2. In that way, noise from a_+ is correlated with noise from a_- such that their effect on system 1 cancels because of the equal and opposite coupling strengths. This means that the remaining dissipation $\Lambda_{\text{eff}} = 2g_2^2B_2^\dagger B_2$ affects system 2 alone. The quantum noise or back-action cancellation on system 1 now enables us to increase the effective coherent coupling strength above the induced decay rate on system 2 by making

g_1 much larger than g_2. Such a setup has been proposed [82, 83, 84] and experimentally realized [46, 47, 50] for atoms coupled to an oscillating mirror. In previous proposals, the importance of back-action cancellation on the atomic ensemble has not been recognized entirely.

1.3.3 Two objects: Loop on system 1

In order to generalize the double-pass interaction from the previous section we assume two objects coupling to the optical mode in a looped configuration as shown in Figs. 1.1(b) and 1.5. Starting from the general expression (1.22), we set $B_3 = B_1 e^{\mathrm{i}\phi}$ and $g_3 = g_1$. The phase shift ϕ is motivated by the discussion of constructive and destructive interference of Hamiltonian interaction in the preceding paragraph. It can readily be implemented by local unitary operations on the optical field between interactions with the systems. Applying this to the general expression gives

$$\begin{aligned} A &= g_1^2(1+\eta_1\eta_2 e^{-\mathrm{i}\phi})\, B_1^\dagger B_1 + \frac{g_2^2}{2} B_2^\dagger B_2 && (1.27) \\ &\quad + g_1 g_2(\eta_1 B_2^\dagger B_1 + \eta_2 e^{-\mathrm{i}\phi} B_1^\dagger B_2). && (1.28) \end{aligned}$$

We write the full master equation as

$$\begin{aligned} \dot{\rho} &= -\frac{\mathrm{i}}{\hbar}[H_{\text{eff}}, \rho] + \mathcal{L}\rho, && (1.29) \\ \mathcal{L}\rho &= \Gamma_1 \mathcal{D}[B_1]\rho + \Gamma_2 \mathcal{D}[B_2]\rho + \mathcal{G}\rho, && (1.30) \end{aligned}$$

with effective Hamiltonian

$$\begin{aligned} H_{\text{eff}} &= -\mathrm{i}\hbar g_1 g_2 \frac{\eta_1 - \eta_2 e^{\mathrm{i}\phi}}{2}\, B_2^\dagger B_1 + \text{h.c.} \\ &\quad - \hbar g_1^2 \eta_1\eta_2 B_1^\dagger B_1 \sin(\phi). && (1.31) \end{aligned}$$

consisting of interaction between S_1 and S_2 in the first line and a self-interaction of S_1 in the second line. The back-action rates for systems 1 and 2 are given by

$$\begin{aligned} \Gamma_1 &= 2g_1^2(1+\eta_1\eta_2\cos\phi), && (1.32) \\ \Gamma_2 &= g_2^2. && (1.33) \end{aligned}$$

Further, the term

$$\begin{aligned} \mathcal{G}\rho &= -\frac{1}{2} g_1 g_2 (\eta_1 + \eta_2 e^{\mathrm{i}\phi})[B_2^\dagger, B_1\rho] + \text{h.c.} \\ &\quad - \frac{1}{2} g_1 g_2 (\eta_1 + \eta_2 e^{-\mathrm{i}\phi})[B_1^\dagger, B_2\rho] + \text{h.c.} \end{aligned}$$

describes collective non-Hamiltonian evolution [39]. We remark that Eq. (1.30) is not manifestly in Lindblad form, but it can be brought into this form by diagonalization of Λ_{eff} as outlined in Appendix A.2.

In the following, we define the mean transmission $\bar{\eta} = (\eta_1+\eta_2)/2$ and the transmission imbalance $\Delta\eta = \eta_1 - \eta_2$. Two interesting cases emerge for different choices of the

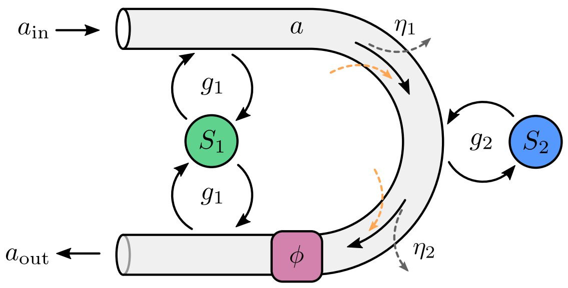

Figure 1.5: Detailed schematic of the coupling scheme involving a loop on system 1.

loop phase ϕ which are analyzed in the following. If $\phi = \pi$, the two light-matter interactions of the first system are out of phase, which corresponds to a time reversal. The case $\phi = 0$ corresponds to concatenating two cascaded interactions with opposite order. We will show that the former leads to Hamiltonian dynamics while the latter reproduces a simple cascaded system.

Coherent dynamics. In the case of $\phi = \pi$, the Hamiltonian reduces to

$$H_{\text{eff}} = \frac{\hbar g}{2\mathrm{i}} \left(B_2^\dagger B_1 - B_1^\dagger B_2 \right), \tag{1.34}$$

which is solely constituted of an interaction between systems 1 and 2 at rate $g = 2\bar{\eta} g_1 g_2$. The self-interaction of system 1 in the second line of Eq. (1.31) cancels. The dissipative part of the evolution reads

$$\begin{aligned} \Lambda_{\text{eff}} &= 2g_1^2(1-\eta_1\eta_2)\, B_1^\dagger B_1 + g_2^2 B_2^\dagger B_2 \\ &\quad + \Delta\eta g_1 g_2 \left(B_2^\dagger B_1 + B_1^\dagger B_2 \right). \end{aligned}$$

Here, the measurement back-action noise on system 1, $\Gamma_1 = 2g_1^2(1-\eta_1\eta_2)$, is partially canceled down to the level of losses between the two interactions. This is directly reflected in the equation of motion

$$\begin{aligned} \dot{b}_1 &= g_1\mu_1 \left(a_{\text{in}}(\zeta_1) - \eta_1\eta_2 a_{\text{in}}(\zeta_3) + \sqrt{1-\eta_1^2\eta_2^2}\, h_{\text{in}}(\zeta_3) \right) \\ &\quad + g_1\nu_1 \left(a_{\text{in}}^\dagger(\zeta_1) - \eta_1\eta_2 a_{\text{in}}^\dagger(\zeta_3) + \sqrt{1-\eta_1^2\eta_2^2}\, h_{\text{in}}^\dagger(\zeta_3) \right) \\ &\quad + \dots \end{aligned}$$

where the ellipsis includes coupling to system 2 and internal dynamics. Here, the destructive interference between the primary input field a_{in} at the two positions ζ_1 and ζ_3 becomes evident. Losses introduce an additional noise input h_{in} which is uncorrelated with a_{in}. The rates of these two noise inputs add up to the same value Γ_1 as obtained from the master equation. We note that time delays add a frequency dependent phase shift between $a_{\text{in}}(\zeta_1)$ and $a_{\text{in}}(\zeta_3)$ that renders the cancellation imperfect. These effects are missing in the master equation because time delays have been neglected. Within the rotating-wave approximation the effect of time delays can be captured by

$a_{\mathrm{in}}(\zeta_1) - \eta_1\eta_2 a_{\mathrm{in}}(\zeta_3) \approx a_{\mathrm{in}}(1 - \eta_1\eta_2 e^{-\mathrm{i}\Omega_1\tau_{13}})$ (see Appendix A.3). Consequently, perfect back-action cancellation requires $\Omega_1\tau_{13} \ll 1$, as expected.

Destructive interference of the input noise on system 1 goes along with destructive interference of the signal in the output field

$$\begin{aligned} a_{\mathrm{out}} &= -\mathrm{i}g_1(\eta_1\eta_2 B_1(t-\tau_{13}) - B_1(t)) - \mathrm{i}\eta_2 g_2 B_2(t-\tau_{23}) \\ &\quad +\eta_1\eta_2 a_{\mathrm{in}} + \sqrt{1-\eta_1^2\eta_2^2}\, h_{\mathrm{in}}. \end{aligned}$$

We see that in the case of $\phi = \pi$, information written onto the light field by system 1 in the first pass is partially erased in the second pass.

A transmission imbalance in the two light-mediated interactions adds collective dissipation to the dynamics at a rate $\Gamma_{12} = |\Delta\eta| g_1 g_2$ [39], which is negligible for a symmetric bi-directional coupling scheme with $\eta_1 \approx \eta_2$. In this case, the collective dynamics are entirely Hamiltonian and noise is only introduced at the level of the individual systems.

Dissipative dynamics. In the case where $\phi = 0$, the Hamiltonian evolution is strongly suppressed and can be made to vanish exactly if $\eta_1 = \eta_2$. Here,

$$H_{\mathrm{eff}} = \hbar\Delta\eta g_1 g_2 \frac{1}{2\mathrm{i}}\left(B_2^\dagger B_1 - B_1^\dagger B_2\right) \tag{1.35}$$

and

$$\begin{aligned} \Lambda_{\mathrm{eff}} &= 2g_1^2(1+\eta_1\eta_2)\, B_1^\dagger B_1 + g_2^2 B_2^\dagger B_2 \\ &\quad +2\bar{\eta} g_1 g_2\left(B_2^\dagger B_1 + B_1^\dagger B_2\right) \end{aligned} \tag{1.36}$$

The main difference of the looped configuration as compared to the simple single pass cascaded interaction lies in the purely dissipative nature of the interaction. Even if the operator $B_2^\dagger B_1 - B_1^\dagger B_2$ is nonzero, one can eliminate the Hamiltonian interaction completely for balanced transmissions $\eta_1 = \eta_2$.

We recover that for full transmission $\bar{\eta} = 1$ the effective dynamics are described by a single dissipative process

$$\dot{\rho} = \mathcal{D}[2g_1 B_1 + g_2 B_2]\rho. \tag{1.37}$$

For the purpose of generating a two-mode squeezed state of two harmonic oscillators via dissipation [24, 93] one chooses the mode b_2 to have positive frequency $\Omega_2 = \Omega > 0$, and the mode b_1 to have negative frequency $\Omega_1 = -\Omega$. In the interaction picture with regard to H_0, we can then write $2g_1\tilde{B}_1 + g_2\tilde{B}_2 = j_+ e^{-\mathrm{i}\Omega t} + j_- e^{\mathrm{i}\Omega t}$ where we defined two jump operators $j_+ = 2g_1\mu_1 b_1 + g_2\nu_2 b_2^\dagger$ and $j_- = g_2\mu_2 b_2 + 2g_1\nu_1 b_1^\dagger$. Care has to be taken that both oscillators couple to the same optical field quadrature such that they both experience the same optical input quantum noise, i.e., $\theta_1 = \theta_2$ and $\phi_1 = \phi_2$. This enables collective decay into an entangled state. Making the rotating-wave approximation one obtains the master equation

$$\dot{\rho} \approx \mathcal{D}[j_+]\rho + \mathcal{D}[j_-]\rho, \tag{1.38}$$

which is equivalent to the master equation in the simple cascaded system. There does not seem to be a clear advantage of the loop geometry in the case of dissipative interaction.

1.3.4 Two objects: Loops on both systems

In the looped interaction discussed in the previous section the measurement back-action on system 2 is still present and poses a fundamental limit to the coherence of the remote interaction. We note, however, that this can in principle be remedied by adding another light-matter interaction with system 2 and opposite phase as depicted in Figs. 1.1(c) and 1.6 with $B_4 = -B_2$ ($\phi = \pi$). In this second pass through system 2, all information about it will be erased from the light but no further enhancement of the coherent coupling between systems 1 and 2 could be obtained because at this point the light does not contain information about system 1 anymore. This represents the ideal scenario because all back-action is canceled such that $\Lambda_{\text{eff}} = 0$ and the coherent dynamics are only disturbed by intrinsic damping of the two systems. In a real experiment, there will always be losses in which this scheme possesses an inherent asymmetry because there are three interaction pathways from S_1 to S_2, but only one from S_2 to S_1. In the following sections, we will analyze the dynamics that can be realized with both the single loop of Fig. 1.1(b) and the double loop.

1.4 Coherent dynamics in the looped geometries

We have seen above that in the looped geometries of Figs. 1.1(b) and (c) it is possible to create coupled dynamics which are entirely Hamiltonian. However, decoherence is inherently present as a result of optical back-action noise and also other system-specific decoherence channels will always be present in experiments. This section is devoted to calculating the achievable cooperativity as a figure of merit for coherent dynamics. Beyond that, we also analyze three experimentally relevant applications of our theory.

1.4.1 Cooperativity

In optomechanics and quantum optics, the relevant light-matter interaction strength for system i is the single-pass measurement rate g_i^2. Optical cooperativity is commonly defined as the ratio of measurement rate over the intrinsic thermal decoherence rate, $c_i = g_i^2/\gamma_{i,\text{th}}$ for each system i [39, 94], referred to as the single-pass cooperativity in the following. The thermal decoherence rate can be expressed as $\gamma_{i,\text{th}} = \gamma_i(\bar{n}_i + 1/2)$ with intrinsic damping rate γ_i and thermal bath occupation $\bar{n}_i$. The contribution $\gamma_i/2$ represents spontaneous scattering.

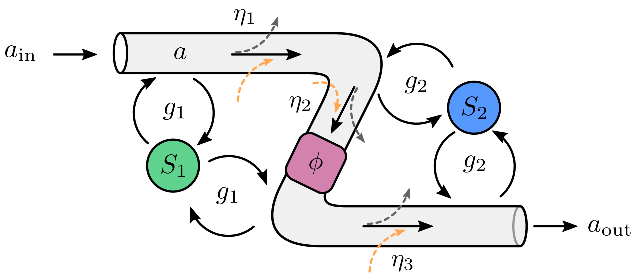

Figure 1.6: Detailed schematic of the double-loop coupling scheme.

In a rotating-wave approximation, the dissipative part (1.30) of the master equation excluding collective dissipation $\mathcal{G}$ and adding intrinsic decoherence reads

$$\begin{aligned}\mathcal{L}\rho &= \sum_i \left[\gamma_i(\bar{n}_i+1)+\mu_i^2\Gamma_i\right]\mathcal{D}[b_i]\rho \\ &\quad +\sum_i(\gamma_i\bar{n}_i+\nu_i^2\Gamma_i)\mathcal{D}[b_i^\dagger]\rho. \qquad (1.39)\end{aligned}$$

This motivates defining a total decoherence rate $\gamma_{i,\text{tot}} = \gamma_{i,\text{th}} + \Gamma_i/2$ covering both intrinsic and light-induced noise processes. The effective Hamiltonian

$$H_{\text{eff}} = H_{\text{BS}} + H_{\text{TMS}} \qquad (1.40)$$

is composed of a beam-splitter (BS) Hamiltonian $H_{\text{BS}} = \mathrm{i}\hbar g\alpha(b_1^\dagger b_2 - b_2^\dagger b_1)$ and a two-mode-squeezing (TMS) Hamiltonian $H_{\text{TMS}} = \mathrm{i}\hbar g\beta(b_1 b_2 - b_1^\dagger b_2^\dagger)$. Here, we have set $\phi_1 = \phi_2 = 0$ for simplicity. The weights are then $\alpha = (\mu_1\mu_2 - \nu_1\nu_2)/2 = \cos(\theta_1+\theta_2)/2$ and $\beta = (\mu_2\nu_1 - \mu_1\nu_2)/2 = \sin(\theta_1-\theta_2)/2$. Coupling is maximized if both oscillators couple to orthogonal optical quadratures, e.g., $\theta_1 = \pi/4 = -\theta_2$ such that $\alpha = \beta = 1/2$. Which one of these two interactions is resonant depends on the oscillator frequencies Ω_1 and Ω_2. While the BS Hamiltonian enables state swaps or the generation of superposition states for $\Omega_1 = \Omega_2$, the TMS Hamiltonian generates non-classical correlations for $\Omega_1 = -\Omega_2$. The following discussion of cooperativity applies to both of them.

The cooperativity $\mathcal{C}$ of the cascaded system compares the strength g of the coherent light-mediated coupling with the intrinsic and light-induced decay rates $\gamma_{i,\text{tot}}$, i.e.,

$$\mathcal{C} = \frac{g^2}{\gamma_{1,\text{tot}}\,\gamma_{2,\text{tot}}}. \qquad (1.41)$$

In the following we set $\eta_1 = \eta_2 = \eta$ such that in the looped geometry 1-2-1 we have a coupling constant $g = 2\eta g_1 g_2$ and the back-action rates are $\Gamma_1 = 2(1-\eta^2)g_1^2$ and $\Gamma_2 = g_2^2$. For zero losses we obtain the asymptotic expression $\mathcal{C} \sim 4c_1/(1/2+1/c_2)$ which is in principle limited by the single-pass cooperativity of system 1. For finite losses and assuming all individual dissipation rates are small, i.e., large optical cooperativity $c_i \gg 1$, we approximately have

$$\mathcal{C} = \frac{8\eta^2}{1-\eta^2}. \qquad (1.42)$$

For linearized couplings as commonly encountered in cavity optomechanics [56] and atom-light interfaces [39] with a single local oscillator experiencing the same losses as the quantum field (i.e. $g_3 = \eta^2 g_1$ and g_2 replaced by ηg_2), the rates become $g = (\eta^2+\eta^4)g_1 g_2$, $\Gamma_1 = (1-\eta^4)g_1^2$, and $\Gamma_2 = \eta^2 g_2^2$. Consequently, we have the scaling

$$\mathcal{C} = \frac{4(\eta^2+\eta^4)}{1-\eta^2}. \qquad (1.43)$$

Note that in this case the interaction is never fully balanced and additional collective dissipation arises at a rate $\Gamma_{12} = 2(\eta^2-\eta^4)g_1 g_2$. However, the ratio $g/\Gamma_{12} = (1+\eta^2)/(1-\eta^2) = \mathcal{C}/\eta^2$ is always larger than $\mathcal{C}$. We remark that in principle the loss of the coherent

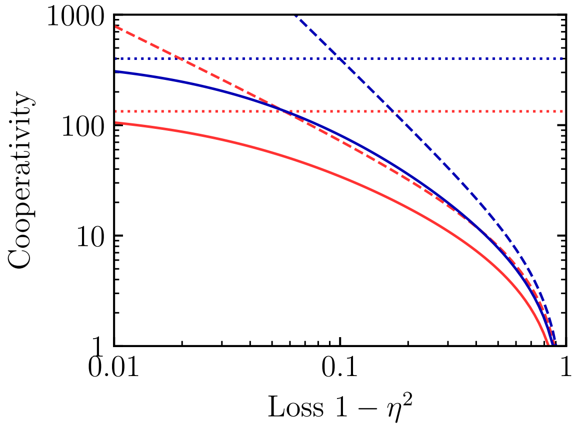

Figure 1.7: Cooperativity as a function of optical power loss between systems. Cooperativity for the single-loop Eq. (1.42) (solid red line) and the double-loop Eq. (1.44) (solid blue line). Also shown are the maximum achievable cooperativities with zero losses (dotted lines). These amount to $4c_1/(1/2+1/c_2)$ for the single loop and to $4c_1c_2$ for the double loop. For $c_2 < 1$, the cooperativities of these two geometries would almost coincide; for large c_2, they differ by a factor of $\sim c_2/2$. The dashed lines correspond to the limiting cases of infinite single-system cooperativities as given by Eqs. (1.42) for the single loop and (1.44) for the double loop.

field can be compensated, provided the quantum fields in the sideband frequencies can be separated from the carrier [51].

In the double-loop geometry 1-2-1-2 with $g = \eta(3-\eta^2)g_1g_2$ and $\Gamma_i = 2g_i^2(1-\eta^2)$, we obtain the loss-limited cooperativity

$$\mathcal{C} = \frac{\eta^2(3-\eta^2)^2}{(1-\eta^2)^2}, \tag{1.44}$$

while for zero losses it is $\mathcal{C} = 4c_1c_2$.

In Fig. 1.7, we plot the resulting cooperativity of the light-mediated dynamics for the two schemes 1-2-1 and 1-2-1-2 as a function of the optical loss $1-\eta^2$. Here, we choose imbalanced systems with single-system cooperativities of $c_1 = 25$ and $c_2 = 4$. This imbalance is chosen in order to keep light-induced back-action on system 2 small compared to the coupling strength. Keeping c_1c_2 constant and diminishing c_2 will asymptotically lead to the same cooperativity for the single loop and the double loop schemes. Remarkably, the figure shows that even for substantial optical losses of a few tens of percent, coherent light-mediated interactions between the two systems can be engineered.

1.4.2 Sympathetic cooling

The probably simplest experiment that can be done using light-mediated Hamiltonian coupling is to study the thermalization of two oscillators in the presence of the beam-splitter coupling. Experimentally, this has been achieved in the context of sympathetic

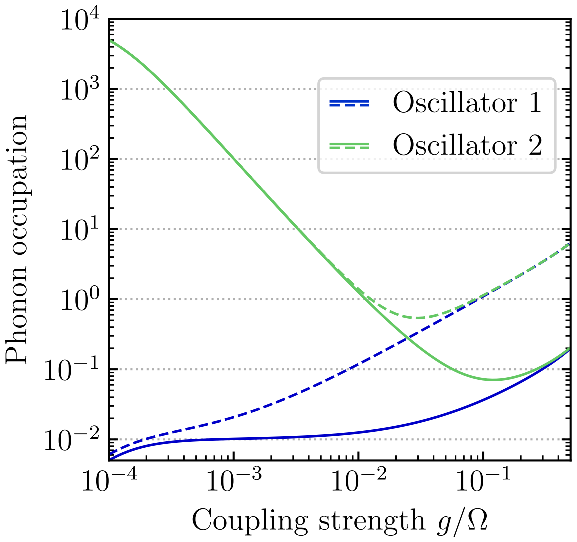

Figure 1.8: Steady-state phonon numbers of both oscillators in the sympathetic cooling scenario described in the main text comparing the performance with losses ($\eta = 0.9$, dashed lines) to the one without ($\eta = 1$, solid lines).

cooling of a mechanical oscillator coupled to the center-of-mass motion of a cloud of ultracold atoms [47, 48, 50]. These experimental setups are equivalent to Fig. 1.1(b) and we will focus on it in this section. In such a hybrid system the two oscillators exhibit fairly different characteristics. While the first oscillator (the ultracold atoms) is coupled to a vacuum bath ($\bar{n}_1 \approx 0$) with large damping rate γ_1, the second oscillator (the mechanical oscillator) couples to a hot bath with a very low damping rate γ_2. Efficient sympathetic cooling of oscillator 2 via oscillator 1 occurs in a regime where the light-mediated coupling strength g exceeds the thermal dissipation rate of oscillator 2 while remaining smaller than the damping rate γ_1 of oscillator 1. The minimum achievable phonon occupation is then limited by the cooperativity of Eq. (1.41) [83]. It is also evident from Eq. (1.39) that back-action noise on the two oscillators increases their effective bath occupation, thus limiting the cooling efficiency. In the coupling geometry 1-2-1, the optimal strategy consists in choosing $c_1 \gg c_2 \approx 1$ such that the back-action rate Γ_2 on oscillator 2 remains insignificant compared to the cooling rate $\sim g^2/\gamma_1 = 2\eta^2 c_1 \Gamma_2$ [83].

In order to directly evaluate the steady-state phonon occupation of both oscillators, we treat the Gaussian dynamics of the coupled system using the covariance matrix formalism [95] (see Appendix A.4). For the simulations, we choose two oscillators with equal frequency Ω. Both interact with the light field via quantum-nondemolition (QND) interactions, i.e., $\theta_1 = \pi/4 = -\theta_2$ such that $\alpha = 1$ is maximal and no additional optical cooling of oscillator 2 occurs. Oscillator 1 has a large damping rate $\gamma_1 = 0.1\Omega$ that couples it to a vacuum bath ($\bar{n}_1 = 0$). Contrarily, oscillator 2 is connected to a hot bath with $\bar{n}_2 = 10^4$ but its damping rate is very low ($\gamma_2 = 10^{-7}\Omega$) such that thermalization occurs at the comparably low rate $\gamma_{2,\mathrm{th}} = 10^{-3}\Omega \ll \gamma_1$. This is the typical situation encountered in hybrid atom-optomechanical systems [47, 50].

The resulting steady-state phonon occupations of the two oscillators in the sympathetic cooling scenario are plotted in Fig. 1.8 as a function of the coherent coupling strength $g = 2\eta g_1 g_2$ keeping a fixed ratio of $g_1/g_2 = 10$. This ensures that $\Gamma_2 \ll g$. In the lossless case, cooling below unity phonon occupation of the mechanical oscillator is possible for a coupling strength of $g \approx \gamma_1 = 0.1\Omega_i$. Increasing the coupling strength further leads to a breakdown of the simple cooling picture from above. As soon as $g > \gamma_1$, the modes hybridize which causes heating of oscillator 1 by oscillator 2. In the lossy case with $\eta = 0.9$, substantial back-action heating of oscillator 1 leads to a much higher minimum phonon number in oscillator 2. Nevertheless, this value still lies below 1 indicating a certain robustness against losses.

1.4.3 Entanglement

As a second application, we consider the generation of entanglement between two oscillators, comparing the different looped and cascaded schemes of Fig. 1.1. Entanglement between two bosonic modes can be generated by the two-mode squeezing Hamiltonian H_{TMS} which produces squeezing in the quadratures $X_1 + X_2$ and $P_1 - P_2$ and anti-squeezing in $X_1 - X_2$ and $P_1 + P_2$, thus creating nonclassical correlations. In order to realize it using the looped cascaded interaction, we consider the mode b_1 to have negative frequency $\Omega_1 = -\Omega < 0$ and the mode b_2 to have positive frequency $\Omega_2 = \Omega > 0$. An inverted oscillator with $\Omega_1 < 0$ can directly be realized experimentally with a collective atomic spin pumped to its highest energy state [28] or, effectively, in cavity optomechanical systems driven by two optical tones [96, 97]. In this setting H_{TMS}, is stationary in the interaction picture and the steady-state two-mode squeezing parameter r is approximately given by the ratio of all noise rates over the coherent coupling strength, i.e.,

$$r \approx \frac{\gamma_{1,\text{th}} + \gamma_{2,\text{th}} + (\Gamma_1 + \Gamma_2)/2}{2g\beta}. \tag{1.45}$$

We see that the requirements for squeezing ($r < 1$) are more restrictive than those for achieving large cooperativity because all decoherence rates need to be individually smaller than the coupling strength. In order to quantify the degree of entanglement, we evaluate two established non-separability criteria for Gaussian states, the logarithmic negativity [98, 99] and the EPR variance [100, 101] (see Appendix A.5).

In Fig. 1.9 we show the bipartite entanglement as quantified by EPR variance ($\Delta_{\text{EPR}} < 1$) and logarithmic negativity ($E_{\mathcal{N}} > 0$) as a function of (a) the interaction time between the two oscillators and (b) the optical loss $1 - \eta^2$. We plot them for four relevant cases: (i) the looped geometry of Fig. 1.1(b) with interaction order 1-2-1 (solid line), (ii) the looped geometry with reversed interaction order 2-1-2 (dashed line), and (iii) the double loop of Fig. 1.1(c) with interaction order 1-2-1-2 (dot-dashed line). For comparison, we also show (iv) the achievable steady-state entanglement using the simple cascaded scheme 1-2 of Fig. 1.1(a) (dotted lines). In the simulations, we deliberately choose a slight asymmetry in the damping rates and thermal bath occupations in order to describe the situation encountered in ongoing experiments in hybrid atom-optomechanics [47, 51]. While oscillator 1 couples to a vacuum bath with $\bar{n}_1 = 0$ and intrinsic decay rate $\gamma_1 = 10^{-3}\Omega$, oscillator 2 has a lower damping rate $\gamma_2 = 10^{-4}\Omega$ but a larger thermal occupation $\bar{n}_2 = 10$. For oscillator 1, we choose the QND light-matter

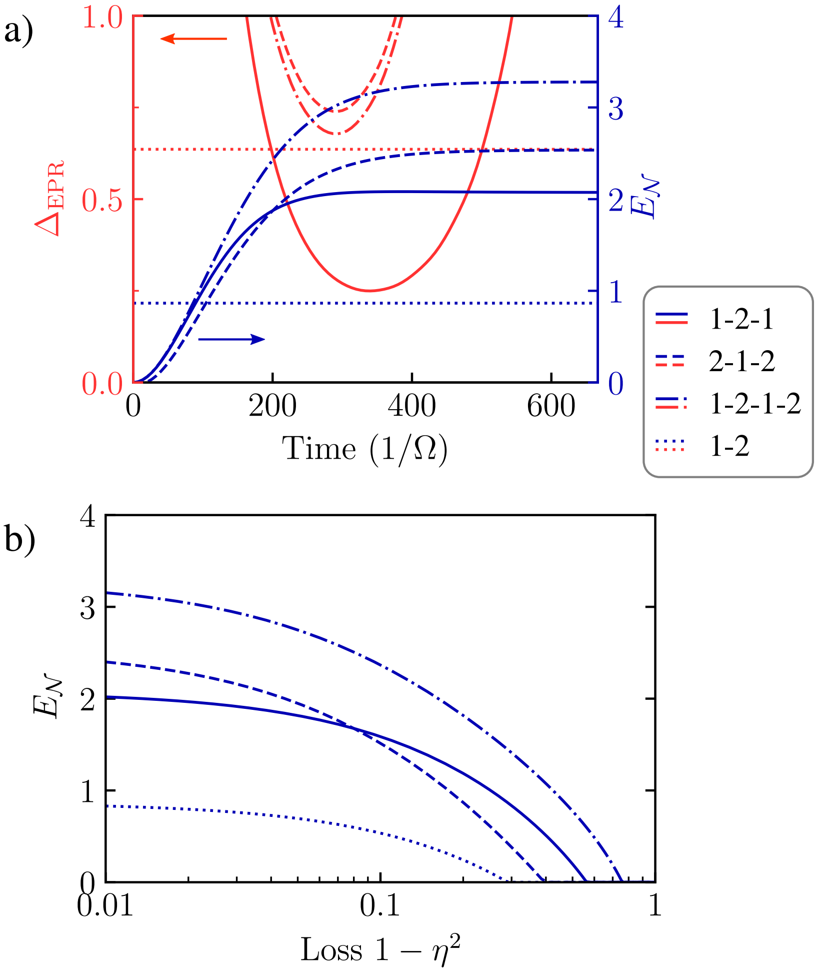

Figure 1.9: Entanglement as characterized by the EPR variance (red color) and measured by the logarithmic negativity (blue color) in four relevant cases: (i) the looped geometry 1-2-1 (solid lines), (ii) the looped geometry with reverse order 2-1-2 (dashed lines), (iii) the double loop with interaction order 1-2-1-2 (dot-dashed lines), and (iv) the steady state of the simple cascaded scheme 1-2 (dotted lines). (a) Entanglement measures vs interaction time in the lossless case $\eta = 1$. (b) Steady-state logarithmic negativity vs optical loss $1 - \eta^2$.

interaction with $\theta_1 = \pi/4$ while for oscillator 2 a value of $\theta_2 = -0.8\pi/4$ introduces an imbalance between beam-splitter and parametric gain interactions with the purpose of further cooling its thermal fluctuations. For the single-pass scheme, we set $\theta_2 = +0.8\pi/4$ such that both oscillators couple predominantly to the same optical quadrature [93, 85]. The coupling constants g_1 and g_2 have been chosen in order to minimize the back-action rates while fixing $c_1 c_2 = 100$ and thus keeping g constant. For the schemes 1-2 and 1-2-1-2, the choice is symmetric with $c_1 = c_2 = 10$. In either of the schemes 1-2-1 and 2-1-2, only one oscillator is protected from quantum noise and we increase the single-pass cooperativity of this one at the cost of the other. This leads us to the choices $c_1 = 25$, $c_2 = 4$ for 1-2-1 and $c_1 = 4$, $c_2 = 25$ for 2-1-2 such that the oscillator without back-action cancellation has a weaker coupling.

In Fig. 1.9(a) the dynamics start from an initial thermal state with $\bar{n}_1 = 0$ and $\bar{n}_2 = 10$. Strong entanglement is achieved after a short interaction time required to overcome the initial thermal noise in oscillator 2. The logarithmic negativities in the three cases (i)–(iii) reach steady states with similar values, with the double loop (iii) being optimal. This is a direct consequence of the efficient quantum noise cancellation on both systems, while in the single-loop schemes (i) and (ii) only a single system benefits from quantum noise cancellation. However, for cascaded systems with imbalanced single-pass cooperativities, these schemes are already close to optimal implying that the advantage of full back-action cancellation in (iii) can only be fully exploited if the experimentally achievable single-system cooperativities are high and if losses are low.

Entanglement is demonstrated and quantified clearly in terms of the negativity. On top of that, we show the EPR variance, demonstrating how close the entangled state is to the "canonical" two-mode squeezed state. This is a relevant question regarding applications of the entangled state for quantum information protocols such as teleportation [102]. We see that the performance of the different schemes in terms of EPR entanglement is quite different from that in terms of the negativity. While scheme 1-2-1 attains a minimum of $\Delta_{\mathrm{EPR}} \approx 0.25$, the schemes 2-1-2 and 1-2-1-2 only achieve weak squeezing of the EPR variance. This behavior can be understood from the strong imbalance of the thermal and back-action noise processes acting on the two oscillators that leads to a deviation of the squeezed quadratures from $X_1 + X_2$ and $P_1 - P_2$. In the schemes 1-2 and 1-2-1, however, optical back-action cooling of oscillator 2 reduces its thermal noise and increases its damping rate, thereby partially lifting the imbalance and reducing Δ_{EPR}. This mechanism is absent in the other schemes 2-1-2 and 1-2-1-2 where optical back-action on oscillator 2 cancels. Moreover, all schemes merely show transient EPR entanglement as for long interaction times growing noise in the anti-squeezed quadrature enters $X_1 + X_2$ and $P_1 - P_2$ and leads to an increase of Δ_{EPR}. However, we emphasize that all schemes do indeed achieve entanglement in the stationary state as witnessed by the logarithmic negativity.

As compared to steady-state entanglement that would be achieved in the simple cascaded scheme 1-2 with identical light-matter interactions, the looped geometries perform better. We note, however, that entanglement in the simple cascaded scenario can in principle be further optimized by additional tuning of the local light-matter interactions [85]. Another advantage of the coherent entanglement achieved via the looped geometries is a faster entanglement rate that does not rely on reaching a steady state after a much longer interaction time.

Finally, in Fig. 1.9(b), we analyze the dependence of the achievable entanglement on optical losses. Here we only show logarithmic negativity because the entanglement of bipartite Gaussian states is solely determined by two-mode squeezing [100, 87]. Remarkably, all schemes are very robust against losses of up to 10% without strong degradation and still show $E_{\mathcal{N}} > 0$ until $1 - \eta^2 = 40\%$ for 1-2 and 2-1-2, 50% for 1-2-1, and even 70% for 1-2-1-2.

1.4.4 Unconditional squeezing of a single oscillator

Having discussed the coherent dynamics between two distinct quantum systems interacting via an optical mode, we devote this last section to engineering coherent dynamics in a single quantum system. If we consider the scheme in Fig. 1.1(b) and leave out system 2, the remaining dynamics of system 1 alone are very interesting on its own. Multipass interactions between light and atomic ensembles have been subject to several theoretical studies investigating quantum memory and atom-light entanglement [103] or spin squeezing [104, 105].

Here, we investigate the effect of a phase shift ϕ on the light field quadratures in between the two light-matter interactions. The discussion in Sec. 1.3.3 already revealed the two effects: There is a light-mediated self-interaction and interference of back-action noise. For $\phi = \pi$, one has full back-action cancellation without self-interaction, meaning that even though the system strongly interacts with light, there is no effect visible to an external observer. For intermediate optical phase shift $\phi \in (0, \pi)$, the system is driven by itself, thus representing a case of coherent quantum feedback [106, 107]. The corresponding master equation is

$$\dot{\rho} \;=\; \mathrm{i}\eta g_1^2 \sin\phi [B_1^\dagger B_1, \rho] + 2g_1^2(1 + \eta\cos\phi)\mathcal{D}[B_1]\rho.$$

For $B_1 = X_1$ being a harmonic oscillator quadrature, the effective Hamiltonian is equivalent to a one-axis twisting Hamiltonian [108] implementing squeezing at rate $g = \eta g_1^2 \sin\phi$. However, there is simultaneous back-action noise at rate $\Gamma_1 = 2g_1^2(1 + \eta\cos\phi)$ which does not cancel for any non-vanishing g. Nevertheless, the ratio of noise rate over squeezing rate

$$r = \frac{\Gamma_1/2}{g} = \frac{1 + \eta\cos\phi}{\eta\sin\phi}, \tag{1.46}$$

can be minimized for a given loss, leading to a value of ϕ close to π where $r \sim (1 - 1/\eta)/(\phi - \pi)$. This scheme can in principle achieve arbitrarily large squeezing provided that g remains large compared to other intrinsic and technical decoherence rates. The ratio r does not give a bound for the minimum achievable squeezing parameter but rather expresses how much excess noise is added to the anti-squeezed quadrature. Besides applications in spin-squeezing similar schemes could equally well be employed to achieve squeezing of a mechanical oscillator in an optomechanical cavity. To this end, one has to recycle the cavity output field by first applying the relative phase shift ϕ between the local oscillator and the quantum field, and then sending it back into the cavity on a different mode.

Recently, Wang et al. [105] have shown that one can erase the remaining back-action of the two-pass scheme in a three-pass configuration to achieve unitary spin-squeezing of an atomic ensemble. With phase shifts ϕ_{ij} between passes i and j, the full master equation in this case reads

$$\dot{\rho} \;=\; -\alpha\, g_1^2\,[X_1, X_1\rho] + \text{h.c.},$$

where $\alpha = \frac{3}{2} + \eta e^{-\mathrm{i}\phi_{12}} + \eta e^{-\mathrm{i}\phi_{23}} + \eta^2 e^{-\mathrm{i}(\phi_{12}+\phi_{23})}$. For full noise cancellation at $\eta = 1$ one needs to solve

$$\mathrm{Re}\,\alpha = \frac{3}{2} + \cos(\phi_{12}) + \cos(\phi_{23}) + \cos(\phi_{12}+\phi_{23}) \overset{!}{=} 0.$$

Setting $\phi_{12} = \phi_{23} = \phi$, the solution is found to be $\phi = \pm 2\pi/3$. The coherent interaction strength is given by $\mathrm{Im}\,\alpha = \mp\sqrt{3}/2$. Using this choice of ϕ for $\eta < 1$, we get

$$\dot{\rho} = -\mathrm{i}\frac{\sqrt{3}(2\eta-\eta^2)}{2} g_1^2[X_1^2, \rho] + (3 - 2\eta - \eta^2) g_1^2 \mathcal{D}[X_1]\rho. \tag{1.47}$$

Here, one obtains a more favorable ratio of

$$r = \frac{\Gamma_1/2}{g} \sim \frac{4(1-\eta)}{\sqrt{3}\eta}, \tag{1.48}$$

which can be smaller than 0.1 up to a power loss per pass of $1-\eta^2 \approx 8\%$.

1.5 Conclusion

Cascaded quantum systems have so far only been considered for dissipative entanglement schemes or unidirectional quantum communication. Here, we have extended this framework to include multiple interactions of an optical field with the individual quantum systems. In this case, light can also mediate coherent interactions between the quantum systems without adding noise to them. For two cascaded quantum systems, this is achieved if the light field interacts twice with the systems and if the second interaction with each of them is the time reversal of the first. In this situation, coherent driving of each system by the other is accompanied by a destructive interference of measurement back-action noise due to the light field, thus realizing an ideal Hamiltonian coupling.

In order to quantify the strength of the coherent light-mediated interaction in the presence of experimental imperfections we have defined a cooperativity as the ratio of the coherent coupling constant over intrinsic and light-induced dissipation rates. Importantly, we have shown that large cooperativity can be achieved even in the presence of significant optical loss that renders the back-action cancellation imperfect. This robustness is very appealing for experiments and we believe that future quantum networks will benefit from the possibilities opened up by Hamiltonian interactions across macroscopic distances. Our scheme is particularly suited to interface hybrid quantum systems with distinct physical properties for which we have demonstrated its potential for ground-state sympathetic cooling and strong two-mode squeezing.

Since the looped cascaded interaction necessarily erases all information about the interacting systems on the optical field, one needs to find an alternative measurement strategy in order to verify the coupled dynamics at the quantum level. One simple solution could be auxiliary readout modes for each system, which would however make experimental realizations more complicated. As a more direct approach, we imagine real-time control of the optical field in order to switch from coherent dynamics to a collective measurement. Simultaneous weak measurement and partial noise cancellation are directly implemented in the cascaded scheme 1-2-1 with a loop on a single system. This presents an interesting intermediate scenario where one could explore the interplay of coherent dynamics and conditional quantum state evolution.

Chapter 2

Membrane optomechanical system

In this chapter, the optomechanical system is introduced and characterized. Contrary to most cavity optomechanics experiments, which are interested in strong and coherent coupling between the mechanical oscillator and the cavity field in the sideband-resolved limit, we aim at the fast-cavity regime, where the mechanical oscillator effectively couples to the external cavity input/output field. This is advantageous for building cascaded quantum systems where delays associated with the cavity decay time can be an issue. The experimental setup consists of a membrane inside an optical cavity whose design and assembly will be described in detail, including a basic characterization of the optomechanical coupling. At the end of this chapter, we present experiments characterizing the optomechanical response in the fast-cavity regime as an alternative to optomechanically-induced transparency.

2.1 Cavity optomechanics

The generic cavity optomechanical model involves an optical cavity that is dispersively coupled to a mechanical degree of freedom, such that the cavity frequency $\omega_c(x_m)$ depends on the mechanical displacement x_m [56] (see Fig. 0.2a) for an illustration). For small mechanical displacement, the cavity Hamiltonian can be Taylor-expanded to first order around the mechanical equilibrium position $x_m = 0$ giving

$$H_c = \hbar\omega_c(x_m)c^\dagger c = \hbar\omega_c(0)c^\dagger c - \hbar G x_m c^\dagger c + \dots \tag{2.1}$$

It consists of the unperturbed energy of the cavity mode and the optomechanical interaction Hamiltonian

$$H_{\text{om}} = -\hbar G x_m c^\dagger c \tag{2.2}$$

which couples the mechanical displacement x_m to the cavity photon number $n_c = c^\dagger c$. The frequency pulling factor $G = -\partial\omega_c/\partial x_m|_{x_m=0}$ determines the cavity frequency shift per mechanical displacement.

We describe the mechanical mode as a harmonic oscillator with Hamiltonian

$$H_m = \frac{p_m^2}{2m_{\text{eff}}} + \frac{m_{\text{eff}}\Omega_m^2 x_m^2}{2} \tag{2.3}$$

where m_{eff} is the effective mass of the specific mechanical mode and Ω_m is its angular frequency. The mechanical position x_m and momentum p_m satisfy the quantum mechanical commutation relation $[x_m, p_m] = \mathrm{i}\hbar$. When considering the optomechanical dynamics in the quantum regime, it is convenient to rescale mechanical displacement and momentum in terms of the displacement caused by single mechanical quanta, i.e. phonons. In the quantum mechanical ground state, zero-point fluctuations cause a root-mean-squared (rms) displacement of $x_0 = \sqrt{\hbar/(2m_{\text{eff}}\Omega_m)}$. Hence, we define dimensionless mechanical operators

$$X_m = \frac{x_m}{\sqrt{2}x_0}, \quad P_m = \frac{\sqrt{2}x_0 p_m}{\hbar} \tag{2.4}$$

with commutation relation $[X_m, P_m] = \mathrm{i}$. In terms of the mechanical annihilation and creation operators b_m and $b_m^\dagger$, respectively, they read $X_m = (b_m + b_m^\dagger)/\sqrt{2}$ and $P_m = -\mathrm{i}(b_m - b_m^\dagger)/\sqrt{2}$. This allows us to write the Hamiltonian in a simple way, i.e.

$$H_m = \frac{\hbar\Omega_m}{2}\left(X_m^2 + P_m^2\right) = \hbar\Omega_m\left(b_m^\dagger b_m + \frac{1}{2}\right). \tag{2.5}$$

In this language, the optomechanical interaction becomes

$$H_{\text{om}} = -\hbar g_0 (b_m + b_m^\dagger) c^\dagger c. \tag{2.6}$$

where $g_0 = Gx_0$ is called the single-phonon optomechanical coupling strength. Cavity optomechanics enables very precise measurements of mechanical displacement by measuring the phase shift $\delta\phi = 4Gx_m/\kappa$ imparted on the cavity output field. Here, κ is the cavity linewidth. Fluctuations of the mechanical zero-point motion translate to phase fluctuations $\langle\delta\phi^2\rangle = (4g_0/\kappa)^2$. Consequently, a large optomechanical coupling in terms of the ratio $g_0/\kappa > 1$ would be desirable to be able to resolve the cavity frequency shift induced by a single mechanical excitation. This would enable truly quantum nonlinear dynamics at the single-phonon and single-photon level like the observation of mechanical quantum jumps or photon-blockade phenomena [56]. However, state of the art experiments with solid-state mechanical resonators [109, 61, 77, 6, 78] operate in a regime where $g_0 \ll \kappa$. Only cold atom experiments have so far reached the regime $g_0/\kappa > 1$ [110, 111]. In order to still reach a high sensitivity to mechanical zero-point motion in the measurement of the cavity output field, a large cavity photon number $\bar{n}_c \gg 1$ is needed. Before we discuss the quantum dynamics in this regime, it is important to recognize that the inherent nonlinearity of the optomechanical coupling can lead to some complicated static phenomena that have to be taken into account.

2.1.1 Static phenomena

Consider the cavity being driven by an external laser field to a large intra-cavity field amplitude with mean photon number $\bar{n}_c$. This exerts a radiation pressure force

$$F_{\text{rad}} = \hbar G \bar{n}_c \tag{2.7}$$

on the mechanical oscillator, which displaces it to a new equilibrium position $\bar{x}_m = \hbar G\bar{n}_c/(m\Omega_m^2)$ and alters the mechanical frequency. As the cavity frequency changes with mechanical displacement, it detunes the cavity from the external laser and causes the cavity photon number to adapt, i.e.

$$\bar{n}_c = \frac{\bar{n}_0}{1 + 4(\Delta + G\bar{x}_m)^2/\kappa^2} \tag{2.8}$$

where $\Delta = \omega_L - \omega_c(0)$ is the laser-cavity detuning and $\bar{n}_0$ is the cavity photon number for the laser on resonance ($\Delta = 0$). We see that the mean mechanical displacement and the mean cavity photon number depend on each other in a nonlinear way. When the ratio $G\bar{x}_m/\kappa$ is appreciable, the optomechanical interaction strongly modifies both the mechanical potential and the cavity response. In particular this happens for red detuning ($\Delta < 0$) where the mechanically induced cavity frequency shift pulls the cavity frequency towards the laser frequency, thus reducing the laser-cavity detuning and causing a further rise of the photon number. Above a critical photon number corresponding to $\bar{n}_c \sim \Omega_m \kappa / g_0^2$ this gives rise to optical and mechanical bistability that may lead to unstable behavior [56].

2.1.2 Linearized theory

Consider a single-sided optomechanical cavity which couples to an external continuous-mode optical field a_L with coupling strength κ. This coupling can be described by the Hamiltonian [90]

$$H_{\text{ext}} = \mathrm{i}\hbar\sqrt{\kappa} \int \frac{\mathrm{d}\omega}{\sqrt{2\pi}} \left[a_L^\dagger(\omega) c - c^\dagger a_L(\omega) \right] \tag{2.9}$$

We assume that the mode a_L is driven by a laser with photon flux $\langle a_L^\dagger a_L \rangle = \Phi_L$. In the following, we separate the dynamics of the coherent field with amplitude $\bar{a}_L = \sqrt{\Phi_L}$ from the small fluctuations $a_L - \bar{a}_L$ by redefining $a_L \to \bar{a}_L + a_L$. It is convenient to work in a rotating frame at the laser frequency ω_L where the bare cavity Hamiltonian is $H_c = -\hbar\Delta c^\dagger c$, with $\Delta = \omega_L - \omega_c(0)$ being the laser-cavity detuning. Ignoring the optomechanical interaction, we can calculate the steady state cavity field amplitude

$$\bar{c} = \frac{\sqrt{\kappa}}{\kappa/2 - \mathrm{i}\Delta} \bar{a}_L = \sqrt{\bar{n}_c} e^{\mathrm{i}\phi_c} \tag{2.10}$$

Here, we defined the cavity photon number $\bar{n}_c = |\bar{c}|^2$ and the cavity phase shift $\phi_c = \arctan(2\Delta/\kappa)$. The cavity phase shift is nonzero for $\Delta \neq 0$ and rotates the cavity quadratures relative to those of the input and output fields of a_L. With the cavity field displaced by a large photon number we can linearize the dynamics of the small fluctuations by displacing $c \to \bar{c} + c$. Keeping only terms linear in $\bar{c}$ yields the linearized optomechanical interaction

$$H_{\text{om}} = -\hbar g_0 \sqrt{\bar{n}_c} (b_m + b_m^\dagger)(c\, e^{-\mathrm{i}\phi_c} + c^\dagger e^{\mathrm{i}\phi_c}) \tag{2.11}$$

This Hamiltonian contains a linear coupling between the cavity field c and the mechanical oscillator with the optomechanical coupling strength $g_{\text{om}} = g_0\sqrt{\bar{n}_c}$ that is enhanced by the coherent cavity amplitude. We dropped the term $-\hbar g_0 \bar{n}_c (b_m + b_m^\dagger)$ which describes static effects mentioned before, as its effects can be absorbed into a shift of the equilibrium displacement and cavity photon number.

The coupled optomechanical equations of motion are linear and can be solved exactly. To this end, we work in the quadrature basis $X_c = (c + c^\dagger)/\sqrt{2}$, $P_c = -\mathrm{i}(c - c^\dagger)/\sqrt{2}$. To simplify the calculation, we work with rotated fields $\check{c} = ce^{-\mathrm{i}\phi_c}$ and $\check{a}_L = a_L e^{-\mathrm{i}\phi_c}$. For now we drop the check marks on top of the cavity and external light operators for convenience. The equations of motion can be written in matrix form

$$\begin{pmatrix} \dot{X}_c \\ \dot{P}_c \end{pmatrix} = \begin{pmatrix} -\frac{\kappa}{2} & -\Delta \\ \Delta & -\frac{\kappa}{2} \end{pmatrix} \begin{pmatrix} X_c \\ P_c \end{pmatrix} + 2g_{\mathrm{om}} \begin{pmatrix} 0 \\ X_m \end{pmatrix} - \sqrt{\kappa} \begin{pmatrix} X_L^{(\mathrm{in})} \\ P_L^{(\mathrm{in})} \end{pmatrix} \tag{2.12}$$

$$\begin{pmatrix} \dot{X}_m \\ \dot{P}_m \end{pmatrix} = \begin{pmatrix} 0 & \Omega_m \\ -\Omega_m & -\gamma_m \end{pmatrix} \begin{pmatrix} X_m \\ P_m \end{pmatrix} + 2g_{\mathrm{om}} \begin{pmatrix} 0 \\ X_c \end{pmatrix} + \sqrt{2\gamma_m} \begin{pmatrix} 0 \\ F_{\mathrm{th}} \end{pmatrix} \tag{2.13}$$

Here, we defined the optical input fields like in chapter 1 and F_{th} is a stochastic force describing thermal noise which couples to the mechanical oscillator via its support. In the Fourier domain we find the solution

$$\begin{pmatrix} X_c(\omega) \\ P_c(\omega) \end{pmatrix} = -\sqrt{\kappa} M_c(\omega) \begin{pmatrix} X_L^{(\mathrm{in})}(\omega) \\ P_L^{(\mathrm{in})}(\omega) - \frac{2g_{\mathrm{om}}}{\sqrt{\kappa}} \frac{\Omega_m \sqrt{2\gamma_m}}{D_m(\omega)} F_{\mathrm{th}}(\omega) \end{pmatrix} \tag{2.14}$$

$$X_m(\omega) = \frac{\Omega_m}{D_{m,\mathrm{eff}}(\omega)} \left[-\sqrt{2\gamma_m} F_{\mathrm{th}}(\omega) + \frac{4g_{\mathrm{om}}}{\sqrt{\kappa}} F_L^{(\mathrm{in})}(\omega) \right] \tag{2.15}$$

where we defined

$$D_c(\omega) = \left(\frac{\kappa}{2} - \mathrm{i}\omega \right)^2 + \Delta^2 \tag{2.16}$$

$$D_m(\omega) = \Omega_m^2 - \omega^2 - \mathrm{i}\gamma_m \omega \tag{2.17}$$

$$D_{c,\mathrm{eff}}(\omega) = D_c(\omega) + 4g_{\mathrm{om}}^2 \Delta \frac{\Omega_m}{D_m(\omega)} \tag{2.18}$$

$$D_{m,\mathrm{eff}}(\omega) = D_m(\omega) + 4g_{\mathrm{om}}^2 \Omega_m \frac{\Delta}{D_c(\omega)} \tag{2.19}$$

and the matrix

$$M_c(\omega) = \frac{1}{D_{c,\mathrm{eff}}(\omega)} \begin{pmatrix} \frac{\kappa}{2} - \mathrm{i}\omega & -\Delta \\ \Delta + 4g_{\mathrm{om}}^2 \frac{\Omega_m}{D_m(\omega)} & \frac{\kappa}{2} - \mathrm{i}\omega \end{pmatrix} \tag{2.20}$$

which relates the input quadratures to the cavity quadratures. The precise form of the optical force on the mechanical oscillator $F_L^{(\mathrm{in})}$ is given by

$$F_L^{(\mathrm{in})}(\omega) = \frac{\kappa/2}{D_c(\omega)} \left[\left(\frac{\kappa}{2} - \mathrm{i}\omega \right) X_L^{(\mathrm{in})}(\omega) - \Delta P_L^{(\mathrm{in})}(\omega) \right] \tag{2.21}$$

which tends to $F_L^{(\mathrm{in})} \sim X_L^{(\mathrm{in})}$ in the non-resolved sideband regime and for small detuning $|\Delta| \ll \kappa$. An important effect of the optomechanical interaction is the modification of the mechanical susceptibility to thermal noise, which is given by

$$\chi_m(\omega) = \frac{\Omega_m}{D_{m,\mathrm{eff}}(\omega)} \tag{2.22}$$

If the coupling is weak, i.e. $g_{\mathrm{om}} \ll \kappa$, it effectively induces shifts $\delta\Omega_{\mathrm{om}}$ and $\delta\gamma_{\mathrm{om}}$ of the mechanical frequency and damping rate, respectively, given by

$$\delta\Omega_{\mathrm{om}} = 2g_{\mathrm{om}}^2 \,\mathrm{Re}\left\{\frac{\Delta}{D_c(\Omega_m)}\right\} \tag{2.23}$$

$$\gamma_{\mathrm{om}} = -4g_{\mathrm{om}}^2 \,\mathrm{Im}\left\{\frac{\Delta}{D_c(\Omega_m)}\right\} \tag{2.24}$$

In the non-resolved sideband regime with $\Omega_m \ll \kappa$, they amount to

$$\delta\Omega_{\mathrm{om}} \approx 8g_{\mathrm{om}}^2 \frac{\Delta}{\kappa^2 + 4\Delta^2} \tag{2.25}$$

$$\delta\gamma_{\mathrm{om}} \approx -64g_{\mathrm{om}}^2 \frac{\Delta\kappa\Omega_m}{(\kappa^2 + 4\Delta^2)^2} \tag{2.26}$$

The optomechanical damping rate is positive for red laser detuning ($\Delta < 0$) where it leads to cooling of the mechanical mode via the optical bath. In this regime the cavity mode acts as a strongly damped oscillator with whom the mechanical oscillator thermalizes. As the cavity field is driven by optical vacuum noise, sufficiently strong optomechanical damping allows the mechanical oscillator to be cooled into its quantum ground state [112, 113]. However, this only works in the sideband-resolved limit $\Omega_m > \kappa$, where quantum back-action due to the optical vacuum noise is suppressed. In the sideband-resolved limit the optomechanical interaction is then effectively a beam-splitter coupling $\sim b_m^\dagger c + c^\dagger b_m$ between the mechanical and cavity mode, which can be used to swap optical and mechanical states.

For blue detuning ($\Delta > 0$), however, damping turns into amplification as $\delta\gamma_{\mathrm{om}} < 0$. This is caused by a parametric instability as the cavity mode effectively realizes an oscillator with negative frequency. The coupling then leads to correlated optomechanical excitations in analogy to two-mode squeezing which manifest themselves as mechanical amplification. For a sideband resolved system, the optomechanical interaction realizes a two-mode squeezing Hamiltonian $\sim b_m c + b_m^\dagger c^\dagger$, which enables entanglement protocols between the mechanical oscillator and the optical field [114, 68].

On cavity resonance ($\Delta = 0$) the effect of dynamical back-action vanishes and the optomechanical coupling realizes an interaction $\propto X_m X_c$.

In our experiment, we are interested in the non-resolved sideband regime where $\kappa \gg \Omega_m$ and the optical cavity serves as an amplifier for sensitive quantum measurement of the mechanics by the cavity output field. The requirement $\kappa \gg \Omega_m$ arises because delays due to finite cavity response have to be minimized for measurement-based quantum control [64, 115] or cascaded coupling to other quantum systems [47, 51, 36].

2.1.3 Effective coupling to the external field

In the limit of a broad cavity with $\kappa \gg \Omega_m$, the optomechanical interaction can effectively be reduced to a coupling between the mechanical oscillator and the external optical field a_L. This is the regime that we are interested in, when considering a cascaded coupling between the optomechanical system and other quantum systems coupling to the same light field [36]. Working in the resolved sideband-regime would introduce a strong delay between the input and output fields that leads to a rotation of the optical quadratures upon reflection. This can be used as a feature for linear cascaded quantum systems [76, 85], but makes the design of cascaded systems with loops [36] more complicated. For an adiabatic elimination of the cavity without the non-resolved sideband condition see appendix A.7.

With these assumptions, the equations of motion for the cavity field quadratures X_c and P_c decouple. Assuming weak optomechanical coupling $g_{\mathrm{om}} \ll \kappa$, the cavity fields adiabatically follow the inputs, i.e.

$$X_c \approx -\frac{2}{\sqrt{\kappa}} X_L^{(\mathrm{in})} \tag{2.27}$$

$$P_c \approx -\frac{2}{\sqrt{\kappa}} P_L^{(\mathrm{in})} + \frac{4 g_{\mathrm{om}}}{\kappa} X_m \tag{2.28}$$

This leads to the mechanical equations of motion (ignoring thermal noise)

$$\dot{X}_m = \Omega_m P_m \tag{2.29}$$

$$\dot{P}_m = -\gamma_m P_m - \Omega_m X_m - \frac{4 g_{\mathrm{om}}}{\sqrt{\kappa}} X_L^{(\mathrm{in})} \tag{2.30}$$

and the output fields

$$X_L^{(\mathrm{out})} = -X_L^{(\mathrm{in})} \tag{2.31}$$

$$P_L^{(\mathrm{out})} = -\left[P_L^{(\mathrm{in})} - \frac{4 g_{\mathrm{om}}}{\sqrt{\kappa}} X_m\right] \tag{2.32}$$

Note, that the minus signs are due to reflection from the cavity on resonance. However, also the coherent field $\bar{a}_L$, the carrier, experiences the π-phase shift upon reflection. Hence, in the reference frame of the carrier, there is no phase shift of the sideband fields X_L, P_L. The above equations of motion for the mechanical oscillator and input/output relations for the light field can then be described by a Hamiltonian coupling

$$H_{\mathrm{eff}} = \hbar 2 \sqrt{\Gamma_m} X_m X_L(z_m) \tag{2.33}$$

Here, z_m is the location of the optomechanical system along the path of the light field, and

$$\Gamma_m = \frac{4 g_{\mathrm{om}}^2}{\kappa} = \left(\frac{4 g_0}{\kappa}\right)^2 \Phi_L \tag{2.34}$$

is the optomechanical measurement rate. The measurement rate [89] is proportional to the phase-modulation depth produced by a single mechanical phonon on the cavity output field. Another interpretation of Γ_m can be given in terms of the quantum back-action of light onto the mechanical oscillator [94]. The mechanical oscillator is subject to both thermal force noise F_{th} and optical vacuum noise through $X_L^{(\mathrm{in})}$, i.e. in the Fourier domain

$$X_m(\omega) = \chi_m(\omega) \left[\sqrt{2\gamma_m} F_{\mathrm{th}}(\omega) - 2\sqrt{\Gamma_m} X_L^{(\mathrm{in})}(\omega)\right] \tag{2.35}$$

Using this expression, it is straightforward to compute the mechanical displacement fluctuations as quantified by the variance

$$\frac{1}{2}\langle X_m^2 + P_m^2 \rangle = \frac{1}{2} + \bar{n}_{\mathrm{th}} + \frac{\Gamma_m}{\gamma_m} \tag{2.36}$$

which consists of zero-point fluctuations, thermal occupation and quantum back-action, respectively. Consequently, the ratio of the back-action contribution over thermal fluctuations to mechanical motion is expressed in terms of the quantum cooperativity [77]

$$C_m = \frac{\Gamma_m}{\gamma_{m,\mathrm{th}}} \tag{2.37}$$

where $\gamma_{m,\mathrm{th}} = \gamma_m \bar{n}_{\mathrm{th}}$ is the thermal decoherence rate for a thermal bath occupation $\bar{n}_{\mathrm{th}}$. Achieving a large quantum cooperativity is a key requirement for many optomechanical entanglement protocols [114, 116] and measurement-based quantum-control [64, 65].

2.1.4 Homodyne detection

Cavity optomechanics enables straightforward measurement of mechanical displacement by homodyne detection of the cavity output field [37]. The cavity output field with flux Φ_L is mixed with a strong local oscillator with flux $\Phi_{\mathrm{LO}} \gg \Phi_L$ on a 50:50 beam splitter and its two output fields are detected on a balanced photodetector (see Fig. 2.17). A homodyne detector measures $D = \sqrt{2\Phi_{\mathrm{LO}}}[\cos(\phi)X_L^{(\mathrm{out})} + \sin(\phi)P_L^{(\mathrm{out})}]$, where ϕ is the local-oscillator phase. When ϕ is tuned continuously, the resulting DC signal $D_0 = 2\sqrt{\Phi_{\mathrm{LO}}\Phi_L}\cos(\phi)$ can be used to determine the interference contrast $D_{\max} = 2\sqrt{\Phi_{\mathrm{LO}}\Phi_L}$ proportional to the coherent field amplitudes, which is useful for normalization of the detector signal. Since the mechanical signal is entirely encoded in the P_L quadrature, best signal-to-noise ratio for a measurement of X_m is obtained at $\phi = \pi/2$. Then, we have

$$\frac{D}{D_{\max}} = \frac{4g_0}{\kappa}\sqrt{2}X_m + \frac{1}{\sqrt{2\Phi_L}}P_L^{(\mathrm{in})} \tag{2.38}$$

which allows to determine X_m provided g_0 and κ have been independently calibrated, e.g. using the method in [117]. The homodyne phase-noise power spectral density (PSD) is given by [56, 94]

$$\bar{S}_{PP,L}^{(\mathrm{out})}(\omega) = \bar{S}_{PP,L}^{(\mathrm{in})}(\omega) + 4\Gamma_m \bar{S}_{XX,m}(\omega) \tag{2.39}$$

$$= \frac{1}{2} + 8\Gamma_m\gamma_m|\chi_m(\omega)|^2\left(\frac{1}{2} + \bar{n}_{\mathrm{th}} + \frac{\Gamma_m}{\gamma_m}\right). \tag{2.40}$$

In the second line, we used $\bar{S}_{FF,\mathrm{th}} = \bar{n}_{\mathrm{th}} + 1/2$. The homodyne PSD is thus composed of vacuum noise of the optical input field, i.e. shot noise $\bar{S}_{PP,L}^{(\mathrm{in})} = 1/2$, and the mechanical noise. The mechanical noise itself comprises zero-point motion, thermal noise and quantum back-action. The latter is only relevant for large quantum cooperativity, i.e. $\Gamma_m \gg \gamma_m \bar{n}_{\mathrm{th}}$. This leads to the standard quantum limit as the trade-off between shot noise limiting the precision of the measurement at low optical power and quantum back-action disturbing the measurement at large power [89, 56].

2.2 Membrane optomechanical cavity

The canonical optomechanical system consists of an optical cavity with a vibrating end mirror. For optimal performance, this requires combining a high-quality mechanical resonator with low mass and a high-reflectivity mirror structure in a single device, which is a challenging task. Indeed, such a device has been realized using nanobeams with a dieletric mirror structure fabricated on top [118]. Most state-of-the-art optomechanical devices, however, exploit different coupling mechanisms. The general recipe for optomechanical coupling is to equip an optical resonance with a mechanically compliant element whose displacement modifies the optical resonance frequency. Today, integrated optomechanical crystal devices can be fabricated that have co-localized mechanical and optical modes with very large optomechanical coupling strengths [119].

Our research group follows a different approach which combines separate mechanical and optical resonators by inserting a dielectric silicon nitride membrane into a standard Fabry-Perot optical cavity [40, 120]. Due to its index of refraction, the membrane shifts the optical resonance frequency by an amount that is proportional to the local optical intensity at the membrane. Since the membrane is much thinner than the optical wavelength this generates a potential for the cavity mode that periodically depends on the membrane displacement relative to the standing wave optical intensity. The benefit of such membrane-in-the-middle (MIM) cavities is that it is possible to independently optimize their mechanical and optical properties. The membranes can be engineered to have both extraordinarily high mechanical quality factors and low effective mass [57, 58, 59]. The quality of the optical resonance only depends on the reflectivity of the mirrors used and the optical absorption and scattering by the membrane material. For state-of-the art membranes made of silicon-nitride, optical loss in the near infrared is very low ($\lesssim 10^{-5}$ [120, 121]) which enables high finesse optical resonances.

The optical resonances and optomechanical coupling in such a MIM cavity can be understood from a classical coupled-wave analysis. For this purpose, we reduce the membrane to a simple beam-splitter inside the cavity with a certain (amplitude) reflectivity $r_m < 1$ (see Fig. 2.1a). The right and left mirrors have reflectivities r_1 and r_2, respectively, both $r_1, r_2 \approx 1$. We define the cavity length L_c as the distance between the mirrors and the membrane position x_m as the distance from the left mirror. One can then solve a set of coupled wave equations [122, 78, 123] to obtain the cavity field amplitudes. The results of this treatment are well established. One finds that the cavity resonance frequency $\omega_c(x_m)$ can locally be approximated as a periodic function of the membrane position with a periodicity of $\lambda/2$ (see Fig. 2.1b). In essence, the membrane divides the cavity into one subcavity with length x_m and another with length $L - x_m$. If the membrane position increases, it makes the left subcavity longer and the right subcavity shorter, thus decreasing and increasing their respective resonance frequencies. Since the membrane transmission is rather high, the resonances of both subcavities are strongly coupled and show avoided crossings, which then results in the periodic modulation of the full cavity resonance. Linear optomechanical coupling as in (2.1), where the cavity resonance changes linearly with x_m, is achieved at the points where one subcavity is resonant with the light and the other anti-resonant. This produces a large optical amplitude in the former and a small amplitude in the latter such that the resulting radiation pressure on the membrane is maximal. Moreover, since the two end mirrors have unequal reflectivities, the redistribution of light between the subcavities also modifies the cavity linewidth and coupling efficiencies to the external fields [120, 124]. In the following we will present the expected optomechanical parameters for our experimental device.

For practical reasons we decided to position the membrane not in the middle of the cavity, but near the end, close to the high-reflectivity end mirror 2, which greatly simplifies the alignment procedure (see Fig. 2.1c). Such a membrane-at-the-end (MATE) cavity design is used in various other research groups [124, 78, 123]. Placing the membrane close to one end mirror significantly changes the variation of optomechanical coupling G and cavity linewidth κ due to the asymmetry between the subcavity lengths.

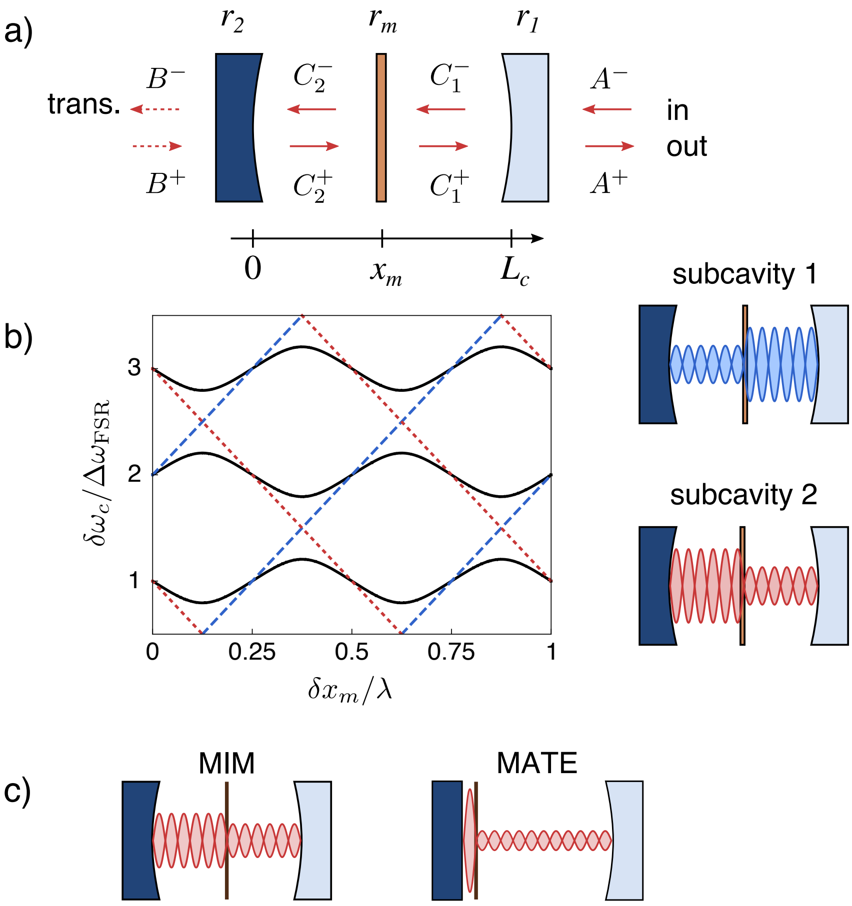

Figure 2.1: Schematic of a single-sided membrane optomechanical cavity. a) Transfer matrix model. Fields are coupled into the cavity with high efficiency through mirror 1 on the right which has lower reflectivity $r_1 < r_2$ than mirror 2. The high-reflectivity back-mirror 2 permits only weak transmission. b) Calculated spectrum of the cavity (black, solid lines) for $r_m = 0.6$ as a function of membrane position change δx_m for three adjacent longitudinal modes. The resonance frequencies of the left subcavity 2 and right subcavity 1 are drawn as the red dotted and blue dashed lines, respectively. Images on the right sketch the intracavity field intensities in the situations where the full cavity is either resonant with subcavity 1 or with subcavity 2. c) Comparison of the MIM with the MATE configuration, which shows a much stronger field asymmetry between the two subcavities.

Resonance frequency Solving the coupled-wave problem yields cavity field amplitudes of the form

$$C_{1,2}^{\pm} \propto \frac{1}{1-\xi}, \qquad \xi = r_1 r_2 e^{\mathrm{i}2kL} + r_2 r_m e^{\mathrm{i}2kx_m} - r_1 r_m e^{\mathrm{i}2k(L-x_m)} \tag{2.41}$$

Setting $r_1 = r_2 = 1$ and assuming $1 - r_m^2 \gg 1 - r_1^2, 1 - r_2^2$, the resonance condition can be found by solving $\xi = 1$ for $\omega_c = ck$. This transcendental equation can only be solved numerically, but approximate solutions can be found in the MIM and MATE geometries for small displacements $x_m = \bar{x}_m + \delta x_m$ with $\delta x \ll L_c$. In the MIM geometry ($\bar{x}_m = L_c/2$) one finds

$$\omega_n(\delta x_m) = \Delta\omega_{\mathrm{FSR}} \left\{ n - \frac{(-1)^n}{\pi} \arcsin\left[r_m \sin(2k\delta x_m) \right] \right\} \tag{2.42}$$

which is displayed in Fig. 2.1b) and in the MATE geometry ($\bar{x}_m = 0$)

$$\omega_n(\delta x_m) = \Delta\omega_{\mathrm{FSR}} \left\{ n - \frac{1}{\pi} \arctan\left[r_m \frac{\sin(2k\delta x_m)}{1 - r_m \cos(2k\delta x_m)} \right] \right\} \tag{2.43}$$

Here, $\Delta\omega_{\mathrm{FSR}} = \pi c/L_c$ is the empty cavity free-spectral range (FSR) and c is the speed of light. The mode index $n = 1, 2, \ldots$ labels different longitudinal modes. The wavenumber $k = 2\pi/\lambda$ appearing in the equations is fixed due to the assumption $\delta x_m \ll L$ made in deriving these equations. The change in cavity resonance frequency $\delta\omega_c$ as a function of membrane displacement is plotted in Fig. 2.2a). Three different cases are shown, the MIM configuration with $\bar{x}_m = L_c/2$, the MATE configuration with $\bar{x}_m = 0$ and an intermediate case $\bar{x}_m = 0.2L_c$ which is the one implemented in the experiment. These three cases indicate the transition from the symmetric modulation of ω_c in MIM configuration towards the asymmetric MATE configuration where $\delta\omega_c$ has one steep slope where the short subcavity is resonant and one gentle slope for the long subcavity. Fig. 2.2 also shows other relevant parameters of the membrane cavity which are discussed below. All calculations use $r_m = 0.6$ like in the experiment.

Optomechanical coupling The optomechanical coupling constant $G = -\partial\omega_c/\partial x_m$ could be calculated from the above approximate resonance frequencies. However, an analytic solution can be found [78] using a more insightful method. The radiation pressure force on the membrane is given by [40]

$$F_{\mathrm{rad}} = 2\hbar k (p_2 - p_1) \tag{2.44}$$

where $p_i = |C_i^+|^2 + |C_i^-|^2$ is the circulating optical flux in subcavity i. We can compare this with the expression $F_{\mathrm{rad}} = \hbar G n_c$ where $n_c = \tau_1 p_1 + \tau_2 p_2$ is the total cavity photon number and $\tau_1 = 2x_m/c$ and $\tau_2 = 2(L - x_m)/c$ are the roundtrip times in subcavities 1 and 2, respectively. This gives

$$G = 2k \frac{p_2 - p_1}{\tau_2 p_2 + \tau_1 p_1} \tag{2.45}$$

Inserting the solution of the coupled-wave analysis gives

$$G = \frac{\Delta\omega_{\mathrm{FSR}}}{\lambda} \frac{4 r_m L_c [r_m - \cos(2kx_m)]}{L_c(1 + r_m^2) - 2r_m^2 x_m - 2r_m(L_c - x_m)\cos(2kx_m)} \tag{2.46}$$

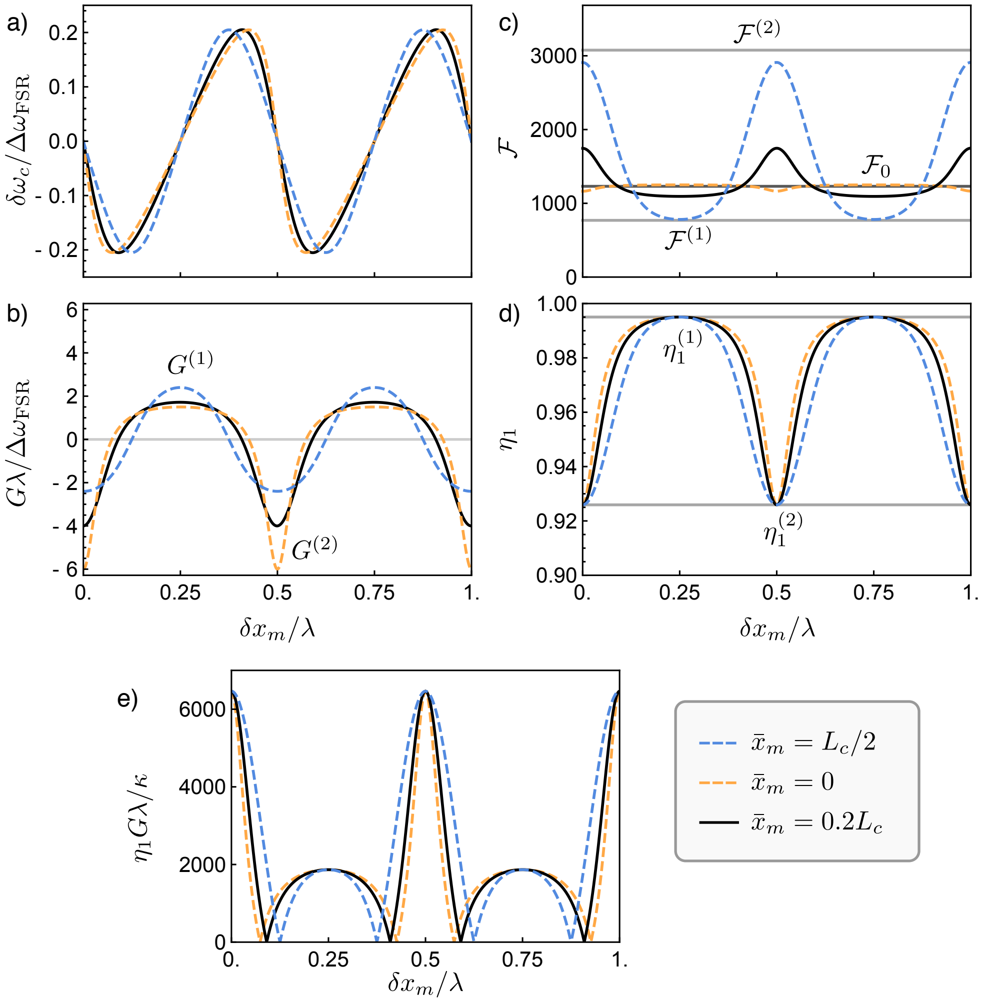

Figure 2.2: Various parameters of the membrane optomechanical cavity as a function of the membrane displacement $\delta x_m = x_m - \bar{x}_m$ for three reference points indicated in the legend. a) Shift of the cavity resonance frequency $\delta\omega_c$. b) Optomechanical coupling strength G. c) Cavity finesse $\mathcal{F}$. d) Coupling efficiency η_1 through mirror 1. e) Displacement sensitivity $\eta_1 G/\kappa$. The calculations use $r_m = 0.6$, $r_1^2 = 0.995$ and $r_2^2 = 0.9999$.

Note that here $k = \omega_c/c$ requires the precise resonance frequency ω_c. Fig. 2.2b) shows G as a function of x_m. The maximum coupling strengths are attained for $2kx_m \mod 2\pi = 0$ for resonant subcavity 2, which we denote $G^{(2)}$, and for $2kx_m \mod 2\pi = \pi$ corresponding to resonant subcavity 1 (and anti-resonant subcavity 2), which we denote $G^{(1)}$. In MIM configuration, one finds the known result $G^{(1)} = -G^{(2)} = 4r_m\Delta\omega_{\mathrm{FSR}}/\lambda =: G_{\mathrm{MIM}}$. In MATE geometry close to mirror 2, one finds $G^{(1)} = G_{\mathrm{MIM}}/(1 + r_m)$ and $G^{(2)} = -G_{\mathrm{MIM}}/(1 - r_m)$. As expected the coupling is enhanced for the short subcavity.

Cavity linewidth An expression for the cavity energy damping rate κ (also: full linewidth at half-maximum) can be derived by the following reasoning [123]. Decay of the cavity photon number has to equal the output photon flux through the two mirrors, i.e.

$$\dot{n}_c = -p_1 t_1^2 - p_2 t_2^2 \tag{2.47}$$

where $t_i^2 = 1 - r_i^2$ are the mirror power transmission coefficients. This can be compared to the exponential law $\dot{n}_c = -\kappa n_c$ or $\kappa = -\dot{n}_c / n_c$. Consequently, we get

$$\kappa = \frac{p_1 t_1^2 + p_2 t_2^2}{\tau_1 p_1 + \tau_2 p_2} \tag{2.48}$$

The full explicit expression is too cumbersome to write down, it can be found in ref. [123]. Fig. 2.2c) shows the calculated cavity finesse $\mathcal{F} = \Delta\omega_{\mathrm{FSR}}/\kappa$ as a function of membrane displacement for $r_1^2 = 0.995$ and $r_2^2 = 0.9999$. We can again define limiting values $\kappa^{(i)}$ (or $\mathcal{F}^{(i)}$) corresponding to the extremal coupling points $G^{(i)}$ defined above. Simple limiting expressions can be found in the relevant single-sided case $t_2 \ll t_1$. In the following, we define the empty cavity linewidth $\kappa_0 = \Delta\omega_{\mathrm{FSR}}/\mathcal{F}_0$ with corresponding finesse $\mathcal{F}_0 = \pi/(1 - r_1 r_2)$. In the MIM geometry, we then have $\kappa^{(1)} = \kappa_0/(1 - r_m)$ and $\kappa^{(2)} = \kappa_0/(1 + r_m)$, i.e. the linewidth is increased in subcavity 1 with the lower-reflectivity mirror and it is decreased in subcavity 2 with the high-reflectivity mirror. With the membrane close to mirror 2, we get $\kappa^{(1)} = \kappa^{(2)} = \kappa_0$ or no change in the linewidth. This is also easy to understand since all losses are dominated by mirror 1. With the membrane close to the low-reflectivity mirror 1, $\kappa^{(1)} = \kappa_0(1 + r_m)/(1 - r_m)$ is increased and $\kappa^{(2)} = \kappa_0(1 - r_m)/(1 + r_m)$ is decreased, giving maximum variation of the cavity dissipation with membrane position, which can be exploited for dissipative optomechanical coupling [125, 123]. Fig. 2.2c) illustrates how the variation of κ increases with distance from mirror 2.

Coupling efficiency A high coupling efficiency η_1 to the cavity through mirror 1 is important to maximize quantum efficiency of detection and minimize added quantum back-action due to vacuum noise entering via mirror 2. The coupling efficiency η_1 through mirror 1 is defined by [56]

$$\eta_1 = \frac{\kappa_1}{\kappa} \tag{2.49}$$

which compares the decay rate κ_1 of the cavity through mirror 1 to the full cavity decay rate κ. For the empty cavity without membrane or internal loss it is given by $\eta_{1,0} \approx t_1^2/(t_1^2 + t_2^2)$, i.e. transmission through mirror 1 divided by total roundtrip loss. Hence for $t_2 \ll t_1$ this value tends to unity as desired. For the cavity including the membrane we can compute η_1 using the ratio of output powers [78]

$$\eta_1 = \frac{t_1^2 |C_1^+|^2}{t_1^2 |C_1^+|^2 + t_2^2 |C_2^-|^2} \tag{2.50}$$

This expression is again relatively complicated and not worth displaying. Calculations are displayed in Fig. 2.2d) with same parameters as in c). For resonant subcavity 1 we find that η_1 is enhanced, while for resonant subcavity 2 it is decreased, due to enhanced loss via mirror 2. The resonant cavity amplitude reflectivity from mirror 1 can be computed as $r_c = 1 - 2\eta_1$.

Displacement sensitivity From the definition of the optomechanical measurement rate $\Gamma_m \propto (g_0/\kappa)^2$ it is clear that the cavity sensitivity to membrane displacements G/κ is the relevant figure of merit for the cavity design. In addition, large coupling efficiency η_1 and non-resolved sideband condition $\kappa \gg \Omega_m$ have to be satisfied as well. From the above discussion we get

$$\frac{G}{\kappa} = 2k \frac{p_2 - p_1}{t_1^2 p_1 + t_2^2 p_2} \tag{2.51}$$

We find that $G^{(i)}/\kappa^{(i)}$ for $i = 1, 2$ is independent of the coarse position $\bar{x}_m$ of the membrane in the cavity and independent of the cavity length L_c. Moreover, for $t_2^2 \ll t_1^2$

$$\frac{G^{(2)}}{\kappa^{(2)}} \frac{\kappa^{(1)}}{G^{(1)}} \approx \frac{1 + r_m}{1 - r_m} \tag{2.52}$$

which makes it more favorable to position the membrane such that subcavity 2 is resonant. For a membrane reflectivity $r_m = 0.6$ this enhancement amounts to 4, but it could be increased even further with photonic-crystal patterned membranes [126, 57, 127, 128] for which reflectivities $r_m^2 > 0.99$ have been demonstrated.

2.3 Silicon-nitride membranes

Having discussed the optical properties of membrane optomechanical cavities, we now focus on the mechanical properties of silicon nitride (SiN) membranes. Due to their extremely high tensile stress and nanometer-scale thickness, stoichiometric Si_3N_4 membranes combine several appealing properties: high quality factors (Q-factors) $> 10^6$, MHz mechanical frequencies and low effective masses ~ 10 ng [40, 120, 129, 130, 131, 57, 58, 59]. These exceptional mechanical properties render them highly promising for nanomechanical force sensing [132, 133] and quantum optomechanics [134, 66, 51, 135].

The membranes we use are standard square SiN films suspended from a 200 μm thick silicon substrate. The SiN thickness of $h = 100$ nm has been chosen to maximize optical reflectivity to $r_m \approx 0.6$ at $\lambda = 780$ nm. A photograph of such a device is shown in Fig. 2.3a). As detailed below, the silicon chip around the membrane is patterned with a phononic bandgap structure [41, 130] to shield particular modes from mechanical noise and dissipation induced by the frame. The out-of-plane vibrations of a SiN film with side length $a \gg h$ can be described in terms of the normal modes

$$u_{jk}(x, y) = \sin(j\pi x/a) \sin(k\pi y/a) \tag{2.53}$$

(see Fig. 2.3b) where $x, y \in [0, a]$ are in-plane coordinates and $j, k = 1, 2, \ldots$ are mode indices. The total membrane displacement is hence given by

$$u(x, y) = \sum_{jk} u_{jk}(x, y) z_{jk} \tag{2.54}$$

Each mode forms a harmonic oscillator with linear displacement z_{jk} and momentum p_{jk} which can be quantized using the formalism presented in section 2.1 using mode creation and annihilation operators b_{jk} and $b_{jk}^\dagger$, respectively. This allows the membrane

Hamiltonian to be decomposed into a sum of harmonic oscillator Hamiltonians

$$H_m = \sum_{j,k} \hbar\Omega_{jk} \left(b^\dagger_{jk} b_{jk} + \frac{1}{2} \right) \tag{2.55}$$

over all modes j, k with mode frequencies given by

$$\Omega_{jk} = \Omega_{11} \sqrt{\tfrac{j^2+k^2}{2}}, \quad \Omega_{11} = \frac{\pi}{a} \sqrt{\frac{2S}{\rho}} \tag{2.56}$$

Here, $\rho \approx 2.8 \times 10^3$ kg/m^3 is the density of silicon-nitride and $S \approx 0.9$ GPa is the tensile stress [129]. This suggests that modes with indices j, k and k, j are degenerate. In practice, however, a slight asymmetry of the membrane side lengths a_x and a_y in x and y direction, respectively, lifts this degeneracy and leads to a splitting $\delta\Omega_{jk}/\Omega_{jk} \approx \frac{j^2-k^2}{j^2+k^2} \frac{a_y-a_x}{(a_x+a_y)/2}$ which typically is at the percent level. To investigate optomechanics with a single mechanical mode, this small splitting makes it unfavorable to use modes with $j \neq k$. Symmetric modes with $i = j$, on the contrary, are typically well isolated from neighboring modes, e.g. for $i = 1, 2, 3$ with more than 100 kHz frequency distance at $\Omega_{11} > 1$ MHz, and are thus well suited for our purpose. A typical mechanical displacement spectrum obtained for a membrane with $a = 270$ μm side length is shown in Fig. 2.3b). Almost all peaks can be assigned to a particular membrane mode. The spectrum has been recorded by homodyne detection of the cavity output field and the imprecision noise-floor is limited by shot noise of the probe light.

When probed with the fundamental TEM$_{00}$ cavity mode with waist w_0 and intensity distribution

$$|u_\text{opt}(x, y)|^2 = \frac{2}{\pi w_0^2} e^{-2\frac{x^2+y^2}{w_0^2}}, \tag{2.57}$$

the optomechanical coupling strength $G_{jk} = \eta_{jk} G$ to an individual membrane mode is reduced by an overlap factor $\eta_{jk} < 1$. This overlap factor can be calculated using [120, 78]

$$\eta_{jk} = \left| \int_0^a \int_0^a u_{jk}(x, y) |u_\text{opt}(x, y)|^2 \mathrm{d}x\mathrm{d}y \right| \tag{2.58}$$

For an optical mode centered at $0 < x_0, y_0 < a$ with waist $w_0 \ll a$, such that clipping by the membrane edges is negligible, the overlap is simply given by

$$\eta_{jk} = |u_{jk}(x_0, y_0)| e^{-\frac{1}{2}\left(\frac{\pi w_0}{\lambda_{jk}}\right)^2} \tag{2.59}$$

where $\lambda_{jk} = 2a/\sqrt{j^2 + k^2}$ is the effective wavelength of the mechanical mode. Hence, for good overlap it is not only crucial to position the optical spot such that $|u_{jk}(x_0, y_0)| = 1$ is maximal, but also to ensure that the optical waist $w_0 \ll \lambda_{jk}$ is much smaller than the mechanical wavelength. In the experiments reported here we have $a = 400$ μm and $w_0 \approx 35$ μm such that this condition is only satisfied for the lowest order modes. In order to compute g_0, one also has to know the effective mass, which is given by $m_\text{eff} = \rho a^2 h/4$ for any mode, i.e. one quarter of the physical mass [40].

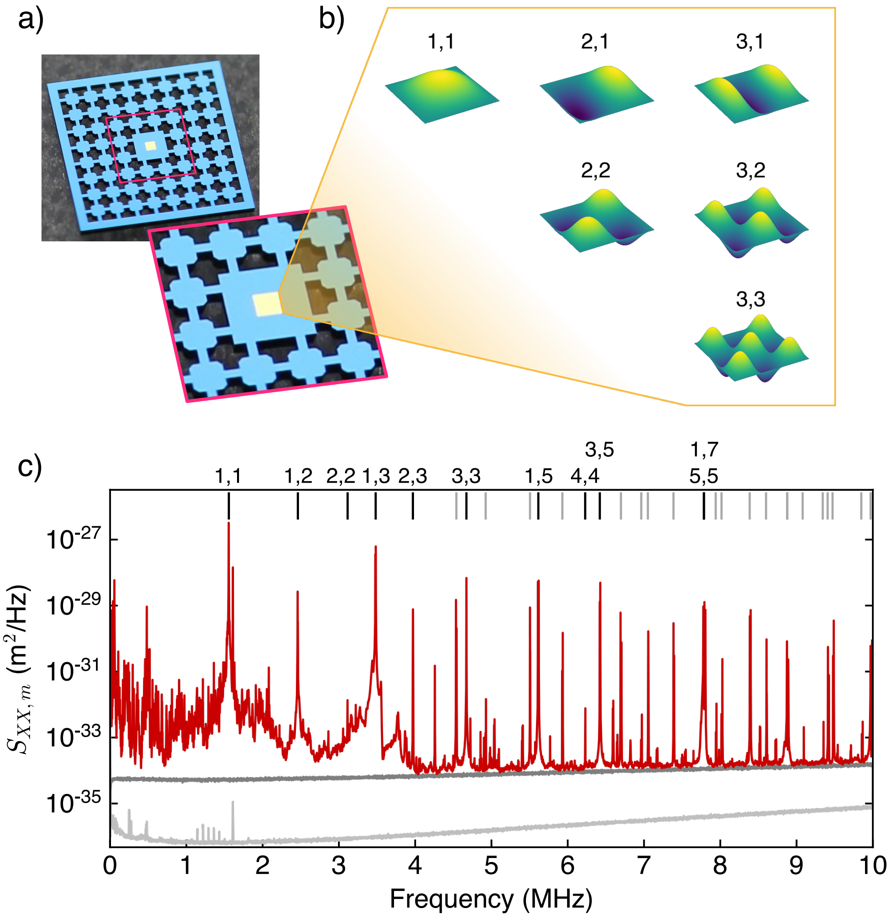

Figure 2.3: The mechanical device. a) Photograph of a silicon nitride membrane embedded in a silicon phononic bandgap structure (light blue) with inset zooming in on the central defect hosting the membrane (light yellow). Here, the size of the silicon chip is 5×5 mm^2 and the membrane has side length 270 μm. b) Mode functions of the lowest vibrational modes of the square membrane. c) Typical thermal displacement spectrum (red) obtained for this device with indicated frequencies of a few selected modes. The cavity mode is aligned to the membrane center such that the odd symmetric modes (1,1), (3,3), etc. have strongest coupling while the even modes (2,2), (4,4), etc. are suppressed. Measurement imprecision shot noise is the dark gray line and detector dark noise is the light gray line.

It is well understood that the high Q-factors achieved in high-stress SiN thin films (thickness < 100 nm) are due to “dilution” of internal dissipation, like bending or clamping losses or material defects, by the extremely large tensile stress of order 1 GPa achieved by low-pressure chemical vapour deposition [129, 136]. In standard square films which are uniformly clamped at the edges, mechanical quality factors are still limited to about $\sim 10^6$ at MHz frequencies because of bending losses induced by the large mode curvature at the SiN-silicon edge [129] and coupling to frame modes [137]. To address the second point and effectively shield particular membrane modes from radiation losses into the

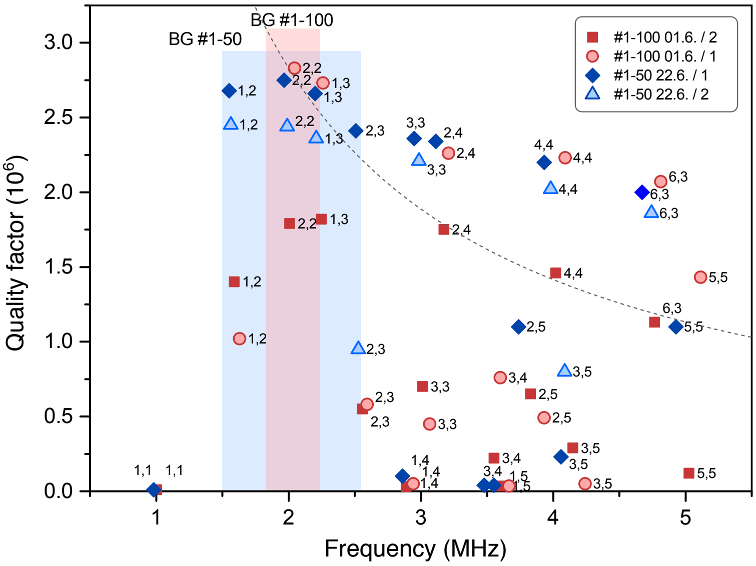

Figure 2.4: Compilation of measured quality factors for two different phononic bandgap membrane designs (1-50: 50 μm bridges and 1-100: 100 μm bridges). The dashed line indicates the thermal phonon occupation at room temperature.

silicon substrate, the silicon chip around the SiN membrane has been patterned with a phononic crystal structure that induces a bandgap for acoustic modes in a certain frequency ranges [41, 130]. In this way, certain target modes of the SiN membrane are well protected from such losses and show reproducible quality factors independent of the way the chip is mounted. Our devices were jointly ordered from NORCADA Inc. (Canada) together with the groups of C. Regal (JILA, USA) and J. Harris (Yale, USA) in 2015. A compilation of mechanical Q-factors of some of our devices are shown in Fig. 2.4. The data were measured by ringdown using a free-space interferometer and optomechanical actuation using an additional, resonantly modulated laser beam. The data belong to two different phononic crystal designs, one with bridges of width 100 μm (#1-100) connecting the islands, and another with 50 μm width (#1-50). The bridge width is inversely proportional to the width of the bandgap, which is indicated for the two designs by the coloured regions in Fig. 2.4. The measured Q-factors clearly scatter a lot, but consistently reach high values $> 10^6$ inside the designated bandgaps for all four measured devices.

An important figure of merit for the quantum coherence of a mechanical oscillator is the ratio between its mechanical frequency and thermal decoherence rate [56]

$$\frac{\Omega_m}{\gamma_{m,\mathrm{th}}} = \frac{Q}{\bar{n}_{\mathrm{th}}} = \frac{h}{k_B T} \cdot Q f_m, \tag{2.60}$$

where $f_m = \Omega_m / 2\pi$. It gives the achievable number of coherent mechanical oscillations before thermal noise has added one phonon. The last equality shows that this number is proportional to the Q-frequency product $Q f_m$ which is widely used as a figure of merit for judging whether a mechanical oscillator can operate in the quantum-coherent regime. It means that both a high Q and high frequency are crucial for quantum coherence in the presence of thermal noise. At room temperature ($T = 293$ K) a value of $Qf_m > 6 \times 10^{12}$ is required to achieve $\Omega_m > \gamma_{m,\mathrm{th}}$. This limit is indicated by the dashed line in Fig. 2.4, which shows that only a few high-order modes can exceed it. However, cryogenic precooling of the membrane to liquid-Helium temperature $T = 4.2$ K reduces thermal noise by almost two orders of magnitude and allows the quantum coherent regime to be reached. Moreover, it has been observed that mechanical quality factors of high-stress silicon nitride membranes tend to increase at low temperatures [130, 138, 131], as internal material defects gradually freeze out. Today, by more sophisticated stress engineering [57, 58] or by integrating phononic crystal structures into the SiN film [59], improved membrane devices have been fabricated with much higher mechanical Q reaching 10^8 and higher. These devices may eventually enable quantum optomechanics experiments at room temperature. For the experiments presented in this thesis, we work with a chip of the #1-50 bandgap design and use the 2,2 mode inside the bandgap. For this mode we have measured $Q = 1.3 \times 10^6$ with the device mounted inside the cavity.

2.4 Cavity assembly

With the goal of doing quantum optomechanics experiments with a SiN membrane, we developed a new cavity design which is compatible with cryogenic cooling to $T \approx 4$ K, following design guidelines found in [124] and [139]. We decided to pursue a near monolithic design, where all optical alignment between the cavity mode and the membrane mode is carried out once at room temperature. The device must then be stable enough to maintain this alignment upon transfer to the cryostat and cool-down. Moreover, it was important to build the cavity such that the membrane can be exchanged without having to sacrifice the remaining parts, like the mirrors and piezos.

Design concept In order to keep the mechanical design and assembly as simple as possible, we use one flat mirror and one curved mirror and choose a MATE geometry. This enables us to first align the membrane parallel to the flat mirror, and in the second step position the curved mirror such that the cavity mode forms at the correct position on the targeted membrane mode. Both alignment steps can be carried out without the need of external micro- or nano positioners holding the membrane or any mirror. In order to lock the cavity to the laser and also position the membrane relative to the intra-cavity standing wave, we mount the mirrors on top of piezo ring chips[1]. These are servicable at 4 K, but relative to room temperature their stroke reduces by about 1/5 and their capacitance decreases from $C_p = 800$ nF to 200 nF. The latter is beneficial for faster control. Reduced stroke can be partly compensated by operating the piezos in bipolar mode between ±100 V at low temperatures only.

Early tests proved that using epoxy makes the design highly vulnerable to misalignment. Consequently, we only use epoxy[2] to fix the mirrors in their sockets. In first attempts, the membrane was also glued to its mount, which always resulted in a tilt upon cool-down. We found that only clamping the membrane maintains alignment, but too strong clamping can couple the silicon chip to low frequency resonances of the entire

---

[1] Piezomechanik GmbH, HPCh 150/15-8/3

[2] STYCAST 2850 FT, catalyst 9

cavity structure which is detrimental for closed-loop piezo control of the cavity. Hence, we have started to use thin, water-jet cut metal and Kapton sheets (both $\sim 100\ \mu$m thick) to gently clamp the membrane chip.

All mechanical parts are machined from Titanium as it is lightweight, stiff, has rather low thermal expansion and keeps a moderate thermal conductivity at cryogenic temperatures. Screws are also made of Titanium for alignment sensitive parts. However, steel screws have proven to be more durable and more fail-safe, as Titanium screws tend to break when fastened too much.

Assembly Here, we give a brief overview of the cavity assembly. The main alignment steps and basic design are illustrated in Fig. 2.5.

1. Before assembly, all metal components are cleaned multiple times in an ultrasonic bath for vacuum compatibility using first water with detergent, then distilled water, then acetone, then isopropanol.

2. The flat mirror-piezo stack is assembled (Fig. 2.5 (1)) and attached to the main frame. A thin copper ring (0.1 mm) is inserted between piezo and mirror mount. The mirror is glued to its mount using three to four drops of epoxy applied on the mirror side walls such that mirror position is defined only by the socket. The membrane chip is clamped onto the main frame facing the flat mirror.

3. By carefully tweaking the alignment screws which clamp the flat mirror-piezo stack to the main frame, the flat mirror surface is aligned parallel to the membrane. Alignment is monitored by sending a collimated laser beam onto the membrane and scanning the piezo by more than $\lambda/2$. The laser beam transmitted through the resulting membrane-mirror etalon is imaged on a CCD camera and produces

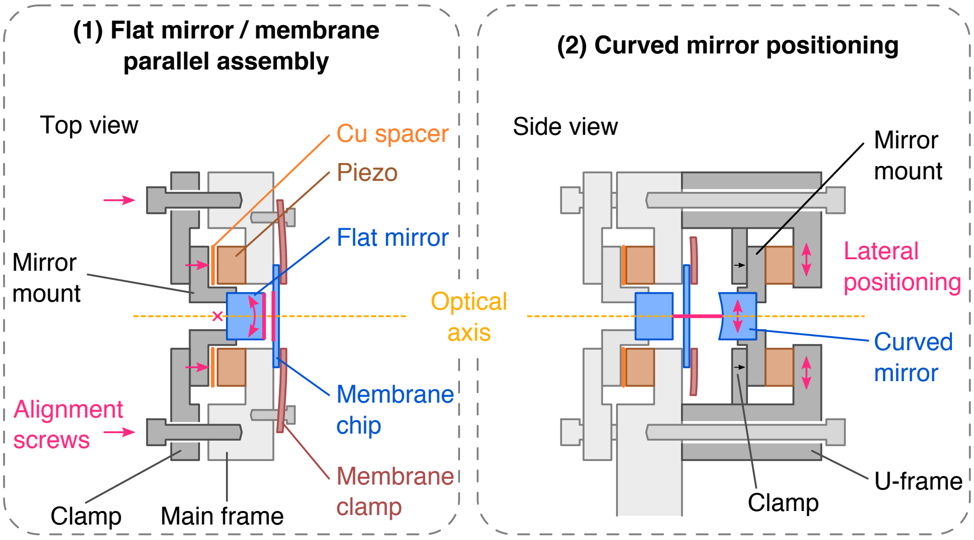

Figure 2.5: Assembly steps of the membrane optomechanical cavity (not to scale). In each step, parts in light gray are fixed, parts in dark gray are moved.

an interference pattern that reveals tilts between membrane and mirror. Tilts are reduced by removing the interference pattern such that the membrane is homogeneously illuminated by the laser beam. With a membrane reflectivity of $r_m \approx 0.6$, the membrane-mirror etalon has a finesse of $\mathcal{F}_m = \pi\sqrt{r_m}/(1 - r_m) \approx 6$. For a membrane side length of $a = 0.4$ mm, this results in a sensitivity of the interference pattern to tilts of order $\lambda/(a\mathcal{F}_m) \approx 3 \times 10^{-4}$, which proves sufficient for our purpose. In this step the copper ring between mirror mount and piezo is supposed to adapt to the pressure and take away stress from the piezo, but maintain alignment. It has to be tested whether a softer Kapton sheet can also be used for that task.

4. Once the membrane is parallel to the flat mirror, the curved-mirror-piezo stack (see Fig. 2.5 (2)) is assembled and clamped to a U-shaped frame that positions the curved mirror above the membrane. The curved mirror is aligned such that all cavity modes are centered on an anti-node of the target mechanical mode. This can still be coarsely aligned with a collimated input beam and scanning of the flat piezo.

5. The cavity input beam is mode-matched to the cavity using a lens and the curved mirror position is finely adjusted to overlap the fundamental cavity mode with the target mechanical mode. Here, the U-shaped mount needs to be pushed from the side either manually or using an external translation stage.

6. By scanning both piezos, a full transmission spectrum of the laser beam through the membrane cavity is measured using a photodetector. This is to confirm that there are no avoided crossings between the fundamental cavity mode and higher order transverse modes, which would indicate a membrane tilt.

7. Optional: before inserting the membrane, the empty cavity should be assembled such that its finesse can be measured and functionality of both piezos can be checked.

Device parameters The final assembled cavity has a nominal length $L_c = 1.2$ mm and $\Delta\omega_{\mathrm{FSR}} = 2\pi \times 125$ GHz, based on design dimensions. The mirrors have been purchased from Layertec GmbH. The flat mirror has specified reflectivity $r_2^2 > 0.9999$, our measurements suggest $r_2^2 = 0.9999$. The curved mirror with radius of curvature 30 mm has a specified reflectivity $r_1^2 = 0.995$. The mirror reflectivities imply an empty cavity finesse $\mathcal{F}_0 = \pi\sqrt{r_1 r_2}/(1 - r_1 r_2) = 1230$ which agrees with our measurements. The membrane chip is positioned with the membrane facing towards the flat mirror, leaving a mirror-membrane gap of $\bar{x}_m = 0.2$ mm. The geometry is hence an intermediate between MATE and MIM. The simulations of Fig. 2.2 (black lines) take this into account.

Photographs of the assembled cavity are displayed in Fig. 2.6. A side view without membrane reveals the 1 mm gap between the flat mirror (left) and curved mirror on U-frame (right). In the front view the phononic crystal membrane is visible through the curved mirror. Piezo wires (Kapton coated) are guided through holes of the main frame or U-frame and attached using epoxy. The back view shows a standard square membrane through the flat mirror and the cross-shaped clamp for the flat-mirror-piezo-stack is visible. An image of the cavity mode aligned to the 2,2 mode of a 400×400 $\mu\mathrm{m}^2$

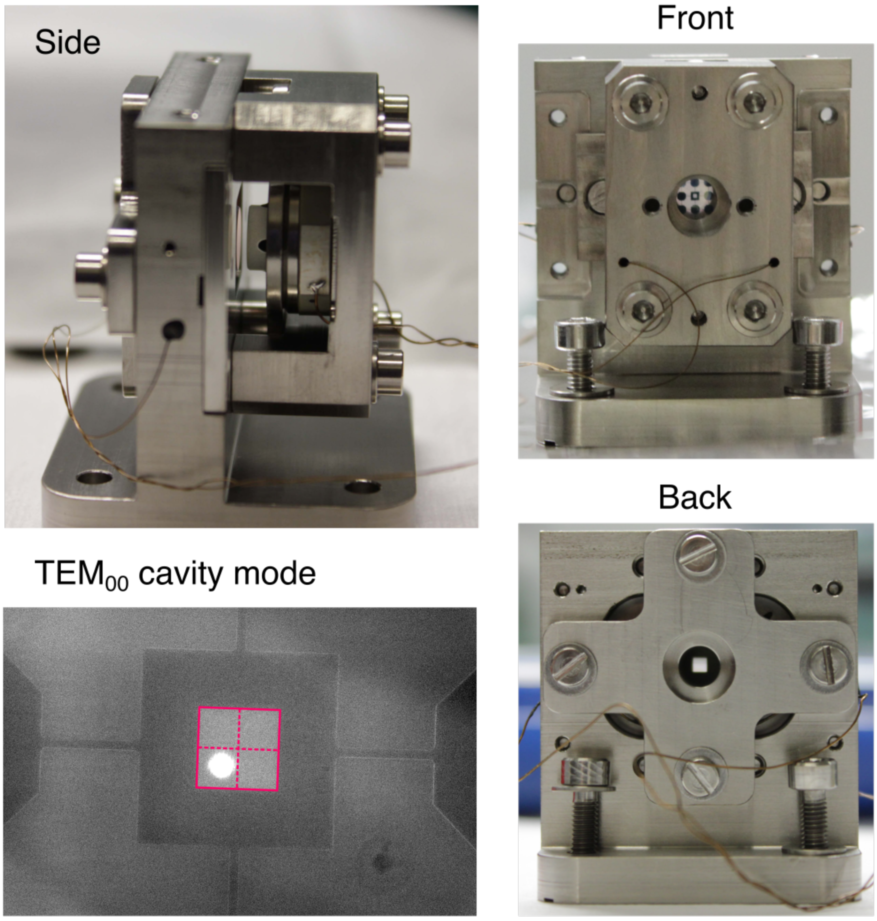

Figure 2.6: Pictures of the assembled cavity. To left: side view without membrane inserted. Top right: front view showing the phononic bandgap-shielded membrane. Bottom right: back view with a standard NORCADA membrane. Bottom left: image of the membrane (purple rectangle) with cavity mode aligned to the 2,2 mechanical mode, whose nodes are drawn as dashed lines.

membrane is shown at the bottom left of Fig. 2.6 and also displays the fragile phononic crystal structure.

Transmission spectrum To demonstrate the performance of the cavity, we show spectra of cavity transmission when tuning the two cavity piezos. In the following, piezo 1 refers to the piezo moving the curved mirror, which has lower reflectivity $r_1^2 = 0.995$, corresponding to mirror 1 in the simulations of section 2.2. Piezo 2 moves the flat, high-reflectivity mirror, corresponding to mirror 2 in the simulations. Fig. 2.7 shows a density plot of the cavity transmission spectrum obtained by recording transmitted optical power while the voltage on piezo 1 is ramped and the voltage on piezo 2 is slowly stepped between consecutive ramps of piezo 1. This tunes the mirror positions such that the cavity length L_c and membrane position x_m are changed along diagonal axes

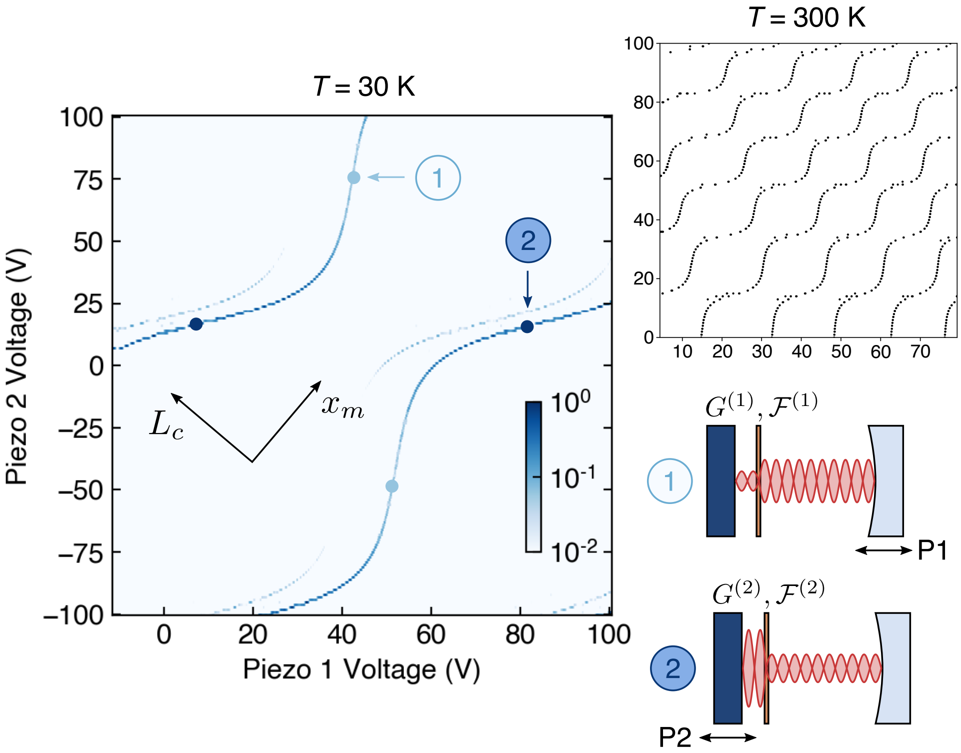

Figure 2.7: Cavity transmission spectrum obtained by ramping piezo 1 and stepping piezo 2, measured at cryogenic temperature $T = 30$ K. The circles correspond to positions of maximum linear optomechanical coupling and labels refer to the sketches at the bottom right. The inset on top right shows a measurement of the cavity resonance positions (data points) at ambient temperature $T = 300$ K.

as indicated by the coordinate system. We clearly observe the cavity resonances being modulated by the membrane displacement in agreement with the simulation of Fig. 2.1. The strong line corresponds to the fundamental cavity mode while the faint line is a higher order transverse mode. The positions of maximum linear optomechanical coupling are marked by circles, whose labels (1) and (2) refer to the sketches at the bottom right. Low resonant transmission corresponds to the right subcavity being resonant (1), i.e. low finesse $\mathcal{F}^{(1)}$ and low coupling $G^{(1)}$. On the contrary, high cavity transmission implies that the left subcavity is resonant (2) where the finesse $\mathcal{F}^{(2)}$ and coupling $G^{(2)}$ are high. A benefit of tuning the mirror positions is that the lengths of the two subcavities can be tuned independently. At the positions of linear optomechanical coupling the effects of the two piezos are then largely decoupled. For example, in position (2) piezo 2 locks the cavity to the laser while piezo 1 can be used to independently maximize G.

This measurement was recorded at a temperature $T = 30$ K and demonstrates clean resonances without any couplings to higher order transverse modes, which would lead to avoided crossings with the fundamental mode and distort the spectrum [121]. For reference, the inset at the top right shows a measurement of the transmission spectrum at ambient temperature $T = 300$ K. Here, data points indicate resonance positions. At room temperature, the piezo stroke is about a factor of 5 larger, such that a much bigger part of the cavity spectrum can be accessed.

Although these measurements demonstrate that the cavity design operates well at cryogenic temperatures and is immune to misalignment, we were not yet able to carry out optomechanical experiments at cryogenic temperatures. The reason is that the current membrane chip exhibits kHz-range mechanical resonances with very high quality factors ($\sim 10^3$) when clamped. In the presence of these resonances it was impossible to lock the cavity at cryogenic temperatures. All optomechanical experiments reported in this thesis thus had to be carried out at room temperature.

In summary, we list some advantages of the cavity design:

- The mechanical construction uses only a minimum amount of glue which allows it to passively maintain alignment under thermal contraction and expansion.
- The membrane can be firmly clamped to the main frame for maximum thermal contact.
- The piezos are clamped, which increases stability and also provides some pre-load for improved dynamic behaviour. Measurements of the piezo transfer-functions showed that the lowest resonance is at 17 kHz for both piezos.
- Each mirror can be finely positioned using its own piezo. This enables full control to both adjust the cavity resonance frequency, i.e. near an atomic resonance, and to position the membrane where optomechanical coupling is maximal.

2.5 Experimental setup

2.5.1 Cryostat

For our purpose, cooling to liquid helium (LHe) temperature $T = 4.2$ K represents a good compromise between large cooling factor and a manageable complexity of the experimental setup on top of the optical table. For optomechanical experiments in particular, vibrational stability of the cryogenic sample platform is of utmost importance, both for cavity lock stability as well as to prevent mechanical excitation of the membrane. During the process of finding a suitable cryogenic solution, commercial closed-cycle cryostats were tested and ruled out due to their high mechanical noise level extending into the MHz range. Following the advice of other groups, we opted for a compact and low-noise LHe flow cryostat[3].

The cryostat is enclosed in a custom CF-flanged vacuum chamber (inner diameter 130 mm) that is first evacuated via a turbo pump and then held at low pressure ($< 10^{-7}$ mbar) using an ion-getter pump[4]. The cryogenic sample platform (50 mm diameter, gold-plated copper) sits on top of a heat exchanger which is continuously cooled by the liquid helium flowing through it and evaporating. It is surrounded by a radiation shield at an intermediate temperature (~ 30 K) and supported by a stable stainless steel construction. In total, the sample space has diameter of 68 mm and height of 60 mm.

---

[3] KONTI-Micro from CryoVac GmbH

[4] NEXTorr D100-5 by SAES Getters

Optical windows in the radiation shield (25 mm diameter) and the vacuum chamber (CF 40) with anti-reflection (AR) coating in the near infrared allow good optical access to the cavity along a free-space axis 15 cm above the optical table.

Maintaining a stable temperature at low cryogen consumption is achieved using the setup depicted in Fig. 2.8. Liquid helium is stored in a dewar (150 L capacity) equipped with a level sensor and extracted via a flexible transfer line. A manual needle valve adjusts the maximum flow rate towards the cryostat. The flow rate through the heat exchanger in the cryostat can be controlled by two mechanisms. For continuous operation the gas overpressure inside the dewar is stabilized by a voltage-controlled proportional valve to about 50 mbar, ensuring a small flow of LHe to the cryostat. After the heat exchanger, exhaust gas is collected and sent to the helium recovery system of the physics department. For temperature stabilization of the sample platform we employ a magnetic flow-control valve in the exhaust gas line. Sample temperature is sensed using a silicon diode temperature sensor read out using a control unit which adjusts the flow-control valve by PID feedback. This feedback works well at the minimum temperature < 5 K or at 30 K and above. In between, the feedback causes temperature oscillations which we presume originate from unstable flow involving both liquid and gas sections inside the heat exchanger. At the lowest temperatures, LHe consumption is about 1.5 L/h. To save LHe, we typically set the temperature to 30 K over night such that only 0.5 L/h of LHe are consumed. This allows long hold times of up to one week with a single dewar. For longer cryogenic operation we simply exchange the empty against a full dewar within about 10 min. During this time the cryostat temperature rises only by about 30 K. Cooldown of the sample platform from room temperature to 4 K typically takes about 2 h at a consumption of 2 L LHe using a relatively large flow driven by a dewar pressure of about 0.2 bar. Moreover, a resistive heater has been integrated into the sample platform to accelerate warm-up or as an alternative for temperature control.

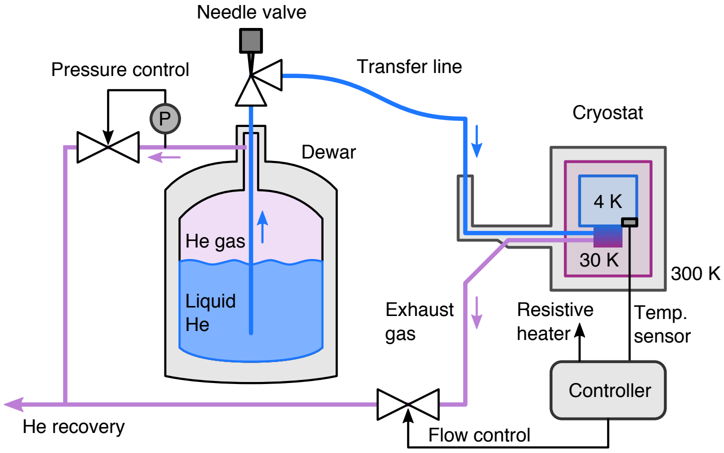

Figure 2.8: Cryogenic setup.

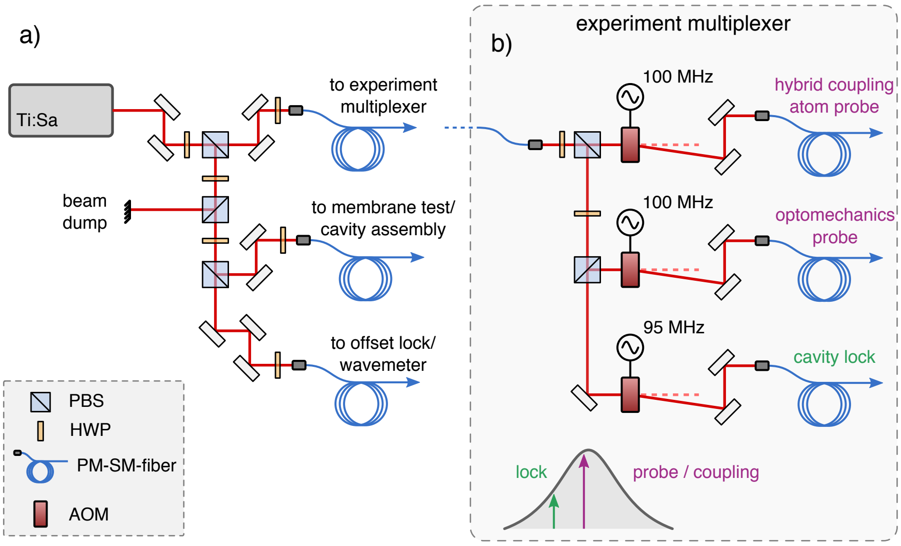

Figure 2.9: Distribution of laser light from the Ti:Sapphire laser to various parts of the experimental setup.

2.5.2 Optical setup

The laser setup used for all experiments described in this thesis is depicted in Fig. 2.9. A Ti:Sapphire laser (Ti:Sa) from MSquared (SolsTiS), pumped by a Nd:YAG laser (532 nm, 7 W, Lighthouse Photonics) is the main laser source of the experiment, providing about 1.5 W laser light in a wavelength range between 700 and 900 nm. For the experiments presented here, its wavelength is tuned to 780 nm in the vicinity of the Rubidium D_2 transition (see chapter 3). At the optical power levels < 1 mW required for the optomechanical and spin-light interfaces, the Ti:Sa is shot-noise limited in both amplitude (X_L) and phase quadrature (P_L) for Fourier frequencies above 1.5 MHz. To further lower the amplitude noise, the pump power can be reduced, which shifts the relaxation oscillation peak to lower frequencies.

The Ti:Sa light is distributed among the various parts of the experimental setup as shown in Fig. 2.9. For the main experiment, light at three different detunings relative to the optomechanical cavity is created using acousto-optic modulators (AOM) (Fig. 2.9b) driven at different frequencies: the hybrid coupling/atom probe beam, the optomechanics probe beam and the cavity lock beam. The AOMs also allow analog optical power control (bandwidth 30 kHz), MHz-bandwidth modulation and digital switching of the laser beams with rise times as low as 100 ns and off/on extinction ratio of 10^{-4}. In order to keep the level of technical laser noise low, care has been taken to design low noise AOM drivers using individually selected RF oscillators. The most stringent noise requirements hold for the optomechanical and atomic probe beams. The respective AOMs are driven by fixed-frequency quartz oscillators[5] at 100 MHz, with a specified phase noise floor of -170 dBc/Hz at offset frequencies above 0.1 MHz. Since the cavity lock beam is typically used at much lower laser power, its noise requirements are not as stringent.

---

[5] CRYSTEK CRBSCS-01-100.000

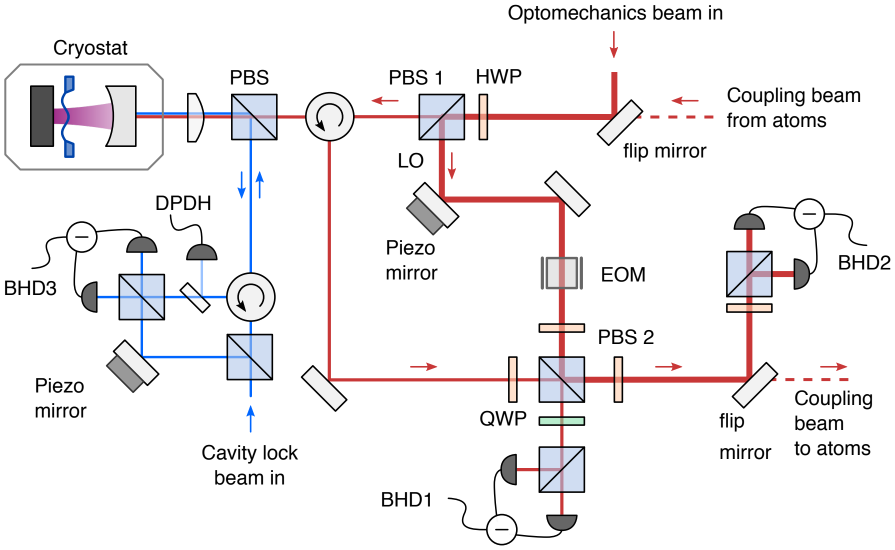

Figure 2.10: Optical setup for experiments involving the optomechanical system.

Consequently, we use a commercial signal generator (Rohde&Schwarz SMB100A 1GHz) for variable frequency shifting relative to the coupling/probe beams. For the main experiment, the cavity lock beam is shifted by 95 MHz, such that the cavity can be locked at red-detuning to provide some optomechanical cooling. The cavity lock point is then adjusted such that the atom and optomechanics probe beams are on resonance with the cavity (see Fig. 2.9b). For other experiments, the cavity lock beam can also be shifted to a higher frequency, such that the probe/coupling beams are red-detuned for stronger optomechanical cooling. As a remark, we use the AOMs in single-pass configuration instead of double-pass, to avoid imposing twice the AOM driver's noise onto the laser beam. For the cavity lock beam a double-pass configuration could make sense in the future, in order to be more flexible when changing the relative detuning between the lock and probe/coupling beams.

A schematic of the optical layout used for experiments involving only the optomechanical setup is shown in Fig. 2.10. The setup independently couples the cavity lock beam and the optomechanics probe beam to the cavity on orthogonal polarizations via the low-reflectivity mirror, each with a mode-matching efficiency of about 95% as quantified by the suppression of transmission peaks due to higher-order transverse modes. For the cavity lock beam, the reflected light returning from the cavity is split between a direct detector (DPDH) for cavity stabilisation using the Pound-Drever-Hall (PDH) technique (see subsequent section) and a balanced homodyne detector (BHD3). The balanced detection is used both for monitoring of the membrane signal and for feedback cooling of the membrane's fundamental 1,1-mode.

The optomechanics probe beam employs a similar setup. Here, the beam path forms a Mach-Zehnder interferometer with the cavity in one arm. Since the input and output use polarizing beam-splitters (PBS), we refer to it as a polarization interferometer, that we use to map between field quadratures X_L, P_L at the optomechanical cavity and Stokes vector components S_y, S_z relevant for the atom-light interface (see chapters 3 and 4). By adjustment of the half-wave plate (HWP) in front of the first PBS, about 10% of the total input power are sent to the cavity, the remaining light passes through a reference arm. The reference arm contains a free-space electro-optic phase-modulator (EOM)[6] which is useful to generate phase-modulation sidebands to either simulate a membrane signal at arbitrary frequency or generate an error signal to lock the interferometer. At the output of the interferometer (PBS 2), the cavity and reference arms are recombined with a typical mode-matching $> 90\%$. A small portion of the light from both arms (3% each) are sent to balanced homodyne detector BHD1 which is used for interferometer locking by feedback onto the piezo mirror in the reference arm. Most of the interferometer output is sent to BHD2 for detection. Alternatively, a flip mirror allows to direct the latter beam directly to the atomic setup. Likewise, a flip mirror at the input of the interferometer can be switched to receive light arriving from the atoms. This configuration allows easy switching between different coupling schemes between membrane and atoms with little re-alignment.

For atom-membrane coupling, we need to set up the interferometer such that phase-modulation in one of the arms translates to modulation of the Stokes vector component S_z, i.e. circular polarization, in the output beam going towards the atoms (cf. section 3.1). For characterisation we detect this beam on BHD2. The two balanced detectors BHD1 and BHD2 are set up such that they detect orthogonal light field quadratures, by introducing a relative phase shift of $\pi/2$ between them using a QWP in front of BHD1. When we sweep the interferometer phase using the the piezo mirror, we observe the detector signals approximately as cosine and sine functions of the interferometer phase shift, as demonstrated by the measurement in Fig. 2.11a). The correlated voltages of BHD1 and BHD2 describe an almost perfect circle. A small ellipticity indicates a phase error of about 5°. This phase error is also seen in the modulation of the grey line, which is the magnitude of the vector in the complex plane spanned by BHD1 and BHD2. When the interferometer is locked to a zero-crossing of BHD1, the output at BHD2 is maximal, indicating that BHD1 measures the phase quadrature P_L or S_z, while BHD2 measures X_L or S_y. In order to optimize the relative phase, we apply a phase-modulation tone using the EOM and adjust the detector waveplates such that the phase-modulation signal is maximal on BHD1 and minimal on BHD2.

If we sweep the cavity resonance instead of the reference arm piezo mirror, the two detectors measure the real and imaginary parts of the cavity reflectivity (see Fig. 2.11b). Here, the correlated voltages BHD1 vs BHD2 do describe more an ellipse because of a residual phase error between them. Moreover, the ellipse does not cover the full area due to finite cavity coupling efficiency $\eta_c \approx 0.9$.

2.5.3 Cavity lock

The optomechanical cavity can be tuned via the two piezos, which independently shift the two mirror positions. These two control channels allow to tune the cavity into resonance with the laser light and at the same time position the membrane relative to the cavity field where the optomechanical interaction is maximal. For coarse control, we apply static voltages to each piezo derived from a low-noise high-resolution digital-

---

[6] QUBIG EODC3L-NIR, broadband 0-200 MHz, transmission $> 98\%$

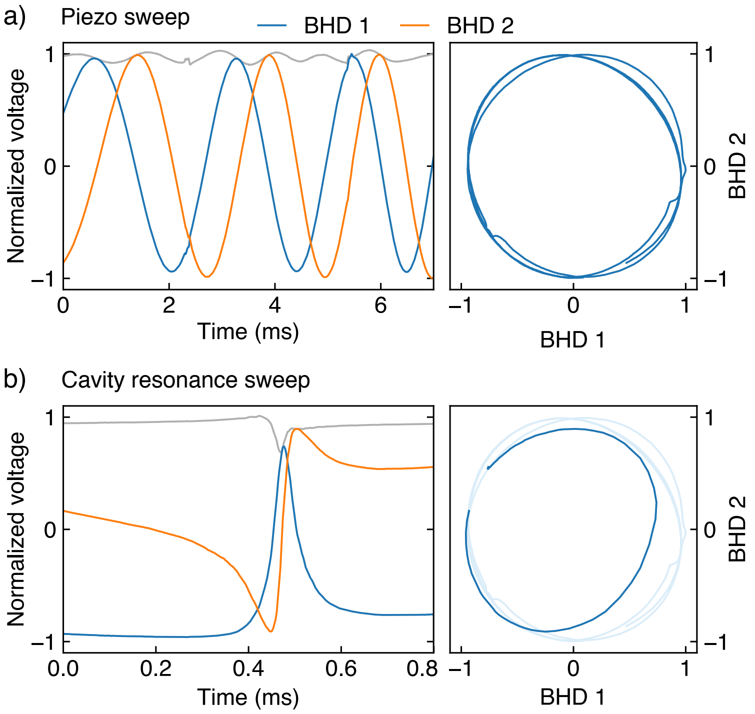

Figure 2.11: a) Normalized voltages on BHD1 and BHD2 while the interferometer phase is swept in time by applying a linear voltage ramp to the piezo mirror. The panel on the right shows that the correlations between BHD1 and BHD2 are almost perfectly $\pi/2$ out of phase and describe a circle. b) Same measurement as in a) but with a sweep of the cavity resonance.

to-analog converter[7] (LN-DAC), and amplified by high-voltage amplifiers[8] to the range 0..100 V. The LN-DAC channels can be computer controlled via a serial connection.

Once the cavity piezos are adjusted close to the cavity lock beam, the cavity is locked to the laser using the Pound-Drever-Hall (PDH) method [140]. In brief, this heterodyne technique detects the cavity phase shift across resonance and uses it as an error signal which is fed back to one of the piezos using dedicated lock electronics shown in Fig. 2.12a).

The lock circuit is depicted schematically in Fig. 2.12a). First, the cavity lock beam is weakly phase-modulated using an fiber electro-optic phase modulator (EOM)[9] at a modulation frequency of 340 MHz, larger than the cavity linewidth. The phase-modulation sidebands then serve as a local-oscillator to detect the cavity phase shift of the carrier light in a heterodyne setup. In the RF stage, light reflected from the cavity is first detected on a fast photodetector[10] with high gain such that no further pre-amplifier is needed. After splitting off the DC signal containing the reflected optical power using a bias-tee, the AC part of the photodetector voltage is then demodulated at

---

[7] Physics Basel LN-HR-DAC, SP 927, output range ±10 V, 24 bit precision

[8] Physics BaselHVA, SP-908

[9] Jenoptik PM785

[10] Menlo FPD610, DC-600 MHz

the modulation frequency using a double-balanced mixer[11]. Next, the lock error signal at DC is separated from AC fluctuations of the cavity frequency, which correspond to membrane signal and leakage of the modulation tone, that are separately measured on a spectrum analyzer at 50 Ω, to avoid parasitic reflections.

In the filter stage, the error signal is first amplified to a voltage range of ±1 V using a home-built operational amplifier (op-amp) circuit[12] with gain 100 to match the input range of the subsequent analog-to-digital converter (ADC). The signal then passes through a digital filter circuit implemented on a field-programmable gate-array (FPGA, Xilinx Zynq 7010 SOC) on a Red-Pitaya board (STEMLAB 125-14). The finite-impulse-response (FIR) filter is implemented using the FPGA code developed by the research group of J. Simon, University of Chicago [141]. Its purpose is to counter mechanical resonances of the optomechanical cavity which would otherwise lead to instabilities of the feedback. After the FPGA and an analog low-pass filter the filtered error signal is fed to an analog lock box which allows convenient toggling between open-loop piezo

---

[11] Minicircuits ZX05-10-S+

[12] inverting amplifier using Texas Instruments OPA227

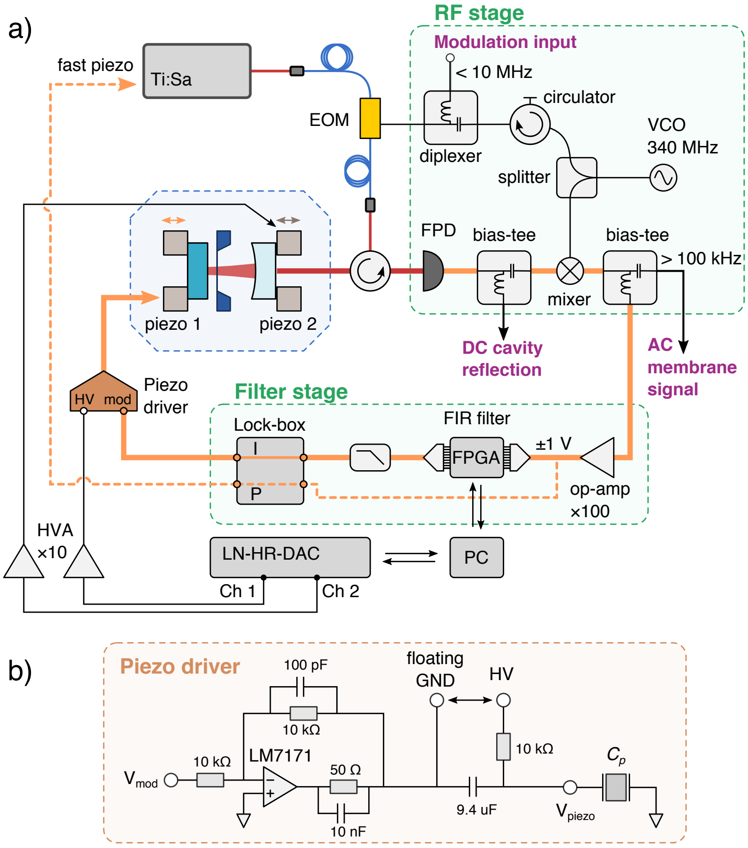

Figure 2.12: a) Schematic of the optical and electronic setup used to lock the cavity using the Pound-Drever-Hall technique. b) Basic schematic of the piezo driver lock circuit that combines the analog feedback voltage (V_{in}) from the lock-box with a static high voltage (HV) offset.

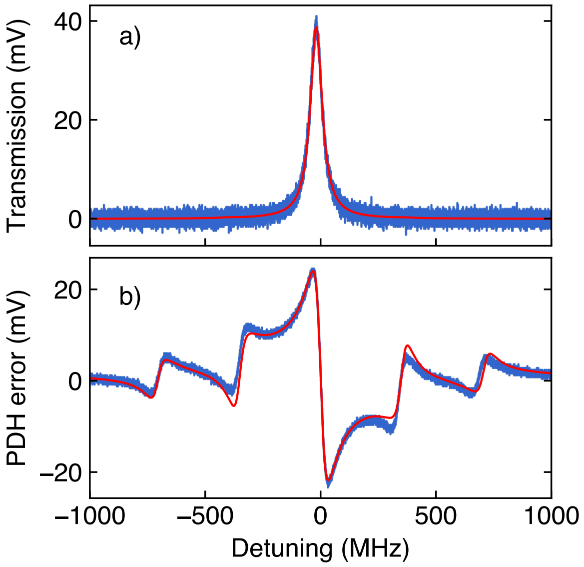

Figure 2.13: Cavity transmission (a) and PDH error signal (b). Fits are red lines.

scan functionality and lock point adjustment, and closed-loop control. The lock box consists of an integrator (I) channel, whose output is added to the static high-voltage from the LN-HR-DAC using a home-built piezo-driver circuit (see Fig. 2.12b) inspired from ref. [142]. This closes the feedback loop using the piezo actuator to stabilize the cavity length. In addition, using the proportional (P) output of the lock box to control the Ti:Sa laser frequency (via its fast resonator piezo) can be used as a faster feedback channel to correct small-amplitude (< 40 MHz) fluctuations of the laser-cavity detuning. This is advantageous because the bandwidth of the cavity piezo-lock alone is often limited by low-frequency mechanical resonances of the optomechanical cavity assembly.

An example measurement of the optical cavity resonance and PDH error signal are shown in Fig. 2.13a) and b), respectively. The PDH error signal can be fit using the model from ref. [140] and known EOM modulation frequency. This allows for a calibration of the laser-cavity detuning and yields a cavity linewidth of $\kappa = 2\pi \times 65$ MHz in the high-finesse configuration of the cavity (resonant subcavity 2). In this measurement, the EOM phase-modulation amplitude was rather large such that higher order sidebands appear. No sidebands appear in the cavity transmission signal because it is measured in orthogonal polarisation using the optomechanics probe beam.

The measured linewidth at low-finesse is $\kappa^{(1)} = 2\pi \times 115$ MHz. Based on the FSR $\Delta\omega_{\mathrm{FSR}} = 2\pi \times 125$ GHz (calculated assuming $L_c = 1.2$ mm) we get $\mathcal{F}^{(1)} = 1050$ and $\mathcal{F}^{(2)} = 1900$. Together with the measured empty cavity finesse $\mathcal{F}_0 = 1250$, these values agree very well with the cavity transfer matrix model with $\bar{x}_m/L_c = 0.2$ and membrane reflectivity $r_m = 0.6$.

The setup involving the cavity lock beam alone already provides a number of important capabilities to monitor and characterize the optomechanical coupling. The membrane signal can be detected on a spectrum analyzer using the AC part of the PDH error signal. Moreover, using the EOM one can apply a calibrated phase-modulation tone to the cavity lock beam that we use to determine g_0 for a particular membrane mode of interest [117]. Finally, membrane quality factors can be measured by driving a membrane mode using an amplitude modulation pulse of the cavity lock beam applied via its AOM, and then measuring the mechanical ringdown using a lock-in amplifier. For this purpose the membrane is positioned at low optomechanical coupling and the cavity is locked close to resonance with very little optical power (< 100 nW) to avoid optomechanical damping.

2.6 Basic optomechanical characterisation

For all experiments presented in this thesis we focus on the 2,2 mechanical mode at $\Omega_{2,2} = 2\pi \times 1.958$ MHz which is located in the bandgap of the BG #1-50 phononic crystal design.

2.6.1 Determining the coupling strength

A standard characterisation of the optomechanical setup is to measure the single-photon optomechanical coupling constant g_0 by comparison with a calibrated phase-modulation tone [117]. For this measurement, we employ the cavity lock beam only and lock the cavity on resonance with a low power of about 10 nW to avoid dynamical back-action damping of the membrane. The membrane signal of the 2,2 mode at 1.958 MHz is measured directly using the AC component of the PDH error signal (see Fig. 2.14a) on a spectrum analyzer. The calibration tone is applied at 1.97 MHz via the fiber EOM. With the membrane in thermal equilibrium, the measurement of g_0 is simply a matter of comparing the integrated noise PSD around the membrane peak δD_{th} to that of the calibration peak δD_{PM}. They amount to (see section 2.7)

$$\langle(\delta D_{\mathrm{PM}})^2\rangle = 2\beta_0^2 \left(\eta_c \frac{2\Omega_0}{\kappa}\right)^2 D_{\mathrm{PDH}}^2 \tag{2.61}$$

$$\langle(\delta D_{\mathrm{th}})^2\rangle = 2\bar{n}_{\mathrm{th}} \left(\eta_c \frac{4g_0}{\kappa}\right)^2 D_{\mathrm{PDH}}^2 \tag{2.62}$$

where D_{PDH} is the amplitude of the PDH error signal. The calibrated amplitude of the PM tone β_0 is determined by heterodyne detection and Ω_0 is the modulation frequency. Consequently, the optomechanical single-photon coupling strength can be determined from [117]

$$g_0^2 = \frac{\beta_0^2\Omega_0^2}{4\bar{n}_{\mathrm{th}}} \frac{\langle(\delta D_{\mathrm{th}})^2\rangle}{\langle(\delta D_{\mathrm{PM}})^2\rangle} \tag{2.63}$$

The spectral regions used for determining the membrane and PM noise powers are coloured red and blue in Fig. 2.14a), respectively. We now perform this measurement as a function of the membrane position inside the cavity. To this end we slowly step the voltage of the static cavity piezo 1 and keep the cavity locked via piezo 2. After every step, we record a spectrum and determine g_0. We note that the resolution bandwidth setting of the spectrum analyzer in this measurement is not fine enough to resolve the mechanical linewidth of about 1 Hz. The variation of the membrane and calibration tone powers is depicted in Fig. 2.14b) as the red and blue line, respectively. The membrane noise power experiences a strong periodic modulation by 20 dB while the calibration tone is only weakly modulated. The modulation of the PM tone $\propto \eta_c^2/\kappa^2$ is due to both a variation of the cavity linewidth κ and the cavity coupling efficiency η_c. We note, however, that the determination of g_0 is not sensitive to this variation. Sample spectra for maximum and minimum membrane signal are depicted as the upper and lower spectra in Fig. 2.14a), respectively, demonstrating a complete suppression of the membrane signal at a point of vanishing linear optomechanical coupling. Fig. 2.14c) depicts the piezo 2 lock voltage required to keep the cavity locked while piezo 1 is stepped. This visualizes the periodic cavity resonance dispersion exactly as measured in Fig. 2.7.

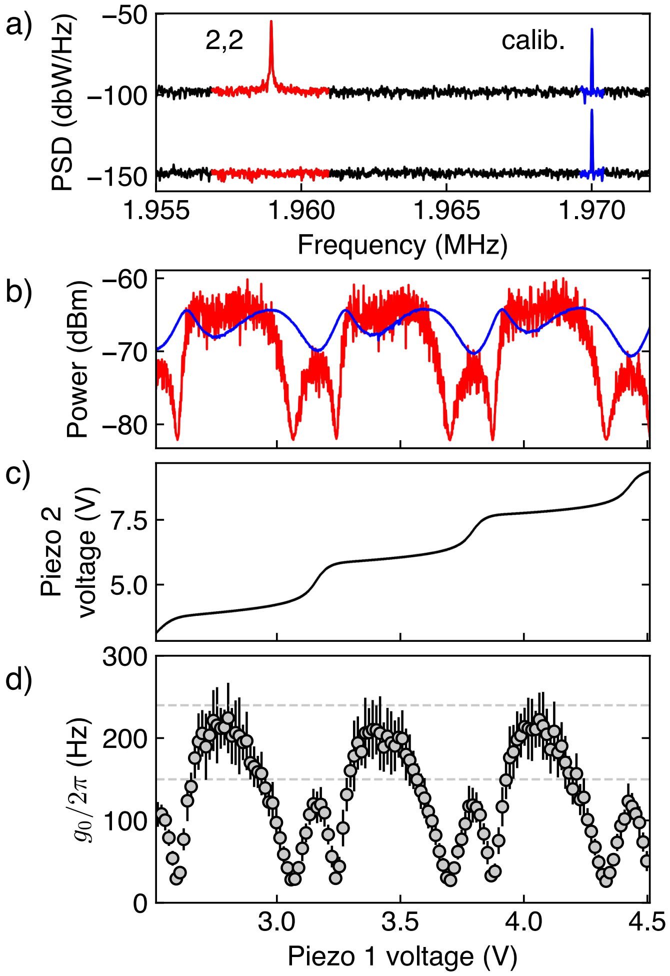

Figure 2.14: Variation of the optomechanical coupling as a function of membrane position tuned by the cavity piezo 2 voltage.

Finally, we show the results of the g_0 calibration in 2.14d). Clearly, the optomechanical coupling alternates between situations of strong coupling of up to $g_0/2\pi \approx 220$ Hz and weak coupling with $g_0/2\pi \approx 115$ Hz, with zero-crossings in between. This confirms the theoretical model for a membrane-at-the-end cavity. We can also compare the strength of the measured g_0 to the theoretical expectation. Here, the lower dashed line corresponds to the calculated g_0 in the weak-coupling configuration, which is around 150 Hz for the given mode, and the upper dashed line is the expectation for a MIM configuration at 240 Hz. The theoretical value for the strongly coupled MATE configuration ($\bar{x}_m = 0.2L_c$) would be at $g_0/2\pi \approx 400$ Hz, which is off the axes limits. The quite large discrepancy between theory and data cannot alone be explained by imperfect optomechanical mode-matching, because it does not explain why g_0 is reduced so much only in the strong-coupling configuration. Instead, two explanations are possible. One likely explanation is that optomechanical cooling reduces the phonon number, which was assumed to be constant for this measurement. This would also reduce the maximum measured g_0. Whether this is the case could be resolved by a careful analysis of the membrane linewidth in this type of measurement.

2.6.2 Optomechanical cooling

For coupling experiments between the membrane and the atomic spin, it is advantageous to operate with the coupling laser on resonance with the cavity. For this reason, optomechanical cooling by the coupling laser beam itself is not possible. However, the room temperature thermal noise level of $\bar{n}_m \approx 3 \times 10^6$ at $\Omega_m = 2\pi \times 1.958$ MHz is so high that it would almost saturate the collective atomic spin with length $\sim 10^7$. Instead of detuning the coupling beam, we detune the cavity lock beam to provide some pre-cooling of the room-temperature membrane to a reduced phonon number of $\bar{n}_m \approx 10^4$. A set of measurements to characterize the optomechanical cooling using the cavity lock beam is shown in Fig. 2.15. First, we measure the mechanical ringdown of the 2,2 mode in the cavity at a point of low coupling and low optical power to avoid dynamical back-action (Fig. 2.15a) which could either increase or decrease the observed damping rate. From the exponential decay fitted to the ringdown we determine a Q-factor of $Q = 1.3 \times 10^6$.

For the cooling measurement, we detect the 2,2 mode by homodyne detection of the coupling beam which is set to a low cavity input power of < 1 μW. We lock the cavity such that the lock-beam is red-detuned at a fixed detuning of $\Delta/2\pi \approx -5$ MHz and the optomechanical probe beam is resonant. The spectra in Fig. 2.15b) are acquired for varying lock beam power and show how the membrane resonance is damped and shifted. Moreover, the mode is cooled as can be seen in 2.15c) where the extracted phonon number is plotted as a function of the fitted linewidth. The membrane's mean-squared displacement is determined from the integrated power spectral density. A calibration in terms of phonon number is obtained when fitting the measured peak area and linewidth with the expression $\bar{n}_m = \bar{n}_{\text{th}}\gamma_{m,0}/\gamma_m$ for weak optomechanical damping. We assume the intrinsic linewidth $\gamma_{m,0} = 2\pi \times 1.5$ Hz obtained from the ringdown measurement. This value is also confirmed when fitting the measured linewidth as a linear function of lock beam power. This yields an extrapolated linewidth of 1.5 Hz at vanishing optical power. Knowing the phonon number, we can use the calibrated phase-modulation tone applied to the probe beam at 1.963 MHz to determine $g_0 = 2\pi \times 370$ Hz. This value is significantly larger than what was observed using the cavity lock beam.

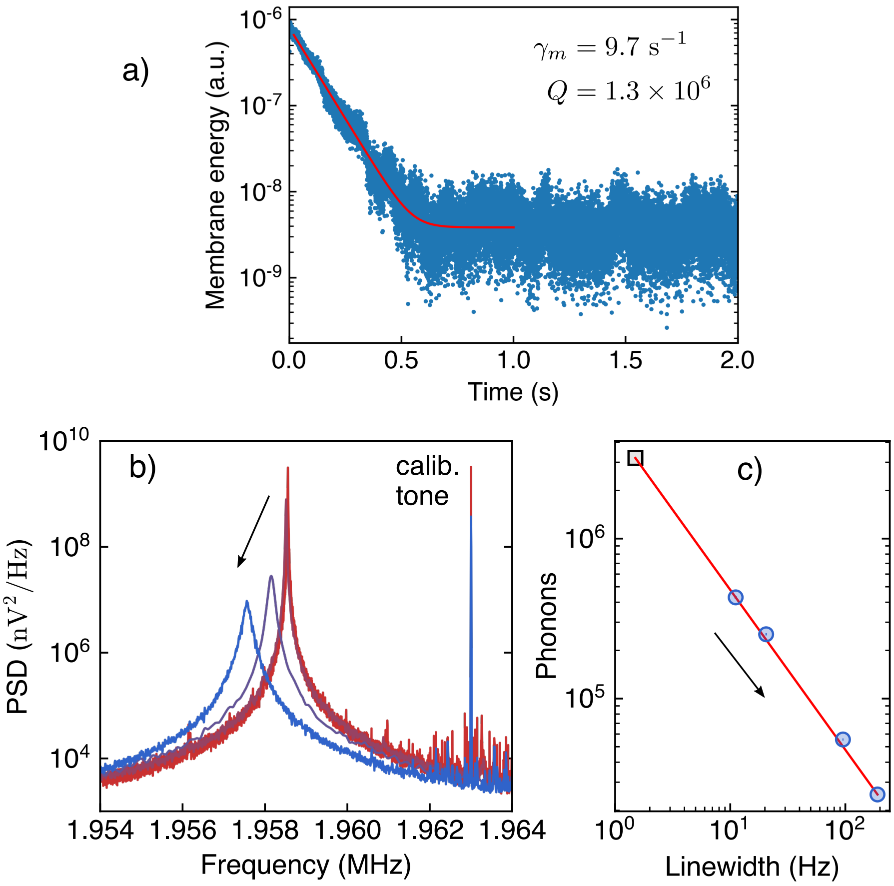

Figure 2.15: Optomechanical cooling of the 2,2 mode using the cavity lock beam. a) Mechanical ringdown measured at low intra-cavity power. b) Uncalibrated membrane displacement spectra for different cavity lock powers measured by homodyne detection of the optomechanics probe beam. Arrow indicates behaviour under increase of lock-beam power. A phase-modulation tone is applied to the probe beam at 1.963 MHz. Its height changes because the spectra are acquired with different resolution bandwidths of the spectrum analyzer. b) Extracted phonon numbers vs membrane linewidth (blue data points). Square is theoretical thermal occupation without optomechanical cooling at the intrinsic linewidth $\gamma_{m,0} = 2\pi \times 1.5$ Hz determined by an independent ringdown measurement.

2.6.3 Feedback cooling

In the non-resolved sideband regime, measurement and classical feedback is much more efficient for cooling a mechanical oscillator than dynamical back-action [143, 144]. Here, we employ feedback cooling to reduce spurious noise at the 2,2 mode frequency, which is due the second harmonic of the fundamental 1,1 mode that appears at a frequency $2\Omega_{1,1} \approx \Omega_{2,2}$. The second harmonic appears not in the phase-quadrature P_L, but in the amplitude quadrature X_L because subsequent harmonics are phase-shifted by $\pi/2$ [56]. Due to large thermal occupation of the fundamental 1,1 membrane mode and low cavity damping, this produces a substantial noise peak near the 2,2 mode. This is clearly seen in the recorded homodyne PSD without feedback ($K = 0$) of the optomechanics probe beam in Fig. 2.16. Potentially, this second harmonic can also drive the 2,2 mode because it produces a near-resonant intra-cavity amplitude modulation. Indeed, a small bump appears in the 2,2 spectrum at $2\Omega_{1,1}$.

In order to get rid of this spurious noise, we employ feedback cooling to selectively dampen the 1,1 mode without increasing the damping rate of the 2,2 mode. This is important for the hybrid spin-membrane coupling experiment. The feedback is implemented using the homodyne detector of the reflected cavity lock beam (BHD3). For this purpose, the detector signal is passed through a digital band-pass filter with adjustable delay. It is implemented using a Red Pitaya running the PyRPL[13] software [145]. The

---

[13] website at `https://pyrpl.readthedocs.io`

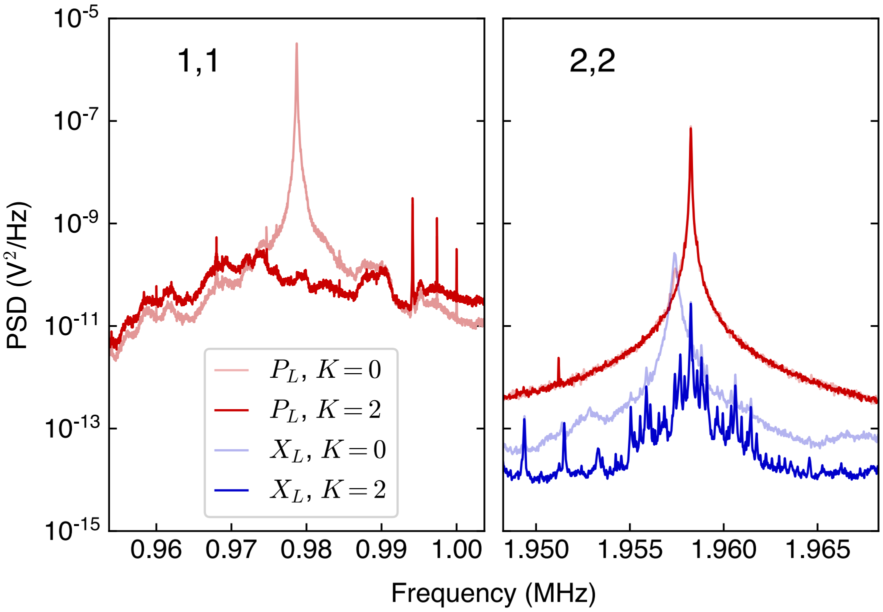

Figure 2.16: Feedback cooling of the 1,1 mode. a) out-of-loop PSD (P_L quadrature) for the 1,1 mode with feedback off ($K = 0$) and feedback on ($K = 2$). With feedback, the integrated spectral power is reduced by 20 dB. b) Corresponding PSD around the 2,2 mode frequency in both X_L and P_L. The data show suppression of the second harmonic of the 2,2 mode frequency which appears in X_L.

filter circuit first demodulates the input signal at frequency $\Omega_{1,1}$. Both demodulated I and Q quadratures are low-pass filtered using a fourth-order low-pass filter with bandwidth 78 kHz, and then mixed again with the demodulation frequency at an adjustable phase shift. The signal is subsequently amplified with feedback gain K and converted to one of the Red Pitaya analog outputs. To close the feedback loop, the filtered signal is applied as a modulation to the AOM of the cavity lock beam to modulate its power.

In Fig. 2.16, we show spectra with feedback gain $K = 2$ and optimized feedback delay. These are out-of-loop spectra. Feedback results in a 40 dB reduction of the 1,1 peak and a corresponding 20 dB reduction of the integrated power in a 20 kHz bandwidth. The effect is also clearly visible at the 2,2 mode, where the second harmonic of the 1,1 mode disappears. The residual noise in X_L is due to the 2,2 mode, most likely because of noise in the homodyne phase lock and the cavity lock. The data show a suppression of the 2,2 signal in X_L of about 34 dB. Increasing the feedback gain further does not improve the noise floor at the 2,2 mode, but eventually results in an instability.

2.7 Measurement of the optomechanical response

For experiments investigating light-mediated coupling between the optomechanical system and other quantum systems it is important to find an experimental method that allows one to determine the optomechanical coupling strength. Since the optomechanical interaction is linear, the homodyne measurement output is a linear function of the optical input fields and can be described using a transfer-matrix model [146]. Consequently, a convenient method to characterize the optomechanical interaction is by measuring the optomechanical response to a classical modulation of the laser field. Such methods are commonly used to study optomechanically induced transparency (OMIT) [147] or to calibrate the measured optical phase noise spectrum by phase-modulating the laser with a known modulation depth [117].

2.7.1 Optical transfer matrix

From the solution of the cavity field (2.14) we can derive the optomechanical transfer matrix from cavity input fields to cavity output fields. The standard input-output relation for an optical cavity with a single input/output port is given by [90]

$$a_L^{(\mathrm{out})} = a_L^{(\mathrm{in})} + \sqrt{\kappa} c \tag{2.64}$$

To solve the cavity, we rotated the input field and cavity quadratures by an angle ϕ_c. Hence the input output relation is given by (omitting the ω dependence of operators for brevity)

$$\begin{aligned} \begin{pmatrix} X_L^{(\mathrm{out})} \\ P_L^{(\mathrm{out})} \end{pmatrix} &= R_c(\omega) \begin{pmatrix} X_L^{(\mathrm{in})} \\ P_L^{(\mathrm{in})} \end{pmatrix} & (2.65) \\ &\quad -2 g_{\mathrm{om}} \frac{\sqrt{2\kappa\gamma_m}}{D_m(\omega)} U_{\phi_c} M_c(\omega) \begin{pmatrix} 0 \\ F_{\mathrm{th}} \end{pmatrix} & (2.66) \end{aligned}$$

Here, we defined the cavity reflection matrix

$$R_c(\omega) = \mathbb{1} - \kappa\, U_{\phi_c} M_c(\omega) U_{\phi_c}^T \tag{2.67}$$

with rotation matrix

$$U_{\phi_c} = \begin{pmatrix} \cos(\phi_c) & -\sin(\phi_c) \\ \sin(\phi_c) & \cos(\phi_c) \end{pmatrix} = \frac{1}{\sqrt{\kappa^2 + 4\Delta^2}} \begin{pmatrix} \kappa & -2\Delta \\ 2\Delta & \kappa \end{pmatrix} \tag{2.68}$$

The coherent input field $\bar{a}$ also experiences a similar transformation R_0 under reflection which is obtained by setting $g_{\mathrm{om}} = 0$ and $\omega = 0$ in the expression (2.67) for $R_c(\omega)$. Any homodyne measurement of the light field reflected from the cavity will take place in the reference frame of the coherent field $\bar{a}$, as this one is used to lock the homodyne phase relative to the local oscillator. Hence, we have to calculate the transfer matrix of the field quadratures in the reference frame of the coherent field, which is then given by

$$S_{\mathrm{om}}(\omega) = R_0^{-1} R_c(\omega) \tag{2.69}$$

The contribution of the thermal mechanical signal on the output field also needs to be multiplied by R_0^{-1}. While the complete expression is rather complicated, it simplifies dramatically for small detuning $|\Delta| \approx 0$, where

$$S_{\mathrm{om}}(\omega) \approx e^{\mathrm{i}2\theta_c(\omega)} \left[\mathbb{1} + \frac{16 g_{\mathrm{om}}^2 \kappa}{\kappa^2 + 4\omega^2} \chi_m(\omega) \begin{pmatrix} 0 & 0 \\ 1 & 0 \end{pmatrix} \right] \tag{2.70}$$

Here, $\theta_c(\omega) = \arctan(2\omega/\kappa)$ is the phase angle, by which inputs to and outputs from the cavity get delayed due to the finite cavity response time $2/\kappa$.

When the coupling to the cavity is not perfectly efficient, because of internal cavity losses or transmission through the second cavity mirror, this slightly modifies the expression for the transfer matrix. We assume that the cavity couples through the input/output port with rate κ_1 and cavity losses are summarized by another rate κ_0. Then, the total cavity linewidth is the sum $\kappa = \kappa_1 + \kappa_0$ and the coupling efficiency through the first port is $\eta_c = \kappa_1/\kappa$. When sweeping a laser across a cavity with $\eta_c < 1$, the amplitude reflectivity as a function of detuning is given by

$$r_c(\Delta) = 1 - \eta_c \frac{\kappa}{\kappa/2 - \mathrm{i}\Delta} = (1 - \eta_c) - \eta_c \frac{\kappa/2 + \mathrm{i}\Delta}{\kappa/2 - \mathrm{i}\Delta} \tag{2.71}$$

On resonance $r_c(0) = 1 - 2\eta_c$ implying a power reflectivity of $(1 - 2\eta_c)^2$. The transfer matrix S_0 of the coherent field reduces to the identity in the case without losses. Including losses, we have to multiply S_0 with the absolute value of the reflectivity $|r_c(\Delta)|$ such that on resonance $S_0 = (2\eta_c - 1)\mathbb{1}$. For the quadratures of the quantum field, cavity loss changes the transfer matrix to

$$S_{\mathrm{om}}(\omega) \approx (\eta_c - 1)\mathbb{1} + e^{\mathrm{i}2\theta_c(\omega)} \begin{pmatrix} \eta_c & 0 \\ 4\Gamma_m \chi_m(\omega) & \eta_c \end{pmatrix} \tag{2.72}$$

Here, we have re-defined the optomechanical measurement rate (compare equation (2.34))

$$\Gamma_m = \frac{\eta_c}{1 + 4\frac{\Omega_m^2}{\kappa^2}} \frac{4 g_{\mathrm{om}}^2}{\kappa} \tag{2.73}$$

We remark that another factor of η_c is hidden in g_{om}^2 because of its dependence on the cavity photon number, which scales as $\bar{n}_c \propto \eta_c|\bar{a}|^2$. Explicitly, the measurement rate can be expressed in terms of the input photon flux $\Phi_L = |\bar{a}|^2$ as

$$\Gamma_m = \frac{\eta_c^2}{1+4\frac{\Omega_m^2}{\kappa^2}}\left(\frac{4g_0}{\kappa}\right)^2 \Phi_L \tag{2.74}$$

In summary, for negligible detuning $\Delta \ll \kappa$, the cavity output field can be written as

$$\begin{aligned}\begin{pmatrix} X_L^{(\mathrm{out})} \\ P_L^{(\mathrm{out})} \end{pmatrix} &= e^{\mathrm{i}2\theta_c(\omega)}\begin{pmatrix} \eta_c & 0 \\ 4\Gamma_m\chi_m(\omega) & \eta_c \end{pmatrix}\begin{pmatrix} X_L^{(\mathrm{in})} \\ P_L^{(\mathrm{in})} \end{pmatrix} + (\eta_c - 1)\begin{pmatrix} X_L^{(\mathrm{in})} \\ P_L^{(\mathrm{in})} \end{pmatrix} \\ &+ e^{\mathrm{i}2\theta_c(\omega)}\sqrt{\eta_c(1-\eta_c)}\begin{pmatrix} X_h^{(\mathrm{in})} \\ P_h^{(\mathrm{in})} \end{pmatrix} \\ &+ e^{\mathrm{i}\theta_c(\omega)}\sqrt{8\Gamma_m\gamma_m}\chi_m(\omega)\begin{pmatrix} 0 \\ F_{\mathrm{th}} \end{pmatrix}\end{aligned} \tag{2.75}$$

where we added vacuum noise fields X_h, P_h which couple to the cavity via the back-mirror with efficiency $1-\eta_c$. All corrections to this expression are of order $\mathcal{O}(\Delta\omega/\kappa^2)$. Here, χ_m is the effective mechanical susceptibility that takes into account a small amount of optical broadening and frequency shift. This input-output relation is a tool to calculate the response of the optomechanical system to optical modulation inputs.

2.7.2 Model of homodyne detection

The experimental setup to measure the optomechanical transfer function involves an interferometer, shown in Fig. 2.17. The input fields a, b undergo a linear transformation as they pass through the interferometer and are eventually detected at a balanced detector. In the following we refer to the field quadratures of a as $X_a = (a + a^\dagger)/\sqrt{2}$ and $P_a = -\mathrm{i}(a - a^\dagger)/\sqrt{2}$ and equivalent definitions are used for all other fields.

At the first beam splitter with amplitude transmission (reflection) coefficient ϵ ($\sqrt{1-\epsilon^2}$), the input field a is split into a local oscillator (LO) and a weak probe beam. The other input port b is left open and feeds vacuum noise into the interferometer. The beam splitter relations read

$$a' = \epsilon a + \sqrt{1-\epsilon^2}b \tag{2.76}$$

$$b' = \sqrt{1-\epsilon^2}a - \epsilon b \tag{2.77}$$

where a' and b' are the beam-splitter output fields defined in transmission direction of the fields a and b, respectively. The probe field b' is sent through the optomechanical system with transfer matrix S, while the local oscillator field a' is only phase-shifted using a piezo mirror. The two beams are then mixed on a 50:50 beam splitter (i.e. $\epsilon = \sqrt{1/2}$) and its output fields c and d are measured on a balanced photodetector. This gives a detector signal

$$D = c^\dagger c - d^\dagger d \tag{2.78}$$

If the optomechanical cavity is off-resonant, the detector signal in terms of the interferometer fields a' and b' reads

$$D = a'^\dagger b' e^{-\mathrm{i}\phi} + b'^\dagger a' e^{\mathrm{i}\phi} \tag{2.79}$$

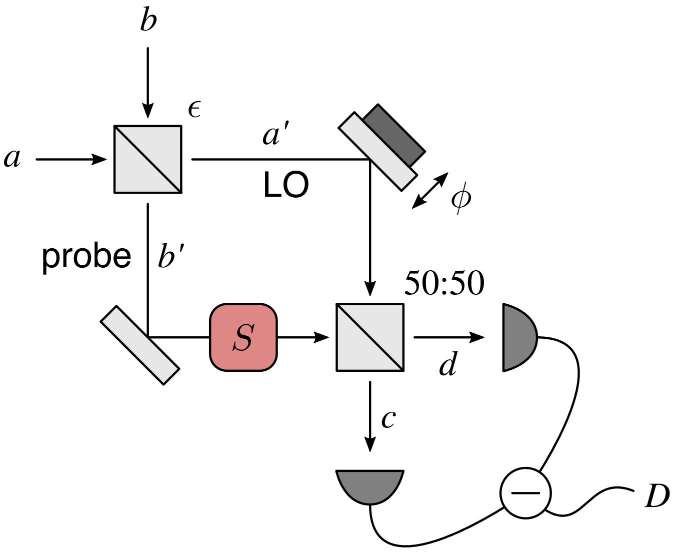

Figure 2.17: An interferometer to probe a system S and measures its output field on a homodyne detector.

If a' is a coherent field with flux Φ_L, one obtains

$$D \approx \sqrt{\Phi_L}(b' e^{-\mathrm{i}\phi} + b'^{\dagger} e^{\mathrm{i}\phi}) = \sqrt{2\Phi_L}(X_{b'} \cos(\phi) + P_{b'} \sin(\phi)) \tag{2.80}$$

This is the standard expression for a homodyne measurement which we used in the previous section to compute the optomechanical signal. By varying the local oscillator phase ϕ one can select to measure any quadrature of the field b'.

To see how fluctuations of the input fields a and b are transduced into the detector output we make use of a transfer matrix formalism in the quadrature basis. The general recipe to compute the transfer matrix of an interferometer with an optomechanical device like in Fig. 2.17 is to compute the total 4×4 transfer matrix

$$M_I(\omega) = M_{\mathrm{BS}}\left(\tfrac{1}{\sqrt{2}}\right) \cdot M_\phi \cdot M_{\mathrm{om}}(\omega) \cdot M_{\mathrm{BS}}(\epsilon) \tag{2.81}$$

where the matrix for a beam-splitter with splitting ratio ϵ is

$$M_{\mathrm{BS}}(\epsilon) = \begin{pmatrix} \epsilon\mathbb{1} & \sqrt{1-\epsilon^2}\mathbb{1} \\ \sqrt{1-\epsilon^2}\mathbb{1} & -\epsilon\mathbb{1} \end{pmatrix}, \tag{2.82}$$

with $\mathbb{1}$ being the 2×2 identity matrix. The local oscillator phase shift induces the matrix

$$M_\phi = \begin{pmatrix} U_\phi & 0 \\ 0 & \mathbb{1} \end{pmatrix}, \quad U_\phi = \begin{pmatrix} \cos(\phi) & -\sin(\phi) \\ \sin(\phi) & \cos(\phi) \end{pmatrix} \tag{2.83}$$

Here, we assume that the two interferometer arms have equal length and do not introduce a relative delay. The transfer matrix for the optomechanical system in the probe arm is

$$M_{\mathrm{om}}(\omega) = \begin{pmatrix} \mathbb{1} & 0 \\ 0 & S_{\mathrm{om}}(\omega) \end{pmatrix}. \tag{2.84}$$

The detector can be modeled as the matrix

$$M_D = \frac{1}{2}\begin{pmatrix} \mathbb{1} & 0 \\ 0 & -\mathbb{1} \end{pmatrix} \tag{2.85}$$

The final measurement outcome can then be computed using

$$D = \mathbf{q}^T M_I^T M_D M_I \mathbf{q} \tag{2.86}$$

where we use the vector $\mathbf{q} = (X_a^{(\mathrm{in})}, P_a^{(\mathrm{in})}, X_b^{(\mathrm{in})}, P_b^{(\mathrm{in})})^T$ containing all the input fields. Sending in a coherent laser field with photon flux Φ_L from port a displaces $\mathbf{q} \to \mathbf{q} + \mathbf{q}_0$, where $\mathbf{q}_0 = (\sqrt{2\Phi_L}, 0, 0, 0)^T$. Since the fields in $\mathbf{q}$ are very weak, we linearize D around the large laser contribution $\propto \Phi_L$, keeping only terms of order $\sqrt{\Phi_L}$. In general, the detector signal D can be divided into a static local oscillator part D_0 at DC (zero frequency) and a modulated part δD which is proportional to the quantum fields, i.e.

$$\begin{aligned} D(\omega) &= D_0\sqrt{2\pi}\delta(\omega) + \delta D(\omega) && (2.87)\\ D_0 &= \mathbf{q}_0^T M_I(0)^T M_D M_I(0)\mathbf{q}_0 && (2.88)\\ \delta D(\omega) &= 2\mathbf{q}_0^T M_I(0)^T M_D M_I(\omega)\mathbf{q}(\omega) && (2.89) \end{aligned}$$

By modulation of the input field, one can generate a signal $q_i(t) = \sqrt{2\Phi_L}\beta_0\cos(\Omega_0 t)$ in a specific quadrature with modulation depth $\beta_0 \ll 1$ and frequency Ω_0. In general, setting all input fields other than q_i to zero, this modulation then transfers to a detector signal

$$\delta D_i(\omega) = \sqrt{2\Phi_L} h_i(\omega) q_i(\omega) \tag{2.90}$$

where the modulation transfer function h_i can be calculated based on eq. (2.89). With $q_i(\omega) = \beta_0\sqrt{\pi\Phi_L}[\delta(\omega-\Omega_0) + \delta(\omega+\Omega_0)]$, we get the time domain signal

$$\delta D_i(t) = 2\Phi_L\beta_0\Big\{\mathrm{Re}[h_i(\Omega_0)]\cos(\Omega_0 t) + \mathrm{Im}[h_i(\Omega_0)]\sin(\Omega_0 t)\Big\} \tag{2.91}$$

Consequently, the cosine and sine components of the detector signal are proportional to the real and imaginary parts of $h_i(\Omega_0)$, respectively, at the modulation frequency. Demodulating the detector signal at the drive frequency Ω_0 using a lock-in amplifier allows to directly measure h_i. For the setup depicted in Fig. 2.17 we get

$$\begin{aligned} D_0 &= 2\Phi_L\epsilon\sqrt{1-\epsilon^2}\cos(\phi) && (2.92)\\ \delta D(\omega) &= \epsilon\sqrt{1-\epsilon^2}(\mathbf{q}_0^{(a)})^T\left[U_\phi^T S_{\mathrm{om}}(\omega) + S_0^T U_\phi\right]\mathbf{q}^{(a)}(\omega) \\ &\quad + (\mathbf{q}_0^{(a)})^T\left[(1-\epsilon^2)S_0^T U_\phi - \epsilon^2 U_\phi^T S_{\mathrm{om}}(\omega)\right]\mathbf{q}^{(b)}(\omega) && (2.93) \end{aligned}$$

where the vectors $\mathbf{q}^{(i)} = (X_i^{(\mathrm{in})}, P_i^{(\mathrm{in})})^T$ and $\mathbf{q}_0^{(a)} = (\sqrt{2\Phi_L}, 0)^T$ have been defined. For normalization of the experimental data, it is useful to define the DC amplitude $D_{\max} = 2\Phi_L\epsilon\sqrt{1-\epsilon^2}$ that can be measured by continuously sweeping the phase ϕ.

In the following, we consider a few special cases.

Laser amplitude modulation In the specific case of laser amplitude modulation (AM), i.e. $a(t) = \sqrt{\Phi_L}(1 + \beta_0 \cos(\Omega_0 t))$, the transfer function is given by

$$h_{X_a}(\omega) = 4\Gamma_m \chi_m(\omega) e^{2i\theta_c(\omega)} \sin(\phi) + \left[2(\eta_c - 1) + \eta_c \left(1 + e^{2i\theta_c(\omega)}\right)\right] \cos(\phi) \tag{2.94}$$

where we suppressed the constant pre-factor $\epsilon\sqrt{1-\epsilon^2}$ for convenience. This is a superposition of the mechanical response $\propto \sin(\phi)$ and the input modulation $\propto \cos(\phi)$. By varying the phase ϕ and fitting the measured transfer function with the above model provides valuable information about the optomechanical system, e.g. the measurement rate Γ_m and the mechanical susceptibility χ_m.

Laser phase modulation For phase modulation (PM), i.e. $a(t) = \sqrt{\Phi_L}(1+\mathrm{i}\beta_0 \cos(\Omega_0 t))$, the transfer function for $|\Delta|, |\omega| \ll \kappa$ is given by

$$h_{P_a}(\omega) = -\mathrm{i}\eta_c \frac{4\omega}{\kappa} \epsilon\sqrt{1-\epsilon^2} \sin(\phi) \tag{2.95}$$

This is independent of the mechanical system and only determined by the cavity delay, which is a consequence of the membrane only coupling to X_L at $\Delta = 0$. In order to measure OMIT, one would have to detune the cavity significantly to $\Delta \sim \sqrt{\Omega_m^2 + \kappa^2/4}$. Then the membrane also couples to P_L and the transfer function h_{P_a} is proportional to the effective cavity susceptibility $\chi_c \sim \Delta/D_{c,\mathrm{eff}}$.

Mechanical displacement In general, for any mechanical displacement we get the detector signal

$$\delta D_m = \frac{4g_0}{\kappa} \sqrt{2} X_m D_{\max} \sin(\phi) \tag{2.96}$$

For thermal noise $X_m(\omega) = \sqrt{2\gamma_m}\chi_m(\omega) F_{\mathrm{th}}(\omega)$.

Calibration of g_0 As pointed out in reference [117], probing the optomechanical system with a calibrated phase modulation tone is a powerful method to calibrate the single-phonon optomechanical coupling constant g_0. We can compare the integrated noise powers of the phase modulation and the mechanical signal. They amount to

$$\langle(\delta D_{\mathrm{PM}})^2\rangle = 2\beta_0^2 \left(\eta_c \frac{2\Omega_0}{\kappa}\right)^2 D_{\max}^2 \sin^2(\phi), \tag{2.97}$$

$$\langle(\delta D_{\mathrm{th}})^2\rangle = 2\bar{n}_{\mathrm{th}} \left(\eta_c \frac{4g_0}{\kappa}\right)^2 D_{\max}^2 \sin^2(\phi), \tag{2.98}$$

respectively. Consequently, the optomechanical single-photon coupling strength can be determined from

$$g_0^2 = \frac{\beta_0^2 \Omega_0^2}{4\bar{n}_{\mathrm{th}}} \frac{\langle(\delta D_{\mathrm{th}})^2\rangle}{\langle(\delta D_{\mathrm{PM}})^2\rangle} \tag{2.99}$$

as was done in section 2.6.1.

2.7.3 Determining the measurement rate

Having developed the formalism that allows us to compute the transfer function for any optical input modulation, we set out to measure the optomechanical response to laser amplitude modulation and thus determine Γ_m. In the experiment, we amplitude-modulate the optomechanics probe beam using its AOM and detect the light passing through the interferometer on BHD 2 (see Fig. 2.10). The interferometer is locked to a variable phase ϕ using feedback from BHD 1 onto the piezo mirror. The optomechanical response is then measured using a lock-in amplifier[14] which sweeps the modulation frequency across the mechanical resonance and demodulates the detector signal. This represents a phase-sensitive measurement of h_{X_a} as derived in the previous section.

Fig. 2.18a) and b) show the measured amplitude and phase of the optomechanical response, respectively. Here the cavity input power is 100 μW. The different curves (solid lines) correspond to measurements at different LO phases ϕ as given in the legend. The data clearly show the interference between the directly detected modulation and the mechanical response, whose relative phase varies across the resonance at 1.958 MHz and with ϕ. The traces in a) are fitted using the model $|h_{X_a}|$ from equation (2.94) with fit parameters $\Gamma_m, \gamma_m, \Omega_m, \kappa$ and ϕ. The coupling efficiency $\eta_c = 0.9$ has been determined independently from the resonant reflectivity. To get a reliable fit, all traces at different LO phase are fitted simultaneously with the same fit parameters $\Gamma_m, \gamma_m, \Omega_m, \kappa$. Only ϕ is adapted individually for each trace. We find that the fitted LO phase deviates by at most 2° from the nominal phase set point. Overall we find very good agreement between the data and the fit. The fitted cavity linewidth is $\kappa = 2\pi \times 65$ MHz which exactly corresponds to the linewidth obtained from the PDH fit. In Fig. 2.18b) we plot the other fit parameters measurement rate Γ_m, damping rate γ_m and frequency red-shift $-\delta\Omega_m$ obtained in three such measurements at the different cavity input powers 15, 40 and 100 μW. The lines in this figure are linear fits to the data, without intercept for Γ_m, showing perfect linear relationship as expected. The increase of damping and frequency shift with optical power results from a small, intentional red detuning of the probe laser to avoid parametric optomechanical instability. From the fit to the measurement rate we extract a vacuum optomechanical coupling constant $g_0 \approx 2\pi \times 200$ Hz. This value is consistent with the previous measurement in section 2.6.1 and also includes a slight reduction due to finite cavity-mode matching. In principle, also interferometer mode-matching would have to be taken into account to get an accurate value for g_0. In the end, however, Γ_m is the relevant parameter for our hybrid spin-membrane coupling application.

The optomechanical response measurement presented here can be regarded complementary to optomechanically-induced transparency in the non-resolved sideband regime [78]. In both cases, the interference between an incident field and the field scattered by the optomechanical system is probed and reveals the optomechanical coupling.

---

[14] Zurich instruments HF2LI

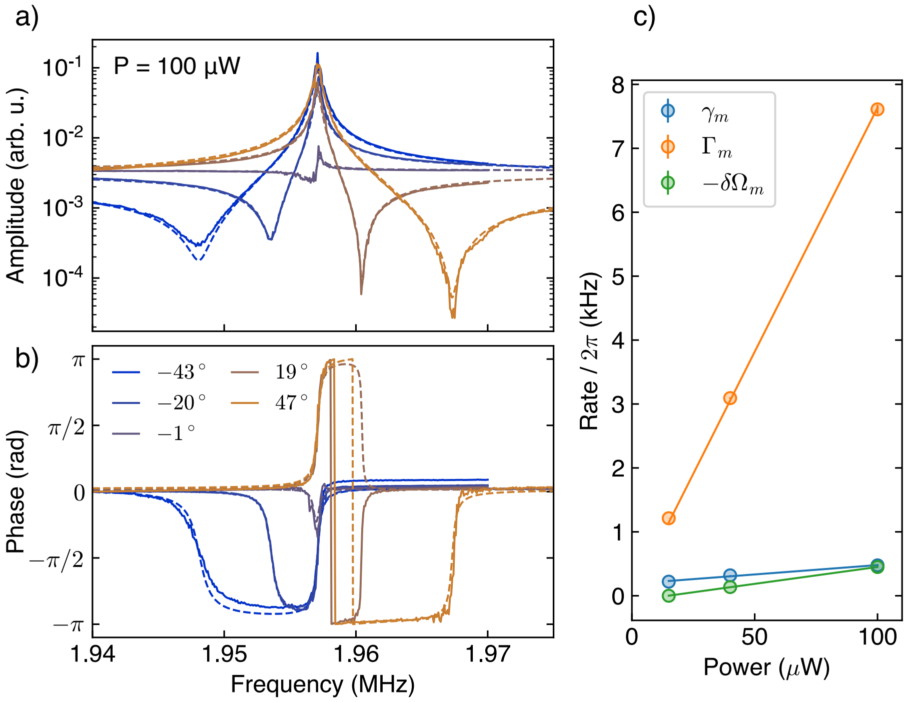

Figure 2.18: Measurement of the membrane optomechanical response. Amplitude (a) and phase (b) of the optomechanical response measured using laser-amplitude modulation. Data are solid lines, fits are dashed lines. Fit is done simultaneously to all curves allowing to adapt the homodyne phase angle. Values are given in legend and deviate by at most 2 degrees from interferometer set points. c) Rates extracted from fit parameters vs cavity optical input power.

2.8 Conclusion

In this chapter, the basic theoretical concepts of cavity optomechanics were introduced and the experimental setup, a membrane-at-the-end cavity, was presented. The newly developed membrane cavity is compatible with cryogenic operation, a prerequisite for quantum optomechanics experiments. We characterized the room-temperature optomechanical coupling of the phononic-bandgap shielded 2,2 mode at $\Omega_m = 2\pi \times 1.958$ MHz. In summary, we determined $Q = 1.3 \times 10^6$, $g_0 = 2\pi \times 200$ Hz for the membrane and $\kappa = 2\pi \times 65$ MHz for the cavity, in good agreement with predictions from the membrane-cavity model. These values are also consistent with a homodyne measurement of the optomechanical response, which yields a measurement rate $\Gamma_m = 2\pi \times 7.5$ kHz at 100 μW input power. The optomechanical setup thus exhibits strong coupling to the external input/output fields with a large coupling efficiency $\eta_c = 0.9$. This value can still be improved by using better optical coatings for the cavity mirrors, which will make the cavity more single-sided. By measuring the optomechanical transfer function, we have also confirmed that the simplified model which describes a direct coupling between the membrane and the external field is accurate. Only a finite cavity delay $\tau_c = 2/\kappa \approx 5$ ns has to be taken into account. This delay will become important in the context of the cascaded coupling between spin and membrane.

Chapter 3

Atomic Ensemble

This chapter summarizes the experimental progress towards a quantum interface between light and a cold, dipole-trapped atomic ensemble. The quantum interface between light and atoms [39] is based on the collective atomic spin degree of freedom and the polarization state of a traveling, free-space optical field. In order to achieve strong atom-light coupling in this geometry, it is crucial to realize a high atomic optical depth. This chapter starts with a theoretical introduction to the atom-light quantum interface. Next, we detail the experimental setup and preparation sequence of the spin-polarized atomic ensemble. Finally, we present a full characterization of the spin-light interface based on the off-resonant Faraday interaction.

3.1 Theory of the atom-light interface

3.1.1 Interaction between light and atomic ensembles

Scattering of light from atoms is usually a three-dimensional (3D) problem since atoms are point-like particles and do not have a permanent electric dipole moment [148, 8, 149]. When irradiated with light in free-space, a single atom scatters light isotropically into all directions. This situation is undesirable since the efficiency of collecting the scattered photons on a detector is very poor. Instead, it would be ideal if the atom scattered photons only into a single, well-defined optical mode. Several strategies have been developed to approach this idealized scenario. First, atoms can be placed inside a high-finesse optical cavity, which enhances the atomic interaction with the cavity mode over that to all other modes by the finesse of the cavity. This has enabled interfaces between even a single atom and single photons in the strong coupling regime [10]. Similarly, the photonic environment of an atom can be altered by putting it in the vicinity of a nanophotonic structure [20, 21] like photonic crystal waveguides or nanofibers. Due to near-field optical effects, the scattering of an atom to and from such a waveguide can be very efficient and highly-directional, which has triggered research in the field of chiral quantum optics [20].

A simple alternative approach to enhance the scattering efficiency into a single mode is to use an atomic ensemble [8, 39], i.e. a collection of a large number of atoms. When such an ensemble is irradiated by an off-resonant laser beam with wavelength λ, the light scattered by all atoms interferes constructively in the forward direction of the incoming laser beam [150]. Remarkably, this works in particular for dilute and disordered atomic samples, meaning that the atomic density $n_{\text{at}} < \lambda^{-3}$, i.e. there is less than one atom per cubic wavelength. Atomic ensembles thus enable coherent interfaces between atoms and free-space light that have been used in a number of setups involving both cold atoms [151, 152, 153] and hot atomic vapours [28, 51].

Since the light-scattering from atomic ensembles is highly directional, the physics can usually be reduced from a 3D to a 1D description. A number of theoretical works have investigated this problem [8, 154, 149, 155]. It is worth noting a few of the assumptions which are typically made to allow for this reduction. First, the sample needs to obey a certain geometry such that the scattered light is well characterized by a single mode that overlaps well with the input field. For a cigar-shaped atomic ensemble with waist w_a and length l_a, the Fresnel number

$$F = \frac{\pi w_a^2}{\lambda l_a} \tag{3.1}$$

is often quoted as a quantity that describes whether the scattered light can be ascribed to a single paraxial mode. It compares the "atomic Rayleigh length" $\pi w_a^2/\lambda$ to the length of the atomic ensemble. If $F \approx 1$ the single-mode assumption is said to be justified. Instead, if $F \gg 1$ for a wide sample, emission can occur into a large number of modes, while $F \ll 1$ for a very long sample implies that the scattered light diverges strongly due to diffraction. However, F only takes into account the geometry of the atomic ensemble. In addition, the shape of the optical input mode has to be matched to that emitted by the atomic cloud. In applications with dipole-trapped atomic ensembles this is approximately satisfied if the waist of the optical beam w_0 matches that of the atomic ensemble [154, 155].

Another important assumption is that the atoms behave as independent scatterers. This means that a photon scattered by one atom is not scattered a second time by another atom. These multiple scattering events may occur at very high atomic densities where $n_{\text{at}} \gtrsim \lambda^{-3}$. In this scenario, atoms can strongly interact via the light field, leading to the related phenomena of superradiance [156, 157, 30, 158] and optically-induced dipole-dipole interactions [159, 149, 160]. Depending on the application, these collective effects can either be desired or not. In the context of this work, it is best to avoid them because they lead to increased noise of the collective spin state.

The performance of an ensemble-based atom-light interface is typically quantified by the optical depth d_0 of the atomic ensemble. In free-space, the probability of a single atom to scatter light into a given free-space paraxial mode[1] with cross section A is given by the single-atom optical depth $\sigma_0/A \ll 1$, where $\sigma_0 \sim \lambda^2$ is the resonant absorption cross section on the probed transition [161]. For scattering from N atoms, the optical depth $d_0 = N\sigma_0/A$ gets enhanced by the atom number N and can thus become very large ($d_0 \gg 1$) such that it loses its meaning as a probability. Rather, the optical depth of an atomic ensemble specifies the ratio of collective atom-light coupling over single-atom decay due to spontaneous emission, i.e. the cooperativity of the interface [162]. Consequently, achieving a large optical depth $d_0 \gg 1$ is a prerequisite for coherent

---

[1] This does not distinguish between forward and backward scattering.

atom-light interaction. In particular, it is a criterion for efficient spin squeezing by quantum-non-demolition measurement [44]

3.1.2 Model atom-light interaction

The assumptions concerning geometry and diluteness of the atomic ensemble are approximately satisfied in our experimental setup. Hence, we only consider the interaction of the atoms with a single paraxial optical mode defined by the laser beam which drives the atomic transition. If necessary, it is straightforward to extend this description to multiple transverse modes [39, 155]. In our lab, we work with the alkali species ^{87}Rubidium (Rb)[2]. A level diagram of the D_2 transition of Rb is shown in Fig. 3.1a). Due to nuclear spin $i = 3/2$, the $^2S_{1/2}$ ground state splits into the two $f = 1, 2$ hyperfine manifolds which can be addressed using independent laser fields tuned to the $^2S_{1/2} \rightarrow ^2P_{3/2}$ transition. Since the hyperfine splitting complicates things quite a bit, we consider a model Rb atom without nuclear spin ($i = 0$) in this section, whose level diagram is shown in 3.1b). We are interested in the limiting case of large detuning $\Delta = \omega_L - \omega_0$ between the laser frequency ω_L and the atomic transition frequency ω_0, where this simple model is appropriate. The geometry for the atom-light interface is depicted in Fig. 3.1c). A light field is propagating along the z-axis with right-hand (σ^+) and left-hand (σ^-) circular polarization components. These polarization components drive transitions marked by red and blue colors, respectively, in Figs. 3.1a) and b).

In the following, atomic ground (excited) states with total spin $j = 1/2$ ($j' = 3/2$) and magnetic quantum number m are labelled g_m (e_m). In a rotating frame at the laser frequency, the interaction Hamiltonian between the atomic dipole and the one-dimensional (1D) $\sigma^{\pm}$-polarized light fields $a_{\pm}$ can be written as

$$\begin{aligned} H_{\text{int}} &= \hbar\tilde{\Omega}_{jj'}\Big[\left(\mu\left|e_{+3/2}\right\rangle\left\langle g_{+1/2}\right| + \nu\left|e_{+1/2}\right\rangle\left\langle g_{-1/2}\right|\right)a_+ \\ &\qquad + \left(\nu\left|e_{-1/2}\right\rangle\left\langle g_{+1/2}\right| + \mu\left|e_{-3/2}\right\rangle\left\langle g_{-1/2}\right|\right)a_-\Big] + \text{h.c.} \end{aligned} \tag{3.2}$$

Here, the vacuum Rabi coupling strength is $\tilde{\Omega}_{jj'} = D_{jj'}\mathcal{E}_0/\hbar$ (unit is Hz/$\sqrt{\text{Hz}}$, i.e. coupling density) with reduced atomic dipole moment $D_{jj'}$ and vacuum electric field density $\mathcal{E}_0 = \sqrt{\hbar\omega_L/(2\epsilon_0 c A)}$ with beam cross-sectional area A, speed of light c and vacuum permittivity ϵ_0 [37]. Here, $A = \pi w_0^2$ for a Gaussian beam with waist w_0, such that $2\epsilon_0 c\mathcal{E}_0^2\langle a_{\pm}^{\dagger}a_{\pm}\rangle$ is the mean optical intensity in $\sigma^{\pm}$ polarization [37]. We note that the optical fields $a_{\pm}$ have unit s$^{-1/2}$ such that $a_{\pm}^{\dagger}a_{\pm}$ describes photon flux in $\sigma^{\pm}$ polarization. The atomic dipole moment $D_{jj'}$ is related to the spontaneous emission rate γ_e via the expression [37]

$$\gamma_e = \frac{\omega_0^3}{3\pi\epsilon_0 c^3\hbar}\frac{2j+1}{2j'+1}D_{jj'}^2 \tag{3.3}$$

and the relative transition line strengths are given by the Clebsch-Gordan coefficients $\mu = 1$ and $\nu = 1/\sqrt{3}$. Moreover, the internal atomic Hamiltonian is

$$H_0 = -\hbar\Delta\sum_{m'=-j'}^{j'}\left|e_{m'}\right\rangle\left\langle e_{m'}\right|. \tag{3.4}$$

---

[2] Relevant spectroscopic data of ^{87}Rb can be found in ref. [163].

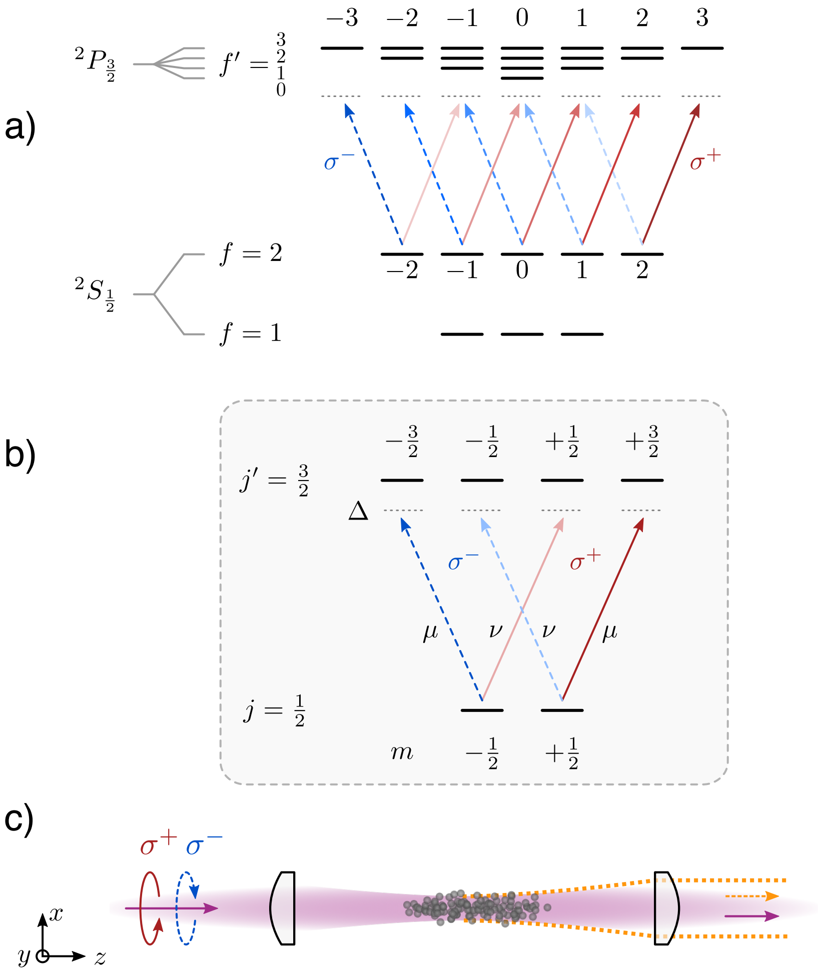

Figure 3.1: Atomic level diagrams. a) Level diagram of the ^{87}Rb D$_2$ line, only transitions from $f = 2$ are shown for clarity. Transitions for σ^+ polarization are drawn as red solid lines, σ^- transitions are drawn as blue dashed lines. The color luminosity illustrates relative strength of the dipole matrix element. b) Level scheme of a model spin-1/2 atom without nuclear spin. c) A laser beam (purple) interacts with the atomic ensemble. The scattered light (yellow dashed lines) is emitted in forward direction.

For large detuning $|\Delta| \gg \gamma_e$ much larger than the excited state spontaneous emission rate γ_e, the excited state can be adiabatically eliminated [39]. This leads to an effective master equation for the atomic ground states interacting with the light field, i.e.

$$\dot{\rho} = -\mathrm{i}V\rho + \mathrm{i}\rho V^\dagger + (\dots) \tag{3.5}$$

where $(\dots)$ contains quantum jump terms. The effective interaction reads

$$\begin{aligned} V &= \frac{\tilde{\Omega}^2_{jj'}}{\Delta + \mathrm{i}\gamma_e/2} \left|g_{-1/2}\right\rangle \left\langle g_{-1/2}\right| \left(\mu^2 a^\dagger_- a_- + \nu^2 a^\dagger_+ a_+\right) \\ &\quad + \frac{\tilde{\Omega}^2_{jj'}}{\Delta + \mathrm{i}\gamma_e/2} \left|g_{+1/2}\right\rangle \left\langle g_{+1/2}\right| \left(\nu^2 a^\dagger_- a_- + \mu^2 a^\dagger_+ a_+\right) \end{aligned} \tag{3.6}$$

It can be separated into a hermitian part describing an effective Hamiltonian interaction, and an anti-Hermitian part which together with the quantum jump terms causes decoherence. For large detuning we have $\frac{1}{\Delta+\mathrm{i}\gamma_e/2} \approx \frac{1}{\Delta} - \mathrm{i}\frac{\gamma_e}{2\Delta^2}$. This implies that the incoherent processes are suppressed relative to the coherent processes by a factor $\gamma_e/(2\Delta) \ll 1$. We will thus focus on the coherent part of V. The quantity

$$\frac{2\tilde{\Omega}^2_{jj'}}{\gamma_e} = \frac{\sigma_0}{A} \tag{3.7}$$

is the ratio between resonant absorption cross-section $\sigma_0 = 3\lambda^2/2\pi$ on the $|j = 1/2, m = 1/2\rangle \to |j' = 3/2, m' = 3/2\rangle$ transition and the cross-section of the optical beam $A = \pi w_0^2$ with waist w_0. This is the resonant optical depth for a single atom, i.e. the scattering probability for a single atom [161].

The effective interaction (3.6) can be interpreted as a level shift operator. Due to the imbalance between μ^2 and ν^2 the atomic levels $m = \pm 1/2$ experience a different light shift if the polarization is σ^+ or σ^-. In turn, also the optical fields $a_\pm$ experience different phase shift if the atom is in state $m = +1/2$ or $m = -1/2$. To present this relationship more directly, we define the ground state spin operator

$$j_z = \frac{1}{2}\left(\left|g_{+1/2}\right\rangle\left\langle g_{+1/2}\right| - \left|g_{-1/2}\right\rangle\left\langle g_{-1/2}\right|\right). \tag{3.8}$$

and projector $\mathbb{1}_g$ on the ground state manifold. Moreover, the polarization state of light can be described by the Stokes operator with components

$$\begin{aligned} S_0 &= \frac{1}{2}\left(a^\dagger_+ a_+ + a^\dagger_- a_-\right) \\ S_x &= \frac{1}{2}\left(a^\dagger_+ a_- + a^\dagger_- a_+\right) \\ S_y &= \frac{1}{2\mathrm{i}}\left(a^\dagger_+ a_- - a^\dagger_- a_+\right) \\ S_z &= \frac{1}{2}\left(a^\dagger_+ a_+ - a^\dagger_- a_-\right) \end{aligned} \tag{3.9}$$

They correspond to total photon flux $\Phi_L = 2S_0$, in-phase coherence between σ^+ and σ^-, (imbalance between horizontal vs vertical polarization, S_x), out-of-phase coherence between σ^+ and σ^- (imbalance between ±45° polarization, S_y), and imbalance between σ^+ and σ^- (S_z). Using this notation, the effective Hamiltonian $\hbar(V + V^\dagger)/2$ can be written in the form

$$H_{\text{eff}} = \hbar\alpha_0 \mathbb{1}_g S_0 + \hbar\alpha_1 j_z S_z \tag{3.10}$$

The two terms correspond to scalar and vector polarizability, respectively, of the atomic ground states. The dimensionless polarizability coefficients are defined as

$$\alpha_0 = \frac{\tilde{\Omega}^2_{jj'}}{\Delta}(\mu^2+\nu^2) = \frac{\sigma_\pi}{A}\frac{\gamma_e}{\Delta} \tag{3.11}$$

$$\alpha_1 = \frac{2\tilde{\Omega}^2_{jj'}}{\Delta}(\mu^2-\nu^2) = \frac{\sigma_\pi}{A}\frac{\gamma_e}{\Delta} \tag{3.12}$$

where $\sigma_\pi = \lambda^2/\pi$ is the cross-section for linear polarization. This description of the dispersive atom-light interaction in terms of a polarizability tensor is universal and allows us to distinguish between different effects. The scalar polarizability leads to an atomic refractive index which shifts the phase of the transmitted optical field proportional to the atom number. The vector polarizability generates a circular birefringence, that rotates the polarization of a linearly polarized input field by an angle proportional to j_z. This is called Faraday rotation and allows dispersive readout of the spin.

Finally, we look at the non-Hermitian part of V, which can be related to damping of spin coherence by spontaneous scattering. We assume linear polarization such that $S_0 = \Phi_L/2$ and $S_z = 0$. Tracing out the light field we find: $\mathrm{i}(V - V^\dagger)/2 = (\gamma_{\mathrm{sc}}/2)\mathbb{1}_g$. Then, the atomic spontaneous scattering rate is given by

$$\gamma_{\mathrm{sc}} = \frac{\tilde{\Omega}^2_{jj'}\gamma_e}{\Delta^2}(\mu^2+\nu^2)S_0 = \alpha_0 S_0\frac{\gamma_e}{\Delta} = \frac{\sigma_\pi}{2A}\left(\frac{\gamma_e}{\Delta}\right)^2\Phi_L \tag{3.13}$$

This value is consistent with a calculation of the scattering rate using the formula [163]

$$\gamma_{\mathrm{sc}} = \frac{\gamma_e}{2}\frac{2\Omega_\pi^2}{\gamma_e^2+4\Delta^2+2\Omega_\pi^2} \sim \frac{\Omega_\pi^2}{4\gamma_e}\left(\frac{\gamma_e}{\Delta}\right)^2 \tag{3.14}$$

where $\Omega_\pi = 2\sqrt{2/3}\tilde{\Omega}_{jj'}\sqrt{\Phi_L}$ is the Rabi frequency for a laser beam with linear polarization and photon flux Φ_L. A more refined analysis of decay and noise processes for the Faraday atom-light interaction has been done by Vasilyev et al. [93].

3.1.3 Atomic tensor polarizability

Including the full hyperfine structure of Rb atoms adds more complexity to the system, but the central results of the spin-1/2 model concerning scalar and vector polarizability remain the same. The simple spin-1/2 model (3.10) includes only light shifts due to two-photon transitions with $\Delta m = 0$ in the $\sigma^\pm$-basis. For spin $f \geq 1$, also two-photon transitions with $\Delta m = 2$ are possible, as is clear from Fig. 3.1a). These lead to a rank-2 tensor polarizability.

In order to describe the full tensor polarizability of a single hyperfine ground state manifold of ^{87}Rb (or any other alkali atom), we now introduce the relevant operators for spin and light. The components of the spin orientation vector $\mathbf{f}$ are defined in the

z-basis (alternative definition by cyclic permutation $x \to y \to z \to x$) by

$$f_z = \sum_{m=-f}^{f} m \left|m\right\rangle \left\langle m\right| \tag{3.15}$$

$$f_x = \frac{1}{2}(f_+ + f_-) \tag{3.16}$$

$$f_y = \frac{1}{2\mathrm{i}}(f_+ - f_-) \tag{3.17}$$

where the ladder operators $f_\pm = f_x \pm \mathrm{i} f_y$ are

$$f_+ = \sum_{m=-f}^{f-1} C(f,m) \left|m+1\right\rangle \left\langle m\right|, \quad f_- = f_+^\dagger \tag{3.18}$$

with $C(f,m) = \sqrt{f(f+1) - m(m+1)}$. The commutation relations for the spin operators are $[f_k, f_l] = \mathrm{i}\epsilon_{klm} f_m$ where ϵ_{klm} is the Levi-Civita symbol. Also, $[f_+, f_-] = 2f_z$. Spin alignment tensors are defined as

$$t_{x^2-y^2} = f_x^2 - f_y^2 = \frac{1}{2}(f_+^2 + f_-^2) \tag{3.19}$$

$$t_{xy} = f_x f_y + f_y f_x = \frac{1}{2\mathrm{i}}(f_+^2 - f_-^2) \tag{3.20}$$

Here, we give the commutation relation with f_z which is important for rotations about the z-axis: $[t_{x^2+y^2}, f_z] = -\mathrm{i}2t_{xy}$ and $[t_{xy}, f_z] = \mathrm{i}2t_{x^2-y^2}$. The Stokes operators for light have already been defined in (3.9). Their commutation relations are $[S_k(z), S_l(z')] = \mathrm{i}\epsilon_{klm} c\delta(z - z') S_m(z)$.

Using these definitions, we are able to write down the total dispersive interaction Hamiltonian for a single ground state hyperfine manifold [164, 151, 165, 166]

$$H_{\text{eff}} = \hbar\alpha_0 \mathbb{1}_f S_0 + \hbar\alpha_1 f_z S_z + \hbar\alpha_2 \left[t_{x^2-y^2} S_x + t_{xy} S_y + \left(\frac{\mathbf{f}^2}{3} - f_z^2 \right) S_0 \right] \tag{3.21}$$

which now contains scalar α_0, vector α_1 and tensor polarizability α_2. The precise form of the coefficients α_i strongly depends on the detuning relative to the different excited state hyperfine levels. In the far-detuned limit, where the excited state hyperfine splitting is small compared to Δ, simple asymptotic expressions can be derived. For the scalar and vector polarizability we then have

$$\alpha_0 = \frac{\lambda^2}{2\pi A} \frac{\gamma_e}{\Delta} \tag{3.22}$$

$$\alpha_1 = \frac{\lambda^2}{8\pi A} \frac{\gamma_e}{\Delta} (-1)^f \tag{3.23}$$

and the tensor polarizability α_2 has the following different asymptotic expression for $f = 1, 2$,

$$\alpha_2^{f=1} \sim \frac{\lambda^2}{8\pi A} \frac{\gamma_e}{\Delta} \frac{-4\delta_0 + 5\delta_1 - \delta_2}{4\Delta} \tag{3.24}$$

$$\alpha_2^{f=2} \sim \frac{\lambda^2}{8\pi A} \frac{\gamma_e}{\Delta} \frac{-\delta_1 + 5\delta_2 - 4\delta_3}{20\Delta} \tag{3.25}$$

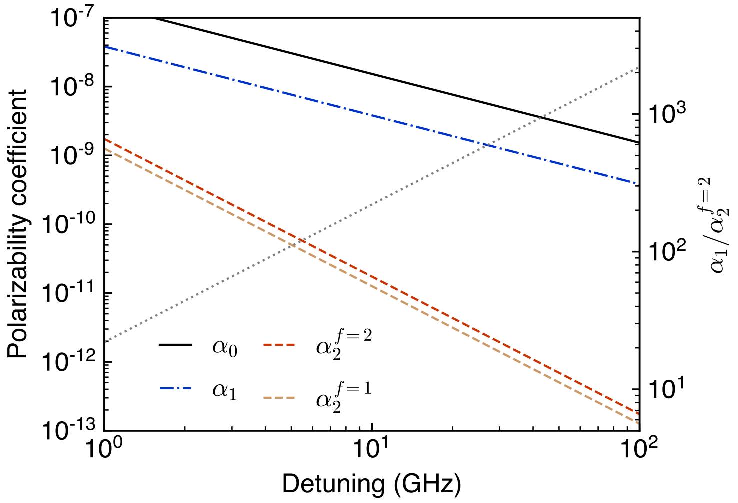

Figure 3.2: Rb polarizability coefficients as a function of detuning for a beam waist $w_0 = 35\ \mu$m. The ratio $\alpha_1/\alpha_2^{f=2}$ is shown as the dotted line belonging to the right hand axis.

Here, $\delta_{f'}$ are the frequency offsets of the excited state hyperfine levels relative to the ${}^2P_{3/2}$ level. From these equations we see that $\alpha_2 \sim 1/\Delta^2$ as opposed to $\alpha_0, \alpha_1 \sim 1/\Delta$ for large Δ. This means that for a detuning which is large compared to the excited state hyperfine splittings, the atomic polarizability becomes more similar again to that of a spin-1/2.

Still, there are some differences. As a consequence of the reduced dipole matrix elements in the presence of hyperfine structure, α_0 is reduced by 1/2 compared to the spin-1/2 model. At the same time, $\gamma_{\mathrm{sc}} \propto \alpha_0$ is reduced by the same amount. On top of that, the vector polarizability α_1 decreases by an extra factor of $1/4 = j/(i+j)$ which is due to the coupling to the nuclear spin $i = 3/2$. While the total spin increases from $j = 1/2$ to $f = i \pm j$, the atom's electric dipole moment remains unchanged. This reduces the light shift per quantum of spin which is expressed in terms of α_1. Hence, it is unfavorable to use atomic species with large nuclear spin. When comparing $f = 1$ to $f = 2$, it is clear that α_1 is equal in magnitude, only f_z changes. Since an atom in $|f = 2, m = 2\rangle$ produces a larger Faraday rotation than in the state $|f = 1, m = 1\rangle$, $f = 2$ is preferred. In Fig. 3.2, the polarizability coefficients are plotted as a function of detuning between 1 and 100 GHz, and for a beam waist $w_0 = 35\ \mu$m used in the experiment. This shows that α_2 quickly becomes negligible compared to $\alpha_{0,1}$ above 10 GHz detuning.

As a remark, the Hamiltonian (3.21) only considers a single hyperfine manifold $f = 1$ or $f = 2$. In reality, there are also vector and tensor couplings $f = 1 \leftrightarrow f = 2$ which have a similar magnitude as α_1 and α_2, respectively [167]. However, they oscillate at frequencies close to the ground state hyperfine splitting $\Delta_{\mathrm{hf}} = 2\pi \times 6.835$ GHz. On the contrary, we consider coherences of the hyperfine spin $\mathbf{f}$ which oscillate at MHz frequencies for small magnetic fields. The presence of hyperfine couplings $f = 1 \leftrightarrow f = 2$ also means, that decoherence processes now contain decay of an atom from $f = 2$ to

$f = 1$ (optical pumping), or vice versa. Experimentally, this has to be countered by adding another laser that pumps the atoms back to the original hyperfine manifold.

3.1.4 Faraday atom-light interface

Having established the dispersive atom-light interaction in terms of the atomic polarizability tensor, we can now investigate the dynamics of the quantum interface. We choose the vector polarizability for the interface because the favorable scaling $\alpha_1 \sim \Delta^{-1}$ allows spontaneous scattering $\gamma_{\text{sc}} \sim \Delta^{-2}$ to be suppressed at large detunings. Because of this argument, we also neglect the rank-2 tensor polarizability in this discussion.

So far we have only dealt with the coupling between light and a single atom. For an atomic ensemble consisting of $N \gg 1$ atoms ($N \sim 10^7$ in our experiment), we define the collective spin vector

$$\mathbf{F} = \sum_{i=1}^{N} \mathbf{f}^{(\mathrm{i})} \tag{3.26}$$

with length $F_0 = |\mathbf{F}| = fN$. For independent atoms, the components F_x, F_y, F_z of the collective spin satisfy the commutation relations $[F_k, F_l] = \mathrm{i}\epsilon_{klm}F_m$ of a vector. To keep the discussion simple at this point, we assume a uniform atom-light coupling and non-interacting atoms. The atom-light Faraday interaction can then be written in the form

$$H_{\text{int}} = \hbar\alpha_1 F_z S_z \tag{3.27}$$

which couples F_z to S_z. As a consequence, the light-field passing through the atomic ensemble is subject to the input-output relations [164, 152]

$$\begin{aligned} S_x^{(\text{out})} &= S_x^{(\text{in})} - \alpha_1 F_z S_y^{(\text{in})} && (3.28) \\ S_y^{(\text{out})} &= S_y^{(\text{in})} + \alpha_1 F_z S_x^{(\text{in})} && (3.29) \\ S_z^{(\text{out})} &= S_z^{(\text{in})} && (3.30) \end{aligned}$$

which map F_z onto a rotation of S_y and S_x about S_z with Faraday rotation angle

$$\theta_F = \frac{1}{2}\alpha_1 F_z. \tag{3.31}$$

For an atomic ensemble where all spins are polarized along the z-axis, $\bar{F}_z = Nf$ is a macroscopic quantity enabling $\theta_F \sim 1$ at small detuning. Hence, Faraday rotation provides a direct way to characterize the atom-light interaction strength. The optical depth $d_0 = N\lambda^2/(\pi A)$ for linearly polarized light can be determined using the relation

$$\theta_F = d_0 \frac{\gamma_e}{8\Delta} \tag{3.32}$$

which only depends on the known parameters γ_e and Δ [152].

In the following, we consider the experimental setting that the ensemble is probed by a linear, x-polarized laser beam with $S_x \approx \bar{S}_x = \Phi_L/2$. Then, one can make a Holstein-Primakoff approximation for the transverse Stokes vector components, i.e.

$$\begin{aligned} S_y &\approx \sqrt{\frac{\bar{S}_x}{2}}\left(a_y + a_y^\dagger\right) = \sqrt{\bar{S}_x}X_L && (3.33) \\ S_z &\approx -\mathrm{i}\sqrt{\frac{\bar{S}_x}{2}}\left(a_y - a_y^\dagger\right) = \sqrt{\bar{S}_x}P_L && (3.34) \end{aligned}$$

that maps S_y onto the amplitude quadrature X_L and S_z onto the phase quadrature P_L of the y-polarized quantum field a_y, i.e. orthogonal to the laser polarization. The fluctuations of X_L, P_L can conveniently be measured by homodyne detection, using the x-polarized laser field as the local oscillator. A combination of quarter- and half-wave plates can be used to select any field quadrature of a_y for detection (see section 3.5).

For the atom-light quantum interface, the atomic ensemble is spin-polarized by optical pumping along a transverse magnetic field $\mathbf{B}_0$ pointing along the x-axis. We choose x here, but any other direction in the xy-plane works. This prepares a collective spin with $\bar{F}_x \approx Nf$, i.e. a coherent spin state pointing along x [44]. Here, we also make a Holstein-Primakoff approximation to describe the transverse spin components F_y, F_z in terms of the harmonic oscillator quadratures

$$X_s = \frac{F_z}{\sqrt{|\bar{F}_x|}}, \qquad P_s = -\operatorname{sgn}(\bar{F}_x)\frac{F_y}{\sqrt{|\bar{F}_x|}} \tag{3.35}$$

which satisfy the canonical commutation relations $[X_s, P_s] = \mathrm{i}$. In this mapping, the coherent spin-state with $F_x = Nf$ corresponds to the vacuum $|0\rangle_s$ and the spin creation (annihilation) operator $b_s^\dagger = (X_s - \mathrm{i}P_s)/\sqrt{2}$ $(b_s = (X_s + \mathrm{i}P_s)/\sqrt{2})$ excites (destroys) a Dicke state [44], i.e. a symmetric superposition of one out of N atomic spins being flipped by 1 quantum of angular momentum.

The magnetic field induces the linear Zeeman Hamiltonian [163]

$$H_0 = \hbar\Omega_0 F_x \tag{3.36}$$

where $\Omega_0 = \gamma_f|B_0|$ is the Larmor frequency and γ_f is the gyromagnetic ratio. This leads to spin-precession of F_y and F_z about F_x. In the Holstein-Primakoff approximation, $F_x \approx \bar{F}_x - \operatorname{sgn}(\bar{F}_x)(X_s^2 + P_s^2)/2$ such that

$$H_0 \approx \hbar\Omega_0\bar{F}_x - \operatorname{sgn}(\bar{F}_x)\frac{\hbar\Omega_0}{2}(X_s^2 + P_s^2) \tag{3.37}$$

becomes a harmonic oscillator Hamiltonian. One can define the effective spin-oscillator frequency $\Omega_s = -\operatorname{sgn}(\bar{F}_x)\Omega_0$ which is positive for $\bar{F}_x < 0$ and negative for $\bar{F}_x > 0$ [28]. Consequently, if the spin is in its lowest energy state with $\bar{F}_x = -Nf$ it realizes a spin oscillator with $\Omega_s > 0$, which corresponds to a standard harmonic oscillator with positive mass. If instead the spin is initialized by optical pumping in its highest energy state $\bar{F}_x = +Nf$, the oscillation frequency is negative and the spin oscillator realizes a negative-mass oscillator [69]. The fact that any excitation of the negative-mass oscillator actually reduces its energy is an important feature which has been harnessed for the observation of parametric instabilities [70], entanglement between remote atomic ensembles [28], and for quantum back-action evading measurements [51]. In this work, we will use it to generate parametric-gain dynamics between a collective atomic spin and a membrane oscillator.

Using the Holstein-Primakoff approximation for both the spin and the light, we arrive at the effective interaction

$$H_{\text{int}} = \hbar 2\sqrt{\Gamma_1}X_s P_L \tag{3.38}$$

where we defined the spin measurement rate

$$\Gamma_1 = \frac{\alpha_1^2|\bar{F}_x||\bar{S}_x|}{4} \tag{3.39}$$

In this description, the spin-light interaction is written in a form that is equivalent to the effective optomechanical coupling in equation (2.33). Consequently, one can also define a quantum cooperativity for the spin (in absence of thermal noise), which is given by

$$C_s = \frac{2\Gamma_1}{\gamma_{\text{sc}}} = \frac{d_0}{32} \tag{3.40}$$

for $f = 2$. Here, we used the definition $\gamma - \text{sc} = \alpha_0 S_0(\gamma_e/\Delta)$ as in equation (3.13). We see that the cooperativity is proportional to the optical depth, but it is reduced significantly by the factor $1/32$. This mismatch stems in part $(1/8)$ from the reduction of the vector polarizability due to nuclear spin. Thus, for a spin-1/2, one would obtain $C_s = d_0/4$. Another reduction by $1/2$ is due to the fact, that the optical depth considers both forward and backward scattering appropriate for a cavity, while our free-space setup only uses the forward scattered light [161]. It is important to note, that the cooperativity is independent of detuning in the far-detuned limit. This means that the performance of the atom-light quantum interface is entirely determined by the atom number and the geometric overlap between the atomic ensemble and the probe light.

3.1.5 Non-uniform atom-light coupling

The above description of the atom-light interface considered an idealized scenario with homogeneous optical intensity p_L/A where $p_L = \hbar\omega_L\Phi_L$ is the optical power of the laser beam. In reality, the optical electric field has a spatial mode function u_0, e.g. a Gaussian mode with peak intensity $2p_L/A$ in the focus (cf. section 4.2.2).

For an atomic ensemble distributed randomly across the laser beam, each atom i experiences a different local optical intensity $\propto |u_0(\mathbf{r}_i)|^2$. Accordingly, this rescales both the polarizability α_1 as well as the decoherence rate γ_{sc} of each atom. An important consequence of this is that the atom-light coupling involves non-uniform collective operators or spin-waves $X_s^{\text{eff}}, P_s^{\text{eff}}$, i.e. [155, 168]

$$X_s^{\text{eff}} = \frac{1}{\sqrt{fN\eta_{\text{eff}}}} \sum_{i=1}^{N} |u_0(\mathbf{r}_i)|^2 f_z^{(i)}, \tag{3.41}$$

$$P_s^{\text{eff}} = -\frac{\text{sgn}(\bar{F}_x)}{\sqrt{fN\eta_{\text{eff}}}} \sum_{i=1}^{N} |u_0(\mathbf{r}_i)|^2 f_y^{(i)}, \tag{3.42}$$

which satisfy the canonical commutation relations $\langle [X_s^{\text{eff}}, P_s^{\text{eff}}] \rangle = \text{i}$. Here, a normalization factor

$$\eta_{\text{eff}} = \frac{1}{N} \sum_{i=1}^{N} |u_0(\mathbf{r}_i)|^4 \tag{3.43}$$

has been defined, implying an effective atom number $\eta_{\text{eff}} N$. The effective spin measurement rate is

$$\Gamma_1^{\text{eff}} = \eta_{\text{eff}} \frac{\alpha_1^2}{4} \frac{fN\Phi_L}{2}. \tag{3.44}$$

The atom-light coupling Hamiltonian then takes the same form as equation (3.38) with all atomic quantities replaced by effective ones. Decoherence of the non-uniform atomic states becomes more complicated because single-atom decay can now change the spatial mode of the collective spin wave [155].

3.1.6 Dynamics of the tensor polarizability

Having established the Faraday atom-light interface using the vector polarizability, we aim to understand how the remaining terms belonging to the full tensor polarizability affect the dynamics. In order to analyze the meaning of the various terms in the atomic tensor polarizability, we first simplify the Hamiltonian (3.21) assuming a spin-polarized ensemble and linear optical polarization.

Light We first choose a suitable reference frame for the optical fields. The laser's input polarization is linear with angle θ relative to the laboratory x-axis, which is defined by a magnetic field around which the spin precesses. Approximated as a plane wave, the positive-frequency component of the laser electric field is thus

$$\mathbf{E}^{(+)} = \mathcal{E}_0 \left[(\sqrt{\Phi_L} + a_{x'})\mathbf{e}_{x'} + a_{y'}\mathbf{e}_{y'} \right] e^{\mathrm{i}k_L z} \tag{3.45}$$

with linearly polarized quantum fields $a_{x'}$ and $a_{y'}$ belonging to the polarization vectors

$$\mathbf{e}_{x'} = \begin{pmatrix} \cos\theta \\ \sin\theta \end{pmatrix}, \quad \mathbf{e}_{y'} = \begin{pmatrix} -\sin\theta \\ \cos\theta \end{pmatrix}, \tag{3.46}$$

respectively. The Stokes vector components transform under the basis rotation like

$$S_x = S_{x'}\cos(2\theta) - S_{y'}\sin(2\theta) \tag{3.47}$$

$$S_y = S_{y'}\cos(2\theta) + S_{x'}\sin(2\theta) \tag{3.48}$$

where the primed coordinates refer to the frame fixed to the laser. In terms of the linearly polarized fields, the Stokes vector definitions are

$$\begin{aligned} S_0 &= \frac{1}{2}\left(a^\dagger_{x'}a_{x'} + a^\dagger_{y'}a_{y'}\right), \\ S_{x'} &= \frac{1}{2}\left(a^\dagger_{x'}a_{x'} - a^\dagger_{y'}a_{y'}\right), \\ S_{y'} &= \frac{1}{2}\left(a^\dagger_{x'}a_{y'} + a^\dagger_{y'}a_{x'}\right), \\ S_z &= \frac{1}{2i}\left(a^\dagger_{x'}a_{y'} - a^\dagger_{y'}a_{x'}\right). \end{aligned} \tag{3.49}$$

The laser field (3.45) has a strong coherent component in x'-direction with flux Φ_L. For the mean fields we have $\bar{S}_0 = \bar{S}_{x'} \approx \Phi_L/2$ and $\bar{S}_{y'} = \bar{S}_{z'} = 0$. Again, we make a Holstein-Primakoff approximation,

$$S_{x'} \approx \bar{S}_0 + \sqrt{\bar{S}_0}X_L^{(x')} \tag{3.50}$$

$$S_{y'} = \sqrt{\bar{S}_0}X_L^{(y')} \tag{3.51}$$

$$S_{z'} = \sqrt{\bar{S}_0}P_L^{(y')} \tag{3.52}$$

which allows us to represent the light-field in terms of the quadratures ($k = x', y'$)

$$X_L^{(k)} = \frac{1}{\sqrt{2}}\left(a_L^{(k)} + (a_L^{(k)})^\dagger\right) \tag{3.53}$$

$$P_L^{(k)} = \frac{1}{\sqrt{2}\mathrm{i}}\left(a_L^{(k)} - (a_L^{(k)})^\dagger\right) \tag{3.54}$$

Spin In the presence of a magnetic field along x, the transverse f_y and f_z components precess about x, i.e.

$$f_y = \tilde{f}_y \cos(\Omega_0 t) - \tilde{f}_z \sin(\Omega_0 t) \tag{3.55}$$
$$f_z = \tilde{f}_z \cos(\Omega_0 t) + \tilde{f}_y \sin(\Omega_0 t) \tag{3.56}$$

where $\tilde{f}_y, \tilde{f}_z$ are slowly varying envelopes that correspond to an interaction picture with respect to H_0. Since f_x commutes with H_0, $\tilde{f}_x = f_x$. Similarly, the tensor components can be written as

$$\begin{aligned}
t_{x^2-y^2}(t) &= \tilde{f}_x^2 - \frac{\tilde{f}_y^2 + \tilde{f}_z^2}{2} - \frac{\tilde{f}_y^2 - \tilde{f}_z^2}{2}\cos(2\Omega_0 t) - \frac{\{\tilde{f}_y, \tilde{f}_z\}}{2}\sin(2\Omega_0 t) \\
t_{xy}(t) &= \{\tilde{f}_x, \tilde{f}_y\}\cos(\Omega_0 t) + \{\tilde{f}_x, \tilde{f}_z\}\sin(\Omega_0 t) \\
f_z^2(t) &= \frac{\tilde{f}_y^2 + \tilde{f}_z^2}{2} - \frac{\tilde{f}_y^2 - \tilde{f}_z^2}{2}\cos(2\Omega_0 t) - \frac{\{\tilde{f}_y, \tilde{f}_z\}}{2}\sin(2\Omega_0 t)
\end{aligned}$$

We see that $\tilde{t}_{x^2-y^2}$ and $\tilde{f}_z^2$ both have a stationary part and a part rotating at $2\Omega_0$, while $\tilde{t}_{xy}$ rotates only at Ω_0. Since we are interested in the dynamics of $\tilde{f}_y$ and $\tilde{f}_z$ which rotate at Ω_0, we ignore the fast and off-resonant $2\Omega_0$ dependence. This assumes that the optical field has no frequency component at $2\Omega_0$. Using $f_x^2 + f_y^2 + f_z^2 = f(f+1)$ this leads to

$$t_{x^2-y^2} \approx \frac{1}{2}\left[3f_x^2 - f(f+1)\right] \tag{3.57}$$
$$f_z^2 \approx \frac{1}{2}\left[f(f+1) - f_x^2\right] \tag{3.58}$$

Further, if all spins have been polarized to one of the $m = \pm f$ stretched states, we can approximate [169, 164]

$$t_{xy} \approx \operatorname{sgn}(f_x)(2f-1)f_y \tag{3.59}$$
$$t_{xz} \approx \operatorname{sgn}(f_x)(2f-1)f_z \tag{3.60}$$

This can be seen by evaluating the matrix elements for the subspaces $m = f, f-1$ or $m = -f, -f+1$, using the definitions (3.15) to (3.18) with x as the quantization axis.

Single-spin interaction Combining the effects of rotated laser polarization and the approximations for the spin, we arrive at the Hamiltonian (omitting all constant contributions)

$$\begin{aligned}
H_{\text{eff}} = {} & \hbar\alpha_1\sqrt{\bar{S}_0} f_z P_L^{(y')} \\
& + \hbar\alpha_2\sqrt{\bar{S}_0}(2f-1)\operatorname{sgn}(f_x) f_y \left[\cos(2\theta)X_L^{(y')} + \sin(2\theta)X_L^{(x')}\right] \\
& + \hbar\alpha_2\bar{S}_0 \frac{3\cos(2\theta)+1}{2} f_x^2
\end{aligned} \tag{3.61}$$

The first line is the normal Faraday interaction coupling f_z to the phase quadrature $P_L^{(y')}$ of the quantum field in polarization orthogonal to the laser. The second line is a tensor-induced coupling between f_y and the amplitude quadratures $X_L^{(y')}$ and $X_L^{(x')}$ in y' and

x'-polarization, respectively. The coupling to $X_L^{(y')}$ is of potential relevance for spin-spin interactions mediated by the light field, since $X_L^{(y')}$ carries information about f_z from other atoms due to the Faraday interaction. Moreover, the coupling to $X_L^{(x')}$ is important because this quadrature contains technical laser amplitude noise. Additionally, when the laser beam is suddenly switched on timescales comparable to $2\pi/\Omega_0$, this creates frequency components which can drive the spin. The coupling strengths of f_y to these two optical fields depend on the laser polarization angle θ which allows their relative strength to be adjusted. For example at $\theta = 0°, 90°$ there is only a coupling to $X_L^{(y')}$ while at $\theta = \pm 45°$ only to $X_L^{(x')}$.

Finally, in the last line of (3.61), we have a static term proportional to f_x^2 and the mean laser intensity $\sim \bar{S}_0$. This term induces a quadratic energy-shift of the different Zeeman levels m by an amount $\hbar\delta\Omega_2 m^2$, where

$$\delta\Omega_2 = \alpha_2 \bar{S}_0 \frac{3\cos(2\theta)+1}{2} \tag{3.62}$$

is called the tensor light shift. Although the tensor polarizability $\alpha_2 \sim 1/\Delta^2$ becomes small at large detuning, this term can be very large since it is proportional to $\bar{S}_0$. It has similar magnitude as the scattering rate γ_{sc} which also scales like $1/\Delta^2$ and thus cannot be neglected at any detuning. If the tensor shift were identical for all atoms, it could simply be accounted for by a change of the Larmor frequency. However, since atoms are randomly distributed inside the laser beam focus, they experience different optical intensities. Hence, the tensor light shift potentially leads to an inhomogeneous broadening and causes dephasing of spin precession. To avoid this issue, the angular dependence of $\delta\Omega_2$ can be exploited. Working at $\theta \approx 54.7°$ where $3\cos(2\theta)+1 \approx 0$ suppresses unwanted effects due to the tensor light shift [170].

Atomic ensemble Here, we consider only the interaction of the spin with the y'-polarized fields and drop the superscript. Including the tensor terms of (3.61) we can extend the atom-light interaction Hamiltonian of (3.38) to

$$H_{\mathrm{int}} = \hbar 2\sqrt{\Gamma_1} X_s P_L + \hbar 2\sqrt{\Gamma_2} P_s X_L \tag{3.63}$$

Now, there is another coupling between P_s and X_L with tensor measurement rate

$$\Gamma_2 = \frac{\alpha_2^2 \bar{S}_x \bar{F}_x}{4}(2f-1)^2\cos^2(2\theta) \tag{3.64}$$

that depends on the laser polarization angle θ. The propagation equations for the light quadratures in this situation read

$$\left(\frac{\partial}{\partial t} + c\frac{\partial}{\partial z}\right) X_L(z,t) = +2c\delta(z-z_a)\sqrt{\Gamma_1} X_s(t) \tag{3.65}$$

$$\left(\frac{\partial}{\partial t} + c\frac{\partial}{\partial z}\right) P_L(z,t) = -2c\delta(z-z_a)\sqrt{\Gamma_2} P_s(t) \tag{3.66}$$

where z_a denotes the position of the ensemble. This is highly simplified because actually light is gradually reading out information from each spin as it propagates through the

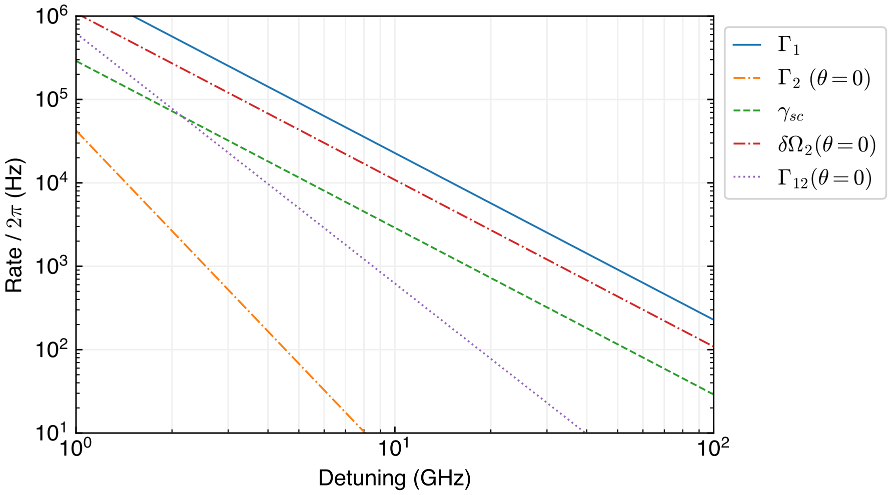

Figure 3.3: Rates of the atom-light interface as a function of detuning.

atomic cloud. Moreover, the Heisenberg-Langevin equations for the spin quadratures read

$$\dot{X}_s = -\frac{\gamma_s}{2}X_s + \Omega_s P_s - 2\sqrt{\Gamma_2}X_L(z_a) - \sqrt{\gamma_s}F_{s,X} \tag{3.67}$$

$$\dot{P}_s = -\frac{\gamma_s}{2}P_s - \Omega_s X_s - 2\sqrt{\Gamma_1}P_L(z_a) - \sqrt{\gamma_s}F_{s,P} \tag{3.68}$$

where $F_{s,X}, F_{s,P}$ are additional noise terms due to vacuum and thermal noise. We see that X_s and P_s are damped at a rate γ_s which includes both intrinsic and light-induced effects. Moreover, the spin components oscillate at Ω_s and are driven by the light field quadratures. Combining the propagating equations for light with the equations of motion for the spin reveals that X_L contains a contribution from X_s and P_L contains a contribution from P_s. Consequently there is some dynamical back-action of the atomic ensemble onto itself, which would lead to damping in our naive picture, but it actually consitutes a light-mediated interaction between different atoms in the ensemble. The simple 1D picture we give here most probably breaks down at this point. In order to obtain a quantitative understanding one must both approach the problem from a many-body perspective [171] and respect the 3D-character of the atom-light interaction [149, 172]. Still, for an order of magnitude we can evaluate the cross-coupling rate

$$\Gamma_{12} = 2\sqrt{\Gamma_1\Gamma_2} \propto |\cos(2\theta)|\Delta^{-3} \tag{3.69}$$

which lies in between the vector and tensor measurement rates.

To conclude this theoretical part on the atom-light interface, we show a plot of the calculated coupling rates as a function of detuning in Fig. 3.3. Here, we choose an atom number $N = 10^7$, a laser power $\hbar\omega_L\Phi_L = 1$ mW and a beam waist $w_0 = 35\ \mu$m. Moreover, for the tensor-related rates we choose the maximum value at a polarization angle of $\theta = 0$. The plot shows that Γ_1, γ_{sc} and $\delta\Omega_2$ run in parallel since they all scale with Δ^{-2}. It is obvious that the tensor shift is significant and must be suppressed by appropriate polarization. Further, we see that the tensor measurement rate falls off very quickly and is completely negligible for $\Delta/2\pi \geq 10$ GHz. However, the cross-coupling rate $\Gamma_{12} \sim \Delta^{-3}$ remains relatively large. Thus, even though $\Gamma_{12}/\gamma_{\mathrm{sc}} < 1$, this does not exclude that light-mediated atom-atom interactions can be a significant source of spin noise. These numbers also mean that if the spin ensemble is limited by quantum spin noise, the large cooperativity $C_s \approx 10$ would allow quantum coherent readout of the spin using light far in the quantum back-action dominated regime [51].

Finally, we look at the dependence of these rates on the laser polarization relative to the transverse magnetic field (Fig. 3.4), choosing a detuning of $\Delta = 2\pi \times 10$ GHz. Here we note the $3\cos(2\theta)+1$ dependence of $\delta\Omega_2$, with a minimum at $\theta \approx 55°$ that minimizes dephasing due to inhomogeneous tensor light shifts. Moreover, Γ_{12} is proportional to $|\cos(2\theta)|$ and has a zero-crossing at $\theta = 45°$. Simultaneous cancellation of both rates is not possible. It is important to stress, however, that the size and effect of Γ_{12} are still a matter of speculation.

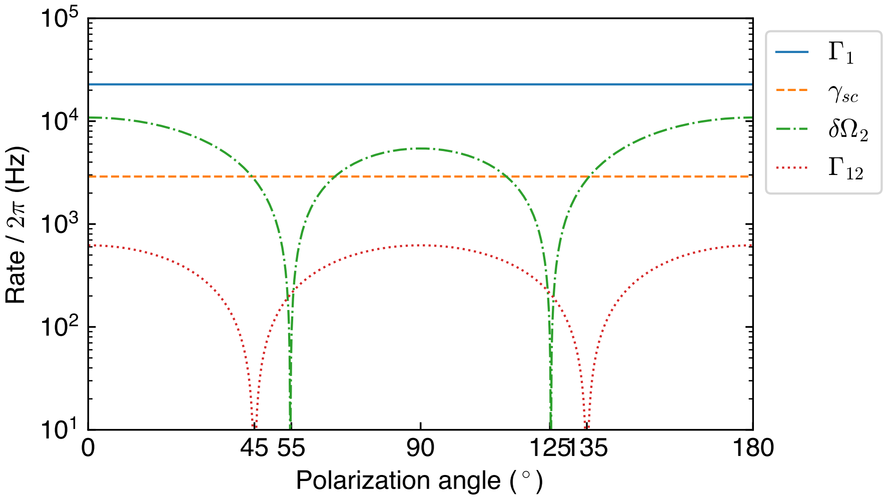

Figure 3.4: Rates of the atom-light interaction as a function of the laser polarization angle relative to the magnetic field.

3.2 Experimental setup

Having discussed the theoretical aspects of the Faraday atom-light interface, we now present the experimental setup, which is shown in Fig. 3.5. The optical setup is centered around a ultra-high vacuum octagonal glass cell with good optical access. The atomic ensemble is prepared in an optical dipole trap that is formed in the focus of a far off-resonant high-power laser beam at 1064 nm propagating along the z-axis from the left. To load the dipole trap, an atomic beam is generated by a two-dimensional magneto-optical trap (2D-MOT) in an adjacent vacuum chamber filled with Rb vapor, separated from the main chamber by a differential pumping tube. The atomic beam then loads a large three-dimensional MOT (3D-MOT) with a rate of about 4×10^9 atoms per second, from which up to 2×10^7 atoms are transferred into the dipole trap at a temperature of 50 μK. Stable magnetic fields are generated using a set of coils, which is described in detail below. A charge-coupled device (CCD) camera allows the atomic cloud to be imaged along the y-axis. Optical pumping is performed on the vertical x-axis using circularly polarized light.

Coupling laser beam The coupling laser beam at 780 nm is derived from the Ti:Sa laser (see Fig. 2.9) and is amplitude-controlled using an AOM. After a fiber collimator[3] it first passes through a Glan-Thompson polarizer[4] which creates a clean linear polarization, and is then focused onto the atomic cloud using a singlet $f = 200$ mm lens. The coupling beam propagates in opposite direction to the 1064 nm trap beam. Dichroic mir-

---

[3] Schäfter & Kirchhoff 60FC-F-4-A18-02 or 60FC-F-4-M12-10

[4] B-Halle GmbH, extinction ratio 10^{-8}

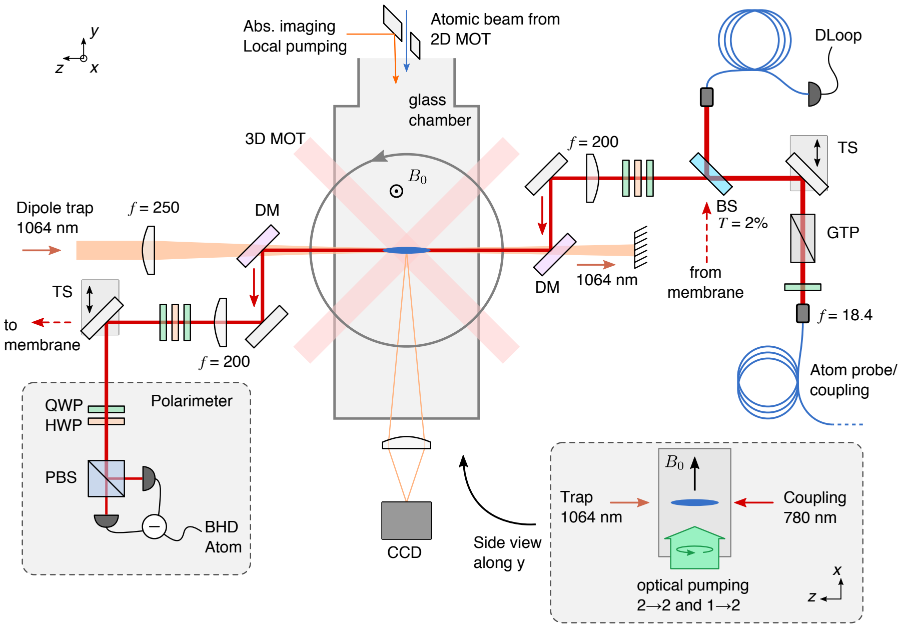

Figure 3.5: Schematic of the experimental setup.

rors[5] (DM) are used to combine and separate the two wavelengths. Since the experiment is highly sensitive to laser polarization, we use special mirrors with optimized coating[6] to avoid birefringence. Nevertheless, the coupling laser polarization in front of the atomic vacuum chamber has to be fine tuned using a QWP-HWP-QWP stack[7], compensating birefringence of the dichroic mirror. This achieves an extinction ratio of about 10^3 for any linear input polarization and implies residual circular polarization $S_z/S_0 \approx 0.03$. Another such wave-plate stack compensates for birefringence of the second dichroic mirror after the vacuum chamber. The chamber itself does not measurably degrade the laser polarization at this level. After the coupling beam has passed through the atomic ensemble, the polarization rotation done by the atoms is measured using a polarimeter consisting of a QWP-HWP stack, a polarizing beam splitter[8] and a balanced detector[9]. By adjusting the waveplates, any Stokes vector component can be measured.

In order to connect the atomic setup with the optomechanical setup or realize multi-pass atom-light interactions, we pass the coupling beam through an input coupler with 2% transmission (BS in Fig. 3.5). Moreover, a translation stage (TS) at the input can displace the beam such that it intersects the atomic cloud under an angle, which is required for the atom-membrane and multi-pass experiments. After the atomic setup, the coupling beam can be sent to the optomechanical setup (see Fig. 2.10) by moving away the pick-up mirror for the polarimeter using another TS.

Experiment control Experiments done with the atomic ensemble follow a hardware-timed sequence which is depicted schematically in Fig. 3.6. This sequence is loosely structured into three main sections: loading the dipole trap, initializing the spin state, and probing the spin using the coupling laser. Variations and repetitions of the sequence can then be performed to scan the experimental parameter space and acquire statistics. In order to execute the sequence which spans up to a few seconds with microsecond time resolution for the individual steps, we employ the software package *labscript suite* [173]. Labscript is a programme written in Python which allows computer control of the entire experimental hardware, like digital and analog input/output (IO) cards or data acquisition devices, and execute timed sequences. Labscript's workflow consists of a manual mode, e.g. for device testing, and a buffered mode during which a timed sequence is executed.

Running an experiment using labscript works in the following way. First, a Python script must be written which specifies the requested hardware changes and their timings. Moreover, the script also contains non-realtime commands which are issued before ("pre-seq") or after the sequence ("post-seq"). This is useful, for example, to upload settings to a signal generator whose output is later triggered within the timed sequence, or to read data from a data acquisition device after the sequence. The script is then compiled and labscript uploads all hardware change instructions to the devices. Execution of the sequence is controlled by a pseudoclock, a microcontroller with internal clock, that sends out triggers to all devices whenever a hardware change is programmed in the

---

[5] Layertec GmbH

[6] Lens-Optics GmbH, $R > 99.8\%$, s/p phase difference $< \lambda/90$ at 780 nm, 45°

[7] B-Halle GmbH

[8] Qioptiq thin film polariser.

[9] Physics Basel SP 1023

script. In principle, the microcontroller[10] in our implementation enables a maximum sampling rate of 10 MHz and a maximum of 15k instructions. However, sampling rate is limited to 100 kHz in our case due to the National Instruments IO cards we use. The pseudoclock also has the important functionality to wait with its next instruction until it has received a trigger input. We use this option to synchronize our sequence with the 50 Hz line frequency before spin-state initialization.

Labscript is a very versatile software package that is continuously being developed [11]. Since it is open source and written in Python, labscript allows one to use high-level programming for creating complex sequences and adapt it to one's own needs.

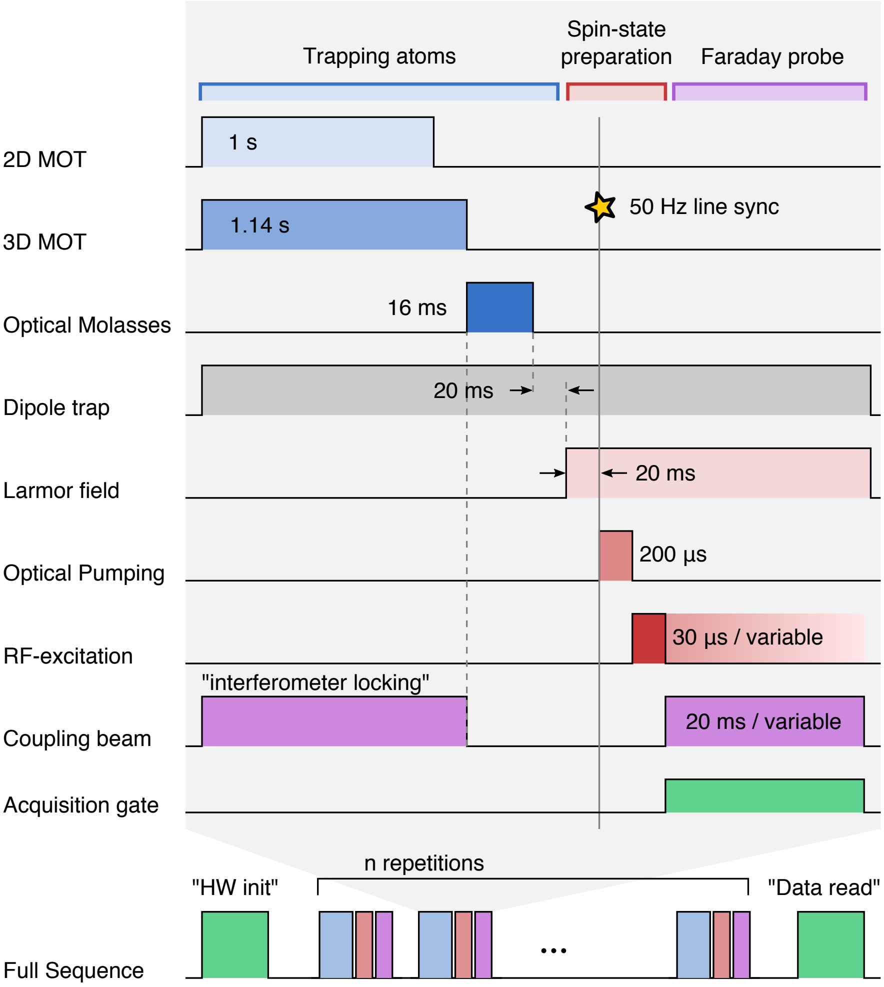

Figure 3.6: Schematic of the experimental sequence.

---

[10] DIGILENT pineblaster

[11] see the labscript_suite repository on `bitbucket.org`

3.3 Preparation of the atomic ensemble

Preparing ultracold atomic ensembles builds upon a number of cooling and trapping techniques [174] that have been invented in the course of making quantum degenerate atomic gases like Bose-Einstein condensates [175]. Since our primary goal is to achieve a high density of atoms and not so much an ultralow temperature, the experimental sequence is rather simple. A detailed description of the experimental apparatus for laser cooling has been given in references [47] and [176]. The level diagram of the D_2 transition of ^{87}Rubidium (Rb) at $\lambda_0 = 780.241$ nm ($\omega_0 = 2\pi \times 384.228$ THz) between the electronic ground state $^2S_{1/2}$ and excited state $^2P_{3/2}$ is depicted in Fig. 3.7. This diagram also indicates the relevant transitions on the hyperfine structure that are relevant for laser cooling and optical pumping. All atomic quantities of ^{87}Rb have been obtained from Steck [163].

Optical dipole trap The goal of the atom preparation sequence is to load an optically dense ensemble into an elongated single-beam optical dipole trap [177], which is formed in the focus of a high-power, far off-resonant laser beam. This provides a conservative and state-independent trap, ideal for experiments involving the atomic spin state. We employ a high power Nd:YAG laser[12] at $\lambda_{\text{trap}} = 1064$ nm which delivers up to 16 W of power to the atomic cloud. It propagates along the z-axis of the lab frame and is focused onto the atomic ensemble (see Fig. 3.5). The details of the dipole trap setup have been described in ref. [178]. At this large detuning, the light shift due to the linearly-polarized trap laser induces the potential

$$U_{\text{dip}}(\mathbf{r}) = \frac{3\pi c^2}{2\omega_0^3} \frac{\gamma_e}{\Delta} I_L(\mathbf{r}) \tag{3.70}$$

proportional to the laser intensity I_L. Here, $\mathbf{r}$ is position and $\gamma_e = 2\pi \times 6.1$ MHz is the spontaneous emission rate of the excited state. The potential is attractive ($U_{\text{dip}} < 0$) for red-detuning. At this large detuning, incoherent photon scattering at rate $\gamma_{\text{sc}} = U_{\text{dip}}\gamma_e/(\hbar\Delta)$ and therefore heating is strongly suppressed. The trap beam is focused to a waist of $w_{\text{trap}} = 90$ μm, which results in a trap depth of $U_0 = U_{\text{dip}}(0) \approx k_B \times 300$ μK at the peak intensity. At low temperatures $k_B T \ll U_0$, the atoms assume a thermal density distribution [177]

$$n(\mathbf{r}) = n_0 \exp\left(-\frac{U_{\text{dip}}(\mathbf{r})}{k_B T}\right) \tag{3.71}$$

with peak density n_0. At the beam focus, the laser intensity can be expanded to second order giving a harmonic potential such that the density of a cold ensemble in the trap obeys a Gaussian distribution. This is a suitable model which can be used to numerically calculate various quantities of the atom-light interface. Another important property of the optical dipole trap is its large aspect ratio, which in our case is given by $\sqrt{2}\pi w_{\text{trap}}/\lambda_{\text{trap}} \approx 400$. This huge aspect ratio is advantageous for atom-light interfaces as it automatically prepares the ensemble in a geometry that maximizes the optical depth along the trap axis [152].

---

[12] Mephisto MOPA, Innolight GmbH

Laser cooling In order to load atoms into the dipole trap, we have to cool them to μK temperatures, which we accomplish using laser cooling [174]. Laser cooling is to some extent a variant of optomechanical cooling, but it makes use of the atom's intrinsic optical resonance (although optical cavity cooling of atoms is also an established technique [86]). In a two-level picture, an atom will continuously scatter photons from a laser beam that is tuned near the atomic resonance. If the laser beam is red-detuned, an atom moving towards the laser beam experiences a Doppler shift that reduces the laser-atom detuning and increases the scattering rate, as opposed to an atom at rest, for which the scattering rate is reduced. This velocity-dependence of the atomic scattering rate leads to a friction force since in every scattering event (absorption and spontaneous re-emission) an atom experiences a photon recoil of $\hbar k_L$ on average. Here $k_L = 2\pi/\lambda$. In order to effectively cool an atom in 3D space, three orthogonal pairs of counter-propagating laser beams are required. This constitutes the working principle of optical molasses. Doppler cooling of a two-level atom allows to reach a minimum temperature of $\hbar\gamma_e/(2k_B)$, which amounts to ≈ 140 μK for Rb. Since Rb is not a two-level atom more efficient sub-Doppler cooling mechanisms are possible [179]. This allows us to cool the atoms into the low μK regime such that they are cold enough to be trapped in the dipole trap.

Optical transitions Rb being a multi-level atom also means that a number of lasers are required to control its spin state within the $^2S_{1/2}$ electronic ground state (see Fig. 3.7). Everywhere in this thesis, we refer to $f = 1, 2$ as the two ground state

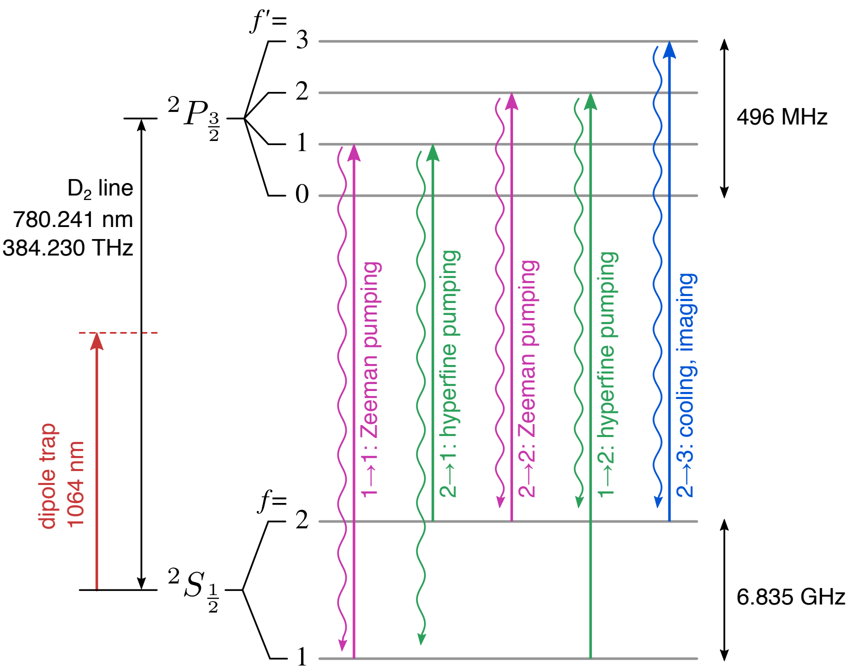

Figure 3.7: Level diagram of the D_2 transition of ^{87}Rb with hyperfine structure. Laser transitions and corresponding desired decay processes are indicated by straight arrows and wavy arrows, respectively.

hyperfine levels, while $f' = 0, 1, 2, 3$ with a prime indicates hyperfine states of the excited $^2P_{3/2}$ state. For laser cooling, the $f = 2, m_f = \pm 2 \rightarrow f' = 3, m'_f = \pm 3$ "cycling transitions" are addressed using $\sigma^\pm$ polarized light. These transitions are the only ones suitable for laser-cooling since dipole selection rules dictate that spontaneous emission returns the atom only to the initial state $f = 2, m_f = \pm 2$ which is not the case for different states. In the course of laser cooling or spin-state preparation atoms may still decay into the $f = 1$ ground state so a hyperfine re-pumping laser on the $f = 1 \rightarrow f' = 2$ transition is required to pump them back into $f = 2$. The $f = 2 \rightarrow f' = 2$ transition is the main Zeeman optical pumping transition to prepare atoms in a Zeeman state with magnetic quantum number $m_f = \pm 2$ in $f = 2$ using circularly polarized $\sigma^\pm$ light, respectively. This is because the states $m_f = \pm 2$ are dark states in this configuration as they possess no resonant transition for $\sigma^\pm$-polarized light, respectively. Besides these three main transitions, we also occasionally use the $f = 1 \rightarrow f' = 1$ transition for Zeeman optical pumping to $f = 1, m_f = \pm 1$. We also employ a laser on the $f = 2 \rightarrow f' = 1$ transition for hyperfine pumping from $f = 2$ to $f = 1$.

Laser system Laser light at the different transitions of Rb is generated by a diode-laser system, which is schematically depicted in Fig. 3.8. The RB $f = 1$ and $f = 2$ ground states are separated by a hyperfine splitting of ≈ 6.8 GHz [163], while the excited state hyperfine splitting is only ≈ 0.5 GHz. Consequently, one diode laser (MASTER) is used to generate light at the $f = 2 \rightarrow f'$ transitions while another diode laser (REPUMPER) addresses the $f = 1 \rightarrow f'$ transitions. Precise tuning to the different transitions is accomplished by frequency shifting using acousto-optic modulators (AOM), which in combination with mechanical shutters are also used to switch the beams on and off. The MASTER and REPUMPER laser are grating-stabilized diode lasers which are individually frequency stabilized using frequency-modulated saturated absorption spectroscopy on Rb vapour cells. In order to generate a large power of light for laser cooling, the MASTER laser seeds another diode laser, the SLAVE, which is then amplified using a tapered amplifier (Toptica photonics, BOOSTA) to a power of about 1 W. From there on, the light is distributed towards laser-cooling and absorption imaging. A double-pass AOM between MASTER and SLAVE allows for fast frequency shifting of the MOT light between different laser-cooling stages and for imaging. A third interference-filter stabilized diode laser REPUMPER2 addressing the $f = 2 \rightarrow f' = 1$ transition has been added recently and is locked to the MASTER laser using a digital phase-locked loop (DPLL) following Appel et al. [180]. Here, we simply measure the beat-note between the MASTER and REPUMPER2 and use a digital phase-locked-loop (PLL)[13] to detect the phase-frequency error relative to a reference frequency. This technique produces an error signal suitable for stable locking and is currently also investigated for locking our lasers to an in-house optical frequency comb.

Dipole trap loading sequence Here, we give a brief account of the experimental sequence to prepare the atomic ensemble inside the optical dipole trap, which is the starting point for doing experiments using the spin-light interface. We refer to the schematics of the setup in Fig. 3.5 and the sequence in Fig. 3.6. The first step in

---

[13] Analog devices ADF4002 with modified evaluation board EV-ADF4002SD1Z

the atomic preparation sequence is to load a large number of atoms in the magneto-optical trap (MOT) [174]. A 2D MOT generates an atomic beam from a source chamber holding a low-density vapour of Rb which is pushed using a resonant beam through a differential pumping tube into the main ultra-high vacuum chamber of the experiment at a pressure of$< 10^{-9}$ mbar. Here, atoms are received by a 3D MOT with three pairs of counterpropagating laser beams with additional confinement provided by a quadrupole magnetic field gradient of about 10 G/cm, with magnetic zero aligned to the crossing point of all laser beams. Due to Zeeman splitting in combination with the circularly polarized laser beams, the magnetic field gradient creates a cm-scale volume inside which atoms are non-conservatively trapped by radiation pressure. The MOT atom number saturates to about $\sim 10^{10}$ with a loading time constant of 0.7 s. After usually 1s of MOT loading, the 2D MOT is switched off and the MOT magnetic field gradient is ramped down within 150 ms. Simultaneously the cooling laser power is ramped down and its detuning is increased to transition into sub-Doppler optical molasses cooling without magnetic field. At this point, the atoms are cooled into the optical dipole trap, which has been turned on during the entire laser cooling stage. Due to the atomic light shift in the dipole trap of about one linewidth γ_e, atoms get further red-detuned from the laser cooling light inside the dipole trap and scatter less photons. Reducing the repump power also helps to accumulate cold trapped atoms inside the dipole trap in $f = 1$, where they are off-resonant to MOT light. Optimizing the dipole trap loading efficiency is hence mostly a matter of preventing that atoms are heated out of the trap again due to light scattering from the MOT light. A careful optimization [178] has achieved fast loading of up to 2×10^7 atoms after 15 ms of optical molasses. After some evaporative cooling, the atomic temperature reaches around 50 μK, which we determine from the thermal velocity measured by imaging the cloud after time-of-flight expansion. The life time in

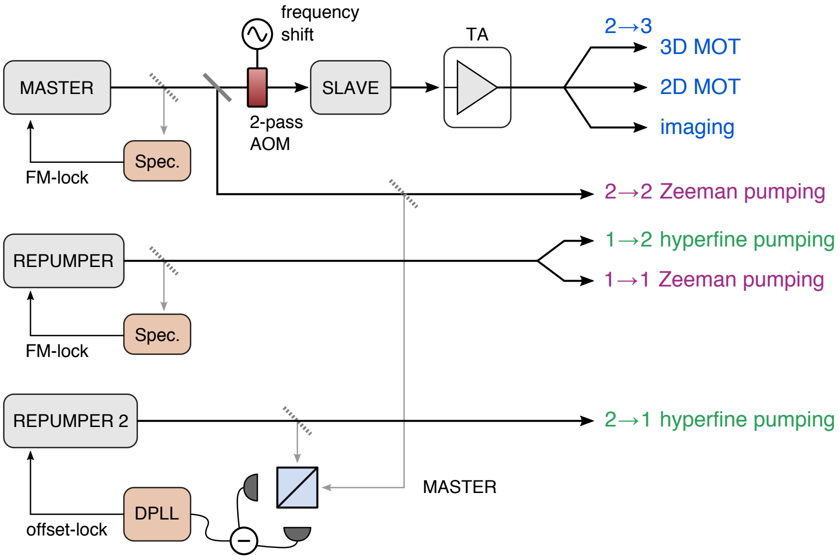

Figure 3.8: Overview of the lasers used for addressing the different optical transitions for cooling and optical pumping of ^{87}Rubidium.

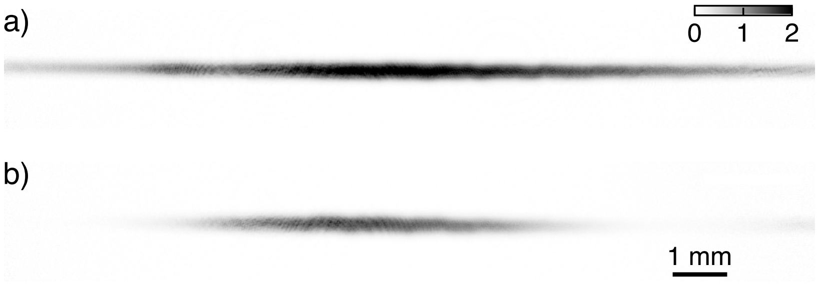

Figure 3.9: Absorption image of the atomic ensemble after release from the dipole trap and 1 ms time-of-flight. a) Fully loaded dipole trap with 20 M atoms. b) Reduced ensemble with 9 M atoms. The greyscale denotes optical density.

the trap is about 10 s, which is sufficient for our purpose.

Absorption imaging For characterization and monitoring purposes, the atomic cloud can be imaged along the transverse y-axis, where the optical density is significantly reduced (see Fig. 3.5). Absorption images are obtained by measuring the transmission of a large-diameter laser beam through the atomic cloud on a triggered CCD camera. The resonant imaging beam is absorbed by the atoms such that the images record the shadow cast by the atoms. We take one image I_{atom} with atoms, and another I_{ref} without atoms for reference. The atomic column density n_{2D} along the imaging axis can be calculated from the Lamber-Beer law [175]

$$n_{2D} = \frac{1}{\sigma_0} \ln\left(\frac{I_{\text{ref}}}{I_{\text{atom}}}\right) \tag{3.72}$$

where σ_0 is the resonant absorption cross section on the imaging transition. The optical density is the absorbance $\ln(I_{\text{ref}}/I_{\text{atom}})$. Sample images of atoms released from the dipole trap are shown in Fig. 3.9a). Integrating the imaged atomic density allows us to determine the atom number N_{at}, which is shown in Fig. 3.10 as a function of the MOT loading time. The loading curve is fit with an exponential saturation $N_{\max}(1 - e^{-t/\tau})$ which yields a time constant of $\tau = 0.71(2)$ s and a maximum atom number of $N_{\max} = 2.23(2) \times 10^7$. After 1 s we load about $N_{\text{at}} \approx 1.7 \times 10^7$ atoms. Absorption images in the dipole trap yield an in-situ $1/e^2$ radial waist of $w_a \approx 30$ μm. The axial $1/e^2$ waist is $l_a \approx 10$ mm. This gives an aspect ratio of about 300. For some experiments, this extreme aspect ratio and high optical depth leads to undesired atom-atom interactions and had to be reduced by selecting only the central part of the atomic cloud. This is achieved by locally de-pumping atoms into $f = 1$ at the center using a focused laser beam on the $f = 2 \rightarrow f' = 1$ transition. Then, the remaining atoms in $f = 2$ are removed by shining resonant light on the $2 \rightarrow 3$ transition using the imaging beam. Finally the atoms in $f = 1$ are re-pumped into $f = 2$. An image of the reduced cloud with half the atom number at half the original length is shown in Fig. 3.9b). The cloud-size reduction sequence takes about 0.6 ms and can be executed right before spin-state preparation to avoid atoms spreading back across the entire length of the dipole trap.

Faraday rotation Due to the high optical depth, an on axis characterization of the atomic ensemble by resonant absorption is impractical. Instead, we use the coupling beam, to measure the Faraday rotation due to the spin-polarized atomic ensemble [39, 166]. For this purpose, the spins are polarized along a magnetic field $B_z = 1$ G along the z-axis. To that end, we first pump all atoms along the vertical B-field and then adiabatically rotate the field onto the z-axis within 20 ms, allowing the spins to follow. Faraday rotation is then measured using a ms long pulse and yields a DC signal on the polarimeter. In Fig. 3.10b) we show the measured Faraday rotation angle as a function of the atom number in the dipole trap determined by absorption imaging. The data confirm the expected linear dependence of θ_F on N. From the fitted slope we determine $\alpha_1 = 1.36(1) \times 10^{-9}$, which is a factor 1/2 lower than the theoretical value for the given beam waist $w_0 = 35$ μm and detuning. This is easily explained by inhomogeneous atom-light coupling since $w_0 \approx w_a$ and potentially a mode-mismatch between the scattered field and the laser mode. More importantly, the measurement of θ_F directly provides a number for the atomic optical depth d_0 of the atomic ensemble. For the data of Fig. 3.10b) we obtain a peak optical depth of $d_0 \approx 360$, which is a very good starting point for the atom-light interface.

Faraday imaging For the purpose of aligning the coupling beam to the atomic cloud, we can also image the Faraday rotation of the coupling beam on a CCD camera (see Fig. 3.11a) [181]. The camera position is adjusted such that both the coupling beam and the image of the atomic cloud appear focused on the camera. In contrast to absorption imaging, we obtain two sets of images $I_H^{\text{atom/ref}}$ for horizontal and $I_V^{\text{atom/ref}}$ for vertical polarization component. From these two images we get information about two properties of the atom-light interaction. The scalar part of the atom-light interaction is an effective refractive index that changes the divergence of the coupling beam. We evaluate this

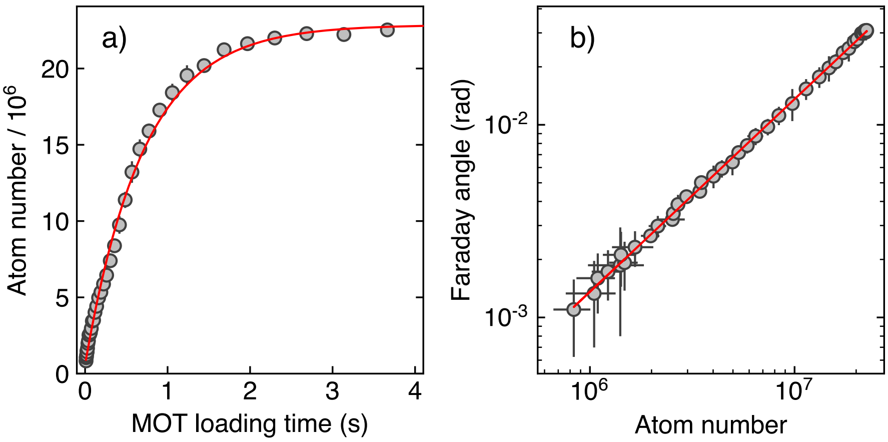

Figure 3.10: Dipole trap loading. a) Atom number as a function of MOT loading time from absorption image. b) Static Faraday rotation of the coupling beam through the on-axis spin-polarized atomic ensemble at detuning of −10 GHz.

effect by calculating

$$I_{\text{sca}} = \frac{(I_H^{\text{atom}} + I_V^{\text{atom}}) - (I_H^{\text{ref}} + I_V^{\text{ref}})}{I_H^{\text{ref}} + I_V^{\text{ref}}} \tag{3.73}$$

which evaluates spatial re-distribution of optical power, i.e. S_0. The vector part of the atom-light interaction results in Faraday rotation. The distribution of Faraday rotation angle across the laser beam can be evaluated by calculating the difference

$$I_{\text{vec}} = \frac{(I_H^{\text{atom}} - I_V^{\text{atom}}) - (I_H^{\text{ref}} - I_V^{\text{ref}})}{I_H^{\text{ref}} + I_V^{\text{ref}}} \tag{3.74}$$

This corresponds to an image of the spatial variation of the Stokes vector component S_y. Typical single-shot images I_{sca} and I_{vec} are shown in Figs. 3.11b) and c), respectively. The data are obtained at a laser-atom detuning of -2 GHz. Clearly, the atomic refractive index leads to strong focusing of the laser beam, which is shown by the positive value of $I_{\text{sca}} \approx 1$ at the center, and $I_{\text{sca}} \approx -1$ at the border of the beam (dashed line). Moreover, Faraday rotation is very strong and achieves up to 45° rotation at the center, where $I_{\text{vec}} = -1$. From the I_{vec}, we calculate the local optical depth which is shown in d) and reaches a peak value of 2000 which is consistent with an estimate based on the atom number and the transverse size of the atomic cloud. From these measurements we also see that the Faraday rotation angle, and thus the OD, is not homogeneous over the cross-section of the laser beam. Hence, the effective integrated OD over the entire laser beam is reduced to about 300 and can be optimized by choosing a laser beam waist closer to the atomic waist [154, 155]. From these measurements, we can also determine the laser beam waist (e^{-2}) was 48 μm, while the radial waist of the atomic cloud was found to be 28 μm.

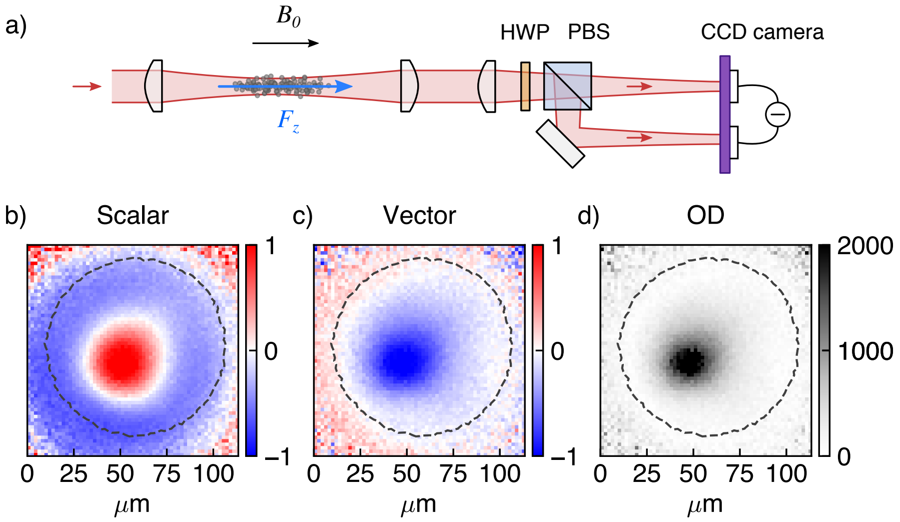

Figure 3.11: Faraday rotation imaging of a spin-polarized atomic ensemble. a) Experimental setup for imaging the polarization rotation by the atomic ensemble. b) Image of laser beam diffraction by the atomic cloud due to its scalar polarizability. c) Image of Faraday rotation due to the vector polarizability. d) Optical depth calculated from the Faraday image. The dashed line represents the e^{-2} contour of the coupling beam obtained from the reference image.

3.4 Spin-state preparation and readout

3.4.1 Optical pumping

In order to prepare atoms in a single Zeeman state $|f, m = -f\rangle$ and create a highly polarized macroscopic coherent spin with $F_x \approx -fN$, we utilize optical pumping [182] using the scheme depicted in Fig. 3.12. Two σ^- polarized optical pumping beams, one on the $f = 2 \to f' = 2$ transition and another on the $f = 1 \to f' = 2$ transition propagate vertically along the magnetic field B_0 (see inset in Fig. 3.5). As an atom scatters light from the two σ^--polarized beams, its magnetic quantum number m changes on average by -1 in every cycle of absorption and spontaneous re-emission. Since the stretched state $|f = 2, m = -2\rangle$ does not resonantly couple to σ^- polarized light it is a dark state and will become strongly populated in steady state.

In order to achieve a high optical pumping efficiency p, which we measure as the population of the target state, a high degree of circular polarization of the pumping beams is critical. Orthogonal σ^+ beams would otherwise de-populate the target state. A simple rate equation model between the final state and all neighbouring states with pumping rate γ_- and de-pumping rate γ_+ due to σ^- and σ^+ polarization, respectively, yields a steady state of $p = \gamma_-/(\gamma_- + \gamma_+)$. This means that the degree of circular optical polarization as quantified by the Stokes component S_z directly translates to the degree of spin polarization.

The shape and polarization of the pumping beams are set up in the following way. First, the Zeeman and hyperfine pumping beams are combined from two optical fibers using a fiber-based, polarization-maintaining 50:50 beam-splitter. After the fiber, the polarization is cleaned using a PBS and the beam is expanded to a cm-scale diameter to cover the entire atomic cloud. A cylindrical lens focuses it along the radial trap-axis to optimize spatial overlap with the dipole-trapped atoms. The pumping beam is combined with the vertical σ^+-polarized MOT beam in orthogonal polarization, which forces it to have σ^--polarization. Circular polarization at the atomic ensemble is adjusted using a half-wave and a subsequent quarter-wave plate before it enters the chamber. Using a home-built polarization analyzer consisting of a photodetector with rotating linear polarizer, we minimize the fringe contrast to $\sqrt{S_x^2 + S_y^2} < 0.1$, implying $S_z > 0.99$ in terms of the Stokes vector of the pumping beam. This confirms a high degree of circular polarization at this stage. It is also verified that circular polarization is preserved after the beam has traveled through the chamber. Experimentally, a real-time estimate of the pumping efficiency can be done by measuring the ringdown of spin precession and minimizing the residual modulation due to interference between different Zeeman transitions (see section 3.4.4). This proved that the pumping efficiency in our case is not limited by the purity of optical polarization, but rather by some other effect that is not entirely understood so far.

Since optical pumping takes place in a rather strong magnetic field of $B_0 \approx 3$G, the different Zeeman levels split up by several MHz. This splitting is unfavorable for the repump transition $f = 1 \to f' = 2$ since the gyromagnetic ratio γ_f in the $f = 1$ ground state is sign-reversed to that of the $f' = 2$ excited state (see Fig. 3.12). Conversely, the $f = 2$ ground state has a comparable gyromagnetic ratio as the excited state. This effect could explain why the maximum optical pumping efficiency for an inverted magnetic field

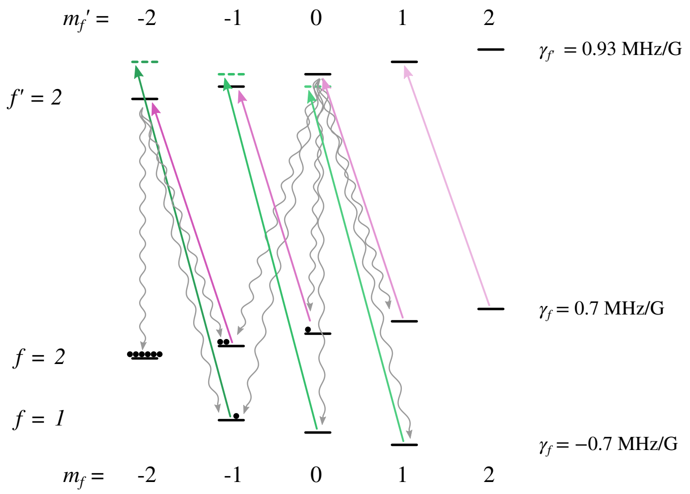

Figure 3.12: Optical pumping to the dark state $|f = 2, m_f = -2\rangle$ using σ^- polarized light on the $1 \rightarrow 2$ and $2 \rightarrow 2$ transitions. Wavy arrows representatively show possible decay channels on selected transitions, indicating that atoms in an excited state m' can fall back to any ground state with $m_f - m'_f = 0, \pm 1$.

of $B_0 = -3$ G is only $p \approx 0.7$, while we achieve $p \approx 0.9$ for $B_0 = +3$ G.

We remark that initial experiments used a re-pumping beam with isotropic polarization as it was applied via all six MOT axes. Later, we switched to the dual σ^- pumping scheme, hoping for better pumping efficiency. However, this turned out to not significantly improve the pumping efficiency.

3.4.2 Magnetic field control

Since the spin Larmor frequency is proportional to the magnetic field, it is critical to the quality of the experiment to provide a stable and homogeneous magnetic field across the entire volume of the atomic ensemble. This is achieved using a coil system centered around the atomic ensemble, which is illustrated in Fig. 3.13 and has been described already in ref. [183]. Static magnetic field offsets are compensated using three pairs of large rectangular coils of size ~ 0.7 m which provide a very homogeneous field at the atomic ensemble. Their maximum field strength is limited to 1.5 G for currents up to 5 A. To realize stronger fields, we employ two smaller, diameter 17 cm, water-cooled coils in approximate Helmholtz configuration, which can produce a field strength of up to 7 G at 3 A. In practice, we use the Helmholtz field to set a certain magnetic field offset along x, and use the compensation coil along the same direction for fine control in closed-loop mode. Closed-loop control of the magnetic field is important to ensure stability and reproducibility of the Larmor frequency, and cancel AC fluctuations at harmonics of the 50 Hz line frequency. Such a closed loop feedback has been implemented using a fluxgate magnetic field sensor[14] positioned on top of the Helmholtz coil to avoid saturation by its large field. The rather large distance between the sensor and the atoms make the setup prone to stabilization errors due to field gradients of the 50 Hz field caused

---

[14] Bartington Mag-03MCTP, range ±2.5 G

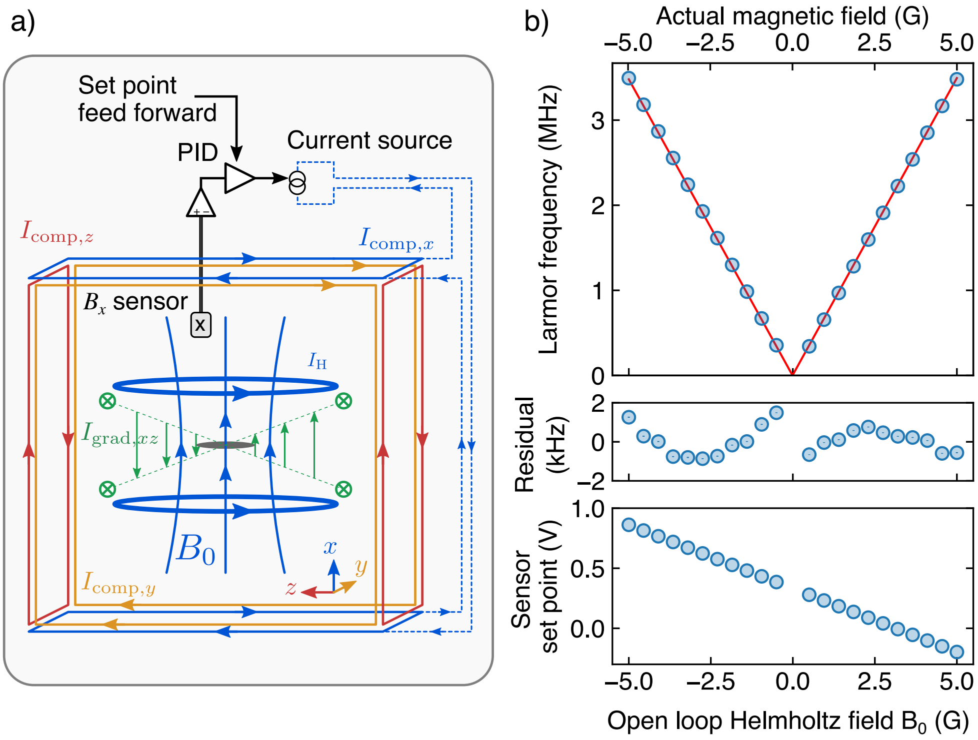

Figure 3.13: Magnetic field control of the experiment. a) Schematic of the coil setup around the atomic ensemble (grey ellipse). b) Measurement of the Larmor frequency as a function of the magnetic field in closed-loop mode. Sensor set point is adapted to the open-loop field B_0 applied using the Helmholtz coil.

by nearby situated electronic equipment. Nevertheless, we achieve a stability of the Larmor frequency of 0.2 kHz [184] that also relies on synchronizing the experimental sequence with the 50 Hz line frequency. We do not observe any detrimental effect due to the large amount of high-frequency magnetic field noise emitted by the flux-gate sensor. In the future, the flux-gate sensor can be replaced by a magnetoresistive sensor with larger bandwidth that will be positioned much closer to the atomic ensemble and should improve the magnetic field stability further.

A closed-loop calibration measurement of the spin Larmor frequency is shown in Fig. 3.13b). For any target magnetic field B_0 in vertical x-direction, the corresponding open-loop magnetic field is applied using the Helmholtz coil. For each value of B_0, we feed forward the appropriate closed-loop sensor set point to the magnetic field stabilization unit[15]. The field stabilization is only active during the spin-sensitive part of the experimental sequence, and set on hold during the MOT stage, where a large field gradient is applied. The Larmor frequency is measured by observing the ringdown of spin precession after RF excitation (see next section 3.4.4). Fitting the data with a model corresponding to equation (3.77) yields very good agreement (residuals below 2 kHz) and returns updated sensor set point values. The model also includes a perpendicular

---

[15] Physics Basel SP 962

offset field $B_\perp$, i.e. $B_0 = \sqrt{B_x^2 + B_\perp^2}$, which is independently nulled to $B_\perp < 10$ mG using independent open-loop magnetic field calibration along the perpendicular y and z axes using the compensation coils.

The above discussion has referred only to the magnetic field averaged over the full volume of the atomic ensemble. In addition, magnetic field gradients are extremely harmful to spin coherence as they lead to inhomogeneous broadening of the spin resonance. Since we apply a very strong bias field along the x-direction, only gradients of this field component are relevant, as all other field components contribute only quadratically to B_0 in lowest order. Moreover, the spatial extent of the atomic cloud is largest along the z-axis (> 1 cm) and negligible along x and y, due to the extreme aspect ratio of the dipole trap. Consequently, the most important gradient is $\partial B_x/\partial_z$. Following the method described in [185], we employ a set of four parallel wires placed symmetrically around the atomic ensemble, each carrying a current along the y-axis (see Fig. 3.13a). The combined magnetic field produced by these wires is an almost pure magnetic field field gradient $\partial B_x/\partial_z$ and allows us to cancel gradients up to several mG/cm. As a result we achieve a minimum spin decoherence rate of $\gamma_{s,0} = 2\pi \times 43$ Hz, i.e. a transverse coherence time of $2/\gamma_{s,0} \approx 7$ ms.

3.4.3 Spin Hamiltonian

To accurately describe the spin dynamics, we must consider the Zeeman effect in the presence of the Rb hyperfine structure (see Fig. 3.7 and 3.12) [163]. Strong coupling between the electron spin and nuclear spin leads to the hyperfine structure with $f = 1, 2$ manifolds and hyperfine splitting $\Delta_{\text{hf}} = 2\pi \times 6.835$ GHz. An external magnetic field $\mathbf{B}_0$ individually couples to the electron and nuclear spins with their magnetic moments $\mu_B g_j \mathbf{j}$ and $\mu_B g_i \mathbf{i}$, respectively. Here μ_B is the Bohr magneton and g_j and $g_i \ll g_j$ are the electron and nuclear g-factors, respectively. In the limit of small magnetic field, where the magnetic energy $\mu_B g_j B_0 \ll \hbar\Delta_{\text{hf}}$, one can treat the coupling between the hyperfine spin f and magnetic field perturbatively. Then, f, m are still good quantum numbers such that the magnetic field effectively couples to $\mathbf{f}$. Considering a magnetic field with B_0 applied along the x-axis, the spin Hamiltonian in a single hyperfine manifold can be expanded up to second order in B_0, giving

$$H_0 = \hbar\Omega_0 f_x + \hbar\delta\Omega_0 f_x^2 \tag{3.75}$$

Here, we have introduced the Larmor frequency $\Omega_0 = \gamma_f B_0$ with gyromagnetic ratio $\gamma_f = \mu_B g_f/\hbar \approx \pm 0.7$ MHz/G (f = 2,1) proportional to the hyperfine g_f-factor [163]. The Hamiltonian (3.75) also contains a small correction term, corresponding to a quadratic Zeeman splitting given by [186]

$$\delta\Omega_0 = -\frac{\Omega_0^2}{\Delta_{\text{hfs}}}. \tag{3.76}$$

From Hamiltonian (3.75), the transition frequency between adjacent $|f, m\rangle$ and $|f, m+1\rangle$ levels is

$$\Omega_{m,m+1} = \Omega_0 + \delta\Omega_0(2m + 1) \tag{3.77}$$

Since $\Omega_0 \sim 1$ MHz in our experiment, the quadratic correction amounts to $\delta\Omega_0/\Omega_0 \sim 10^{-3}$, which still has a measurable effect due to the narrow spin linewidth $\gamma_s/\Omega_0 \sim 10^{-4}$.

The atomic spin can be manipulated using radiofrequency (RF) magnetic fields. The interaction of a single spin with an oscillating magnetic field at frequency Ω_1 and strength V_{RF} along a transverse y-axis is given by

$$H_0 = \hbar\Omega_0 f_x + \delta\Omega_0 f_x^2 + \hbar V_{\mathrm{RF}} \cos(\Omega_1 t) f_y.$$

Qualitatively speaking, we have the following scenarios. If the RF field is resonant, $\Omega_1 = \Omega_0$, and stronger than the quadratic Zeeman splitting, $V_{\mathrm{RF}} \gg \delta\Omega_0$, it drives Rabi oscillation of $\mathbf{f}$ about the f_y axis. This allows to tilt the spin vector from f_x after optical pumping towards the f_y, f_z plane, where it precesses with full amplitude. Another regime uses a weak, continous drive with $V_{\mathrm{RF}} \ll \delta\Omega_0$. This allows the different transitions $\Omega_{m,m+1}$ to be resolved spectroscopically by tuning the RF frequency Ω_1 and thus assess the optical pumping efficiency [186].

In a rotating frame at the drive frequency Ω_1, the time evolution for the density matrix elements $\rho_{m,m'} = \langle m|\,\rho\,|m'\rangle$ is given by [186]

$$\begin{aligned}
\dot\rho_{m,m+1} &= [\mathrm{i}(\Omega_1 - \Omega_{m,m+1}) - \gamma_2]\,\rho_{m,m+1} - \frac{\mathrm{i}V_{\mathrm{RF}}}{2} C(f,m)(\rho_{m+1,m+1} - \rho_{m,m})\\
\dot\rho_{m,m} &= -\gamma_1(\rho_{m,m} - \bar\rho_{m,m}) - \frac{\mathrm{i}V_{\mathrm{RF}}}{2} C(f,m)(\rho_{m,m+1} - \rho_{m+1,m})
\end{aligned}$$

where γ_1 and γ_2 are the spin relaxation and decoherence rates, respectively. We have neglected counter-rotating terms since we assume $V_{\mathrm{RF}}, \gamma_1, \gamma_2 \ll \Omega_{m,m+1}$. The steady state attained by spin relaxation is denoted by the diagonal density matrix $\bar\rho_{m,m}$.

Pulsed regime We consider a short, resonant pulse of length τ, whose bandwidth $\tau^{-1} \gg \gamma_2, \gamma_1, \delta\Omega_0$ is much larger than the spin damping rates and quadratic Zeeman splittings. This ensures that it addresses all transitions with equal Rabi frequency $V_{\mathrm{RF}}/2$. If the pulse is much shorter than the Rabi period $\tau \ll 2\pi/V_{\mathrm{RF}}$, we can find a perturbative solution of the density-matrix time evolution. At $t = 0$, $\rho_{m,m'} = 0$ for $m \neq m'$, such that we find

$$\rho_{m,m+1}(\tau) \approx \frac{-\mathrm{i}V_{\mathrm{RF}}\tau}{2} C(f,m)\,[\Pi_{m+1} - \Pi_m] \tag{3.78}$$

with Zeeman populations Π_m of state $|m\rangle$ at $t = 0$. After the pulse, the spin precesses freely under the Larmor field giving

$$\begin{aligned}
\langle f_z(\tau + t)\rangle &= \sum_{m=-f}^{f-1} \frac{C(f,m)}{2\mathrm{i}} \rho_{m,m+1}(\tau) e^{(-\mathrm{i}\Omega_{m,m+1} - \gamma_2)t} + \mathrm{h.c.}\\
&\approx -V_{\mathrm{RF}}\tau \sum_{m=-f}^{f-1} \frac{C(f,m)^2}{4}\,[\Pi_{m+1} - \Pi_m] \cos(\Omega_{m,m+1} t) e^{-\gamma_2 t}
\end{aligned}$$

A Fourier transform of $\langle f_z(t)\rangle$ yields

$$f_z(\omega) \propto \sum_{m=-f}^{f-1} \frac{C(f,m)^2}{\gamma_2 - \mathrm{i}(\omega - \Omega_{m,m+1})}\,(\Pi_{m+1} - \Pi_m) \tag{3.79}$$

which can be used to fit observed data and extract the populations Π_m.

Continous regime Assuming weak driving $V_{\mathrm{RF}} \ll \gamma_2, \gamma_1$, we approximate $\dot{\rho}_{m,m} \approx 0$ and $\rho_{m,m} \approx \Pi_m$. Then, the steady state yields

$$\rho_{m,m+1} \approx \frac{-\mathrm{i}V_{\mathrm{RF}}}{2} \frac{C(f,m)(\Pi_{m+1} - \Pi_m)}{\gamma_2 - \mathrm{i}(\Omega_1 - \Omega_{m,m+1})} \tag{3.80}$$

and

$$\langle f_z(t)\rangle = \sum_{m=-f}^{f-1} \frac{C(f,m)}{2\mathrm{i}} \left[\rho_{m,m+1} e^{-\mathrm{i}\Omega_1 t} - \rho^*_{m,m+1} e^{\mathrm{i}\Omega_1 t}\right] \tag{3.81}$$

Demodulation of the measured spin signal at Ω_1 yields the complex amplitude

$$A(\Omega_1) = A_0 \sum_{m=-f}^{f-1} \frac{C(f,m)^2}{\gamma_2 - \mathrm{i}(\Omega_1 - \Omega_{m,m+1})} (\Pi_{m+1} - \Pi_m) \tag{3.82}$$

with some constant pre-factor $A_0 \propto V_{\mathrm{RF}}$. This is equivalent to the weak pulse result (3.79) and enables a spectroscopic evaluation of the optical pumping efficiency.

3.4.4 Spin precession measurement

The standard setup to measure spin-precession in the Faraday atom-light interface is depicted in Fig. 3.14. Manipulation of the spin state after optical pumping is done using an RF coil which produces an oscillating field along y, perpendicular to $\mathbf{B}_0$. The RF tone is derived from a function generator or lock-in amplifier and controlled via a switch such that it can be either pulsed or continuous wave. Spin precession is read out via Faraday rotation of the coupling laser beam and detected using the polarimeter. The balanced detector signal is acquired by a lock-in amplifier[16] or spectrum analyzer[17] that demodulate the signal at or close to the Larmor frequency. This delivers the in-phase I and quadrature Q components of the Faraday signal, which correspond to the rotating frame spin components $\tilde{F}_z$ and $\tilde{F}_y$, respectively. With a single half-wave plate in front of the PBS at angle ϕ, the balanced detector outputs a voltage proportional to $D = S_x \cos(4\phi) + S_y \sin(4\phi)$. Here and in the following, we assume an S_x-polarized laser beam. Hence, we first calibrate the detector sensitivity by measuring $\bar{S}_x$ in detector units setting $\phi = 0$. Then, we set $\phi = \pi/8$ such that the detector is balanced. The AC detector signal is then normalized using $\bar{S}_x$ to give the spin signal in units of the Faraday angle

$$\delta D = \frac{S_y^{(\mathrm{out})}}{\bar{S}_x} = \frac{S_y^{(\mathrm{in})}}{\bar{S}_x} + \alpha_1 F_z \tag{3.83}$$

Here, the first term is shot noise and the second is the spin signal.

Signal processing The lock-in demodulator output at frequency Ω_0 and bandwidth B is (we represent the digital signal at sampling rate $\gg B$ as continous data)

$$I = \sqrt{2}\langle \delta D \cos(\Omega_0 t)\rangle_B = \frac{\alpha_1}{\sqrt{2}} \tilde{F}_z + W_I \tag{3.84}$$

$$Q = \sqrt{2}\langle \delta D \sin(\Omega_0 t)\rangle_B = \frac{\alpha_1}{\sqrt{2}} \tilde{F}_y + W_Q \tag{3.85}$$

---

[16] Zurich instruments HF2LI

[17] Rohde&Schwarz, FSV, 7GHz

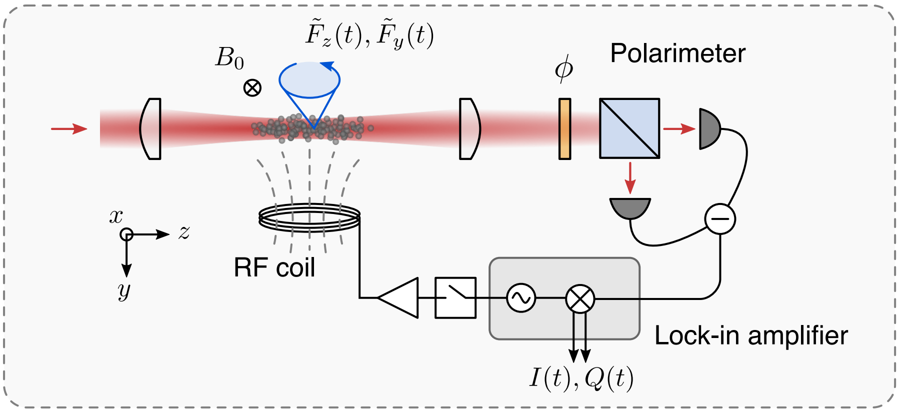

Figure 3.14: Experimental setup to measure spin-precession via Faraday rotation.

where $\langle\cdot\rangle_B$ denotes temporal averaging at bandwidth B and W_I, W_Q are the noise quadratures due to $S_y^{(\mathrm{in})}$. From this record, we typically calculate several quantities. The root-mean-squared (rms) spin signal R is given by

$$R^2 = I^2 + Q^2 = \frac{\alpha_1^2}{2}\left(\tilde{F}_y^2 + \tilde{F}_z^2\right) + W_I^2 + W_Q^2 \tag{3.86}$$

Note, that R has to be multiplied by $\sqrt{2}$ to give the peak oscillation amplitude. The quantity $R^2/\alpha_1^2|\bar{F}_x|$ is the oscillator excitation number in the Holstein-Primakoff picture. Moreover, we calculate the fast Fourier transform (FFT) of $Z = I + \mathrm{i}Q$ and obtain an estimate of its power-spectral density (PSD) [89],

$$S_{ZZ}(\omega) \approx \frac{1}{f_{\mathrm{sa}}M_{\mathrm{sa}}}|\,\mathrm{FFT}[I(t) + \mathrm{i}Q(t)](\omega)|^2 \tag{3.87}$$

where f_{sa} is the sampling rate and M_{sa} is the number of samples in the measurement record. The PSD can be used to calculate the spectral variance

$$\mathrm{Var}[Z] = \int_{\Omega_0-\Delta\omega}^{\Omega_0+\Delta\omega} S_{ZZ}(\omega)\frac{\mathrm{d}\omega}{2\pi} \tag{3.88}$$

in a certain bandwidth $\Delta\omega$ around Ω_0.

Spin precession data Examples of single-shot spin precession data are shown in Fig. 3.15. The pulse sequence to produce this data with an illustration of the spin dynamics on a sphere is given in panel a). After an optical pumping pulse (300 μs) along F_x, a short RF pulse (duration $\tau = 30$ μs and amplitude V_{RF}) is applied to rotate $\mathbf{F}$ by an angle $\theta_{\mathrm{RF}} \propto V_{\mathrm{RF}}\tau$ towards F_z. After the pulse, the probe light is switched on and the spin precession is detected using the polarimeter.

For a short pulse $\theta_{\mathrm{RF}} \approx 0.1$ and weak probing we obtain a spin signal like in panel b), where all components I, Q and R are plotted. The oscillation between I and Q is due to a small detuning between the Larmor frequency and the demodulation frequency. The rms envelope R exhibits a weak modulation due to interference of multiple Zeeman

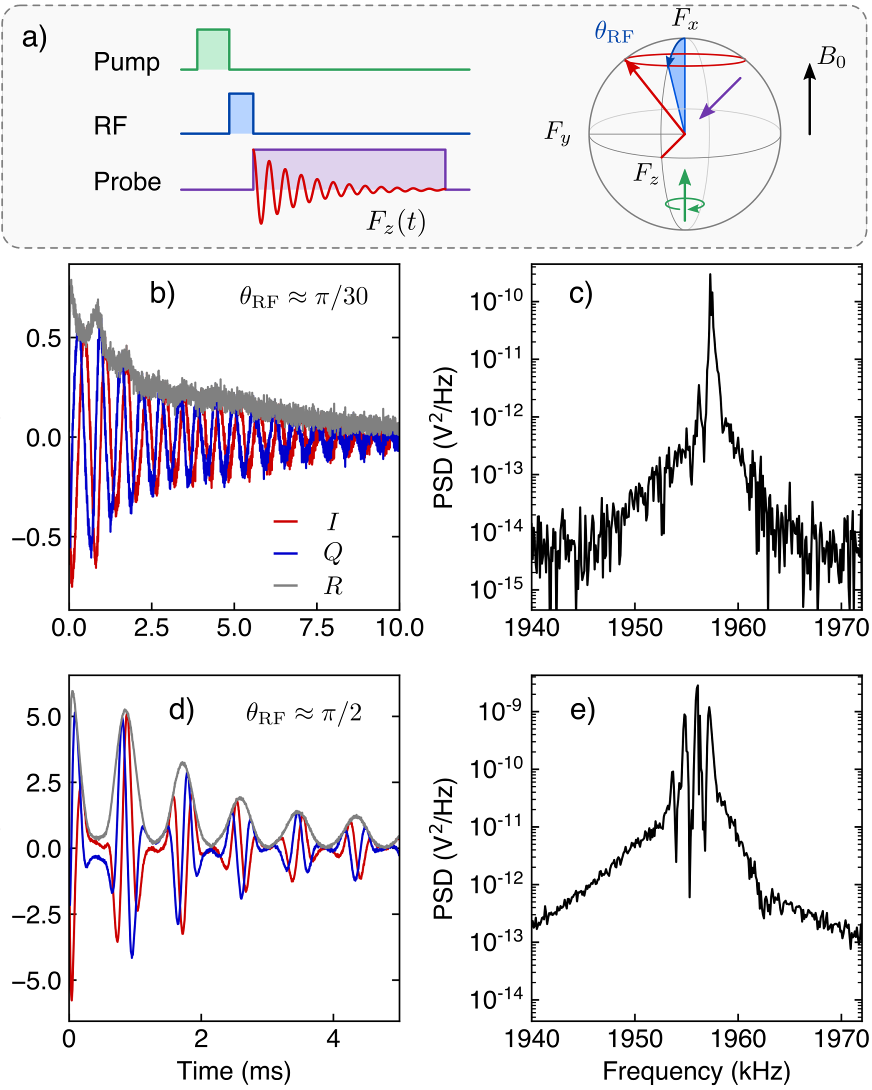

Figure 3.15: Spin precession measured by Faraday rotation. a) Pulse sequence. b) Demodulated spin signal after a weak RF pulse with $\theta_{\mathrm{RF}} \approx 0.1$. c) Corresponding PSD showing a strong peak at the Larmor frequency corresponding to the $m = -1 \to m = -2$ transition, and a weak side peak at the $m = 0 \to m = -1$ transition. d) Spin signal for a strong RF pulse with $\theta_{\mathrm{RF}} \approx \pi/2$. The spin precession shows many decays and revivals due to interference between spin components at the four Zeeman transitions. e) PSD resolving the four transition frequencies split by $2\delta\Omega_0/2\pi = 1.1$ kHz.

coherences $m \leftrightarrow m+1$ with $m = -2, -1$, split by the quadratic Zeeman splitting. Apart from that, the decay of the spin precession is almost exponential with about 3 ms coherence time. The PSD depicted in b) shows a peak at the Larmor frequency $\Omega_0 = 2\pi \times 1.957$ MHz. A small side peak to the left is indicative of the residual population in $m = -1$ and implies a pumping efficiency $\Pi_{-2} \approx 0.95$.

The effects of the quadratic Zeeman splitting become much more pronounced when an

RF $\pi/2$-pulse rotates the spin onto the equator. Such a measurement is shown in panels d) and e). The strong pulse with Rabi angle $\theta_{\mathrm{RF}} = V_{\mathrm{RF}}\tau/2 \approx \pi/2$ rotates $\mathbf{f}$ from f_x to f_z and creates a coherent superposition of all $|m\rangle$ states. The resulting Faraday signal f_z exhibits a beat-note between the different transition frequencies $\Omega_{m,m+1}$, resulting in a coherent decay and revival pattern. The power spectral density clear shows four peaks which are split by $2\delta\Omega_0 \approx 2\pi \times 1.1$ kHz, in very good agreement with the theoretical expectation from (3.76). The observed spin signals can be well fitted using the model

$$R(t) = \left| \sum_{m=-f}^{f-1} \frac{C(f,m)}{2\mathrm{i}} a_m e^{(-\mathrm{i}\Omega_{m,m+1} - \gamma_s/2)t} \right| \tag{3.89}$$

which allows to extract the spin energy damping rate $\gamma_s = 2\gamma_2$, quadratic Zeeman splitting $\delta\Omega_0$ and amplitudes a_m of the individual Zeeman coherences.

Magnetic resonance spectroscopy To directly measure the different Zeeman level populations we perform spectroscopy using a weak continous RF tone from the lock-in amplifier, that is switched on during the Faraday probe. The demodulated trace $Z = I + \mathrm{i}Q$ is then integrated over the first few ms of the pulse duration. The spin response in amplitude and phase measured in this way is shown in Fig. 3.16. It was checked that neither the integration time nor the RF amplitude significantly affect the result. Fig. 3.16 (a,b) and (c,d) correspond to low and high optical pumping efficiencies to $m = -2$, respectively. The data show the four Zeeman resonances $m \to m+1$ with $m = 2 \to 1$ shifted to lower frequency and $m = -1 \to -2$ shifted to higher frequency. A fit to each amplitude response with the function $|A(\Omega_1)|$ of (3.82) yields the pumping efficiencies $p = 0.77$ for (a,b) and $p = 0.86$ for (c,d). Using the fit parameters to calculate $\arg[A(\Omega_1)]$ correctly reproduces the phase response in Figs. 3.16c and d. In order to extract the population of $m = -2$, we assume $\Pi_{+2} \approx 0$ given the absence of the $2 \to 1$ transition in the data. Then, the other populations result from cumulatively summing the fitted, non-normalized population differences $\propto \Pi_{m-1} - \Pi_m$ starting from $m = 2$, and normalizing in the end. The spectroscopic method has proven to consistently deliver lower optical pumping efficiencies than fitting the spin precession envelope or FFT after a weak pulse like in Fig. 3.15b,c), even though they should be equivalent. A possible explanation might be that the time-domain spin signal is modified by the probe light. For example, the data in Fig. 3.15b) exhibit a rather strong modulation due to interfering Zeeman coherences at short times, which then vanishes such that only an exponentially decaying tail remains. It has to be investigated further under which conditions the two methods give identical results. Analysis of the time-domain signal would enable a much faster characterization than spectroscopy.

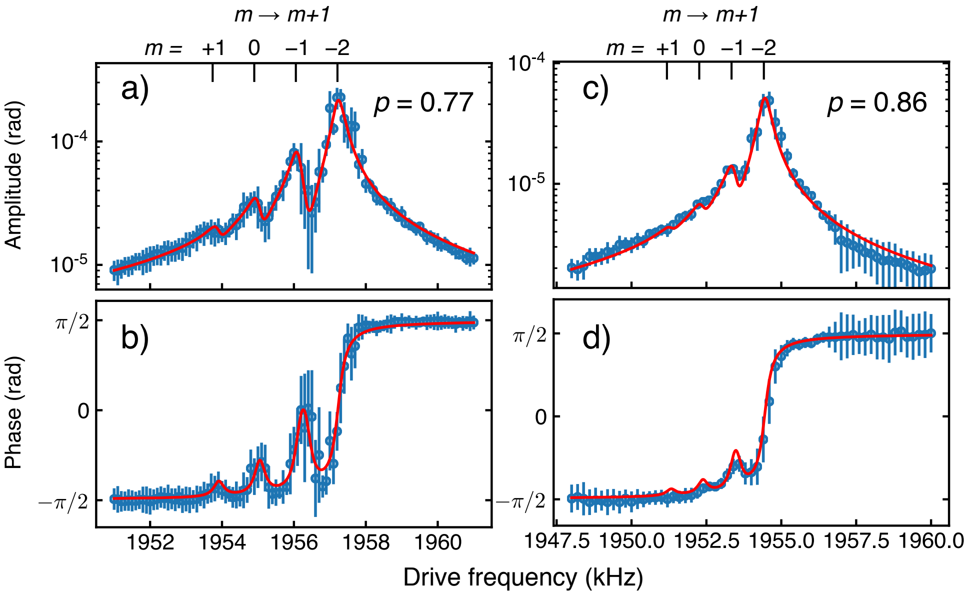

Figure 3.16: Measurement of the magnetic response of the spin ensemble. The two data sets in (a,b) and (c,d) show the amplitude response (a,c) and phase response (b,d) of the spin to a magnetic RF drive with two different optical pumping efficiencies. The extracted populations p of the $m = -2$ level are given in the plots.

3.5 Characterization of the spin-light interface

In order to characterize the Faraday spin-light interface, we have investigated the following topics: (i) characterization of the probe-induced tensor light-shifts, (ii) measurement of the Faraday rotation angle and light-induced spin damping rates, (iii) measurement of the spin response to an optical modulation.

3.5.1 Light shifts

From the discussion of the atomic polarizability tensor we expect that the linearly polarized probe laser induces a quadratic shift of the different Zeeman transitions $m \to m+1$ by an amount $\delta\Omega_2(2m+1)$. The strength of this shift $\delta\Omega_2 \propto (3\cos(2\theta)+1)$ depends on the angle θ between the laser field $\mathcal{E}_L$ and the transverse magnetic field B_0 (see Fig. 3.17). In Fig. 3.17 this effect is illustrated at the three polarization angles $\theta = 0°$ (panel a), $\theta = 90°$ (panel b) and $\theta = 51°$ (panel c), measured at a detuning $\Delta = -2\pi \times 20$ GHz and beam waist $w_0 = 50$ μm. Here, density plots of the spin PSD are shown, with Fourier frequency on the horizontal axis, and probe laser power on the vertical axis (logarithmic scaling). In these experiments, the spin is tilted by almost $\pi/2$ using a strong RF pulse, which creates a superposition of the four Zeeman coherences that are clearly distinguishable in the PSD. At low power, the splitting is only due to the quadratic Zeeman effect $\delta\Omega_0$. When probed with increasing laser power, the tensor light shift changes the splitting. For $\theta = 0$ (a) we observe a strong increase of the quadratic splitting, reaching up to 3 kHz at the largest power. On the contrary, at $\theta = 90°$ the tensor light shift acts against the quadratic Zeeman effect such that all lines merge at the highest powers. The last data set is measured at $\theta = 51°$ where the laser only induces very weak increase of the splitting. In all measurements, the data also show an increase of the spin linewidth due to spontaneous emission. These observations agree with the expectation that $\delta\Omega_2 = \alpha_2\Phi_L(3\cos(2\theta)+1)/2$ at the peak optical intensity. We extract the angle-independent prefactor $\delta\tilde{\Omega}_2 = \alpha_2\Phi_L$ by fitting the spectra of similar measurements, where only the $-2 \to -1$ transition is excited. The results of the extracted tensor light shift $\delta\tilde{\Omega}_2$ and linewidth γ_s are shown in Fig. 3.17d). The fitted linear slope 1.5 Hz/μW of $\delta\tilde{\Omega}_2$ agrees well with the theoretical value. The fitted linewidths also agree with the expression $2\alpha_0 S_0\gamma_e/\Delta$ which holds at the peak intensity. With the rather wide probe beam used in these experiments, most atoms are at the probe beam focus, which also explains why the tensor light shift does not leads to strong inhomogeneous broadening. The observed linewidth of 200 Hz at low power is limited by residual magnetic field fluctuations.

As a consequence of these measurements, we used a laser polarization of $\theta = 55°$ in all subsequent experiments to avoid inhomogeneous broadening and power-dependent Larmor frequency. An interesting result of these measurements is that the tensor light shift could be exploited to exactly cancel the quadratic Zeeman splitting if a purely linear spin Hamiltonian is required.

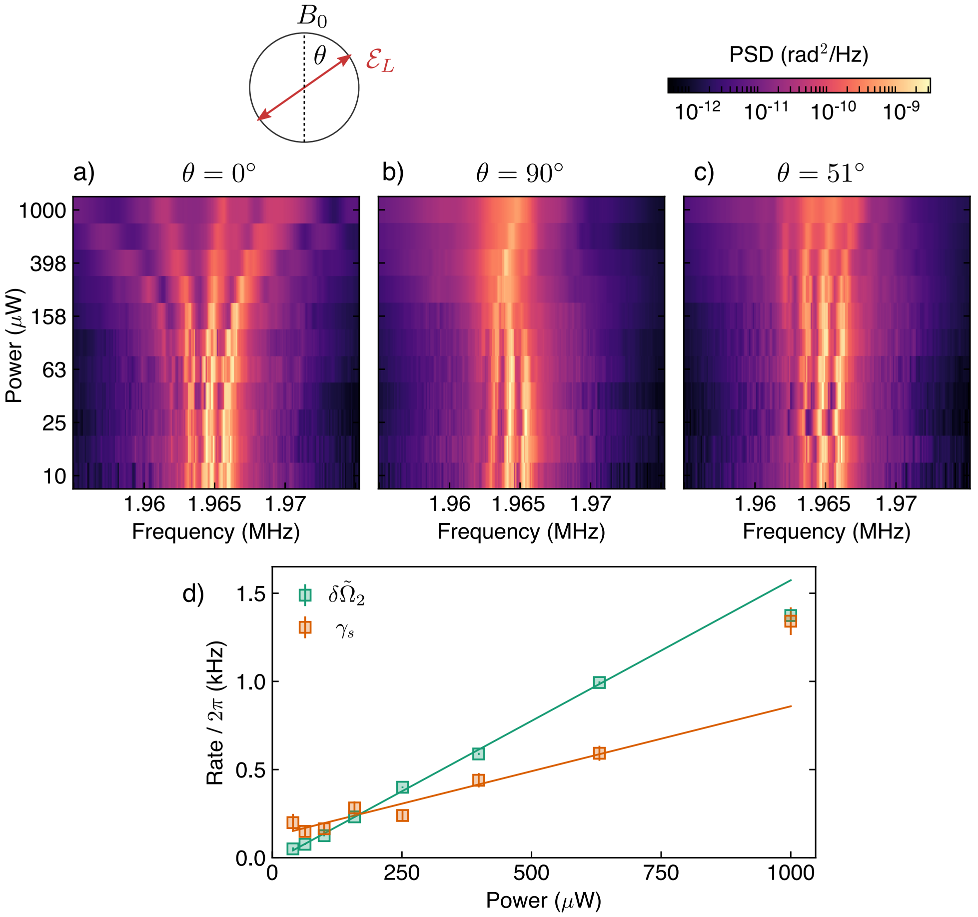

Figure 3.17: Measurement of tensor light shift. Spin FFT vs optical power at a) $\theta = 0°$ (vertical polarization), b) $\theta = 90°$ (horizontal polarization), and c) $\theta = 51°$. d) Fitted tensor light shift and spin linewidth as a function of optical power.

3.5.2 Light-induced decoherence

The most important aspect of the spin-light interface are the optical depth and the light-induced damping rate. In Fig. 3.18a) we determine the optical depth d_0 by measuring the Faraday angle for different laser detunings Δ. We determine the detuning relative to the $f = 2 \to f' = 3$ transition using a wave-meter. In this measurement, the collective spin is first optically pumped along B_0 such that $\bar{F}_x \approx 2N$, and then rotated onto F_z using an RF $\pi/2$ pulse. The Faraday angle is then determined as the peak spin precession amplitude $\theta_F = R_{\max}/\sqrt{2} = d_0\gamma_e/(8\Delta)$. Our chosen detunings ($> 5$ GHz) are large enough to comply with the asymptotic $1/\Delta$ dependence. We fit the data with this model (red line) and obtain $d_0 = 205(8)$. We notice a slight asymmetry between red ($\Delta < 0$) and blue detunings ($\Delta > 0$). The increase of θ_F for $\Delta < 0$ could imply an improved confinement of the atoms at the peak intensity of the probe laser beam due to the additional trapping potential produced by its scalar light shift. For blue detuning the resulting anti-trapping potential would oppose the dipole trap potential and de-confine the atoms. The observed optical depth is smaller by 0.4 than the theoretical value $N\sigma_\pi/A \approx 500$ for the beam waist $w_0 = 50$ μm and atom number $N = 2 \times 10^7$. This implies that an effective atom number $N_{\text{eff}} = 8 \times 10^6$ results from the inhomogeneous beam profile across the entire atomic ensemble.

Next, we also measure the light-induced spin (energy) damping rate γ_s for detunings in the range ±5 to ±70 GHz like in Fig. 3.18a) and optical powers between 50 and 1000 μW. Fitting the measured rms spin signal after an RF $\pi/2$ pulse using the model of equation (3.89), we can determine the spin damping rate γ_s for every setting. Since

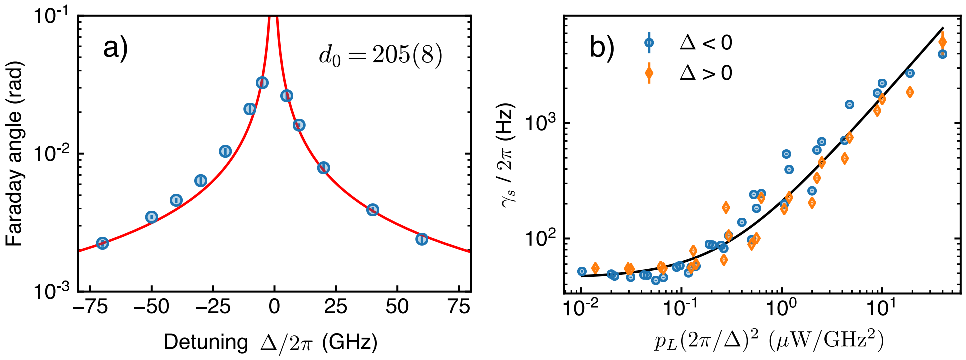

Figure 3.18: a) Measurement of Faraday rotation angle as a function of detuning for $N_{\text{at}} = 2 \times 10^7$, measured as the peak oscillation amplitude after an RF $\pi/2$ pulse. b) Light-induced spin damping rate from fitting the spin oscillation envelope. Nominal beam waist was $w_0 = 55$ μm. From the fit to the damping rate we extract an effective beam waist of $w_0 \approx 46$ μm. Note the slight discrepancy between red and blue detunings, smaller Faraday rotation and lower damping for blue detuning. This can be explained by the fact that blue detuned laser light anti-traps the atoms (scalar shift) opposite to that of the dipole trap. Hence, the atom-light overlap is reduced. Red-detuned light makes the trap deeper. Intrinsic spin damping rate is found to be $\gamma_{s,0} = 2\pi \times 43$ Hz.

we expect spontaneous emission to produce a decoherence rate $\gamma_{\mathrm{sc}} \propto p_L/\Delta^2$, where p_L is laser power, we plot the fitted γ_s vs $p_L(2\pi/\Delta)^2$ in Fig. 3.18b). Data points for red and blue detunings are distinguished as blue circles and yellow diamonds, respectively. The data are well fitted by a model $\gamma_s = \gamma_{s,0} + a p_L/\Delta^2$. Here, $\gamma_{s,0} = 2\pi \times 43$ Hz is the intrinsic spin dephasing rate and $a = \sigma_\pi \gamma_e/(4\pi w_{\mathrm{eff}}^2\, \hbar\omega_L)$ is a prefactor from which we determine the effective beam waist $w_{\mathrm{eff}} = 46$ μm. This is in good agreement with the beam waist of 48 μm determined from a camera image. By comparison of the data for red and blue detuning we see a clear tendency for increased damping at red detuning compared to blue detuning. This is consistent with our previous discussion that the atoms are confined at higher optical intensity for red detuning than for blue detuning. The close agreement between the effective beam waist and the measured waist indicate that our system operates under close to ideal conditions, where spontaneous emission is the limiting spin damping mechanism.

3.5.3 Optical response

In all measurements presented so far, spin precession has been excited using an external RF magnetic field. This corresponds to a magnetometry application rather than a quantum optics application. The coupling strength from light to atoms can be quantified by measuring the spin's response to an optical input. Since the Faraday interaction couples F_z to S_z, we have to create a circularly polarized modulation, which could in principle be accomplished using a suitable electro-optic polarization-modulator. Here, we choose an optical interferometer containing an electro-optic phase-modulator (EOM) to generate S_z modulation as already described in section 2.5.2 (see Fig. 3.19a). This has the additional benefit that the laser polarization is not degraded by the EOM. The degree of phase-modulation over amplitude-modulation was determined to be better than 10^4. Moreover, this setup emulates a one-way coupling from the optomechanical system to the spin, with the membrane replaced by the EOM.

The experimental setup is depicted in Fig. 3.19a) and can be described using the same transfer-matrix formalism as presented in section 2.7. The only difference is that the interferometer involves two orthogonal polarizations instead of two spatial modes. Consequently, setting the phase of the detected quadrature of the probe mode is accomplished using wave-plates. Here, we give a brief picture using the Stokes vector formalism. Note, that the EOM also produces some phase modulation of the laser field, which we neglect because neither does it couple to the spin nor does it contribute to the detector signal. After the interferometer output, the Stokes vector is $\mathbf{S}^{(\mathrm{in})}$, with $\bar{S}_x = \Phi_L/2$ and $\bar{S}_z = \beta_0 \bar{S}_x \cos(\Omega_1 t)$ with modulation depth $\beta_0 \sim 10^{-4}$ and modulation frequency Ω_1. The atom-light interaction leads to the following input-output relations for the light field,

$$\begin{pmatrix} S_x^{(\mathrm{out})} \\ S_y^{(\mathrm{out})} \\ S_z^{(\mathrm{out})} \end{pmatrix} = \begin{pmatrix} S_x^{(\mathrm{in})} \\ S_y^{(\mathrm{in})} + \alpha_1 \bar{S}_x F_z \\ S_z^{(\mathrm{in})} \end{pmatrix} \tag{3.90}$$

The polarimeter first uses a QWP at 45° relative to the laser polarization to rotate $S_x \to -S_z$, $S_z \to S_x$. The subsequent HWP at angle ϕ relative to the QWP axis implements a rotation by 4ϕ about S_z, i.e. it leads to

$$\mathbf{S}^{(\mathrm{det})} = \begin{pmatrix} S_z^{(\mathrm{out})}\cos(4\phi) - S_y^{(\mathrm{out})}\sin(4\phi) \\ S_y^{(\mathrm{out})}\cos(4\phi) + S_z^{(\mathrm{out})}\sin(4\phi) \\ -S_x^{(\mathrm{out})} \end{pmatrix} \tag{3.91}$$

The detector measures $S_x^{(\mathrm{det})}$. Solving the equations of motion for the spin, we find

$$F_z(\omega) = \chi_s(\omega)\alpha_1 \bar{F}_x S_z^{(\mathrm{in})}(\omega) \tag{3.92}$$

in response to the modulation. Here, the spin susceptibility

$$\chi_s(\omega) = \frac{\Omega_s}{\Omega_s^2 - \omega^2 - \mathrm{i}\gamma_s\omega} \tag{3.93}$$

is equivalent to that of a mechanical oscillator. Putting everything together, we find that the modulation in $S_z^{(\mathrm{in})}$ is transduced to the detector with transfer function

$$h_{S_z}(\omega) = \cos(4\phi) + 4\Gamma_s\chi_s(\omega)\sin(4\phi) \tag{3.94}$$

which describes the interference between the directly detected S_z modulation and that filtered by the spin. The same transfer function can also be considered for ponderomotive squeezing [187, 77, 78], where $S_z^{(\mathrm{in})}$ is pure vacuum noise, and also vacuum noise from $S_y^{(\mathrm{in})}$ has to be taken into account.

In the experiment, we choose $4\phi = 50°$ for a near-equal amount of S_y and S_z detection, and apply a continous modulation to the EOM during the Faraday probe. Here, the detuning is $\Delta = -2\pi \times 15$ GHz and the beam waist is $w_0 = 35\ \mu$m. Fig. 3.19b) shows measurements of the spin amplitude response for four different optical power levels between 100 μW and 1 mW. Like in the magnetic response measurement, the individual measurement records are demodulated at the drive frequency and integrated in time to obtain the response. The curves are vertically offset for clarity and demonstrate the characteristic interference between the directly detected modulation and the spin's response, which are in phase below resonance and out-of-phase above resonance. Fits to the data using the model $|h_{S_z}|$ from equation (3.94) including a scaling factor are shown as lines and agree very well with the data. From the fits we obtain the spin measurement rate Γ_s and damping rate γ_s as fit parameters, which are plotted in Fig. 3.19c) as a function of optical power. Both rates are expected to linearly increase with power. The fitted parameters are compared with calculations (dashed lines) based on the experimental parameters. For the measurement rate Γ_s we get good agreement up to 500 μW optical power with a rather low effective atom number $N_{\mathrm{eff}} = 5 \times 10^6$, which could be due to a relatively low optical pumping efficiency in this measurement, and a small, deliberate angle (0.4°) between the laser beam and the atomic cloud (see section 4.2.3). However, the fitted damping rates are about a factor 4 higher than the theory values. To confirm that the linear response model is appropriate, we verified that the data are reproduced when reducing the modulation strength β_0 by 1/10. Although the observed spin damping rates are currently not understood, this measurement confirms the coherent interaction between the collective spin and the optical field, with a coupling strength Γ_s that is enhanced by the atom number N.

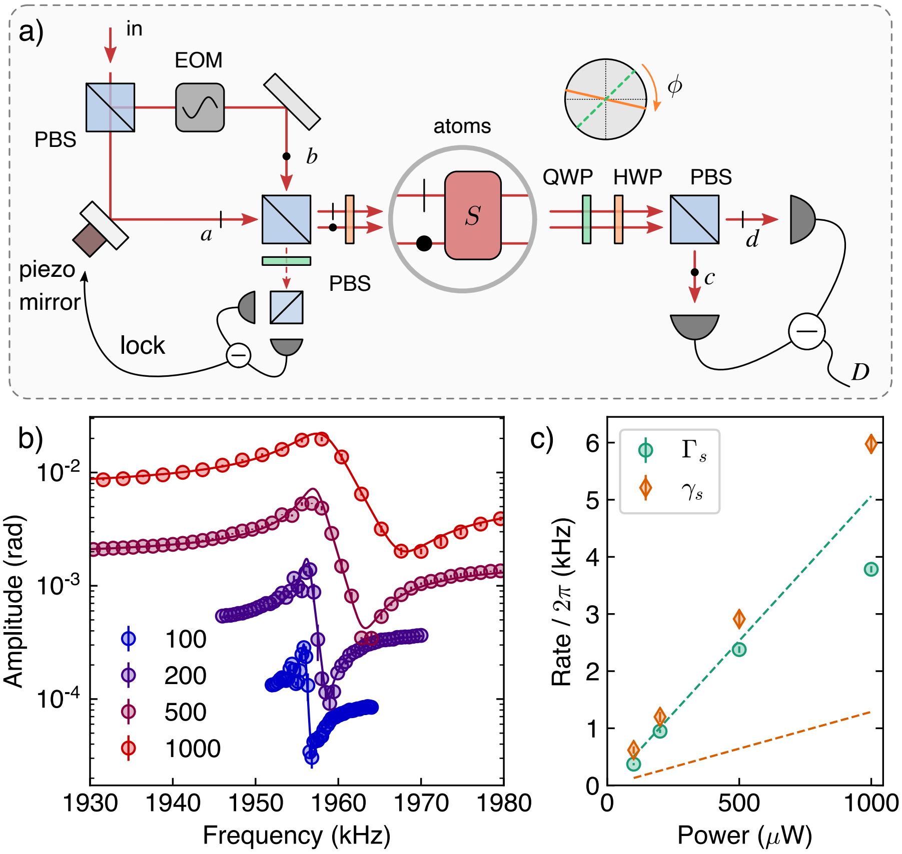

Figure 3.19: Measurement of spin optical response. a) Experimental setup to create a modulation of S_z using an EOM in a polarization interferometer, and measure the response of the spin to this modulation. b) Amplitude of the spin response measured at different optical powers indicated by the legend values in μW. The curves are vertically offset for clarity. Lines are fits based on the model given in the text. c) Measurement rate and damping rates extracted from fits to the data in b). Dashed lines are theoretical expectation for $N = 5 \times 10^6$.

3.6 Collective effects

While characterizing the spin-light interface, it was soon discovered that the spin dynamics under the effect of the probe light cannot be described like a simple damped oscillator any more. This becomes most obvious when measuring spin noise without applying any prior excitation pulse. Given the large optical depth of the atomic ensemble, one would then expect the spin dynamics to be dominated by the intrinsic quantum spin noise [44] and quantum back-action due to the optical input field [89, 31]. However, when we spin-polarize the ensemble and switch on a strong probe beam, we observe that the light triggers large amplitude dynamics, which cannot be understood in the context of an oscillator driven by quantum back-action.

The data in Fig. 3.20a) show rms spin dynamics observed for different atom numbers between $N = 3 \times 10^6$ and $N = 2 \times 10^7$, using a probe beam with waist of 35 μm at a power of $p_L = 1$ mW and detuning $\Delta = -2\pi \times 15$ GHz. In these measurements, the atomic ensemble is first spin-polarized along the magnetic field using optical pumping and the probe laser beam is switched on immediately afterwards. In the time domain data (left panel), we observe a transition from an exponential decay of the spin noise at the lowest atom number, to a burst-like behaviour with fast decay for the larger atom numbers. The burst amplitude appears to grow nonlinearly with atom number. The initial spin amplitude at $t = 0$ can be explained by the fast rise time 100 ns of the optical pulse, which excites the spin due to the tensor coupling. In the PSD shown on the right, the nonlinear dependence of scattered light on atom number is even more striking. As the atom number increases by 7, the peak PSD $S^{(\mathrm{out})}_{XX,L}$ increases by about 5×10^3. This huge increase cannot be explained by quantum back-action, as one would only expect an increase by only ≈ 50. If the spin were modeled as an oscillator driven by an intrinsic force F_s and quantum back-action due to the optical input field (compare equations (3.68)), one would expect the following PSD of the output field X_L (normalized to shot noise),

$$2\bar{S}^{(\mathrm{out})}_{XX,L} = 1 + 16\Gamma_s^2|\chi_s(\omega)|^2 + 16\gamma_s\Gamma_s|\chi_s(\omega)|^2\bar{S}_{FF,s} \tag{3.95}$$

The three terms on the right are shot noise, quantum back-action noise, and intrinsic spin noise. Back-action noise originates from the spin being driven by optical vacuum noise and scales with $\Gamma_s^2 \propto p_L^2 N^2$. The spin noise term can in principle contain any other effect, such as spin thermal noise and zero-point fluctuations, but also other terms arising due to collective interactions between atoms. The data presented in Fig. 3.20a) clearly show a scaling of the spin-noise beyond what can be expected from quantum back-action.

While the data in Fig. 3.20a) were obtained at fixed laser power $p_L = 1$ mW and varying atom number, we have also measured the spin dynamics for fixed atom number $N = 2 \times 10^7$ and varying laser power. These data are presented in Fig. 3.20b). In the time domain, the burst is again observed and accelerates with increasing power. Here the time it takes to reach the maximum spin signal is inversely proportional to laser power, while the peak signal only rises for the highest powers. Since optical power also increases the light-induced damping rate, the bursts also become shorter. In the frequency domain this behaviour is reflected by a strong broadening of the initially very

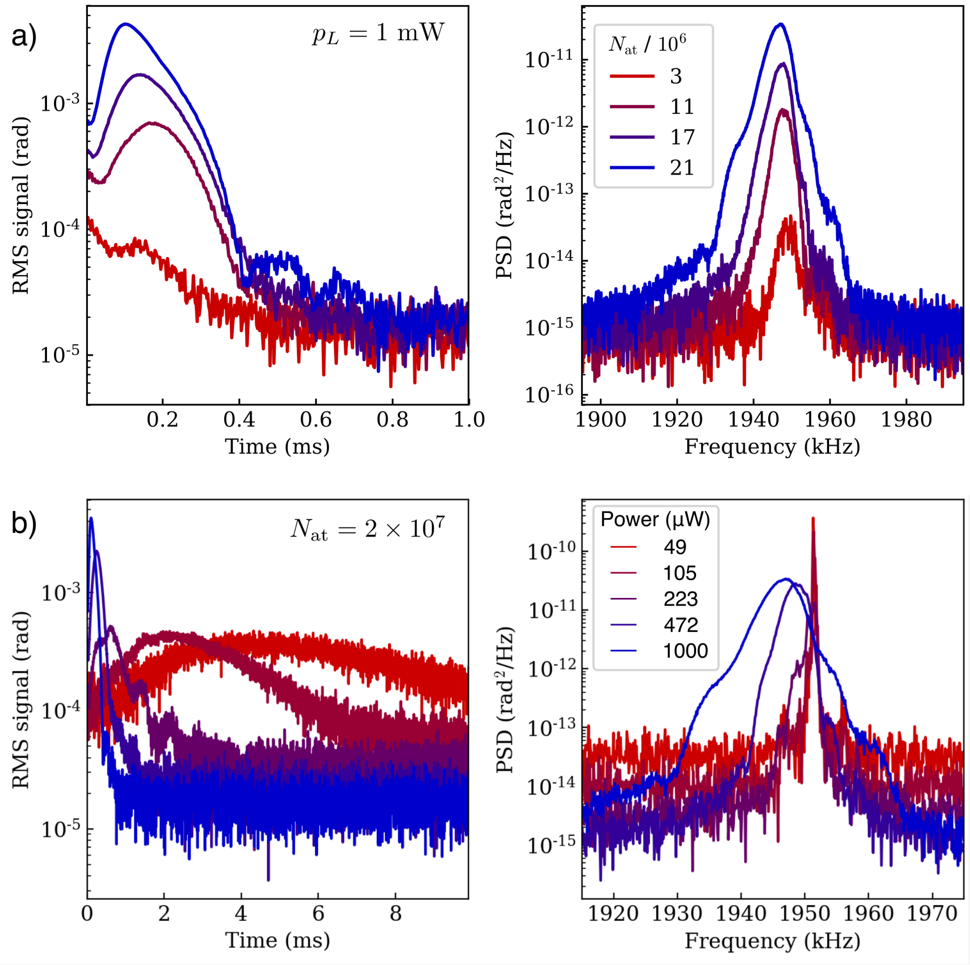

Figure 3.20: Observation of collective spin dynamics. a) Spin noise under the influence of probe light as a function of atom number. Shows nonlinear increase of rms signal with atom number. PSD also shows $\times 10^3$ increase for $\times 10$ increase of atom number. b) Dynamics under varying laser power, show speed up of the burst.

narrow spin resonance. Moreover there is a power-dependent shift of the peak frequency, which is also present in panel a), but weaker. As the spin damping rate increases, the resonances of the different Zeeman transitions start to overlap, which faciliates larger amplitude spin dynamics stretching over the full $f = 2$ hyperfine manifold. At low power, these transitions are split by about 1 kHz due to quadratic Zeeman splitting such that a weak drive is limited to the first transition. It should be investigated how these dynamics change as a function of magnetic field, with varying quadratic splitting.

At the current state of knowledge it is clear that the observed dynamics are not due to some parasitic driving of the spin due to laser or magnetic field noise. Instead, we believe that they are caused by collective atomic scattering (see Fig. 3.21) which leads to an effective long-range interaction between atoms. Since the atomic ensemble has an extreme aspect ratio and a very high optical depth, it seems plausible that the atoms cannot be treated independent any more, but start to interact via the light field. A

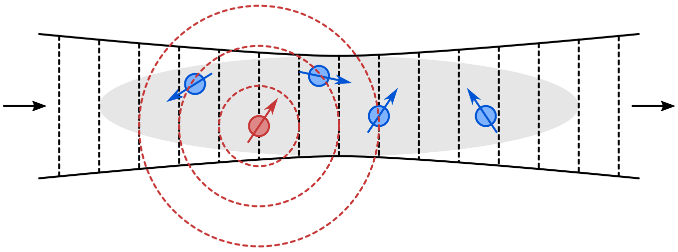

Figure 3.21: Illustration of collective scattering between spins in the atomic ensemble. The wave fronts of the laser beam are drawn as black dashed lines. One spin (red) scatters a spherical wave which is seen by other spins (blue), thus creating collective dynamics.

rough estimate of the peak density in the ensemble with atom number $N = 2 \times 10^7$, waist $w_a = 30\ \mu\text{m}$ and length $l_a = 10$ mm gives

$$n_0 = \left(\frac{2}{\pi}\right)^{3/2} \frac{N}{w_a^2 l_a} \approx 1 \times 10^{12}\ \text{cm}^{-3} \approx \frac{1}{2}\frac{1}{\lambda^3} \tag{3.96}$$

which implies that the diluteness condition of the cloud $n_0\lambda^3 \ll 1$ is not satisfied any more.

Collective scattering in high density atomic clouds is known to generate optically-induced dipole-dipole interactions or superradiance [148, 149]. Superradiance [156, 157, 188] occurs when all atoms are prepared in the excited state and the spontaneous emission by one atom stimulates the cascaded emission of all other atoms. This leads to high fluorescence rates proportional to N^2, and is currently exploited for the development of superradiant lasers [158, 189]. In our experiment, the involved atomic states are not ground and excited states, but in the simplest picture two different ground state sublevels, which are coupled by two Raman transitions. This configuration has been analyzed by Roth [171], where it has been shown that superradiance can also occur for such a scheme. Essentially, the only requirement is that photons emitted by one atom can be scattered by the other atoms in the ensemble. For the Faraday interaction, however, this is not the case, because the light scattered by one atom is in S_y polarization, and does not couple to other atoms via the Faraday interaction. This can only be achieved with a significant tensor polarizability, i.e. at low detuning. However, we observe that the effect persists even at very large detunings > 10 GHz and is observed independent of laser polarization. If the tensor polarizability caused this effect, it would exhibit a strong dependence on polarization [171]. These considerations seem to rule out superradiance as the cause of this effect.

However, this reasoning is still based on the effective 1D model presented in the beginning of this chapter. In reality, the scattered field by one atom is a spherical wave (s-wave) and only the collective field scattered by the elongated atomic ensemble can be approximated as a paraxial mode in the far-field (see Fig. 3.21). Consequently, the effective 1D model is not suitable for describing collective effects of multiple light scattering in the near-field inside the atomic ensemble. Hence, understanding effects like superradiance or optically-induced dipole-dipole interactions between the atoms [149, 172] need a different level of theory.

For future investigations, we summarize here the observations that have been made during this thesis:

- The effect is only observed with the spins initialized parallel to the magnetic field. If spins are flipped by an RF $\pi/2$ pulse, spin decay corresponding to an independent spin model is preserved. This points to an effect that depends on the relative alignment of the spins. Orientation orthogonal to trap axis appears unstable towards collective dynamics, while orientation parallel to trap axis is stable. There seems to be a similarity to dipole-dipole interactions [190, 4].

- Collective dynamics get stronger when tensor-light shift cancels the quadratic Zeeman splitting such that all transitions are resonant and complete spin flips can occur. The magnetic field strength B_0 directly determines the size of the quadratic Zeeman splitting. It should thus be investigated how B_0 affects the dynamics.

- Feedback due to optical back-reflections enhances the effect at small detunings. This has been reduced as much as possible in the presented measurements.

- The effect gets weaker with reduced cloud length. Data that compare spin noise for different atomic cloud geometries are shown in Fig. 3.22. Absorption images of the long and short clouds are depicted in Figs. 3.9 a) and b), respectively. The data for a long cloud with $N = 16 \times 10^6$ shows strong noise. Two other data sets are shown, both with $N = 7 \times 10^6$. The second measurement (purple) uses a reduction of the cloud length to reduce atom number while for the third measurement less atoms were loaded into the full trap. The collective dynamics are strongly reduced for smaller N, but no clear difference is seen between short and long cloud at the same atom number. Since the collective dynamics are suppressed for both the shorter cloud with same density and the long cloud with lower density, it seems that the effect scales with optical depth and not atomic density.

- The effect persists at large detuning, it is thus not entirely explained by tensor polarizability, although tensor polarizability might play a role. One should investigate $\theta = 45^\circ$ laser polarization, where the cross-coupling between Faraday and tensor interaction could lead to collective effects.

- Negative feedback in double-pass interaction appears to cancel the dynamics, which is consistent with the picture of spins interacting via the light field.

- A larger angle between the laser beam and the atomic cloud decreases the size of collective dynamics. However, this also reduces the effective optical depth.

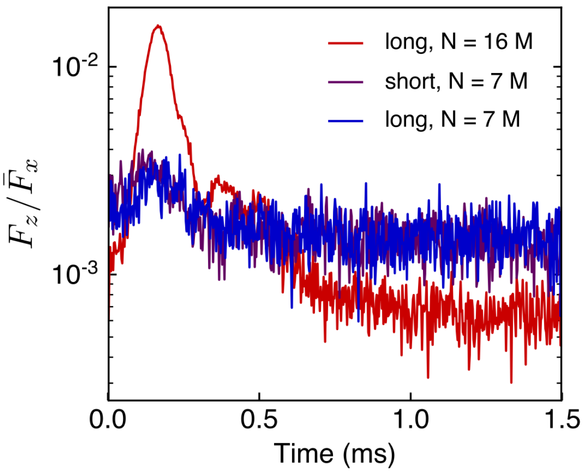

Figure 3.22: Spin dynamics for different cloud geometries. The vertical axis is $F_z/\bar{F}_x$ allowing better comparison between different atom numbers.

3.7 Conclusion

In this chapter, we have presented an interface between the polarization state of light and the collective spin of an atomic ensemble using the Faraday interaction. The atomic ensemble is trapped in an optical dipole trap at a temperature of $\sim 50\ \mu\text{K}$ and contains up to 20 million Rb atoms. This enables a very high optical depth of ~ 300 as measured by Faraday rotation of the spin-polarized ensemble. Images of the Faraday-rotated laser beam show that the peak optical depth reaches up to 2000. These numbers are very promising for atom-light interfaces because the cooperativity is proportional to the optical depth.

By providing a homogeneous and stable magnetic field we achieve spin coherence times up to ~ 7 ms. Due to residual magnetic field fluctuations, the spin linewidth is broadened to 200 Hz, which can be further reduced by improving the closed-loop magnetic field stability. Probing the spin with an off-resonant light field adds certain decoherence mechanisms. By tuning the angle between the laser polarization and the magnetic field, we have characterized and minimized tensor-light shifts induced by the laser. In this setting we found that the probe-induced spin damping is accurately modeled by off-resonant spontaneous emission. This means that the spin is well protected from technical noise. Finally, we have characterized the spin-light interaction by measuring the optical response of the collective spin subject to a modulation of circular polarization. This measurement showed good agreement with a theoretical model of the full experiment. The extracted spin measurement rate could be explained with a slightly reduced atom number due to the inhomogeneous atom-light coupling. However, the observed damping rate was too large by a factor of four, an effect that could not be explained.

Finally, we reported on the observation of strong collective spin dynamics induced by the laser field. We observed highly nonlinear dependence of spin noise on the atom number. The dynamics bear some similarities with superradiant scattering or optically-induced dipole-dipole interactions, but cannot be explained by the simple 1D model for the atom-light interface. In order to minimize these effects, we reduced the length of the atomic cloud by about two, which also reduces the optical depth by the same amount. However, it maintains a similar atomic density at the focus of the laser beam.

CHAPTER 4

Spin-optomechanical interface

This chapter explains the experimental setup that is used to generate strong light-mediated coupling between the membrane and the atomic spin ensemble using cascaded interactions with a double-pass interaction of the spin. It can be read stand-alone or as supporting information for the subsequent chapter, which describes the main experimental results. The first section covers the theory of the optical spin-membrane interface. Next, a detailed analysis of the double-pass spin-light interface is presented. Next to theoretical results, this also includes data which demonstrate the destructive interference of spin signal in the output field, which is a necessary requirement for quantum back-action cancellation in the hybrid spin-membrane system. Finally, the light-coupled dynamics in the spin-membrane system is analyzed theoretically, and conditions for entanglement generation are derived.

4.1 Optical interface between an optomechanical and an atomic spin ensemble

In the last two chapters we have presented individual optomechanical and spin-light interfaces, whose light-matter interactions can both be cast into the form ($k = s, m$)

$$H_{\text{int}} = \hbar\sqrt{4\Gamma_k}X_k X_L^{\phi_k} \tag{4.1}$$

with a measurement rate Γ_k, a system quadrature X_k and a field quadrature $X_L^{\phi_k}$ determined by a phase ϕ_k. This simplified description implies that it is straightforward to interface both systems by sending the light field between them like it has been described on an abstract level in chapter 1. However, the above description is actually too simple because (i) the fundamental light-matter interactions are not linear, and (ii) the optomechanical interaction involves the displaced optical amplitude and phase fluctuations while the spin-light interaction involves optical polarization fluctuations. Consequently, in order to build cascaded quantum systems we have to design the optical interface such that it converts between the polarization-dependent spin interface and the polarization-independent optomechanical interface.

In this section, we describe in detail how the optical setup is designed to mediate an interaction between the spin and optomechanical systems. A detailed drawing of the full

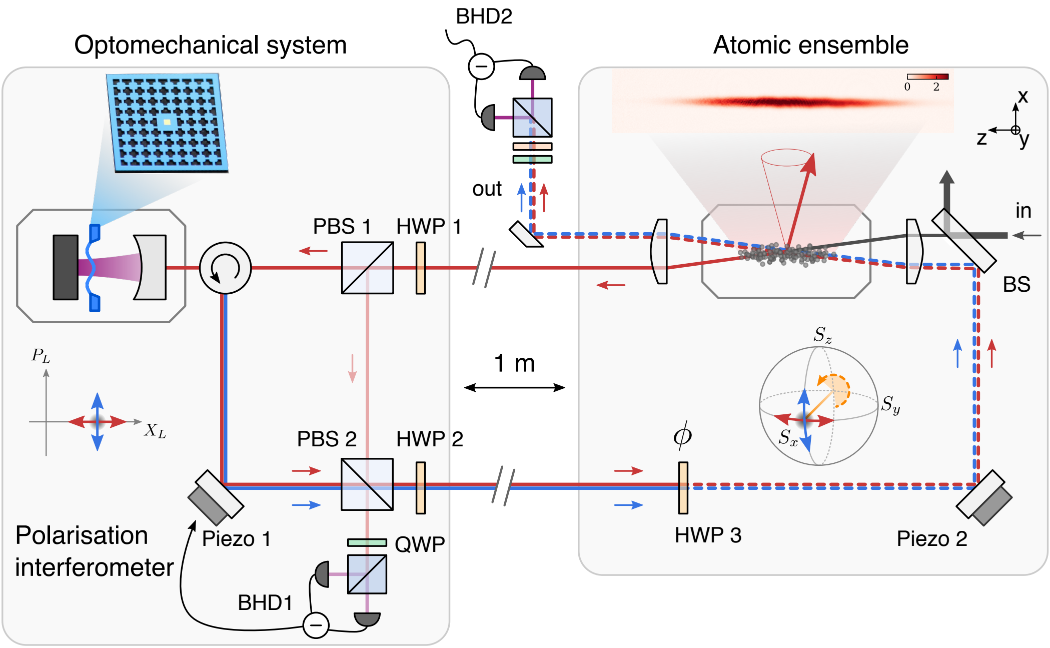

Figure 4.1: Sketch of the experimental setup and the path of the light field used to mediate an effective interaction from the atomic spin ensemble to the membrane oscillator and back. A polarization interferometer maps between the Stokes vector at the atomic ensemble (shown on the Poincaré sphere) and field quadratures of light (drawn as an optical phase space diagram). Light fields carrying spin signal are drawn as red lines, while light fields carrying membrane signals are blue. Before the light field returns to the atomic ensemble, a half-wave plate rotates the Stokes vector about the S_x axis and introduces a phase shift $\phi = \pi$ on the quantum fields in S_y, S_z which carry the spin and membrane signals, respectively.

experimental setup is shown in Fig. 4.1. At the end of this section we will have derived an abstract description of the setup in the language of cascaded quantum systems, which is sketched in Fig. 4.2.

As mentioned before, the atomic spin couples to the polarization state of light, defined by the Stokes vector, while the mechanical oscillator couples to field quadratures of the cavity field. The optical setup shown in Fig. 4.1 translates between these two states of light by means of a polarization interferometer, which is simply an interferometer with polarizing beam splitters and wave-plates at the in- and output that mix horizontal and vertical polarization. In order to mediate a bidirectional Hamiltonian interaction between spin and membrane, the light field interacts twice with the spin ensemble. This generates a looped cascaded system as discussed in chapter 1. In such a system, the character of the effective dynamics depends on the loop phase, i.e. the round-trip phase of a spin signal from the first spin-light interaction to the second one. Here, with full access to the laser beams between the two systems, we manipulate the loop phase by adding a half-wave plate in the optical path from the membrane to the spin. This rotates the Stokes vector about the S_x axis and adds a phase shift $\phi = \pi$ to the quantum fields carrying the spin and membrane signals. For $\phi = 0$, the effective dynamics are dissipative and governed by a Lindblad master equation, while for $\phi = \pi$, the effective dynamics are Hamiltonian.

Description of the setup Outside the polarization interferometer, we describe the polarization state of light using the Stokes vector $\mathbf{S}$. At the input, the laser is linearly polarized along the x-axis such that $\bar{S}_x = \bar{S}_0 = \Phi_L/2$. The field amplitudes read $a_x = \sqrt{\Phi_L} + b_L$ in x-polarization and $a_y = a_L$ in y-polarization, where we have defined a_L and b_L as the quantum fields in y- and x-polarization, respectively. Then, assuming $\langle a_L^\dagger a_L \rangle, \langle b_L^\dagger b_L \rangle \ll \Phi_L$, the Stokes vector components can be linearized and written as

$$\begin{aligned} S_0 &\approx \bar{S}_0 + \sqrt{\frac{\bar{S}_0}{2}}(b_L + b_L^\dagger), \\ S_x &\approx \bar{S}_0 + \sqrt{\frac{\bar{S}_0}{2}}(b_L + b_L^\dagger), \\ S_y &\approx \sqrt{\frac{\bar{S}_0}{2}}(a_L + a_L^\dagger), \\ S_z &\approx -i\sqrt{\frac{\bar{S}_0}{2}}(a_L - a_L^\dagger). \end{aligned} \tag{4.2}$$

The spin-light interaction in the first pass, at optical path coordinate ζ_1, reads

$$H_{s,1} = 2\hbar\sqrt{\Gamma_s/\bar{S}_x} X_s S_z(\zeta_1) \approx 2\hbar\sqrt{\Gamma_s} X_s P_L(\zeta_1) \tag{4.3}$$

where $P_L = -i(a_L - a_L^\dagger)/\sqrt{2}$ is the phase quadrature of the y-polarized quantum field. Likewise, $X_L = (a_L + a_L^\dagger)/\sqrt{2}$ is the amplitude quadrature. Spin precession modulates the light polarization via the input-output relation

$$S_y^{(\mathrm{out}),1} = S_y^{(\mathrm{in}),1} + 2\sqrt{\Gamma_s \bar{S}_0} X_s \tag{4.4}$$

Before entering the polarization interferometer, the laser polarization is rotated by a half-wave plate at angle θ_H (HWP 1). This transforms the Stokes vector as

$$S'_x = S_x \cos(4\theta_H) + S_y \sin(4\theta_H) \tag{4.5}$$

$$S'_y = -S_y \cos(4\theta_H) + S_x \sin(4\theta_H) \tag{4.6}$$

$$S'_z = -S_z \tag{4.7}$$

The photon flux in the interferometer arm containing the optomechanical cavity is given by

$$a_y'^\dagger a'_y = S_0 - S'_x = S_0 - \cos(4\theta_H) S_x - S_y \sin(4\theta_H) \tag{4.8}$$

In the limit of a broad cavity linewidth, the optomechanical interaction can be written as

$$H_m = \hbar \frac{4g_0}{\kappa} \sqrt{2} X_m a_y'^\dagger a'_y \tag{4.9}$$

where we have made the substitution $c^\dagger c = (4/\kappa) a_y'^\dagger a_y'$ of the cavity photon number by the input photon flux. Linearizing about the strong laser field (using equations (4.2)) yields

$$H_m = \hbar \frac{4g_0}{\kappa}\sqrt{\bar{S}_0} X_m \left[(b_L + b_L^\dagger)(1 - \cos(4\theta_H)) - \sin(4\theta_H)(a_L + a_L^\dagger) \right] \tag{4.10}$$

The first term describes coupling to the x-polarized quantum field co-propagating with the laser. In this context, it must be interpreted as noise because the spin does not interact with it. The second term is the y-polarized quantum field which contains the spin signal and is relevant for the cascaded coupling. In order to couple the mechanical oscillator mostly to a_L and not b_L, we choose a small half-wave plate angle $\theta_H \ll 1$ such that only about $1 - \cos(4\theta_H) = 0.1$ of the laser light is transmitted towards the optomechanical cavity. This still results in a large value of $\sin(4\theta_H) \approx 0.5$ while the ratio of back-action due to a_L over the total back-action of a_L and b_L, $\sin(4\theta_H)^2/([1 - \cos(4\theta_H)]^2 + \sin(4\theta_H)^2) \approx 0.93$, is high.

The optomechanical measurement rate is then given by $\Gamma_m = (4g_0/\kappa)^2 \Phi_m$ with an effective photon flux $\Phi_m = \Phi_L \sin(4\theta_H)^2/4$ at the optomechanical cavity. The spin-induced amplitude modulation at the optomechanical cavity amounts to $2\sin(4\theta_H)\sqrt{\Gamma_s \bar{S}_0} X_s$.

Mechanical motion produces a phase-modulation of the cavity output field by an angle $\phi_m = (4g_0/\kappa)\sqrt{2} X_m$. This phase shift between the two interferometer arms, which are locked to zero DC phase-shift using feedback onto piezo mirror 1, maps onto the output Stokes vector as

$$S_x'^{(\text{out})} = S_x'^{(\text{in})} \tag{4.11}$$

$$S_y'^{(\text{out})} = S_y'^{(\text{in})} \cos(\phi_m) + S_z'^{(\text{in})} \sin(\phi_m) \tag{4.12}$$

$$S_z'^{(\text{out})} = S_z'^{(\text{out})} \cos(\phi_m) - S_y'^{(\text{in})} \sin(\phi_m) \tag{4.13}$$

The HWP 2 after the polarization interferometer with identical angle θ_H like HWP 1 rotates the mean Stokes vector $\bar{S}$ back such that it points again along S_x (cf. equation (4.7)). Since $|\phi_m| \ll 1$ and $\langle S_z'^{(\text{in})} \rangle = 0$, $\langle S_y'^{(\text{in})} \rangle = \bar{S}_0 \sin(4\theta_H)$ we obtain that the polarization modulation due to the membrane amounts to $S_z = 2\sqrt{\bar{S}_0 \Gamma_m} X_m$. When the laser beam is sent back to the spin, this will produce a torque proportional to X_m.

The loop phase can be tuned by placing additional wave plates in the optical path before the second atom-light interaction. For the experiments presented in chapter 5, we used a single half-wave plate with fast axis aligned parallel to the laser polarization along x. This retards the orthogonal y-polarization by $\phi = \pi$ and thus inverts both S_y and S_z. A continuous rotation of the Stokes vector about the S_x axis by an angle $\phi \in [0, 2\pi)$ can be performed using a stack of two quarter-wave plates (QWP) and one half-wave plate (HWP) in between. This requires aligning the fast axes of the QWP at 45° ($\pi/4$) relative to the x-axis. For a rotation angle $\phi/4$ of the HWP relative to the QWP axes we obtain

$$\left[\text{QWP}(\frac{\pi}{4}) \circ \text{HWP}(\frac{\pi + \phi}{4}) \circ \text{QWP}(\frac{\pi}{4}) \right] \mathbf{S} = \begin{pmatrix} S_x \\ S_y \cos(\phi) - S_z \sin(\phi) \\ S_z \cos(\phi) + S_y \sin(\phi) \end{pmatrix} \tag{4.14}$$

which is the desired rotation about the S_x axis. We remark that one can perform two such phase rotations, in between subsequent light-matter interfaces, to implement arbitrary couplings.

In order to prevent a second interaction of the membrane with the light field, the laser beam for the second spin-light interaction intersects the atomic cloud at an angle such that it can be separated from the input beam. The two beams are combined on a high-reflectivity non-polarizing beam-splitter (2% transmission) to avoid optical loss of the light coupling the membrane to the spin.

Effective model To summarize, we can describe the experimental setup of Fig. 4.1 by cascaded light-matter interactions as depicted in a more abstract way in Fig. 4.2. We can write the cascaded interaction Hamiltonian with the traveling quantum field a_L as

$$H_{\text{int}} = 2\hbar\sqrt{\Gamma_s}X_s\left[P_L(\zeta_1) + \cos(\phi)P_L(\zeta_3) - \sin(\phi)X_L(\zeta_3)\right] + 2\hbar\sqrt{\Gamma_m}X_mX_L(\zeta_2) \tag{4.15}$$

where $\zeta_1 < \zeta_2 < \zeta_3$ are the spatial coordinates of the three light-matter interactions along the optical path. This interaction Hamiltonian is the starting point to derive a master equation for the effective light-mediated coupling based on the formalism of chapter 1. In the course of adiabatic elimination of the light field we drop propagation delays $\tau_{ij} = (\zeta_i - \zeta_j)/c$, which can be accounted for using Heisenberg-Langevin equations as presented in section 4.4.1. For the moment we also neglect optical loss. The resulting master equation for the effective light-mediated dynamics is

$$\begin{aligned} \dot{\rho} \;=\; & -2\Gamma_s(1+e^{-i\phi})[X_s, X_s\rho] + \text{h.c.} && (4.16)\\ & -\Gamma_m[X_m, X_m\rho] + \text{h.c.} && (4.17)\\ & +2i\sqrt{\Gamma_s\Gamma_m}\left([X_m, X_s\rho] - e^{-i\phi}[X_s, X_m\rho]\right) + \text{h.c.} && (4.18) \end{aligned}$$

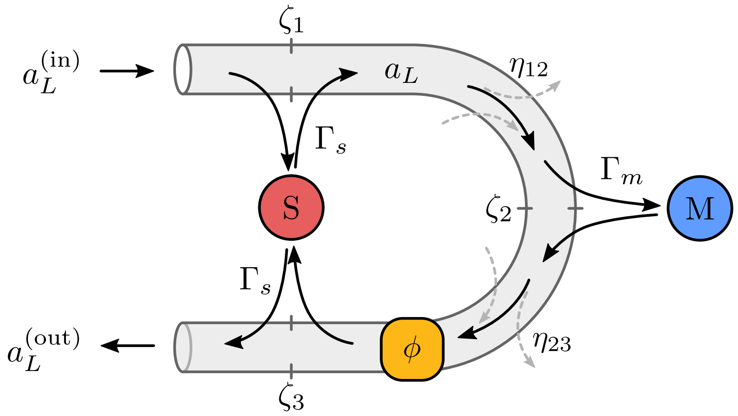

Figure 4.2: Sketch of the cascaded coupling. The optical field a_L takes a path parametrized by a spatial coordinate ζ from the spin system S to the membrane M and back to S. The field experiences loss between the systems, characterized by transmission coefficients η_{ij} and a phase shift ϕ, i.e. the loop phase.

where the first line contains spin diffusion due to vacuum noise of the optical input field and light-mediated spin self-interaction. The second line corresponds to mechanical diffusion due to optical input noise. Spin-membrane interaction, both coherent and dissipative, is contained in the third line. We can separate coherent from dissipative evolution by bringing the master equation (4.18) into Lindblad form, i.e.

$$\dot{\rho} = \frac{1}{i\hbar}[H_{\text{eff}}, \rho] + \mathcal{L}_{\text{eff}}\rho, \tag{4.19}$$

with an effective Hamiltonian

$$H_{\text{eff}} = \hbar[1 - \cos(\phi)]2\sqrt{\Gamma_s\Gamma_m}X_sX_m - \hbar\sin(\phi)2\Gamma_sX_s^2 \tag{4.20}$$

and collective dissipation

$$\mathcal{L}_{\text{eff}}\rho = \mathcal{D}[J]\rho = J\rho J^\dagger - \frac{1}{2}\left(J^\dagger J\rho + \rho J^\dagger J\right) \tag{4.21}$$

with collective jump operator $J = \sqrt{2\Gamma_m}X_m + i\sqrt{2\Gamma_s}\left(1 + e^{i\phi}\right)X_s$.

The effective Hamiltonian H_{eff} contains both the spin-membrane interaction and a self-interaction of the spin. For loop phases $\phi = 0, \pi$, the spin self-interaction vanishes and is thus not important for the experiment. At intermediate phases, the spin self-interaction can be exploited to generate unconditional spin-squeezing [191]. The spin-membrane interaction vanishes for $\phi = 0$ and amounts to $H_{\text{eff}} = \hbar 2gX_sX_m$ for $\phi = \pi$. Here, we define the spin-membrane coupling strength as $g = 2\sqrt{\Gamma_s\Gamma_m}$. The collective jump operator J is composed of a membrane and a spin part. At $\phi = 0$, both parts are non-zero and give rise to collective dissipative interaction between spin and membrane. For $\phi = \pi$, however, the spin part vanishes, and dissipation only affects the membrane. This is a consequence of the destructive interference of optical shot noise driving the spin for $\phi = \pi$, in which case the spin is effectively decoupled from the input and output light fields. Quantum-coherent spin-membrane coupling necessitates this property of the looped cascaded coupling scheme in order to allow the coupling strength g to be larger than all back-action decoherence rates. If intrinsic dissipation rates are low, this is achieved if $\Gamma_s > \Gamma_m$ because $g/\Gamma_m = \sqrt{\Gamma_s/\Gamma_m}$. Including thermal decoherence of the individual oscillators, the full master equation reads

$$\dot{\rho} = \frac{1}{i\hbar}[H_0 + H_{\text{eff}}, \rho] + \mathcal{L}_{\text{eff}}\rho \tag{4.22}$$

$$+\gamma_m(\bar{n}_m + 1)\mathcal{D}[b_m]\rho + \gamma_m\bar{n}_m\mathcal{D}[b_m^\dagger]\rho \tag{4.23}$$

$$+\gamma_s(\bar{n}_s + 1)\mathcal{D}[b_s]\rho + \gamma_s\bar{n}_s\mathcal{D}[b_s^\dagger]\rho \tag{4.24}$$

Here, we introduced the harmonic oscillator Hamiltonian

$$H_0 = \frac{\hbar\Omega_m}{2}(X_m^2 + P_m^2) + \frac{\hbar\Omega_s}{2}(X_s^2 + P_s^2) \tag{4.25}$$

and intrinsic damping rates γ_i with thermal bath occupation numbers $\bar{n}_i$ $(i = s, m)$. For the spin system $\bar{n}_s \approx 0$.

Optical loss leads to a slight modification of the ideal effective dynamics derived above. We introduce the transmission coefficients η_{ij} between light-matter couplings i

and j (see Fig. 4.2). Since the laser field experiences the same loss as the quantum field that mediates the coupling we also need to scale the local coupling strengths Γ_i as they are proportional to the local laser photon flux. The modified master equation with losses reads

$$\begin{aligned}\dot{\rho} &= \frac{1}{i\hbar}[H_0,\rho] + \sum_{i=s,m}\Big(\gamma_i(\bar{n}_i+1)\mathcal{D}[b_i]\rho + \gamma_i\bar{n}_i\mathcal{D}[b_i^\dagger]\rho\Big) \\ &\quad -\Gamma_s(1+\eta_{13}^2+2\eta_{13}^2e^{-i\phi})[X_s,X_s\rho] + \text{h.c.} \\ &\quad -\eta_{12}^2\Gamma_m[X_m,X_m\rho] + \text{h.c.} \\ &\quad -2i\sqrt{\Gamma_s\Gamma_m}\Big(\eta_{12}^2[X_m,X_s\rho] - \eta_{12}\eta_{23}\eta_{13}e^{-i\phi}[X_s,X_m\rho]\Big) + \text{h.c.} \qquad (4.26)\end{aligned}$$

For identical transmission coefficients $\eta_{12} = \eta_{23} = \eta$ and $\eta_{13} = \eta^2$ and $\phi = \pi$, we get a coherent coupling strength of $g = (\eta^2+\eta^4)\sqrt{\Gamma_s\Gamma_m}$, a mechanical back-action rate of $\gamma_{m,\text{ba}} = \Gamma_m\eta^2$, and a spin back-action rate of $\gamma_{s,\text{ba}} = \Gamma_s(1-\eta^4)$.

After the second atom-light interaction, the output field is given by

$$\begin{aligned}a_L^{(\text{out})}(t) &= \eta_{12}\eta_{23}a_L^{(\text{in})}(t) + \eta_{23}\sqrt{1-\eta_{12}^2}h_1^{(\text{in})}(t) + \sqrt{1-\eta_{23}^2}h_2^{(\text{in})}(t) \\ &\quad +2\eta_{12}\eta_{23}\Big[\sqrt{\Gamma_s}X_s(t) + \sqrt{\Gamma_s}X_s(t-2\tau)e^{i\phi} + i\sqrt{\Gamma_m}X_m(t-\tau)e^{i\phi}\Big] \qquad (4.27)\end{aligned}$$

Here, we defined vacuum fields $h_1^{(\text{in})}$ and $h_2^{(\text{in})}$ that enter the coupling light field due to losses on the spin-to-membrane path and membrane-to-spin path, respectively. Since losses affect not only the quantum field a_L, but also the laser field, full interference of the spin output signal can be observed, even if there is significant optical loss in between the two spin-light interactions.

4.2 Double-pass spin-light interface

4.2.1 Geometrical considerations

In order to establish the bidirectional spin-membrane coupling, the laser beam returning from the optomechanical system is sent another time through the atomic cloud. A small angle $2\theta \ll 1$ between the first and second pass allows us to fully separate them after passing through the atomic ensemble while still maintaining good alignment with the atomic cloud and high optical depth (see Fig. 4.3). At the atomic cloud, the two beams have wave-vectors $\mathbf{k}_\pm$ with angle $\pm\theta$ relative to the z-axis, respectively.

The two beams are aligned parallel with displacement d and then focused onto the atomic cloud using a lens with focal length $f = 200$ mm which transforms the parallel offset into a relative angle $\theta \approx d/2f$. In the focal plane, the electric fields of the two beams interfere and form a transverse standing wave with effective wavelength $\lambda_\perp \approx \lambda/2\theta$. The global phase difference between the two beams is stabilized to zero (constructive interference at the center) as shown in Fig. 4.3. The small amount ($\approx 2\%$) of light which is transmitted through the beam-splitter BS in the second pass is overlapped with the directly reflected input light, coupled into a single-mode fiber, and detected on a photodetector. The resulting interference is then used to lock the relative phase between them by feedback onto piezo mirror 2 (cf. section 4.3). Camera images of the single-pass and double-pass laser beam profiles at the position of the atoms are shown in Fig. 4.3. These are measured by picking up the $\approx 0.1\%$ transmission through one of the mirrors which align the beams onto the atomic cloud.

In order to ensure that both beams couple to the same atomic spin wave, it is crucial that the transverse wavelength is equal to or larger than the diameter of the atomic cloud $2w_a$. In order to optimise the mode-matching between the laser and the atomic cloud in single pass, the laser waist w_0 has been chosen to approximately match the waist w_a of the atomic cloud, i.e. $w_0 \approx w_a$. In this situation we require that $\lambda_\perp/2w_0 \approx \pi\theta_0/4\theta > 1$, where $\theta_0 = \lambda/\pi w_0$ is the beam divergence. On the other hand, the ability to separate the two beams in the plane of the lens requires that the beam separation is larger than the collimated beam waist w, i.e. $d/2w = \theta/\theta_0 > 1$. For these two conflicting requirements we find a compromise by choosing $\theta \approx \theta_0$, i.e. a displacement $d \approx 2w$. For this setting,

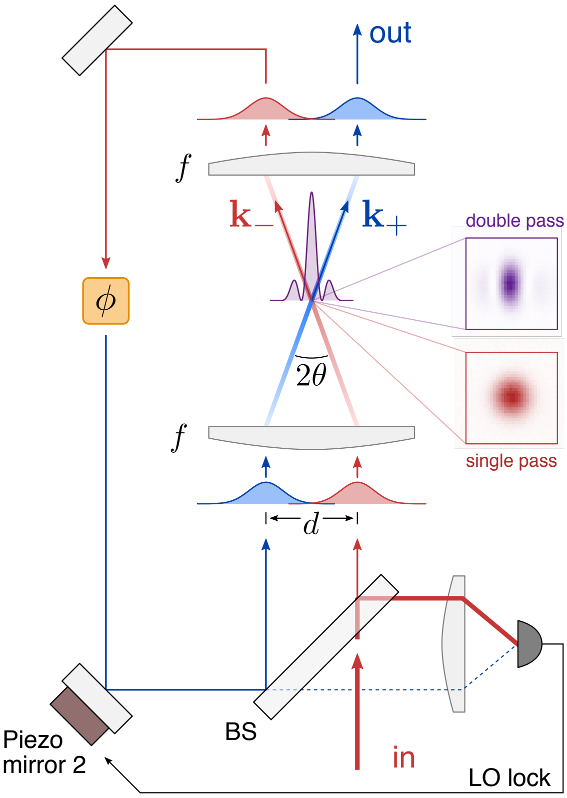

Figure 4.3: Geometry of the double-pass atom-light interface. The red input beam passes through the atomic ensemble under a small angle θ. After passing once through the loop with loop phase shift ϕ on y-polarized quantum fields, the returning beam (blue) is recombined with the input beam on the input high-reflectivity beam-splitter such that they are parallel. At the atomic ensemble the two beams interfere and show a transverse interference pattern (purple). After the second pass, the beam exits. Insets show measured beam profiles of coupling beam in the first pass (red) and of the interfering beams (purple). The relative phase between the laser fields is stabilized by feedback onto the in-loop piezo mirror 2.

the residual beam overlap in the lens plane is approximately 10%. Choosing a larger beam diameter in the focus would allow even smaller angles with better homogeneity on the atomic cloud. There is however another tradeoff with the mode-matching efficiency of the laser beam to the atomic ensemble.

The presence of two laser fields, changes both the spontaneous scattering rate γ_{sc} and the single-pass spin-light coupling strength Γ_s. Since there are now two laser fields of equal flux and with same polarization, the total intensity increases by four and so does γ_{sc}. Since the two beams are nearly collinear, their combined fields can achieve a higher coherent scattering rates into the forward modes going towards the optomechanical system and towards the output. Likewise, optical signals from the optomechanical system couple more strongly to the spin because the pump strength is larger. This results in an enhancement of Γ_s which is, however, smaller than that of γ_{sc}. The reason for this is that spontaneous scattering is a single-atom effect, while collective forward scattering relies on the constructive interference of all fields scattered by the individual atoms [155]. The small angle between the two laser fields results in a transverse phase pattern $\sim 1 + e^{\pm i 2 k_\perp y}$ of the single-atom scattering amplitude into the modes with wave-vectors $\mathbf{k}_\pm$. Here, the transverse wave-number is defined as $k_\perp = 2\pi/\lambda_\perp$. Consequently, atoms at different transverse locations in the laser beam scatter light with different relative phases which reduces the collective enhancement of forward scattering. Furthermore, this phase-pattern results in different spin waves $F_z^{1+\cos}$ and $F_z^{\sin}$ with local amplitudes $1 + \cos(2k_\perp y)$ and $\sin(2k_\perp y)$, respectively [49]. In order to achieve that only the homogeneous spin wave $F_z^{1+\cos}$ has a large coupling strength, one must ensure that the atoms are sufficiently localized such that $k_\perp w_a \ll 1$. Since we have $\theta \approx \theta_0$, this condition requires $w_a \ll w_0$, ie. tight transverse confinement of the atomic ensemble. In the experiment, this condition is not satisfied such that also the spin wave $F_z^{\sin}$ has a non-negligible coupling strength. This has no consequence for coherent coupling as explored in this article, but coupling between the two spin waves can act as a source of noise.

4.2.2 Theoretical description

In order to quantify the considerations of the preceeding paragraph, we derive here the Faraday interaction Hamiltonian for an atomic ensemble with two laser beams intersecting at a small angle $\theta \ll 1$. We start with the general expression for the vector part of the dispersive atom-light interaction [166, 192]

$$H_s = \frac{\hbar\alpha_1}{\mathcal{E}_0^2} \sum_{j=1}^{N} \frac{1}{2i} \left(\mathbf{E}^{(-)}(\mathbf{r}_j) \times \mathbf{E}^{(+)}(\mathbf{r}_j) \right) \cdot \mathbf{f}^{(j)} \tag{4.28}$$

where $\mathbf{E}^{(+)}$ ($\mathbf{E}^{(-)}$) are the positive- (negative-) frequency components of the electric field vector and $\mathcal{E}_0 = \sqrt{\hbar\omega_L/2c\epsilon_0 A}$ is the traveling wave vacuum electric field density with dielectric constant ϵ_0 and mode area A. The Hamiltonian (4.28) can be interpreted as the coupling between the spin vector and an effective magnetic field $\mathbf{B}_{\mathrm{eff}} \sim \left(\mathbf{E}^{(-)} \times \mathbf{E}^{(+)}\right)/2i$. The electric field is a superposition of the fields of the two beams

$$\mathbf{E}^{(+)}(\mathbf{r}) = \mathcal{E}_0 \left[u_1(\mathbf{r})\mathbf{a}_1(\zeta_1) + u_2(\mathbf{r})\mathbf{a}_2(\zeta_2) \right] \tag{4.29}$$

which have spatial mode functions u_1, u_2 and field operators $\mathbf{a}_1$, $\mathbf{a}_2$. The spatial coordinates $\zeta_1 < \zeta_2$ define the positions of the two atom-light interactions along the optical path. We assume here that the spatial mode functions are rotated Gaussian beams, i.e. $u_i(\mathbf{r}) = u_0(R_x(\theta_i)^{-1}\mathbf{r})$, with $\theta_{1,2} = \pm\theta$ and u_0 being the normalized mode function of an on-axis Gaussian beam with waist w_0. Near the focus, we have [193]

$$u_0(x, y, z) \approx \sqrt{2}e^{-\frac{x^2+y^2}{w_0^2}+ik_Lz}. \tag{4.30}$$

Note, that the factor $\sqrt{2}$ accounts for the enhanced peak intensity because in (4.28) we have assumed a mode area $A = \pi w_0^2$, like in the effective 1D description. The matrix $R_x(\theta)$ describes a rotation around the x-axis by an angle θ. With the coherent laser field in x-polarization, the field operators are given by

$$\mathbf{a}_i = \left[\sqrt{\Phi_L} + b_L(\zeta_i)\right]\mathbf{e}_x + a_L(\zeta_i)\mathbf{e}_{\theta_i} \tag{4.31}$$

with unit vectors $\mathbf{e}_\theta = \cos(\theta)\mathbf{e}_y + \sin(\theta)\mathbf{e}_z$ and quantum fields a_L and b_L in x- and y-polarization, respectively. In evaluating (4.28) we linearize around the coherent field with flux Φ_L in x-polarization such that only the quantum field a_L is relevant. We deliberately choose the coherent fields of each beam to have identical polarization such that there is no cross-talk between fields a_L and b_L via the loop. Inserting the expression for the fields into equation (4.28) gives

$$\mathbf{B}_{\text{eff}}(\mathbf{r}) \sim \frac{\sqrt{\Phi_L}}{2i}\left[w_1^*(\mathbf{r})a_L(\zeta_1)\mathbf{e}_{\frac{\pi}{2}+\theta_1} + w_2^*(\mathbf{r})a_L(\zeta_2)\mathbf{e}_{\frac{\pi}{2}+\theta_2}\right] + \text{h.c.} \tag{4.32}$$

Since we have assumed $\theta \approx \theta_0 \sim 10^{-2}$ for the chosen beam waist, we can approximate $\mathbf{e}_{\pi/2+\theta_i} \approx e_z$. Every atom thus has a certain coupling amplitude to $a_L(\zeta_1)$ given by $w_1(\mathbf{r}_j) = u_1(\mathbf{r}_j)^*(u_1(\mathbf{r}_j) + u_2(\mathbf{r}_j))$ and an amplitude $w_2(\mathbf{r}_j) = u_2(\mathbf{r}_j)^*(u_1(\mathbf{r}_j) + u_2(\mathbf{r}_j))$ for the coupling to $a_L(\zeta_2)$. If we neglect the Gaussian envelope, these coupling amplitudes are approximately given by $w_1 \sim 1 + e^{-ik_\perp y}$, and $w_2 \sim 1 + e^{+ik_\perp y}$. This motivates us to define the following symmetric and anti-symmetric spin waves [168]

$$F_z^{j,\cos} = \frac{1}{\eta_{j,\cos}}\sum_{i=1}^{N}\text{Re}\left\{w_j(\mathbf{r}_i)\right\}f_z^{(i)}, \tag{4.33}$$

$$F_z^{j,\sin} = \frac{1}{\eta_{j,\sin}}\sum_{j=1}^{N}\text{Im}\left\{w_j(\mathbf{r}_i)\right\}f_z^{(i)}, \tag{4.34}$$

respectively, with normalization factors given by the ensemble averages

$$\eta_{j,\cos} = \sqrt{\frac{1}{N}\sum_{i=1}^{N}\text{Re}\left\{w_j(\mathbf{r}_i)\right\}^2}, \quad \eta_{j,\sin} = \sqrt{\frac{1}{N}\sum_{i=1}^{N}\text{Im}\left\{w_j(\mathbf{r}_i)\right\}^2}. \tag{4.35}$$

For a symmetric situation $\theta_2 = -\theta_1$, the two anti-symmetric spin waves $F_z^{j,\sin}$ are identical, and also $\eta_{j,\cos} = \eta_{\cos}$, $\eta_{j,\sin} = \eta_{\sin}$. In Fig. 4.4 we show the optical intensities of a single beam and two crossed beams, as well as the spin wave amplitudes $\text{Re}\{w_1\}$ and $\text{Im}\{w_1\}$.

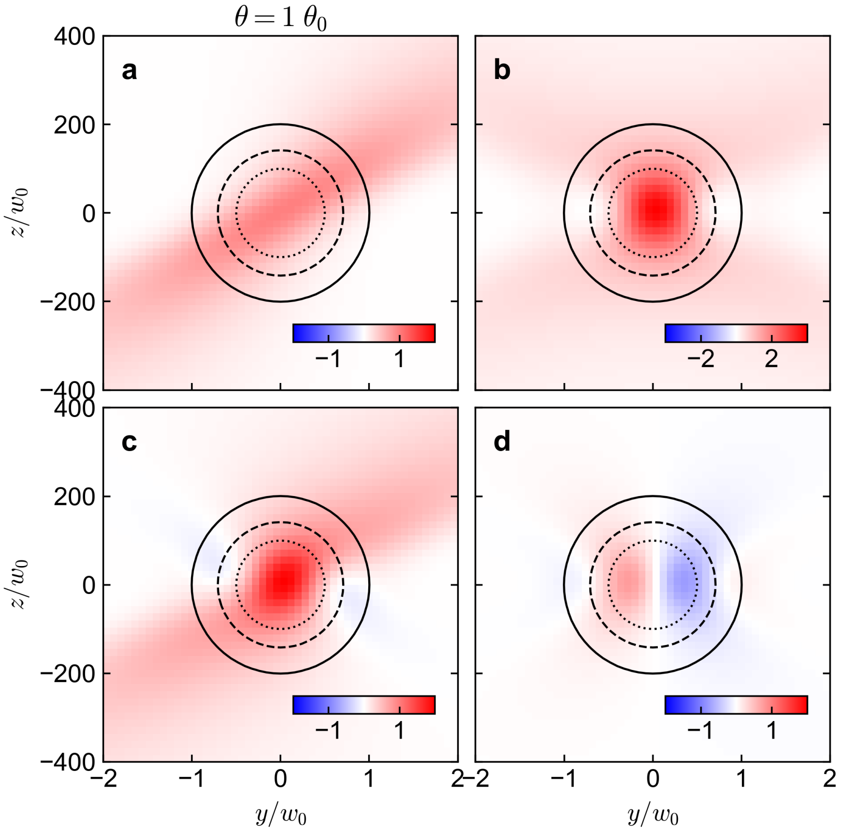

Figure 4.4: Illustration of the laser beam intensity distribution and spin waves at the atomic cloud. **a**, normalized intensity of single beam $|u_1|^2$ at an angle of $\theta = \theta_0$. **b**, normalized intensity of crossed beams $|u_1+u_2|^2$. **c**, symmetric spin wave-amplitude $\mathrm{Re}\{w_1\}$. **d**, anti-symmetric spin wave amplitude $\mathrm{Im}\{w_1\}$. The solid, dashed and dotted lines correspond to e^{-2}, e^{-1} and $e^{-1/2}$ contours of the atomic density, respectively. Here, the atomic waist w_a equals the beam waist w_0.

Similar to the canonical collective spin operators, one can make a Holstein Primakoff approximation to the spin waves, yielding, e.g. $X_s^{1,\cos} = F_z^{1,\cos}/\sqrt{|\bar{F}_x|}$, $P_s^{1,\cos} = -\operatorname{sgn}(\bar{F}_x)F_y^{1,\cos}/\sqrt{|\bar{F}_x|}$. The atom-light coupling Hamiltonian reads

$$H_s = \hbar\sqrt{4\Gamma_s}\left[\eta_{\cos}X_s^{1,\cos}P_L(\zeta_1) + \eta_{\cos}X_s^{2,\cos}P_L^{\phi}(\zeta_2) + \eta_{\sin}X_s^{\sin}(X_L(\zeta_1) - X_L^{\phi}(\zeta_2))\right] \tag{4.36}$$

where we used the notation $X_L^{\phi} = \cos(\phi)X_L + \sin(\phi)P_L$ and $P_L^{\phi} = \cos(\phi)P_L - \sin(\phi)X_L$. We see that the two spin waves couple to orthogonal light quadratures with different relative phases in the first and second pass. For sufficiently small angle, we can approximate $X_s^{1,\cos} = X_s^{2,\cos} =: X_s^{\cos}$. If $\phi = \pi$, we arrive at

$$H_s = \hbar\sqrt{4\Gamma_s}\left\{\eta_{\cos}X_s^{\cos}\left[P_L(\zeta_1) - P_L(\zeta_2)\right] + \eta_{\sin}X_s^{\sin}\left[X_L(\zeta_1) + X_L(\zeta_2)\right]\right\} \tag{4.37}$$

The coupling of $X_s^{\cos}$ to the P_L quadrature is the desired interaction because it creates a signal in the X_L quadrature that drives the mechanical oscillator and it receives the signal from the mechanical oscillator in P_L. On the contrary, the coupling of $X_s^{\sin}$ to the X_L quadratures does not directly couple to the optomechanical system. Furthermore, the coupling of $X_s^{\cos}$ to the input field of P_L interferes destructively while the coupling of $X_s^{\sin}$ to the input field of X_L interferes constructively. This means that the spin wave $X_s^{\sin}$ is subject to quantum back-action which can then be transferred to $X_s^{\cos}$ via couplings between the two spin waves. One possible coupling pathway is via the light field. Since the two spin waves couple to orthogonal light field quadratures with different phase shifts between the locations ζ_1 and ζ_2, the coupling is described by the Hamiltonian

$$H_{\mathrm{spin-spin}} = 4\eta_{\cos}\eta_{\sin}\hbar\Gamma_s X_s^{\cos} X_s^{\sin} \tag{4.38}$$

where we assumed for simplicity that $X_s^{1,\cos} = X_s^{2,\cos}$. Consequently, the inter-spin-wave coupling constant is given by $2\Gamma_s\eta_{\cos}\eta_{\sin}$

Based on this theory, we can calculate a number of important parameters for the double-pass spin-light interface. Here, we assume a Gaussian atomic density distribution with (e^{-2}) radial waist $w_a = 35$ μm and longitudinal waist $l_a = 7$ mm and $N = 10^7$ atoms. Fig. 4.5a shows the mean spin-wave amplitude $\langle w_s \rangle = \sum_{i=1}^{N} \mathrm{Re}\{w_1(\mathbf{r}_i)\}/N$ as a function of the angle between the laser beam and the atomic cloud. This can be used to estimate the size of a classical spin signal, where all spins are excited by an RF pulse with the same phase. The solid lines show the coupling for two laser beams and the dashed lines for a single laser beam. The different colors correspond to different beam waists. The larger the beam waist, the more uniform the coupling across all atoms and the larger $\langle w_s \rangle$. With increasing angle θ, $\langle w_s \rangle$ decreases because the overlap between the beam and the cloud decreases.

In 4.5b, the mean-squared spin wave amplitudes η_s are shown, with s representing the cos spin wave (solid lines), the sin spin wave (dotted lines), or a single beam (dashed lines). Here, the behaviour is similar as in panel a, but η_s decreases more slowly with θ since the relative phase between atoms is not important. The curves show that, even at a large angle $\theta > \theta_0$, the atom-light coupling strength is enhanced by the second pump beam. Only at large angles η_s reduces to the single beam value, meaning that there is no cross-sacttering between the two modes. Moreover, $\eta_{\sin}$ for the anti-symmetric spin wave grows rapidly even for small angle $\theta = \theta_0$ and attains a considerable fraction of $\eta_{\cos}$. Consequently, it seems unjustified to neglect the antisymmetric spin wave for any choice of probe beam waist.

Fig. 4.5c shows the effective optical depth (OD) for scattering into mode u_1, which is calculated as [155]

$$d_{\mathrm{eff}} = \eta_s^2 \frac{N\sigma_\pi}{A} \tag{4.39}$$

for the single-beam case ($u_2 = 0$) and, taking into account increased spontaneous emission in the presence of the second beam,

$$d_{\mathrm{eff}} = \frac{\eta_s^2}{4} \frac{N\sigma_\pi}{A} \tag{4.40}$$

for the two-beam cases ($s = \cos, \sin$). At $\theta = 0$ the OD is identical for the single-beam and two-beam case with symmetric spin wave because in this scenario both are

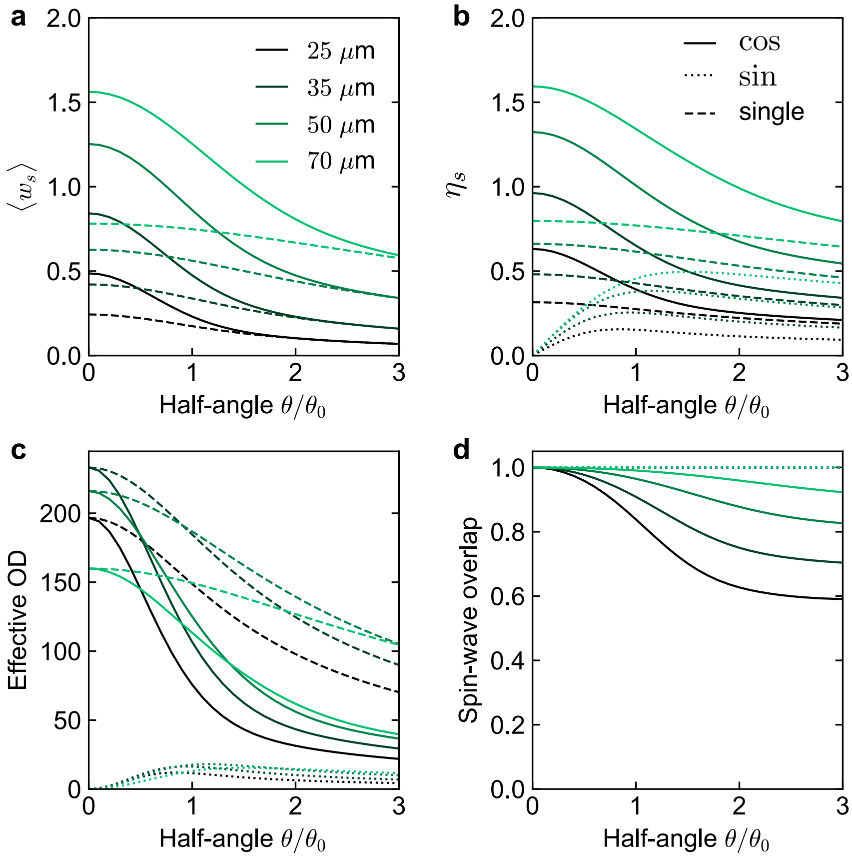

Figure 4.5: Numerical calculation of various atom-light coupling parameters for different laser beam waists as a function of the angle θ between the atomic cloud and the laser beams. Dashed lines are for single laser beam, solid lines are for crossed laser beams symmetric spin wave, dotted lines are for anti-symmetric spin wave.

equivalent. With increased angle, d_{eff} drops more rapidly for the two-beam case, because the overlap between the scattered waves from the two pump laser beams decreases. At larger angle, it is advantageous to choose a larger beam waist such that both pump lasers scatter more efficiently into each other's mode. The anti-symmetric spin wave also has a small non-negligible OD.

Finally, it is important to quantify the mode overlap between the symmetric spin waves addressed in the first and second pass, i.e. [168]

$$\eta_{12,\cos} = \frac{1}{\sqrt{\eta_{1,\cos}\eta_{2,\cos}}} \sum_{i=1}^{N} \operatorname{Re}\{w_1(\mathbf{r}_i)\} \operatorname{Re}\{w_2(\mathbf{r}_i)\} \tag{4.41}$$

For the anti-symmetric spin waves $\eta_{12,\sin} = 1$. The spin-wave overlap factor is displayed in panel d. Apparently, the overlap strongly depends on the probe beam waist. If it is too small, it drops significantly already for a small angle $\theta = \theta_0$. Only a beam waist of 50 μm which is about $w_0 \approx 1.5 \times w_a$ yields $> 90\%$ overlap. In order to evaluate the performance of the spin-light interface in the quantum regime, these quantities have to be taken into account. Of course, the precise values critically depend on the dimensions of the atomic ensemble. These examples show, however, that the probe beam waist and beam angle θ have to be chosen carefully in order to minimize possible noise sources.

To conclude this section, we show experimental data of single-beam Faraday probe experiments where the angle between the probe beam relative to the cloud is varied. The data are shown in Fig. 4.6. Here the beam angle is indicated in terms of the lateral displacement d by which the beam has been translated in the plane of the lens. A beam displacement of 1 mm corresponds to an angle of $\theta = 0.005$. The beam divergence is $\theta_0 = 0.007$ for $w_0 = 35$ μm and $\theta_0 = 0.005$ for $w_0 = 50$ μm, meaning that the relative angle θ/θ_0 is smaller for the smaller waist. Figs. 4.6a) and b) show the measured Faraday angle for probe beam waists of $w_0 = 35$ μm and $w_0 = 50$ μm, respectively. In each panel, data is shown for a long cloud ($l_a = 7$ mm) and a short cloud ($l_a = 3.5$ mm). Clearly, the Faraday signal decreases faster with angle for the smaller waist. As expected, this is much more pronounced for the long cloud, where a small angle already leads to a significant signal reduction because the overlap between the laser beam and the atomic cloud gets reduced. These data correspond to a measurement of $\langle w_s \rangle$. They prove the obvious statement that a larger beam waist is advantageous to maintain good overlap with the cloud even at larger angle. Moreover, for a larger beam waist with smaller divergence, a smaller angle is sufficient to keep the two laser beams in the double-pass interface separate.

Figures 4.6c) and d) show measurements of the spin damping rate for a long cloud and short cloud, respectively, as a function of laser power at a probe beam waist of $w_0 = 35$ μm. Lines are linear fits to guide the eye. The data show that spin damping is not strongly dependent on the beam angle. However, the data scatter more strongly for the long cloud and are also slightly lower than for the short cloud. In this measurement, the damping rate of the long cloud at large powers and zero displacement are most certainly underestimated. For the short cloud, the damping is slightly higher, possibly because the atoms are localized better at the focus of the coupling beam, thus the average optical intensity per atom is higher. The damping rates for the short cloud quantitatively match the theoretical spontaneous emission rate at the peak intensity.

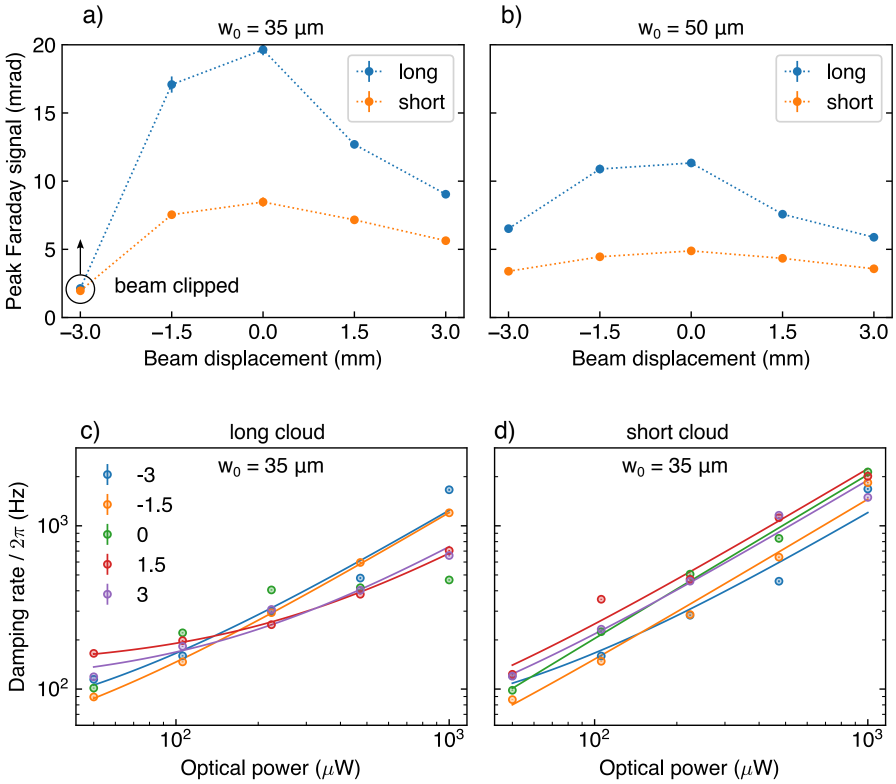

Figure 4.6: Measurement of spin precession probed with a laser beam tilted relative to the long axis of the atomic ensemble. The legend indicates the displacement at the focusing lens. a,b) Faraday signal vs beam displacement for two different beam waists at a detuning of -20 GHz. c,d) Measurement of spin damping rates as a function of laser power for different displacements. The displacement does not affect the damping rate a lot.

4.2.3 Observation of interference in the spin-light interaction

In this section, we provide data showing interference of the spin signal in the coupling beam output field. This intends to show that the coupling scheme presented here is capable of suppressing optical back-action by the light field on the spin, as spin information is prevented from leaking to the environment. Quantum back-action cancellation is an important requirement for quantum coherent coupling between the spin and membrane [38, 36].

For this measurement, the optomechanical cavity is tuned off-resonant from the laser such that there is no coupling of the spin to the membrane. After optical pumping, a short (30 μs) RF-pulse at the Larmor frequency excites spin precession with a small amplitude. Immediately afterwards, the coupling beam is switched on and the spin-induced Faraday rotation is detected on a balanced homodyne detector (BHD 2 in Fig. 4.1). The detector is adjusted such that it measures the X_L quadrature of the output field given by equation (4.27), i.e.

$$\begin{aligned} X_L^{(\text{out})}(t) &\approx \eta^2 X_L^{(\text{in})}(t) + \sqrt{1-\eta^4} X_h^{(\text{in})}(t) \\ &+2\eta^2\sqrt{\Gamma_s}\left\{X_s(t)\Big[1+\cos(\phi)\cos(2\Omega_s\tau)\Big] - P_s(t)\cos(\phi)\sin(2\Omega_s\tau)\right\}. \end{aligned} \tag{4.42}$$

The first line contains shot noise from the input field $X_L^{(\text{in})}$ and an additional contribution $X_h^{(\text{in})}$ due to optical loss along the optical path. Here, we approximated $X_s(t-2\tau) \approx X_s(t)\cos(2\Omega_s\tau) - P_s(t)\sin(2\Omega_s\tau)$. As stated after equation (4.27), the interference contrast of the spin signal when varying ϕ should not be diminished by optical loss because it affects the laser and quantum fields in the same way. Rather, optical delay τ, imperfect optical polarization and differences in laser-atom mode-matching between the two passes are expected to reduce the contrast. From equation (4.42) it is calculated that the root-mean-square spin signal at the output is modulated by

$$\epsilon(\phi) = \sqrt{1+\cos^2(\phi)+2\cos(\phi)\cos(2\Omega_s\tau)}, \tag{4.43}$$

due to interference via the loop.

Fig. 4.7A shows the measured root-mean-squared spin signal in $X_L^{(\text{out})}$ for three different configurations. Two traces correspond to the double-pass atom-light interface with loop phases of $\phi = 0$ and $\phi = \pi$. The third trace shows the spin signal for a single pass interaction which is realized by moving the laser beam away from the atomic cloud in the second pass. The data clearly show a strong suppression of the spin signal for $\phi = \pi$ as compared to $\phi = 0$. Fitting the traces with an exponential decay including an initial detector rise time ($1/e$-time 10 μs) allows us to extract the amplitudes as well as the spin decay rates. First, we note that the double-pass signal for $\phi = 0$ is 3.3 times larger than the single-pass output, which indicates a 1.6-fold enhancement of the scattering efficiency in the presence of the second laser beam. Compared to $\phi = 0$, the spin signal at $\phi = \pi$ is suppressed by a factor 14. This value is in good agreement with $\epsilon(0)/\epsilon(\pi) \approx 12$ for $2\Omega_s\tau = 0.17$. In this measurement, optical delay is only due to optical path length of about 4 m because the cavity is off-resonant.

Next, we discuss the effect of the loop phase on spin damping. The fitted (energy) damping rates are $\gamma_{s,\phi=0} = 2\pi\times 3.1$ kHz in double pass with $\phi = 0$, $\gamma_{s,\phi=\pi} = 2\pi\times 1.9$ kHz

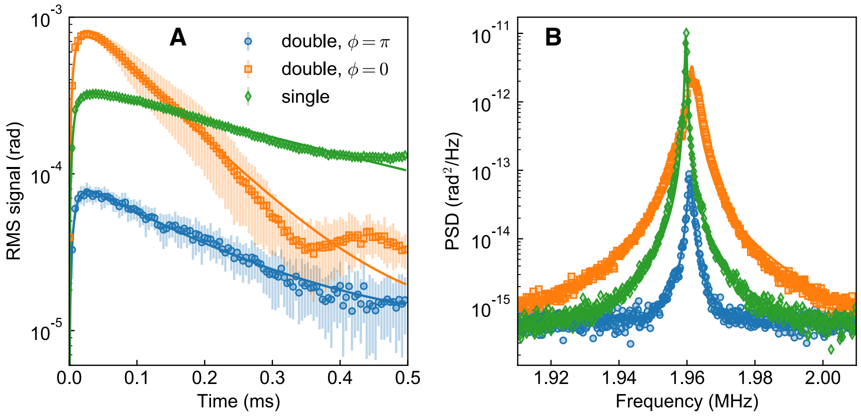

Figure 4.7: Interference of the spin signal in the coupling beam output. (A), root-mean-squared spin signal as a function of time for the three configurations, double pass with $\phi = \pi$, $\phi = 0$, and single pass. Lines are fits with an exponential decay. (B), FFT power spectral densities for the same data as in a. Lines are fits with a Lorentzian model.

in double pass with $\phi = \pi$, and $\gamma_{s,1} = 2\pi \times 0.45$ kHz in single pass. The broadening effect is also very clearly observed in the power spectra of the spin signals which are shown in Fig. 4.7B. The spin linewidths extracted from Lorentzian fits to the power spectra for single pass and double pass $\phi = \pi$ agree reasonably well with the damping rates. Only for double pass with $\phi = 0$, the decay is quite non-exponential such that the spectrum is not well fitted by a Lorentzian lineshape.

The increased damping rate in double pass is expected due to the enhanced spontaneous scattering rate at almost four times the optical intensity. Due to optical loss, the second beam has only about 80% the optical power as the first beam, which should lead to a damping rate of $2\pi \times 1.5$ kHz. However, the measured damping rates in double pass are higher than that. This effect is likely explained by either additional broadening due to light-mediated self-interaction via the loop, or due to inhomogeneous optical light shifts arising from the crossed laser beams.

Although we do not have an independent measurement of the back-action introduced by the coupling beam, observing constructive and destructive interference of the output spin signal clearly indicates leakage of spin information to the environment is suppressed. From the expression for the output field (4.27) it is clear that full cancelation of the spin signal can also occur for nonzero optical loss, if both the laser field and the quantum field undergo the same optical loss as in our experiment. Observing high contrast interference of the spin signal with a contrast > 10 is important because it means that to a high degree both laser fields couple to the same spin wave. Based on the optical roundtrip transmission of $\eta^4 = 0.65$, we estimate a spin back-action reduction to about $1 - \eta^4 = 0.35$. This is already sufficient to reach the quantum-coherent coupling regime as shown in section 4.4.4.

4.3 Details of the experimental setup

In this section we describe specifics of the experiment control system and signal processing for the spin-membrane coupling experiment. A sketch of the detailed experimental setup is shown in Fig. 4.8.

4.3.1 Locks

Polarization interferometer At the output of the polarization interferometer, i.e. after PBS 2 in Fig. 4.8, the two arms must interfere constructively. To lock the phase, we split about 3% of the total power from each arm at PBS 2 and send it to the balanced homodyne detector BHD 1 which measures the relative phase fluctuations between the two beams. The DC part of the detector output is directly used as an error signal to lock the phase difference at BHD 1 to $\pi/2$ by controlling the position of piezo 1. To ensure that the main beam going towards the atomic setup has a phase difference of zero, we place a quarter-wave plate in front of BHD 1 that compensates the $\pi/2$ phase shift of the lock. We use a digital FPGA-based proportional-integral controller [145] which can be set on hold while the coupling beam is off. The coupling beam must for example be switched off during the dipole-trap loading and optical pumping sequence of the atoms.

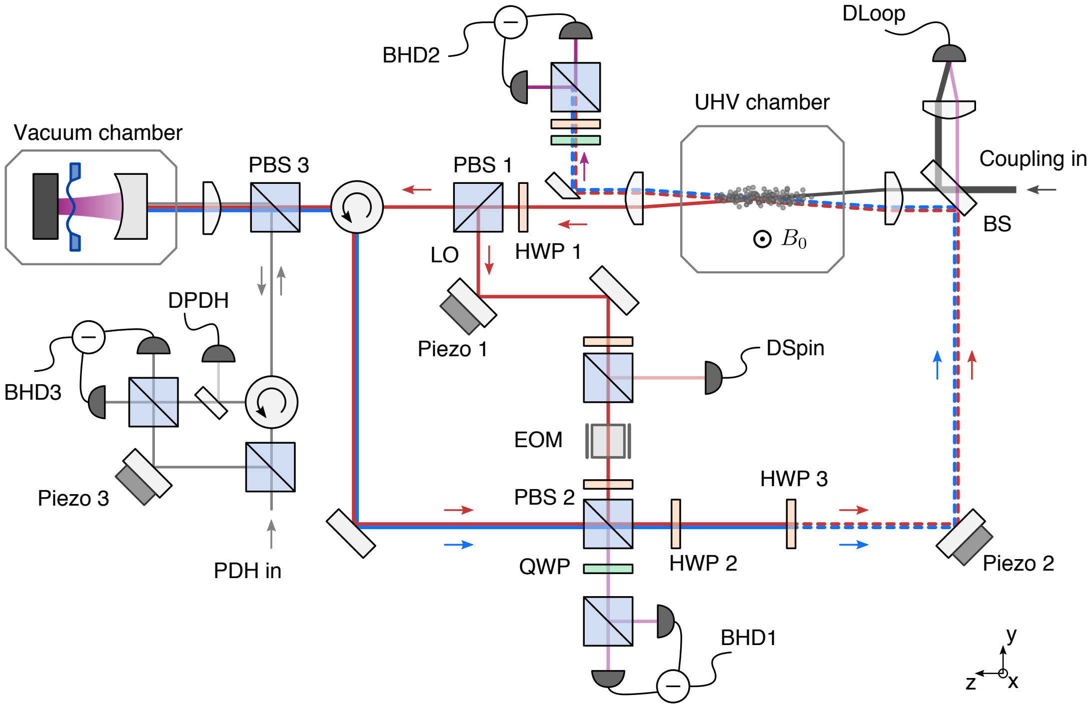

Figure 4.8: Details of the experimental setup. (**A**), Sketch of the experiment showing optical path including relevant polarization optics, detectors and piezo-actuated mirrors for laser phase control. (**B**), Magnified view of the double-pass atom-light interface. Insets show measured beam profiles of coupling beam in the first pass (red) and of the interfering beams (purple).

Cavity lock The optomechanical cavity is locked via the Pound-Drever-Hall technique using a separate laser beam. This lock beam is shifted in frequency by −5 MHz relative to the coupling beam to avoid interference at the mechanical frequency, and in addition provides some optomechanical cooling of the membrane modes by dynamical back-action. Hence, the lock point is adjusted such that the coupling beam is on cavity resonance, and the lock beam is red-detuned. The cavity lock beam is also used to detect the membrane motion by balanced homodyne detection of the reflected beam on BHD3.

Phase lock of the double-pass The phase difference between the two laser beams passing through the atomic ensemble under an angle is stabilized such that they show constructive interference for maximal atom-light coupling (see Fig. 4.3). To achieve this, we stabilize the phase between the light returning from the optomechanical system that is transmitted through the input beam splitter (BS, transmission 2%) and the directly reflected input laser beam. These beams have a transverse displacement of about 2 mm and are first fiber-coupled into a single-mode polarization-maintaining fiber and then detected on the photodetector DLoop. In order to distill the phase information from the large DC signal, we weakly phase-modulate the coupling beam using an electro-optic modulator (EOM, transmission 98 %) placed inside the reference arm of the polarization interferometer. Demodulating the AC part of the beat signal at the modulation frequency (about 700 kHz) generates an error signal which exhibits a zero-crossing for constructive interference of the two beams at the location of the atoms. The feedback loop is closed using another FPGA-based controller that controls the position of piezo 2. Identical to the lock of the polarization interferometer, this lock is paused whenever the coupling beam is switched off.

4.3.2 Signal processing

Signals from the balanced homodyne detector BHD3 measuring the membrane signal and from the direct detector DSpin measuring the spin signal are demodulated at a frequency Ω_0 close to the mechanical frequency Ω_m using a digital lock-in amplifier (Zurich instruments HF2LI). The membrane and spin detector signals normalized to their respective local oscillator powers can be written as

$$D_i(t) = \beta_i X_i(t) + W_i(t) \tag{4.44}$$

where $\beta_m = 8g_0/\kappa$ for the membrane and $\beta_s = \alpha_1\sqrt{\bar{F}_x}$ for the spin. Detector noise is described by the term W_i and includes both optical shot noise and electronic noise. The demodulator outputs the in-phase and quadrature components

$$\begin{aligned} I_i &= \sqrt{2}\langle D_i(t)\cos(\Omega_0 t)\rangle_t, && (4.45)\\ Q_i &= \sqrt{2}\langle D_i(t)\sin(\Omega_0 t)\rangle_t, && (4.46) \end{aligned}$$

respectively, where $\langle\cdot\rangle_t$ denotes temporal averaging with a bandwidth of 40 kHz. We then define the following slowly varying position and momentum quadratures

$$\begin{aligned}
\tilde{X}'_m(t) &= \frac{\sqrt{2}}{\beta_m} I_m(t), && (4.47)\\
\tilde{P}'_m(t) &= \frac{\sqrt{2}}{\beta_m} Q_m(t), && (4.48)\\
\tilde{X}'_s(t) &= \frac{\sqrt{2}}{\beta_s}(\cos(\alpha) I_s(t) + \sin(\alpha) Q_s(t)), && (4.49)\\
\tilde{P}'_s(t) &= \pm\frac{\sqrt{2}}{\beta_s}(\cos(\alpha) Q_s(t) - \sin(\alpha) I_s(t)). && (4.50)
\end{aligned}$$

In the last line $+(-)$ refers to the positive (negative) spin oscillation frequency. The local phase α for the spin quadratures is adjusted to a value of $\alpha = 100°$ in post-processing to optimise the measured spin-membrane correlations for the parametric-gain interaction.

To calculate the number of excitations in each oscillator we use the formula $\tilde{n}_i = (\tilde{X}_i^2 + \tilde{P}_i^2)/2$. Estimates of the symmetrized mechanical power spectral densities are calculated using a fast-Fourier-transform (FFT), i.e.

$$\bar{S}_{XX,m}(\omega) = \frac{1}{M_{\mathrm{sa}} f_{\mathrm{sa}}} |\mathrm{FFT}[I_m(t) + iQ_m(t)](\omega)|^2 \qquad (4.51)$$

where f_{sa} is the sampling rate and M_{sa} is the number of samples of the measurement record.

4.4 Coupled spin-membrane dynamics

In this section, we present a theoretical analysis of the coupled spin-membrane dynamics arising from the light-mediated interaction.

4.4.1 Heisenberg-Langevin equations

Using input-output theory we derive a set of Heisenberg-Langevin equations for the cascaded spin-membrane system that is sketched in Fig. 4.2 [36]. For convenience, we neglect losses in this treatment. The equations of motion for the spin and membrane position and momentum operators read

$$\begin{aligned}
\dot{X}_m &= \quad \Omega_m P_m, && (4.52)\\
\dot{P}_m &= -\Omega_m X_m - \gamma_m P_m - 2g X_s(t-\tau) - \sqrt{4\Gamma_m} X_L^{(\mathrm{in})}(\zeta_2) - \sqrt{2\gamma_m} F_m^{(\mathrm{th})}, && (4.53)\\
\dot{X}_s &= \quad \Omega_s P_s, && (4.54)\\
\dot{P}_s &= -\Omega_s X_s - \gamma_s P_s + 4\Gamma_s \sin(\phi) X_s(t-2\tau) + 2g\cos(\phi) X_m(t-\tau) && (4.55)\\
&\quad - \sqrt{4\Gamma_s}\left[P_L^{(\mathrm{in})}(\zeta_1) + \cos(\phi) P_L^{(\mathrm{in})}(\zeta_3) - \sin(\phi) X_L^{(\mathrm{in})}(\zeta_3)\right] - \sqrt{2\gamma_s} F_s^{(\mathrm{th})}. && (4.56)
\end{aligned}$$

Here, $g = 2\sqrt{\Gamma_m \Gamma_s}$ is the spin-membrane coupling strength, τ is the optical propagation delay between the systems which we assume to be equal for either direction, and $F_m^{(\mathrm{th})}$ and $F_s^{(\mathrm{th})}$ are mechanical and spin thermal noise terms, respectively. Each oscillator is also driven by optical vacuum noise of the input field quadratures $X_L^{(\mathrm{in})}(\zeta_i), P_L^{(\mathrm{in})}(\zeta_i)$ at the different locations ζ_i along the optical path. This leads to quantum back-action of the light that mediates the spin-membrane interaction onto the coupled systems. For the spin oscillator, the optical input terms at the two locations ζ_1 and ζ_3 interfere as can be seen directly in line (4.56). For the membrane there is no such interference as it interacts with the light field only once. Moreover, the two spin-light interactions also enable delayed light-mediated self-interaction of the spin. The effect of this is a modified frequency and linewidth since $X_s(t-2\tau) \approx X_s \cos(2\Omega_s\tau) - P_s \sin(2\Omega_s\tau)$. We thus have a spin frequency shift $\delta\Omega_s = 2\Gamma_s \sin(\phi)\cos(2\Omega_s\tau)$ and a shift of the damping rate $\delta\gamma_s = 4\Gamma_s \sin(\phi)\sin(2\Omega_s\tau)$. Since the atom-light coupling strength is inhomogeneous across the atomic ensemble, this can also lead to inhomogeneous broadening of the spin oscillator if $\phi \mod \pi \neq 0$.

In the following treatment, we assume ϕ to take only the discrete values $0, \pi$. Making a Fourier transform yields

$$\begin{aligned}
\chi_{m,0}(\omega)^{-1} X_m(\omega) + 2g e^{i\omega\tau} X_s(\omega) &= -\sqrt{2\gamma_m} F_m^{(\mathrm{tot})}(\omega) && (4.57)\\
\chi_{s,0}(\omega)^{-1} X_s(\omega) - 2g\cos(\phi) e^{i\omega\tau} X_m(\omega) &= -\sqrt{2\gamma_s} F_s^{(\mathrm{tot})}(\omega), && (4.58)
\end{aligned}$$

with bare (uncoupled) susceptibility defined as

$$\chi_{i,0}(\omega) = \frac{\Omega_i}{\Omega_i^2 - \omega^2 - i\omega\gamma_i}. \quad (4.59)$$

and the combined thermal and optical force terms

$$\begin{aligned} F_m^{(\mathrm{tot})}(\omega) &= F_m^{(\mathrm{th})}(\omega) + \sqrt{\frac{2\Gamma_m}{\gamma_m}} e^{i\omega\tau} X_L^{(\mathrm{in})}(\omega) \qquad (4.60) \\ F_s^{(\mathrm{tot})}(\omega) &= F_s^{(\mathrm{th})}(\omega) + \sqrt{\frac{2\Gamma_s}{\gamma_s}} \left[1 + \cos(\phi) e^{i2\omega\tau}\right] P_L^{(\mathrm{in})}(\omega) \qquad (4.61) \end{aligned}$$

Solving for X_m, X_s yields the solutions

$$\begin{aligned} X_m(\omega) &= \chi_{m,\mathrm{eff}}(\omega) \left[-\sqrt{2\gamma_m} F_m^{(\mathrm{tot})}(\omega) + 2g e^{i\omega\tau} \sqrt{2\gamma_s} \chi_{s,0}(\omega) F_s^{(\mathrm{tot})}(\omega)\right], \qquad (4.62) \\ X_s(\omega) &= \chi_{s,\mathrm{eff}}(\omega) \left[-\sqrt{2\gamma_s} F_s^{(\mathrm{tot})}(\omega) - 2g\cos(\phi) e^{i\omega\tau} \sqrt{2\gamma_m} \chi_{m,0}(\omega) F_m^{(\mathrm{tot})}(\omega)\right] (4.63) \end{aligned}$$

where we have used the effective susceptibilities of the membrane

$$\begin{aligned} \chi_{m,\mathrm{eff}}(\omega)^{-1} &= \chi_{m,0}(\omega)^{-1} + 4g^2 \cos(\phi) e^{i2\omega\tau} \chi_{s,0}(\omega), \qquad (4.64) \\ \chi_{s,\mathrm{eff}}(\omega)^{-1} &= \chi_{s,0}(\omega)^{-1} + 4g^2 \cos(\phi) e^{i2\omega\tau} \chi_{m,0}(\omega). \qquad (4.65) \end{aligned}$$

For the fits of the data in Fig. 5.2A and C of chapter 5 we use the fitting function $a|\chi_{m,\mathrm{eff}}(\omega)|$ with scaling factor a and other fit parameters being $g, \gamma_m, \gamma_s, \Omega_s, \tau$. The argument of $\chi_{m,\mathrm{eff}}$ gives the phase response which is plotted in Figs. 5.2B and D together with the experimental data. The fit of the normal-mode splitting with our theoretical model yields a delay of $\tau = 15$ ns. This value is close to a calculated value of $2/\kappa + d/c = 12$ ns based on the cavity linewidth $\kappa = 2\pi \times 63$ MHz (full width at half-maximum) and optical propagation distance $d = 2$ m between the systems, c being the speed of light. Even though the delay is much shorter than one oscillation period $1/\Omega_{m,s}$, it induces a significant phase shift of the light-mediated coupling that can lead to instabilities.

4.4.2 Normal modes

The normal mode frequencies and damping rates can be obtained more easily from an analysis using the rotating wave approximation, which is a very good approximation because $g, \gamma_i < \Omega_i/10^2$ in the experiment. We perform here the calculation for the positive spin oscillator $\Omega_s > 0$. The coupled equations of motion for the mode operators b_m and b_s in a rotating frame at the center frequency $\bar{\Omega} = (\Omega_m + \Omega_s)/2$ read

$$\begin{aligned} \dot{b}_m &= \left(+i\frac{\delta}{2} - \frac{\gamma_m}{2}\right) b_m - ige^{i\Omega_s\tau} b_s - i\sqrt{\gamma_m} F_m, \qquad (4.66) \\ \dot{b}_s &= \left(-i\frac{\delta}{2} - \frac{\gamma_s}{2}\right) b_s + ig\cos(\phi) e^{i\Omega_m\tau} b_m - i\sqrt{\gamma_s} F_s, \qquad (4.67) \end{aligned}$$

where we defined the spin-membrane detuning $\delta = \Omega_s - \Omega_m$. For the inverted spin oscillator one would replace $b_s \to b_s^\dagger$, $\Omega_s \to -\Omega_s$ and in the second line $g \to -g$. Solving for the eigenvalues of the dynamical matrix gives the frequencies $\Omega_\pm$ and damping rates $\gamma_\pm$ via the relation

$$\Omega_\pm + i\frac{\gamma_\pm}{2} = \bar{\Omega} + i\frac{\gamma_m + \gamma_s}{4} \pm \sqrt{\left(\frac{\delta}{2} + i\frac{\gamma_m - \gamma_s}{4}\right)^2 - g^2 e^{i2\bar{\Omega}\tau} \cos(\phi)}. \qquad (4.68)$$

For illustration, the normal mode frequencies and damping rates are plotted in Figs. 4.9A,C and 4.9B,D, respectively, for a choice of parameters $\gamma_m/g = 0.1$, $\gamma_s/g = 1$ that reflect the situation in the experiment. In Figs. 4.9A,B the delay is set to $\tau = 0$ while in Figs. 4.9C,D we choose $\bar{\Omega}\tau = 0.15$ as in the experiment.

We first discuss the Hamiltonian coupling case ($\phi = \pi$). In a standard instantaneous coupling situation ($\tau = 0$), the normal modes exhibit an avoided crossing at $\delta = 0$ with a splitting of $\Omega_+ - \Omega_- = 2\sqrt{g^2 - (\gamma_m - \gamma_s)^2/16} \approx 2g$. The damping rates are then exactly $\gamma_\pm = (\gamma_m + \gamma_s)/2$ the average of the individual damping rates. With increasing detuning, the normal mode frequencies and damping rates smoothly transform into those of the uncoupled modes (see Fig. 4.9B).

With a small delay $\bar{\Omega}\tau = 0.15$, the situation changes. While the normal mode frequencies are hardly affected, the damping rates change significantly. Looking at Fig. 4.9D (solid lines), we see that the delay induces an asymmetry of the damping rates. The point where both damping rates are equal shifts to positive detunings $\delta > 0$. Moreover, at detunings $\delta < 0$ we see an increased splitting between the damping rates leading to one of them closely approaching zero and even becoming slightly negative for certain detunings. This leads to an instability of the coupled dynamics as observed in Fig. 5.5A of chapter 5.

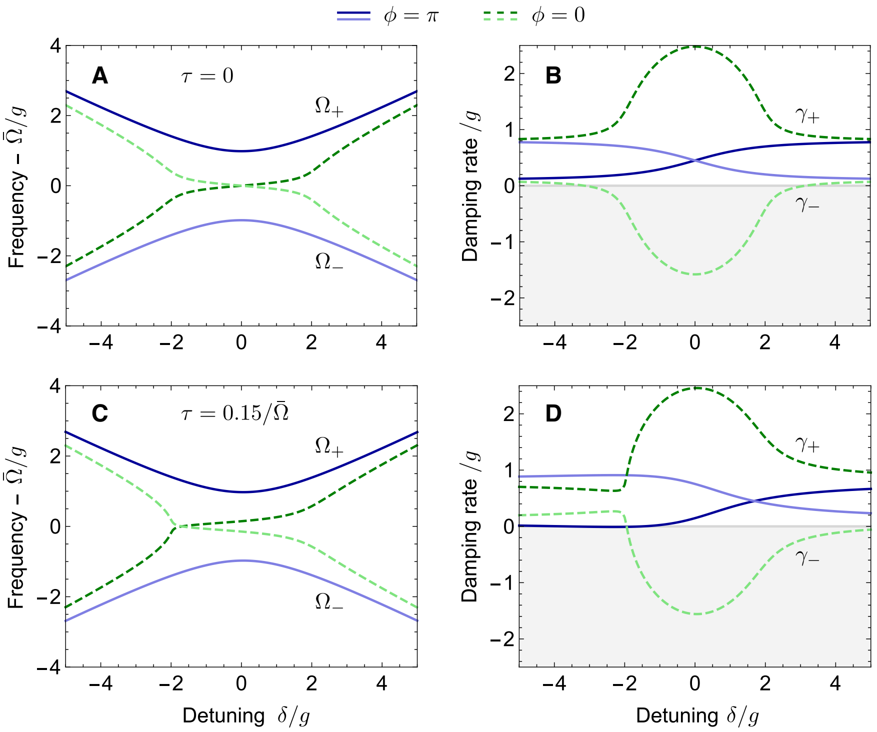

Figure 4.9: Normal mode frequencies (A,C) and damping rates (B,D) as a function of oscillator detuning. The solid blue lines correspond to the Hamiltonian coupling with $\phi = \pi$ while the dashed green lines are for $\phi = 0$. The delay is chosen to be $\tau = 0$ in A,B and $\tau = 0.15/\bar{\Omega}$ in C,D.

For dissipative coupling ($\phi = 0$) the normal modes exhibit level attraction (see Fig. 4.9A, dashed lines). The modes become degenerate only at a single point because of a difference in their individual damping rates. Otherwise the normal modes would merge in the full range $|\delta| < 2g$. The two normal modes exhibit a splitting in terms of their damping rates (see Fig. 4.9B) leading to one strongly damped mode with $\gamma_+ \approx (\gamma_m + \gamma_s)/2 + 2g > 0$ and one amplified mode with $\gamma_- \approx (\gamma_m + \gamma_s)/2 - 2g < 0$. In the parametric-gain configuration ($\phi = \pi$, $\Omega_s = -\Omega_m$) these modes correspond to the squeezed and anti-squeezed modes, respectively. Like in the Hamiltonian coupling, a finite delay introduces an asymmetry both of the degeneracy point of the mode frequencies as well as in the detuned damping rates (see Fig.s 4.9C,D).

In Fig. 5.5 of chapter 5, we globally fit a function $a + b|\chi_{m,\text{eff}}(\omega)|^2$ to the experimental data in panels A and D that exhibit avoided crossings. The fits yields the coupling strength g, detuning δ, linewidths $\gamma_{s/m}$ and delay τ which we use to calculate the theoretical normal mode frequencies $\Omega_\pm$ which are drawn as dashed lines. The data in panels B and C are not fitted, because the dynamics are unstable in these configurations and thus do not reach a steady state. Instead, to calculate the theory curves for B and C we use the same parameters obtained for the fits to the data in A and D, respectively.

4.4.3 Simulation of the covariance dynamics

To simulate the two-mode thermal noise squeezing in Fig. 5.4, we solve the time-dependent Lyapunov equation [95, 36]

$$\dot{\Sigma} = F\Sigma + \Sigma F^T + N, \tag{4.69}$$

for the symmetrized covariance matrix $\Sigma_{jk} = \langle Q_j Q_k + Q_k Q_j \rangle /2 - \langle Q_j \rangle \langle Q_k \rangle$, where $Q = (X_m, P_m, X_s, P_s)$. The drift matrix F and diffusion matrix N are obtained from the master equation (4.26) written in the form

$$\dot{\rho} = -\sum_{j,k} A_{jk} [Q_j, Q_k \rho] + \text{h.c.}, \tag{4.70}$$

The expressions for F and N are [95, 36]

$$F = 2J\,\text{Im}\left\{A\right\}, \quad N = J\,\text{Re}\left\{A + A^T\right\} J^T, \tag{4.71}$$

with commutator matrix $J_{jk} = -i[Q_j, Q_k]$. In the simulation, we choose the experimental parameters as listed in table 4.1. They correspond to $2g = 2\pi \times 5.2$ kHz due to a slight reduction of the spin pumping efficiency in the inverted configuration. Moreover, we find best agreement with $\gamma_s = 2\pi \times 1$ kHz, implying that the spin linewidth observed in the spectroscopy is mostly due to inhomogeneous broadening. To simulate detector noise, we add $\bar{n}_\text{det} = 6 \times 10^3$ to the covariance entries $\langle X_s^2 \rangle - \langle X_s \rangle^2$ and $\langle P_s^2 \rangle - \langle P_s \rangle^2$.

4.4.4 Reaching the quantum regime

In this section we estimate the performance of the presented experimental setup in the quantum regime. Our criterion for quantum coherent coupling in the Hamiltonian coupling ($\phi = \pi$) is the ability to achieve entanglement using the parametric-gain interaction

Parameter	Value
Ω_m	$2\pi \times 1.957$ MHz
Γ_m	$2\pi \times 7.5$ kHz
γ_m	$2\pi \times 0.4$ kHz
$\bar{n}_m$	1.5×10^4
Ω_s	$2\pi \times 1.957$ MHz
Γ_s	$2\pi \times 0.43$ kHz
γ_s	$2\pi \times 1$ kHz
$\bar{n}_s$	0
η	0.9
ϕ	π

Table 4.1: Experimental parameters used for the simulation of two-mode thermal noise squeezing.

which can be realized with a negative-mass spin oscillator [69]. For Gaussian states we can quantify entanglement as a violation of the non-separability criterion [100, 101]

$$\xi := \langle X_-^2 \rangle + \langle P_+^2 \rangle < 1, \tag{4.72}$$

where we defined the collective quadratures $X_\pm = (X_s \pm X_m)/\sqrt{2}$, $P_\pm = (P_s \pm P_m)/\sqrt{2}$.

Next to the coherent coupling, the effective master equation for the light-coupled system

$$\begin{aligned} \dot{\rho} \;&=\; \frac{1}{i\hbar}[H_0 + H_{\text{eff}}, \rho] && (4.73) \\ &+ \sum_{i=s,m} \Big(\gamma_{i,0}(\bar{n}_i + 1)\mathcal{D}[b_i]\rho + \gamma_{i,0}\mathcal{D}[b_i^\dagger]\rho \Big) && (4.74) \\ &+ \sum_{i=s,m} \Big(\gamma_{i,\text{ba}}\mathcal{D}[b_i]\rho + \gamma_{i,\text{ba}}\mathcal{D}[b_i^\dagger]\rho \Big) && (4.75) \end{aligned}$$

features various dissipative terms. Apparently, for each system there are thermal (second line) and an optical (third line) decoherence processes. The thermal decoherence rates are given by $\gamma_{i,\text{th}} = \gamma_{i,0}(\bar{n}_i + 1/2)$, where $\gamma_{i,0}$ is the damping rate and $\bar{n}_i$ is the thermal bath occupation number of system i. The optical back-action decoherence rates are $\gamma_{m,\text{ba}} = \eta^2\Gamma_m$ for the membrane and $\gamma_{s,\text{ba}} = (1 - \eta^4)\Gamma_s$ for the spin, where we have assumed an average amplitude transmission coefficient η per path. In the following, we define the total decoherence rates $\gamma_{i,\text{tot}}$ for each oscillator as the sum of their independent thermal and optical back-action decoherence rates, i.e. $\gamma_{i,\text{tot}} = \gamma_{i,\text{th}} + \gamma_{i,\text{ba}}$.

We now calculate the amount of entanglement realized by the two-mode squeezing interaction in the Hamiltonian configuration with negative-mass spin oscillator ($\phi = \pi$, $\Omega_s = -\Omega_m$). Assuming $\gamma_{m,s} \ll \Omega_m$, we can apply a rotating wave approximation such that the effective Hamiltonian reduces to $H_{\text{eff}} = i\hbar g(b_s^\dagger b_m^\dagger - b_s b_m)$ with a different phase convention than before. Transforming into the basis $X_\pm$, $P_\pm$, we derive a set of coupled differential equations for the entries of the spin-membrane covariance matrix, i.e.

$$\frac{d}{dt}\langle X_+^2\rangle = +\frac{4g-\gamma_{s,0}-\gamma_{m,0}}{2}\langle X_+^2\rangle + \frac{\gamma_{s,0}-\gamma_{m,0}}{2}\langle X_+X_-\rangle + \frac{\gamma_{s,\mathrm{tot}}+\gamma_{m,\mathrm{tot}}}{2} \tag{4.76}$$

$$\frac{d}{dt}\langle X_-^2\rangle = -\frac{4g+\gamma_{s,0}+\gamma_{m,0}}{2}\langle X_-^2\rangle + \frac{\gamma_{s,0}-\gamma_{m,0}}{2}\langle X_+X_-\rangle + \frac{\gamma_{s,\mathrm{tot}}+\gamma_{m,\mathrm{tot}}}{2} \tag{4.77}$$

$$\frac{d}{dt}\langle X_+X_-\rangle = -\frac{\gamma_{s,0}+\gamma_{m,0}}{2}\langle X_+X_-\rangle + \frac{\gamma_{s,0}-\gamma_{m,0}}{4}(\langle X_+^2\rangle + \langle X_-^2\rangle) - \frac{\gamma_{s,\mathrm{tot}}-\gamma_{m,\mathrm{tot}}}{2} \tag{4.78}$$

Note that in rotating-wave approximation, $\langle P_\pm^2\rangle = \langle X_\mp^2\rangle$. The above equations imply that X_- and P_+ are squeezed while X_+ and P_- are anti-squeezed. If the damping rates $\gamma_{i,0}$ or total decoherence rates $\gamma_{i,\mathrm{tot}}$ are unequal, the squeezed and anti-squeezed quadratures deviate slightly from X_-, P_+ and X_+, P_-, respectively, as we see from the terms involving the covariance $\langle X_+X_-\rangle$. Thermal and optical back-action noise appears in form of the constant terms $\gamma_{s,\mathrm{tot}} + \gamma_{m,\mathrm{tot}}/2$. Assuming $(\gamma_{s,0} - \gamma_{m,0})/4g \ll 1$ we find that in steady state,

$$\langle X_-^2\rangle \approx \frac{\gamma_{s,\mathrm{tot}}+\gamma_{m,\mathrm{tot}}}{4g+\gamma_{s,0}+\gamma_{m,0}} + \mathcal{O}\left(\frac{\gamma_{s,0}-\gamma_{m,0}}{4g}\right) \tag{4.79}$$

Entanglement in terms of equation (4.72) is equivalent to reduction of $\langle X_-^2\rangle$ below 1/2. Consequently, to generate entanglement the coupling strength g needs to exceed the average of all decoherence rates on both the mechanical and spin system, i.e. $2g > \gamma_{s,\mathrm{tot}} + \gamma_{m,\mathrm{tot}}$, as

$$\xi = \left(\frac{1}{1+2\bar{n}_{\mathrm{eff}}} + C\right)^{-1} \tag{4.80}$$

where $C = 2g/(\gamma_{m,\mathrm{tot}}+\gamma_{s,\mathrm{tot}})$ is a quantum cooperativity parameter and $\bar{n}_{\mathrm{eff}} = (\gamma_{m,\mathrm{tot}} + \gamma_{s,\mathrm{tot}})/(\gamma_{m,0}+\gamma_{s,0}) - 1/2$ is the average occupation number of the collective mode. The entanglement criterion $\xi < 1$ thus requires $C > 1$, which is equivalent to the condition for quantum coherent coupling of ref. [6].

With a meaningful criterion for quantum coherent coupling, we now estimate the required system parameters to reach this regime. Clearly, thermal noise is the largest contribution to mechanical decoherence. For the current room temperature ($T_m = 295$ K) implementation with $\bar{n}_m \approx k_B T_m/(\hbar\Omega_m) = 3\times10^6$ and a mechanical quality factor of $Q_m = 1.3\times10^6$, we have $\gamma_{m,\mathrm{th}} \approx \gamma_{m,0}\bar{n}_m \approx 2\pi\times 6$ MHz. Lowering the bath temperature to $T_m = 5$ K by cooling with liquid helium and increasing Q_m to 5×10^7 could reduce the thermal decoherence rate to $\gamma_{m,\mathrm{th}} \approx 2\pi\times 2$ kHz. Such quality factors have recently been demonstrated by soft-clamping of mechanical modes in a high-stress silicon nitride membrane [59]. At this level, $\gamma_{m,\mathrm{th}}$ would be of similar magnitude or even lower than the optomechanical measurement rate $\Gamma_m \approx 2\pi\times 8$ kHz in the current experiment, which is also equal to the optical back-action rate $\gamma_{m,\mathrm{ba}}$ for the membrane. Hence, the optomechanical system would reach the regime of large quantum cooperativity $\Gamma_m/\gamma_{m,\mathrm{th}} > 1$ where mechanical fluctuations are dominated by optical back-action instead of thermal noise.

Tuning of the atom-light interaction is achieved by controlling the laser detuning Δ_a from the atomic transition. Both the spin measurement rate Γ_s and the spontaneous photon scattering rate γ_{sc} scale with $\Phi_L \Delta_a^{-2}$. Consequently, $g \propto \sqrt{\Gamma_s} \propto \sqrt{\Phi_L}\Delta_a^{-1}$ can be increased relative to γ_{sc} at large detuning. Since the laser input power Φ_L also affects the optomechanical measurement rate it is kept fixed in this optimization. For a highly spin-polarized cold atomic ensemble, one can assume $\bar{n}_s \approx 0$ which eliminates thermal noise. The spin back-action rate $\gamma_{s,\text{ba}} = (1-\eta^4)\Gamma_s$ is suppressed due to destructive interference in the loop. In the experiment, a system-to-system optical power transmission of $\eta^2 \approx 0.8$ is achieved, resulting in optical back-action suppression down to $1 - \eta^4 \approx 0.35$.

For quantum coherent spin-membrane coupling we need to make $g = (\eta^2+\eta^4)\sqrt{\Gamma_s \Gamma_m}$ larger than $\gamma_{m,\text{tot}}$ and $\gamma_{s,\text{tot}}$. Since there is no back-action cancellation for the membrane, the requirement $g > \gamma_{m,\text{tot}}$ leads to $\Gamma_s \geq \Gamma_m$. This constraint limits the maximum possible laser-atom detuning and therefore entails a minimum spontaneous scattering rate, which reduces spin coherence. A large spin cooperativity is thus crucial for strong coupling in the hybrid system.

In Fig. 4.10 we show calculated rates of the spin-membrane system as a function of the laser-atom detuning Δ_a. Here, we assume $Q_m = 5 \times 10^7$ and a mechanical bath temperature of $T_m = 5$ K. Together with modest optomechanical damping such that $\gamma_{m,0} = 2\pi \times 300$ Hz, this would result in an effective phonon occupation of $\bar{n}_m \approx 7$.

Fig. 4.10A shows the calculated rates for an experimental setup with a loop on the spin, suppressing its optical back-action noise. The black circle is the experimentally determined value of $g = 2\pi \times 3.1$ kHz (see chapter 5), obtained at $\Delta_a/2\pi = -80$ GHz, which agrees very well with the calculated curve. The mechanical damping rate $\gamma_{m,0} = 2\pi \times 300$ Hz is indicated by the blue diamond. The experimentally determined spin damping rate (red square) $\gamma_{s,0} = 2\pi \times 1.5$ kHz is a factor of two larger than the theoretical value $2\pi \times 0.7$ kHz which means that other decoherence effects are present. We note that the spin linewidth (4 kHz) extracted from the normal-mode splitting data is even larger than this value. A possible explanation for this is very likely the more complicated atom-light interface with two crossed laser beams. This could lead to light-induced broadening caused by polarization gradients or atomic self-interaction.

The margin between g and the average damping rate $(\gamma_{s,0} + \gamma_{m,0})/2$ for strong coherent coupling is colored light purple. Dark purple denotes the margin between g and the total decoherence rate $(\gamma_{s,\text{tot}} + \gamma_{m,\text{tot}})/2$ for quantum coherent coupling. Obviously, strong coupling is easier to achieve than quantum coherent coupling, for which there is only a narrow parameter window. Clearly, both the spin damping rate and the mechanical back-action rate are strongly limiting the achievable cooperativity C. Hence, we also show the calculated rates in the cascaded coupling scenario with a loop on the optomechanical system instead of the atomic ensemble (see Fig. 4.10B). Here, optical back-action is suppressed on the membrane, but not on the spin. Moreover, the spin's damping rate decreases because of the reduced scattering rate in a single laser beam. For the membrane, increase of the damping rate can be compensated by a smaller laser-cavity detuning. In this situation the cooperativity C scales more favorably with detuning, leading to a wider region where quantum coherent coupling is possible. Finally, we remark that this situation would improve even more if quantum back-action was canceled on both systems. This requires double pass light-matter interactions on both systems [36] and is therefore more difficult to implement, but possible in principle.

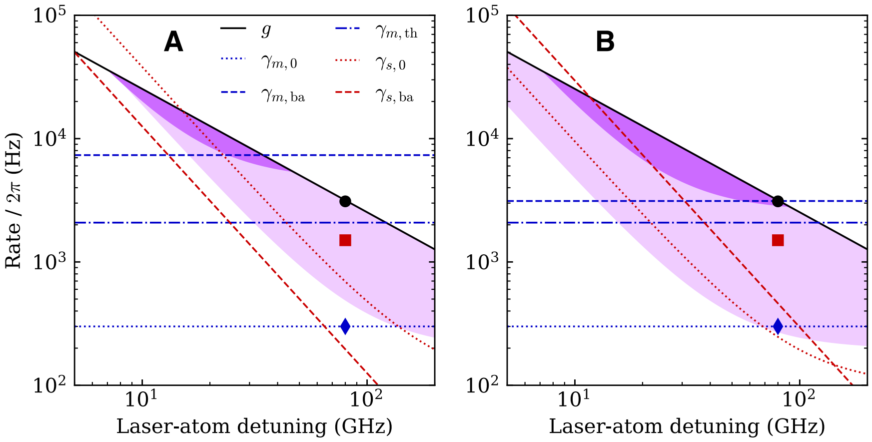

Figure 4.10: Rates of the coupled spin-membrane system as a function of the laser-atom detuning Δ_a. (A), Configuration with quantum noise cancelation on spin. (B), Configuration with quantum noise cancelation on membrane. The lines are calculated rates based on independently measured experimental parameters. The points correspond to experimentally observed parameters for g (black circle), $\gamma_{s,0}$ (red square) and $\gamma_{m,0}$ (blue diamond). The light purple shaded area corresponds to the margin between g and the mean damping rate $(\gamma_{s,0} + \gamma_{m,0})/2$, indicating strong coupling. The margin between g and the total decoherence rate $(\gamma_{s,\mathrm{tot}} + \gamma_{m,\mathrm{tot}})/2$ for quantum coherent coupling is given by the dark purple area.

4.4.5 Dissipative dynamics

In this section we aim to clarify the dynamics in the dissipative coupling regime at $\phi = 0$. For convenience, we neglect losses in this treatment. Here, we generalize the local light-matter interactions like in chapter 1 such that light-matter interaction Hamiltonian can be written as

$$H_{\mathrm{int}} = \hbar \left[\sqrt{2\Gamma_s} a_L(\zeta_1)^\dagger B_s + \sqrt{2\Gamma_m} a_L(\zeta_2)^\dagger B_m + \sqrt{2\Gamma_s} a_L(\zeta_3)^\dagger e^{i\phi} B_s \right] + \mathrm{H.c.} \tag{4.81}$$

Here, we have defined the local operators $B_i = \mu_i b_i + \nu_i b_i^\dagger$ with complex coefficients μ_i, ν_i ($|\mu_i|^2 + |\nu_i|^2 = 1$) that define the Stokes and anti-Stokes scattering amplitudes of the light-matter interactions for the spin and optomechanical systems [36]. In the experiment, $B_s = iX_s$ (i.e. $\mu_s = \nu_s = \mathrm{i}/\sqrt{2}$) and $B_m = X_m$ ($\mu_m = \nu_m = 1/\sqrt{2}$). An imbalance between Stokes and anti-Stokes scattering amplitudes could be implemented in the following way. For the membrane, the coupling beam can be detuned relative to the cavity resonance and a cavity with smaller linewidth would have to be chosen. For the spin, one can reduce the laser detuning such that the tensor interaction becomes stronger, which effectively introduces the required scattering imbalance[24].

We restate the effective master equation (4.19)

$$\dot{\rho} = \frac{1}{i\hbar}[H_{\mathrm{eff}}, \rho] + \mathcal{D}[J]\rho \tag{4.82}$$

Using the more general light-matter interaction (4.81), the effective Hamiltonian is

$$H_{\text{eff}} = \hbar \frac{2\sqrt{\Gamma_s \Gamma_m}}{2i} (B_m^\dagger B_s + e^{-i\phi} B_s^\dagger B_m) + \text{H.c.} \tag{4.83}$$

and the collective jump operator reads

$$J = \sqrt{2\Gamma_m} B_m + \sqrt{2\Gamma_s}(1 + e^{i\phi}) B_s \tag{4.84}$$

For an imbalance in Stokes and anti-Stokes scattering amplitudes μ_i, ν_i, such that $|\mu_i|^2 - |\nu_i|^2 > 0$, the steady state of the dissipative evolution can be engineered to be a two-mode squeezed state [24].

Assuming counter-rotating oscillators $\Omega_m = -\Omega_s = \Omega$, we can split $J = J_+ e^{-i\Omega t} + J_- e^{i\Omega t}$ into its positive and negative frequency components, where

$$\begin{aligned} J_+ &= \sqrt{2\Gamma_m}\mu_m b_m + \sqrt{2\Gamma_s}\nu_s (1 + e^{i\phi}) b_s^\dagger && (4.85) \\ J_- &= \sqrt{2\Gamma_s}\mu_s (1 + e^{i\phi}) b_s + \sqrt{2\Gamma_m}\nu_m b_m^\dagger && (4.86) \end{aligned}$$

In the rotating wave approximation the dissipative master equation becomes

$$\mathcal{D}[J]\rho \approx \mathcal{D}[J_+]\rho + \mathcal{D}[J_-]\rho \tag{4.87}$$

The steady states of $\mathcal{D}[J_\pm]$ are two-mode squeezed states characterized by $J_\pm |\psi_\pm\rangle = 0$ [24]. However, the two squeezing channels only work together if $[J_+, J_-] = 0$, otherwise they compete and the steady state is not squeezed. In the standard single-pass configuration for dissipative entanglement generation, we omit the second spin-light interaction and get

$$\begin{aligned} J_+ &= \sqrt{2\Gamma_m}\mu_m b_m + \sqrt{2\Gamma_s}\nu_s b_s^\dagger && (4.88) \\ J_- &= \sqrt{2\Gamma_s}\mu_s b_s + \sqrt{2\Gamma_m}\nu_m b_m^\dagger && (4.89) \end{aligned}$$

Choosing $\Gamma_m = \Gamma_s$ and $\mu_m = \mu_s, \nu_m = \nu_s$ the condition $[J_+, J_-] = 0$ is easily satisfied. In the cascaded configuration with loop, the commutator is

$$[J_+, J_-] = 2\Gamma_m \mu_m \nu_m - 2\Gamma_s \mu_s \nu_s (1 + e^{i\phi})^2 \tag{4.90}$$

We see that in particular when $\mu_m = \nu_m = 1/\sqrt{2}$, $\mu_s = \nu_s = i/\sqrt{2}$, the difference turns into a sum of positive terms, which must be positive. Hence, it is crucial that $\mu_s \nu_s$ has the same complex phase as $\mu_m \nu_m$. In that case, the effective Hamiltonian is zero, irrespective of ϕ, and the dissipative dynamics are equivalent to the single-pass configuration.

For completeness, we also give an explicit expression for the effective Hamiltonian at $\phi = \pi$,

$$H = -i\hbar g(\beta_{\text{BS}} b_m^\dagger b_s - \beta_{\text{BS}}^* b_m b_s^\dagger) - i\hbar g(\beta_{\text{PG}} (b_m b_s)^\dagger - \beta_{\text{PG}}^* b_m b_s) \tag{4.91}$$

where the first term corresponds to the beam-splitter Hamiltonian H_{BS} with weight $\beta_{\text{BS}} = \mu_m^* \mu_s - \nu_s^* \nu_m$. The second term is the parametric-gain Hamiltonian with weight $\beta_{\text{PG}} = \mu_m^* \nu_s - \mu_s^* \nu_m$. In the experimental configuration with $\mu_m = \nu_m = 1/\sqrt{2}$ and $\mu_s = \nu_s = i/\sqrt{2}$, we have $\beta_{\text{BS}} = i$ and $\beta_{\text{PG}} = i$.

4.5 Conclusion

In summary, we have presented an experimental setup for coupling an atomic spin ensemble and a membrane oscillator using a free-space laser beam. The optical path utilizes a polarization interferometer to map between the Stokes vector, to which the spin couples, and optical field quadratures relevant for the optomechanical interaction. This allows us to reduce the setup to a cascaded quantum system with loops that can be analyzed in the framework of chapter 1. We analyzed the coupled dynamics based on the effective master equation and derived normal mode spectra for Hamiltonian and dissipative coupling configurations. Further, we investigated the possibility for the setup to generate spin-membrane entanglement via two-mode squeezing. The condition for entanglement was identified to be equivalent to the quantum-coherent-coupling condition [6], for which the coherent coupling strength must exceed the average thermal and back-actio decoherence rates of the two systems. This regime is within reach if both the mechanical quality factor can be increased and if the mechanical bath temperature is reduced by cryogenic cooling. We also presented a detailed theoretical analysis of the double-pass spin-light interface, which was found to give rise to multiple spin waves. Coupling between different spin waves could be a source of noise that has to be taken into account when considering quantum dynamics. Finally, we presented data that show strong interference of the spin signal in the output field when the loop phase is varied. This is a means to suppress leakage of spin information into the output field, which is a necessary condition for the observation of quantum back-action cancellation.

Chapter 5

Light-mediated strong coupling between a mechanical oscillator and atomic spins one meter apart

Engineering strong interactions between quantum systems is essential for many phenomena of quantum physics and technology. Typically, strong coupling relies on short-range forces or on placing the systems in high-quality electromagnetic resonators, restricting the range of the coupling to small distances. We used a free-space laser beam to strongly couple a collective atomic spin and a micromechanical membrane over a distance of one meter in a room-temperature environment. The coupling is highly tunable and allows the observation of normal-mode splitting, coherent energy exchange oscillations, two-mode thermal noise squeezing and dissipative coupling. Our approach to engineering coherent long-distance interactions with light makes it possible to couple very different systems in a modular way, opening up a range of opportunities for quantum control and coherent feedback networks.

This chapter has been published in [71].

5.1 Introduction

Many of the recent breakthroughs in quantum science and technology rely on engineering strong, controllable interactions between quantum systems. In particular, Hamiltonian interactions that generate reversible, bidirectional coupling play an important role for creating and manipulating non-classical states in quantum metrology [44], simulation [55], and information processing [194]. For systems in close proximity, strong Hamiltonian coupling is routinely achieved, prominent examples being atom-photon coupling in cavity quantum electrodynamics [10] and coupling of trapped ions [1] or solid-state spins [2] via short-range electrostatic or magnetic forces. At macroscopic distances, however, the observation of strong Hamiltonian coupling is not only hampered by a severe drop in the interaction strength, but also by the fact that it becomes increasingly difficult to prevent information leakage from the systems to the environment, which renders the interaction dissipative [7]. Overcoming these challenges would make Hamiltonian interactions available for reconfigurable long-distance coupling in quantum networks [10] and hybrid quantum systems [42, 45], which so far employ mostly measurement-based or dissipative interactions.

A promising strategy to reach this goal uses one-dimensional waveguides or free-space laser beams over which quantum systems can couple via the exchange of photons. Such cascaded quantum systems [73] have attracted interest in the context of chiral quantum optics [20, 21] and waveguide quantum-electrodynamics [23]. A fundamental challenge in this approach is that the same photons that generate the coupling eventually leak out, thus allowing the systems to decohere at an equal rate. For this reason, light-mediated coupling is mainly seen today as a means for unidirectional state-transfer [12, 195, 196], or entanglement generation by collective measurement [28, 197, 14] or dissipation [25]. Decoherence by photon loss can be suppressed if the waveguide is terminated by mirrors to form a high quality resonator, which has enabled coherent coupling of superconducting qubits [29, 32], atoms [30], or atomic mechanical oscillators [31] in mesoscopic setups. However, stability constraints and bandwidth limitations make it difficult to extend resonator-based approaches to larger distances. Despite recent advances with coupled cavity arrays [33, 34], strong bi-directional Hamiltonian coupling mediated by light over a truly macroscopic distance remains a challenge.

We pursue an alternative approach to realize long-distance Hamiltonian interactions which relies on connecting two systems by a laser beam in a loop geometry [38, 36]. Through the loop the systems can exchange photons, realizing a bidirectional interaction. Moreover, the loop leads to an interference of quantum noise introduced by the light field. For any system that couples to the light twice and with opposite phase, quantum noise interferes destructively and associated decoherence is suppressed. At the same time information about that system is erased from the output field. In this way the coupled systems can effectively be closed to the environment, even though the light field mediates strong interactions between them. Since the coupling is mediated by light, it allows systems of different physical nature to be connected over macroscopic distances. Furthermore, by manipulating the light field in between the systems, one can reconfigure the interaction without having to modify the quantum systems themselves. These features will be useful for quantum networking [10].

We use this scheme to couple a collective atomic spin and a micromechanical membrane held in separate vacuum chambers, realizing a hybrid atom-optomechanical system [42]. First experiments with such setups recently demonstrated sympathetic cooling [47, 50], quantum back-action evading measurement [51] and entanglement [198]. Here, we realize strong Hamiltonian coupling and demonstrate the versatility of light-mediated interactions: we engineer beam-splitter and parametric-gain Hamiltonians and switch from Hamiltonian to dissipative coupling by applying a phase shift to the light field between the systems. This high level of control in a modular setup gives access to a unique toolbox for designing hybrid quantum systems [45] and coherent feedback loops for advanced quantum control strategies [107].

5.2 Description of the coupling scheme

In the experimental setup (Fig. 5.1A and chapter 4), the atomic ensemble consists of $N = 10^7$ laser-cooled Rubidium-87 atoms in an optical dipole trap. The atoms form a collective spin $\mathbf{F} = \sum_{i=1}^{N} \mathbf{f}^{(i)}$ with $\mathbf{f}^{(i)}$ being the $f = 2$ ground state spin vector of atom *i*. Optical pumping polarizes $\mathbf{F}$ along an external magnetic field $\mathbf{B_0}$ in the x-direction such that the spin acquires a macroscopic orientation $\bar{F}_x = -fN$. The small-amplitude dynamics of the transverse spin components F_y, F_z are well approximated by a harmonic oscillator [39] with position $X_s = F_z/\sqrt{|\bar{F}_x|}$ and momentum $P_s = F_y/\sqrt{|\bar{F}_x|}$. It oscillates at the Larmor frequency $\Omega_s \propto B_0$, which is tuned by the magnetic field strength. A feature of the spin system is that it can realize such an oscillator with either positive or negative effective mass [69, 51]. This is achieved by reversing the orientation of $\mathbf{F}$ with respect to $\mathbf{B_0}$, which reverses the sense of rotation of the oscillator in the X_s, P_s-plane (Fig. 5.1B). This feature allows us to realize different Hamiltonian dynamics with the spin coupled to the membrane.

The spin interacts with the coupling laser beam through an off-resonant Faraday interaction [39] $H_s = 2\hbar\sqrt{\Gamma_s/\bar{S}_x}X_sS_z$, which couples X_s to the polarization state of the light, described by the Stokes vector $\mathbf{S}$. Initially, the laser is linearly polarized along x with $\bar{S}_x = \Phi_L/2$, where Φ_L is the photon flux. The strength of the atom-light coupling depends on the spin measurement rate $\Gamma_s \propto d_0\Phi_L/\Delta_a^2$, which is proportional to the optical depth $d_0 \approx 300$ of the atomic ensemble. Choosing a large laser-atom detuning $\Delta_a = -2\pi \times 80$ GHz suppresses spontaneous photon scattering while maintaining a sizable coupling.

The mechanical oscillator is the $(2, 2)$ square drum mode of a silicon-nitride membrane at a vibrational frequency of $\Omega_m = 2\pi \times 1.957$ MHz with a quality factor of 1.3×10^6 [40]. It is placed in a short single-sided optical cavity to enhance the optomechanical interaction while maintaining a large cavity bandwidth for fast and efficient coupling to the external light field. Radiation pressure couples the membrane displacement X_m to the amplitude fluctuations X_L of the light entering the cavity on resonance, with Hamiltonian $H_m = 2\hbar\sqrt{\Gamma_m}X_mX_L$ [56]. Here, we defined the optomechanical measurement rate $\Gamma_m = (4g_0/\kappa)^2\Phi_m$ that depends on the vacuum optomechanical coupling constant g_0, cavity linewidth κ, and photon flux Φ_m entering the cavity (see section 4.1)). In the present setup, the optomechanical cavity is mounted in a room temperature vacuum chamber, making thermal noise the dominant noise source of the experiment.

The light-field mediates a bidirectional coupling between spin and membrane. A spin displacement X_s is mapped by H_s to a polarization rotation $S_y = 2\sqrt{\Gamma_s\bar{S}_x}X_s$ of the light. A polarization interferometer (Fig. 5.1A) converts this to an amplitude modulation $X_L \approx S_y/\sqrt{\bar{S}_x}$ at the optomechanical cavity, resulting in a force $\dot{P}_m = -4\sqrt{\Gamma_m\Gamma_s}X_s$ on the membrane. Conversely, a membrane displacement X_m is turned by H_m into a phase-modulation $P_L = -2\sqrt{\Gamma_m}X_m$ of the cavity output field. The interferometer converts this to a polarization rotation $S_z \approx \sqrt{\bar{S}_x}P_L$, resulting in a force $\dot{P}_s = 4\sqrt{\Gamma_s\Gamma_m}X_m$ on the spin. A small angle between the laser beams in the two atom-light interactions prevents light from going once more to the membrane. Consequently, the cascaded setup promotes a bidirectional spin-membrane coupling. A fully quantum mechanical treatment (cf. section 4.1) confirms this picture and predicts a spin-membrane coupling strength $g = (\eta^2 + \eta^4)\sqrt{\Gamma_s\Gamma_m}$, accounting for an effective optical power transmission $\eta^2 \approx 0.8$ between the systems.

The light-mediated interaction can be thought of as a feedback loop that transmits a spin excitation to the membrane, whose response then acts back on the spin, and vice versa (Fig. 5.1B). After one round-trip, the initial signal has acquired a phase ϕ, the loop phase. The discussion above refers to a vanishing loop phase $\phi = 0$ and shows

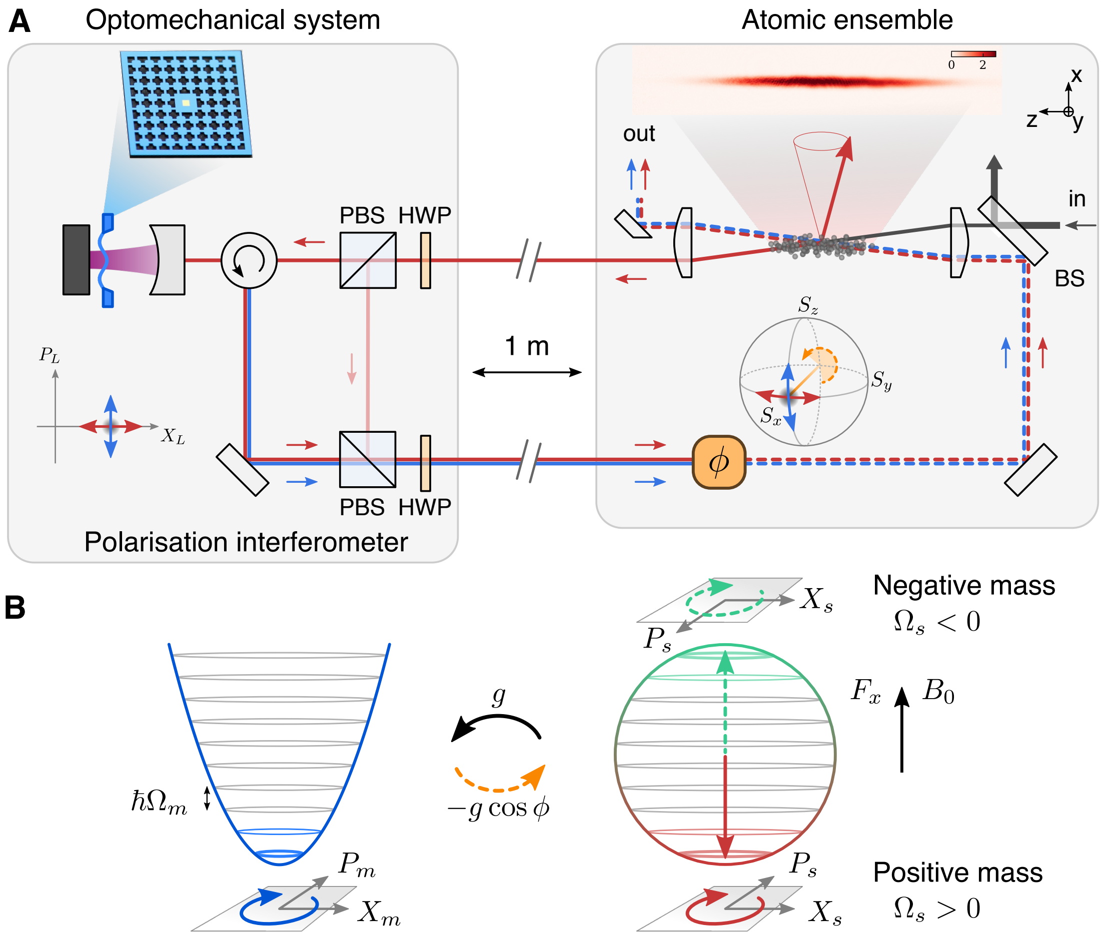

Figure 5.1: Schematic setup for long-distance Hamiltonian coupling. (**A**), Cascaded coupling of an atomic spin ensemble (right) and a micromechanical membrane (left) by a free-space laser beam. The pictures show the silicon-nitride membrane embedded in a silicon chip with phononic crystal structure and a side-view absorption image of the atomic cloud (color bar: optical density). The laser beam first carries information from the atoms to the membrane and then loops back to the atoms such that it mediates a bidirectional interaction. A polarization interferometer (PBS: polarizing beam-splitter, HWP: half-wave plate) maps between the Stokes vector **S** defining the polarization state of light at the atoms and field quadratures X_L, P_L relevant for the optomechanical interaction. The loop phase ϕ is controlled by a rotation of **S** by an angle ϕ in the optical path from the membrane to the atoms. (**B**), Effective interaction. The membrane vibration mode (harmonic oscillator) is coupled to the collective spin of the atoms (represented on a sphere). If the mean spin is oriented along an external magnetic field B_0 to either the south or north pole of the sphere, its small-amplitude dynamics can be mapped onto a harmonic oscillator with positive or negative mass, respectively. The relative phase of the spin-to-membrane coupling constant g and the membrane-to-spin coupling constant $-g\cos\phi$ defines whether the effective dynamics are Hamiltonian ($\phi = \pi$) or dissipative ($\phi = 0$).

that the forces $\dot{P}_m = -2gX_s$ and $\dot{P}_s = +2gX_m$ differ in their relative sign. Such a coupling is non-conservative and cannot arise from a Hamiltonian interaction. With full access to the laser beams, we can tune the loop phase by inserting a half-wave plate in the path from the membrane back to the atoms, which rotates the Stokes vector by an angle $\phi = \pi$ about S_x. This inverts both S_y and S_z, which respectively carry the spin and membrane signals, thus switching the dynamics to a fully Hamiltonian force, $\dot{P}_m = -2gX_s$ and $\dot{P}_s = -2gX_m$.

All these phenomena are unified in a rigorous quantum-mechanical theory [36] of the cascaded light-mediated coupling, which also correctly describes the dynamics for an arbitrary loop phase. It allows us to describe the effective dynamics of the coupled spin-membrane system with density operator ρ by a Markovian master equation

$$\dot{\rho} = \frac{1}{i\hbar}[H_0 + H_{\text{eff}}, \rho] - \frac{1}{2}\left(J^\dagger J\rho + \rho J^\dagger J\right) + J\rho J^\dagger. \tag{5.1}$$

Here, we neglect optical loss and light propagation delay between the systems for brevity. The dynamics consist of a unitary part with free harmonic oscillator Hamiltonian $H_0 = \sum_{i=s,m} \hbar\Omega_i(X_i^2+P_i^2)/2$ and effective interaction Hamiltonian $H_{\text{eff}} = (1-\cos\phi)\hbar g X_s X_m + 2\sin(\phi)\hbar\Gamma_s X_s^2$, and a dissipative part with collective jump operator $J = \sqrt{2\Gamma_m}X_m + i(1+e^{i\phi})\sqrt{2\Gamma_s}X_s$. Next to the coherent spin-membrane coupling, H_{eff} also includes a spin self-interaction which vanishes for the specific cases $\phi = 0, \pi$ considered here. The jump operator contains a constant membrane term and a spin term that is modulated by ϕ due to interference of the two spin-light interactions. From the dependence of H_{eff} and J on ϕ, it is clear that $\phi = 0$ corresponds to vanishing Hamiltonian coupling and maximum dissipative coupling. Accordingly, we refer to $\phi = 0$ as the dissipative regime. On the other hand, $\phi = \pi$ maximizes the coherent spin-membrane coupling in H_{eff} and at the same time leads to destructive interference of the spin term in J, we thus call $\phi = \pi$ the Hamiltonian regime. Both regimes will be experimentally explored in the following, each with the atomic spin realizing either a positive- or negative-mass oscillator. This gives rise to a whole range of different dynamics in a single system, which can be harnessed for different purposes in quantum technology.

5.3 Results

5.3.1 Normal-mode splitting

We first investigate the light-mediated coupling in the Hamiltonian regime ($\phi = \pi$) and with the spin realizing a positive-mass oscillator. At a magnetic field of $B_0 = 2.81$ G the spin is tuned into resonance with the membrane ($\Omega_s = \Omega_m$). In this configuration, the resonant terms in H_{eff} realize a beam-splitter interaction $H_{\text{BS}} = \hbar g(b_s^\dagger b_m + b_m^\dagger b_s)$, which generates state swaps between the two systems. Here $b_s = (X_s + iP_s)/\sqrt{2}$ and $b_m = (X_m + iP_m)/\sqrt{2}$ are annihilation operators of the spin and mechanical modes, respectively.

We perform spectroscopy of the coupled system using independent drive and detection channels for spin and membrane. The membrane vibrations are recorded by balanced homodyne detection using an auxiliary laser beam coupled to the cavity in orthogonal polarization. To drive the membrane, this beam is amplitude modulated.

The spin precession is detected by splitting off a small portion of the coupling beam on the path from spin to membrane. A radio-frequency (RF) magnetic coil drives the spin. We measure the amplitude and phase response of either system using a lock-in amplifier that demodulates the detector signal at the drive frequency (see section 4.3). After spin-state initialization we simultaneously switch on coupling and drive and start recording. The drive frequency is kept fixed during each experimental run and stepped between consecutive runs.

Figs. 5.2A and B show the membrane's response in amplitude and phase, respectively. With the coupling beam off, it exhibits a Lorentzian resonance of linewidth $\gamma_m = 2\pi \times 0.3$ kHz, broader than the intrinsic linewidth due to optomechanical damping by the red-detuned cavity field [56]. For the uncoupled spin oscillator (Figs. 5.2C, D) with cavity off-resonant, we also measure a Lorentzian response of linewidth $\gamma_s = 2\pi \times 4$ kHz, broadened by the coupling beam. When we turn on the coupling to the spin, the membrane resonance splits into two hybrid spin-mechanical normal modes. This signals strong coupling [118, 6], where light-mediated coupling dominates over local damping. Fitting the well-resolved splitting yields $2g = 2\pi \times 6.1$ kHz, which exceeds the average linewidth $(\gamma_s + \gamma_m)/2 = 2\pi \times 2$ kHz and agrees with the expectation based on an independent calibration of the systems (see section 4.4.4). A characteristic feature of

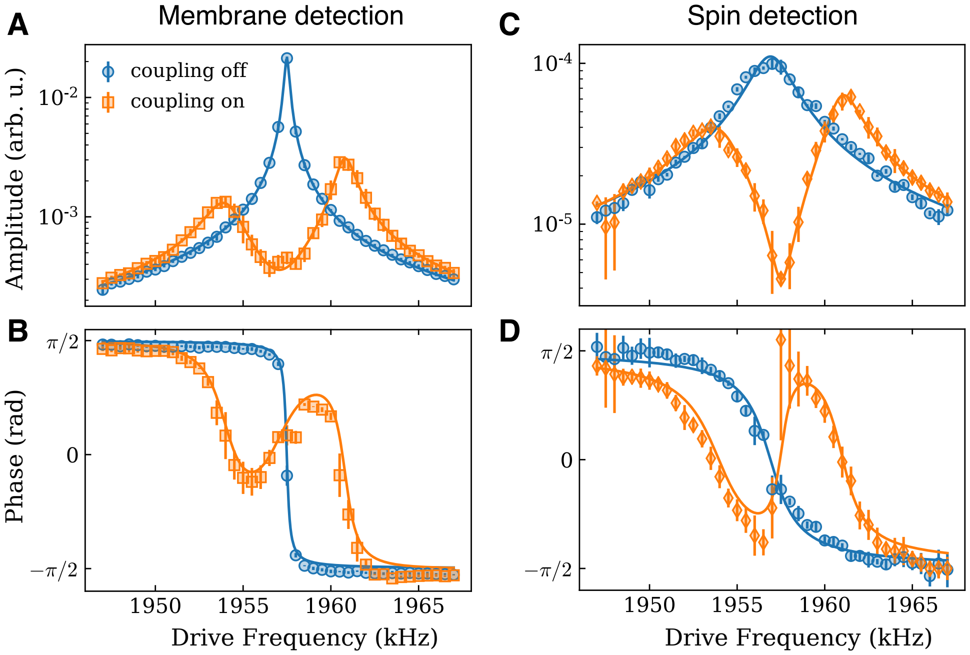

Figure 5.2: Observation of strong spin-membrane coupling. Spectroscopy of the membrane (**A,B**) and the spin (**C,D**), both revealing a normal mode splitting if the coupling beam is on and the oscillators are resonant ($\Omega_s = \Omega_m$). For comparison we show the uncoupled responses of the membrane with coupling beam off (**A,B**) and of the spin with cavity off-resonant (**C,D**). Lines are fits to the data with a coupled-mode model (see section 4.4.1). Error bars are standard deviations of 3 independent measurements.

the long-distance coupling is a finite delay τ between the systems. It causes a linewidth asymmetry of the two normal modes when $\Omega_s = \Omega_m$, which we observe in Fig. 5.2. The fits yield a value of $\tau = 15$ ns, consistent with the propagation delay of the light between the systems and the cavity response time.

We also observe normal-mode splitting in measurements of the spin (Figs. 5.2C and D). Here, the combination of the broader spin linewidth with the much narrower membrane resonance results in a larger dip between the two normal modes and a larger phase shift, in analogy to optomechanically-induced transparency [147].

5.3.2 Energy exchange oscillations

Having observed the spectroscopic signature of strong coupling, we now use it for swapping spin and mechanical excitations in a pulsed experiment. We start by coherently exciting the membrane to $\approx 2 \times 10^6$ phonons, a factor of 100 above its mean equilibrium energy, by applying an amplitude modulation pulse to the auxiliary cavity beam (Fig. 5.3A). At the same time, the spin is prepared in its ground state with $\Omega_s = \Omega_m$. The coupling beam is switched on at time $t = 0$ μs and the displacements $X_s(t)$ and

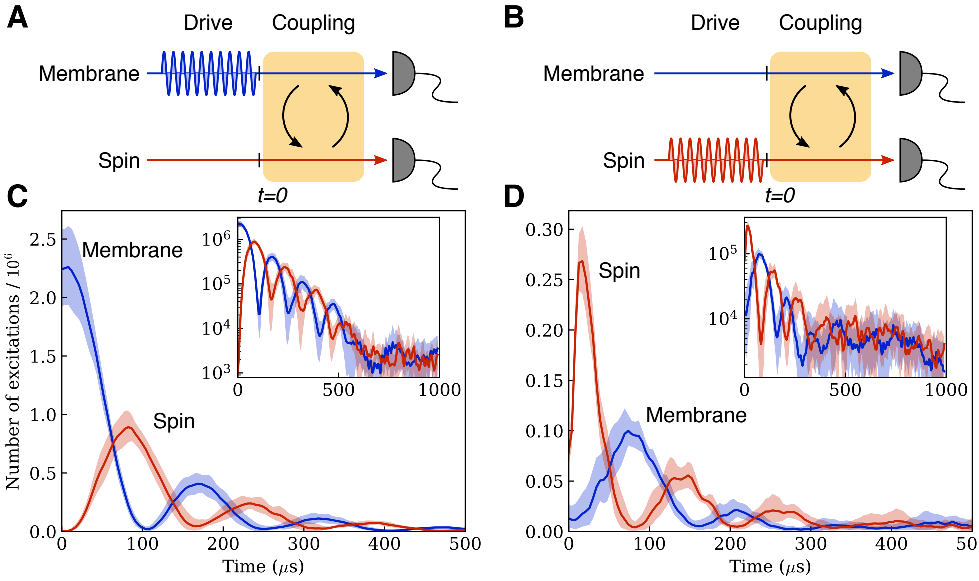

Figure 5.3: Time-domain exchange oscillations showing coherent energy transfer between spin and membrane. (**A**), Pulse sequence for excitation of the membrane by radiation-pressure modulation via the auxiliary laser beam. (**B**), Pulse sequence for spin excitation with an external RF magnetic field. (**C**), Oscillations in the excitation numbers of membrane and spin as a function of the interaction time, measured using the pulse sequence in A. (**D**), Data obtained with pulse sequence B and weaker drive strength than in C. Here, the finite rise time of the spin signal at $t = 0$ corresponds to the turn-on of the coupling beam, which is also used for spin detection. Insets in C,D show the same data on a log-scale. Lines and shaded areas represent the mean and one standard deviation of five measurements, respectively.

$X_m(t)$ of spin and membrane are continuously monitored via the independent detection. From the measured mean square displacements we determine the excitation number of each system (see section 4.3). Fig. 5.3C shows the excitation numbers as a function of the interaction time. The data show coherent and reversible energy exchange oscillations from the membrane to the spin and back with an oscillation period of $T \approx 150\ \mu$s, in accordance with the value π/g extracted from the observed normal-mode splitting. Damping limits the maximum energy transfer efficiency at time $T/2$ to about 40%.

The same experiment is repeated but with the initial drive pulse applied to the spin (Figs. 5.3B and D). Here, we observe another set of exchange oscillations with the same periodicity, swapping an initial spin excitation of $n_s \approx 3 \times 10^5$ to the membrane and back. After the coherent dynamics have decayed, the systems equilibrate in a thermal state of $\approx 3 \times 10^3$ phonons, lower than the effective optomechanical bath of 1.5×10^4 phonons, demonstrating sympathetic cooling [47] of the membrane by the spin. The observed sympathetic cooling strength agrees with simulations using the experimentally determined parameters.

5.3.3 Parametric-gain dynamics

So far we have explored Hamiltonian coupling of the membrane to a spin oscillator with positive effective mass, where the resonant interaction is of the beam-splitter type. If instead we reverse the magnetic field to $B_0 = -2.81$ G but keep the spin pumping direction the same, the collective spin is prepared in its highest energy state with $\bar{F}_x = +Nf$. In this case any excitation reduces the energy such that the spin oscillator has a negative effective mass [28] and $\Omega_s = -\Omega_m$ (Fig. 5.1B). The resonant term of H_{eff} is now the parametric-gain interaction [89] $H_{\text{PG}} = \hbar g(b_s b_m + b_s^\dagger b_m^\dagger)$, which generates correlations between the two systems.

We investigate the dynamics generated by H_{PG} with the membrane driven by thermal noise. In order to quantify the development of spin-mechanical correlations, we determine slowly varying quadratures $\tilde{X}'_{s,m}$ and $\tilde{P}'_{s,m}$ of both systems as the cosine and sine components of the demodulated detector signals, respectively (see section 4.3). Adjusting the demodulator phase allows us to find the basis with strongest correlations. Fig. 5.4A shows histograms of the measured spin-mechanical correlations after an interaction time of $t = 100\ \mu$s. In each subplot, the dashed ellipse corresponds to the Gaussian 1-sigma contour of the measured histogram at $t = 0\ \mu$s while the solid line is the contour at $t = 100\ \mu$s. Compared to the uncorrelated initial state, the histograms show strong amplification along the axes $\tilde{X}_+ = (\tilde{X}'_s + \tilde{X}'_m)/\sqrt{2}$ and $\tilde{P}_- = (\tilde{P}'_s - \tilde{P}'_m)/\sqrt{2}$, and a small amount of thermal noise squeezing along $\tilde{X}_- = (\tilde{X}'_s - \tilde{X}'_m)/\sqrt{2}$ and $\tilde{P}_+ = (\tilde{P}'_s + \tilde{P}'_m)/\sqrt{2}$. The quadrature pairs $\tilde{X}'_s, \tilde{P}'_m$ and $\tilde{P}'_s, \tilde{X}'_m$ remain uncorrelated.

In the time evolution of the combined variances $\tilde{X}_\pm$ and $\tilde{P}_\pm$ (Fig. 5.4B), at $t = 0$ all variances start from the same value indicating an uncorrelated state. As time evolves, the variances of $\tilde{X}_+$ and $\tilde{P}_-$ grow exponentially, demonstrating the dynamical instability in this configuration, while $\tilde{X}_-$ and $\tilde{P}_+$ are squeezed and reach a minimum at $t = 80\ \mu$s before they grow again. The exponential growth rate of $2\pi \times 4.5$ kHz is consistent with the value of $2g - (\gamma_m + \gamma_s)/2$ extracted from the normal-mode splitting. For comparison, we also show simulated variances for the experimental parameters which are given by the lines in Fig. 5.4B (see section 4.4.3). Good agreement between data and simulation is

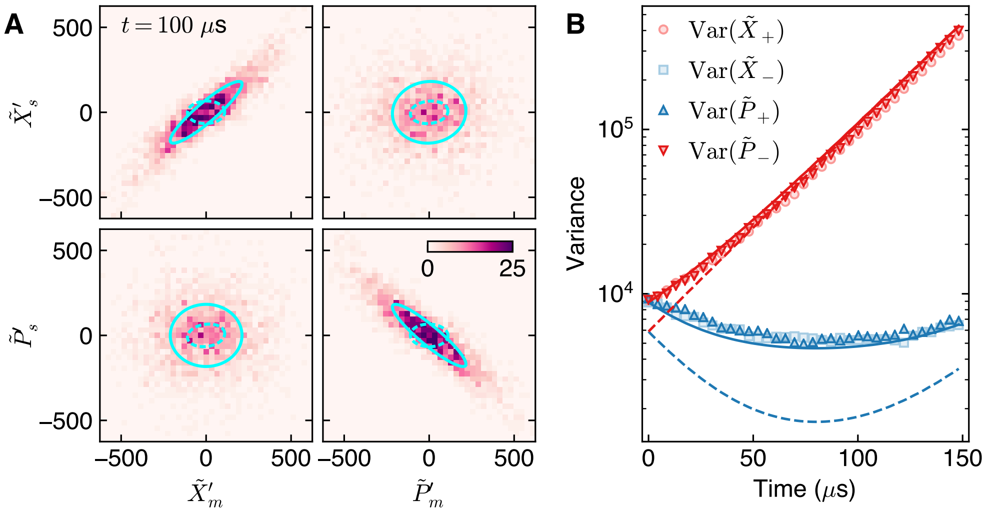

Figure 5.4: Dynamics of the parametric-gain interaction with thermal noise averaged over 2000 realizations. (**A**), Phase space histograms showing correlations between the rotated spin and membrane quadratures after 100 μs of interaction time. The solid (dashed) ellipses enclose regions of one standard deviation at $t = 100$ μs ($t = 0$ μs). (**B**), Variances of the combined quadratures $\tilde{X}_\pm$ and $\tilde{P}_\pm$ as a function of interaction time. Exponential increase is observed for quadratures $\tilde{X}_+$ and $\tilde{P}_-$ while noise reduction is measured for $\tilde{X}_-$ and $\tilde{P}_+$. The solid lines are a simulation of the corresponding variances including a spin detector noise floor of 6×10^3, while the dashed lines assume noise-free detection.

found when accounting for a spin detector noise floor of 6×10^3 (solid lines). The dashed lines correspond to perfect detection and show thermal noise squeezing by 5.5 dB. Realizing the parametric-gain interaction by light-mediated coupling represents an important step towards generation of spin-mechanical entanglement by two-mode squeezing across macroscopic distances. Such entanglement is useful for metrology beyond the standard quantum limit [44].

5.3.4 Control of the loop phase

Equipped with control over both the loop phase and the effective mass of the spin oscillator, we can access four different regimes of the spin-membrane coupling: two Hamiltonian configurations with $\phi = \pi$ and $\Omega_s = \pm\Omega_m$, and the two corresponding dissipative configurations where we set $\phi = 0$ by omitting the half-wave plate in the optical path from membrane to atoms (see section 4.1). Although the dynamics in these configurations are fundamentally different and have different quantum noise properties, we obtain simple equations of motion for the expectation values,

$$\ddot{X}_m + \gamma_m \dot{X}_m + \Omega_m^2 X_m = -2g\Omega_m X_s(t-\tau), \tag{5.2}$$

$$\ddot{X}_s + \gamma_s \dot{X}_s + \Omega_s^2 X_s = +2g\Omega_s \cos(\phi) X_m(t-\tau), \tag{5.3}$$

with the damped harmonic oscillations on the left and the delayed coupling terms on the right. These are derived from Heisenberg-Langevin equations of the full system (see section 4.4.1) and reproduce the dynamics of the master equation in the limit $\tau \to 0$. Two distinct regimes can be identified. If $\Omega_s \cos\phi < 0$ we expect stable dynamics equivalent to a beam-splitter interaction. In the opposite case where $\Omega_s \cos\phi > 0$, the dynamics are equivalent to a parametric-gain interaction and unstable. A simultaneous sign reversal of Ω_s and a π-shift of ϕ should leave the dynamics invariant.

To probe the dynamics in these configurations, we record thermal noise spectra of the membrane while the spin Larmor frequency is tuned across the mechanical resonance $\Omega_m = 2\pi \times 1.957$ MHz. The Hamiltonian configuration with positive-mass spin oscillator is depicted in Fig. 5.5A, showing an avoided crossing at $\Omega_s = \Omega_m$ with frequency splitting $2g = 2\pi \times 5.9$ kHz, as in Fig. 5.2 above. The dashed lines are the calculated normal mode frequencies (see section 4.4.2). The enhancement of the mechanical noise power for $\Omega_s < \Omega_m$ as compared to increased damping for $\Omega_s > \Omega_m$ is again a consequence of the finite optical propagation delay τ modifying the damping (see section 4.4.2).

Switching to the dissipative regime with $\phi = 0$ renders the system unstable due to positive feedback of the coupled oscillations (Fig. 5.5B). Instead of an avoided crossing, the normal modes are now attracted and cross near $\Omega_s = 2\pi \times 1.953$ MHz, forming one strongly amplified and one strongly damped mode. The former leads to exponential growth of correlated spin-mechanical motion, finally resulting in limit-cycle oscillations which dominate the power spectrum. This results in a breakdown of the coupled oscillator model, such that the observed spectral peak shifts towards the unperturbed mechanical resonance. Still, the data are in good agreement with the theoretical model.

In Fig. 5.5C,D we repeat the experiments of Fig. 5.5A,B with negative-mass spin oscillator. The data show that Hamiltonian coupling with negative-mass spin oscillator produces spectra similar to those produced by dissipative coupling with positive-mass spin oscillator. In these configurations, the coupled system features an exceptional point [199] where the normal modes become degenerate [200] and define the squeezed and anti-squeezed quadratures. Conversely, dissipative coupling together with an inverted spin (Fig. 5.5D) shows an avoided crossing with parameters similar to those in the Hamiltonian case (Fig. 5.5A). This equivalence at the level of the expectation values is expected to break down once quantum noise of the light becomes relevant. Due to interference in the loop, quantum back-action on the spin is suppressed in the Hamiltonian coupling configuration but is enhanced in the dissipative configuration.

A necessary condition for quantum back-action cancellation is destructive interference of the spin signal in the output field (see section 4.2.3). Fig. 5.5E and D show homodyne measurements of coherent spin precession on the coupling beam output quadrature $X_L^{(\mathrm{out})}$ in time and frequency-domain, respectively. Toggling the loop phase between $\phi = 0$ and $\phi = \pi$, we observe a large interference contrast > 10 in the root-mean-squared (RMS) spin signal, showing that a spin measurement made by light in the first pass can be erased in the second pass. Optical loss of $1 - \eta^4 \approx 0.35$ inside the loop allows some information to leak out to the environment and brings in uncorrelated noise, limiting the achievable back-action suppression. Full interference in the output is still observed because the carrier and signal fields are subject to the same losses. Since this principle of quantum back-action interference is fully general, it could be harnessed as well for other optical or microwave photonic networks [10, 38].

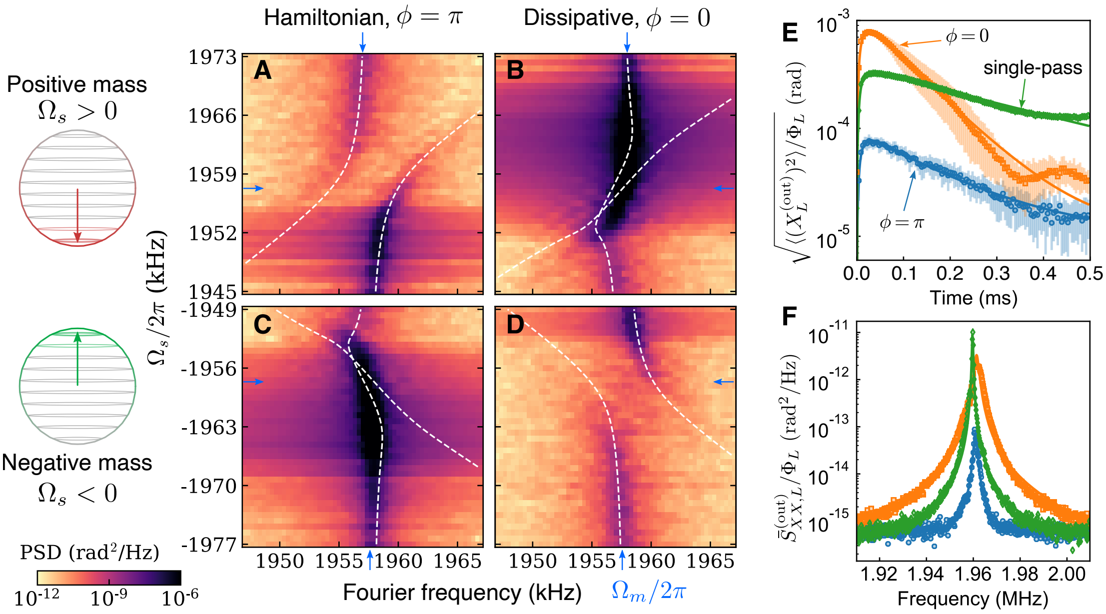

Figure 5.5: Control of the loop phase. (**A–D**) Density plots of the membrane's thermal noise spectra in four different regimes, with membrane Fourier frequency on the horizontal axis (Ω_m indicated by blue arrows) and spin frequency Ω_s (controlled by magnetic field) on the vertical axis. Dashed white lines are the calculated normal mode frequencies. (**A**), Hamiltonian coupling with positive-mass spin oscillator (beam-splitter interaction): an avoided crossing is observed. (**B**), Dissipative coupling with positive-mass spin oscillator: level attraction and unstable dynamics at the exceptional point. (**C**), Hamiltonian coupling with negative-mass spin oscillator (parametric-gain interaction): unstable dynamics and an exceptional point. (**D**), Dissipative coupling with negative-mass spin oscillator: observation of an avoided crossing. (**E**), atomic spin signal (RMS amplitude) on the output light after pulsed excitation: constructive (destructive) interference of the two atom-light interactions is observed for $\phi = 0$ ($\phi = \pi$). Data for a single-pass interaction are also shown for comparison. The membrane is decoupled by detuning the cavity. Error bars are standard deviations of 25 repetitions. (**D**), frequency-domain power spectra corresponding to the data of **E**.

5.4 Conclusion

The observed normal-mode splitting and coherent energy exchange oscillations establish strong spin-membrane coupling, where the coupling strength g exceeds the damping rates of both systems [118]. In order to achieve quantum-coherent coupling [6], g must also exceed all thermal and quantum back-action decoherence rates. This will make it possible to swap non-classical states between the systems or to generate remote entanglement by two-mode squeezing. Thermal noise on the mechanical oscillator is the major source of decoherence in our room-temperature setup. We expect that modest cryogenic cooling of the optomechanical system to 4 K together with an improved mechanical quality factor of $> 10^7$ [59] will enable quantum-limited operation (see section 4.4.4). The built-in suppression of quantum back-action in the Hamiltonian configuration is a crucial feature of our coupling scheme. Interference of the two spin-light interactions reduces the spin's quantum back-action rate to $\gamma_{s,\mathrm{ba}} = (1 - \eta^4)\Gamma_s$, whereas it is $\gamma_{m,\mathrm{ba}} = \eta^2\Gamma_m$ for the membrane. Assuming thermal noise to be negligible, the quantum cooperativity $C = 2g/(\gamma_{s,\mathrm{ba}} + \gamma_{m,\mathrm{ba}})$ can be optimized for a given one-way transmission η^2. We find an upper bound $C \leq \eta(1 + \eta^2)/\sqrt{1 - \eta^4}$, reaching 2.7 for our current setup. The bound is achieved for an optimal choice of measurement rates $\Gamma_s/\Gamma_m = \eta^2/(1 - \eta^4)$, balancing the back-action on both systems. Further improvement is possible with a double-loop coupling scheme that also suppresses quantum back-action on the membrane [36]. In this case, $C = \eta/(1 - \eta^2)$ at $\Gamma_s = \eta^2\Gamma_m$ is inversely proportional to optical loss, scaling more favorably at high transmission so that $C \approx 10$ can be reached for $\eta^2 = 0.9$.

Our results demonstrate a comprehensive and versatile toolbox for generating coherent long-distance interactions with light and open up a range of exciting opportunities for quantum information processing, simulation and metrology. The coupling scheme constitutes a coherent feedback network [107] that allows quantum systems to directly exchange, process and feed back information without the use of classical channels. The ability to create coherent Hamiltonian links between separate and physically distinct systems in a reconfigurable way significantly extends the available toolbox, not only for hybrid spin-mechanical interfaces [45, 51] but quantum networks [10] in general. It facilitates the faithful processing of quantum information and the generation of entanglement between spatially separated quantum processors across a room temperature environment.

Chapter 6

Outlook

In this thesis, we have described the first experiments realizing strong Hamiltonian coupling between a collective spin and a membrane oscillator mediated by laser light across a macroscopic distance. These experiments still operated in a regime where thermal noise dominates over quantum fluctuations and the coupled motion of the two oscillators was observed at large amplitudes above their respective ground states. Despite the large thermal noise level, our experimental results of chapter 5 demonstrate the large variety of dynamical regimes which is accessible by the cascaded light-mediated coupling and thus confirm the theory presented in chapter 1. Supported by these results, the setup offers an unprecedented opportunity to explore light-mediated interactions in hybrid spin-mechanical quantum systems.

The coupled spin-membrane dynamics in the Hamiltonian regime, beam-splitter and parametric-gain interactions, have a clear meaning in terms of state-swap and entanglement generation, respectively. Contrarily, the physics of the dissipative light-mediated coupling regime are much less understood. To some extent it is possible to compare the coupled spin-membrane system to an optomechanical system deeply in the resolved-sideband limit, where the spin takes over the role of the optical cavity. In the optomechanics literature, dissipative optomechanical coupling has been studied by Weiss et al. [125], who consider that the mechanical displacement modifies the cavity damping rate instead of the frequency as in standard dispersive optomechanics. The resulting linearized model is then similar to the dissipative coupling that we realized using cascaded light-mediated interactions. Because of this connection, it would be worth understanding the potential applications of this coupling. Apart from that, the observed exceptional points appearing in the normal-mode spectrum with dissipative coupling could be harnessed for their topological properties [199].

An important goal of this experiment is to observe coupled spin-membrane dynamics in the quantum regime. To get there, a couple of improvements on the setup need to be implemented. First, the membrane oscillator could be upgraded to a soft-clamped membrane [59] which have demonstrated Q-factors exceeding 10^8 at room temperature. As an alternative, tethered membranes [57, 58] could be investigated. The latter are advantageous because of their much lower mode density, although their mechanical frequencies are lower than those of soft-clamped membranes. The combination of increased Q with cryogenic cooling would directly reduce the thermal noise level by almost four orders of magnitude and bring the membrane close to the ground state. This would be an ideal starting point to explore spin-membrane entanglement by two-mode squeezing or attempt ground-state sympathetic cooling of the membrane via the spin [47]. However, even if these dynamics can be realized, they also need to be verified using appropriate measurements. One possible strategy could be to implement dedicated auxiliary measurement beams with quantum-noise limited sensitivity for both the spin and the membrane. As an alternative, the output light of the coupling beam contains information about the membrane and could be used for detection. Still, any sufficiently strong measurement to resolve the quantum ground state necessarily imposes measurement back-action noise [89]. Consequently, continuous readout as it was done in the measurements presented in this thesis is not acceptable. Instead, one would have to either perform stroboscopic readout [201] or, similarly, implement back-action evading readout of a single quadrature [202] by amplitude-modulation of the readout beam at twice the mechanical frequency. Another potential upgrade of the experimental setup concerns the control of the loop phase. In principle, one could replace the wave plates by an electro-optic modulator that would enable fast switching between, e.g., $\phi = \pi$ for Hamiltonian dynamics and $\phi = 0$ for a collective measurement. Since the same laser beam is employed for both the coupling and the collective measurement, this would provide a more elegant approach to entanglement verification than auxiliary detection beams.

In addition, it will be crucial to understand current limitations to spin coherence in the double-pass interface. In all measurements involving the double-pass interface, the observed spin damping rates were much larger than what can be expected from spontaneous emission. One possibility is that this originates from feedback-induced dynamical back-action on the spin, which results from an imperfect loop phase in combination with the propagation delay. Noise of the cavity lock could also produce such phase fluctuations. Another possibility is that the optical polarization of the coupling laser beam is degraded after having traversed the full setup, and produces inhomogeneous broadening due to vector light shifts.

It has been described in section 1.4.4, that optical feedback in the double-pass interaction with a single oscillator can be engineered to produce a squeezing Hamiltonian $H_{\text{eff}} \propto X_s^2$. Consequently, it would be a natural step to first investigate the effect of the light-mediated self-interaction of only the spin system (or the membrane). Besides the intriguing physics this would also benefit the understanding of possible side effects happening in the spin-membrane coupling scheme. Spin squeezing by optical feedback in free-space has been investigated by a few theoretical papers [191, 104, 105]. As discussed in section 1.4.4, this requires setting an intermediate loop phase $\phi \approx \pi/2$ such that the spin Faraday signal from the first pass produces an effective magnetic field that acts back on the spin in the second pass. In a rotating frame at the Larmor frequency, the resulting effective interaction can be written as

$$\tilde{H}_{\text{eff}} = 4\hbar\Gamma_s \tilde{X}_s(t)^2 = 2\hbar\Gamma_s \left[\left(b_s^\dagger b_s + b_s b_s^\dagger \right) + \left(b_s^2 e^{-\mathrm{i}2\Omega_s t} + (b_s^\dagger)^2 e^{+\mathrm{i}2\Omega_s t} \right) \right]. \tag{6.1}$$

The first term in the last expression is stationary and corresponds to a shift of the Larmor frequency. The second term is the squeezing Hamiltonian, but it rotates at $2\Omega_s$. Consequently, in order to achieve squeezing in the presence of a magnetic field, one would have to modulate the coupling strength Γ_s, i.e. the laser power or the loop phase, at $2\Omega_s$. Detection of the coupling beam would then provide readout mainly of the anti-squeezed quadrature [202]. However, quantum back-action by the input field is not fully suppressed due to the intermediate loop phase $\phi \approx \pi/2$. Choosing $\phi = \pi - \epsilon$ with small offset $\epsilon > 0$ could suppress back-action more than the squeezing interaction (cf. section 1.4.4). Here, one still has to take spontaneous emission into account and find a tradeoff between low back-action rate and a squeezing rate that remains larger than the spontaneous emission rate. In the previous discussion, a transverse magnetic field was assumed which is beneficial for AC readout of the spin dynamics. As an alternative, an axial magnetic field along z could also be implemented such that the squeezed spin component F_z is stationary. In this case, however, the detected spin signal would be a DC signal, which renders the measurement more sensitive to electronic noise.

To summarize, the experimental setup opens up a large variety of dynamical regimes. For the spin-membrane system, both Hamiltonian and dissipative dynamics can be investigated for entanglement generation and quantum state transfer. In addition, coherent optical feedback in the double-pass light-matter interaction of a single system can be harnessed for deterministic preparation of squeezed states. From a more general perspective, it will be exciting to see how light-mediated interactions can be used for quantum sensing and for experiments with hybrid quantum networks, where physically different quantum systems are strongly coupled to each other by light.

Appendix A

Cascaded quantum systems

A.1 Proof that Λ_{eff} is positive semidefinite

Here we prove that Λ_{eff} as defined in Eq. (1.18) is always positive semidefinite. Applying this definition to Eq. (1.22) we rewrite

$$\begin{aligned}\Lambda_{\text{eff}} &= \sum_{i=1}^{n}\sum_{j<i}\eta_{ij}g_i g_j(B_i^\dagger B_j + B_j^\dagger B_i) + \sum_{i=1}^{n} g_i^2 B_i^\dagger B_i \\ &= \mathbf{B}^\dagger(\mathbf{g}\mathbf{g}^T \circ M_n)\mathbf{B},\end{aligned}$$

where we defined $\mathbf{B} = (B_1, \ldots, B_n)^T$, $\mathbf{g} = (g_1, \ldots, g_n)^T$ and

$$(M_n)_{ij} = \begin{cases}\eta_{ij} & \text{for } i \neq j \\ 1 & \text{for } i = j.\end{cases}$$

The symbol $\circ$ denotes the Hadamard product of two matrices. If the product $\mathbf{g}\mathbf{g}^T \circ M_n \geq 0$ then also $\Lambda_{\text{eff}} \geq 0$. Since $\mathbf{g}\mathbf{g}^T$ is positive it remains to show that M_n is positive semidefinite for all $n \geq 1$ (Schur product theorem). We can construct recursively

$$M_{n+1} = \left(\begin{array}{c|c} M_n & \mathbf{a}_n \\ \hline \mathbf{a}_n^T & 1 \end{array}\right),$$

using the vector $\mathbf{a}_n = \eta_n(\mathbf{a}_{n-1}^T, 1)^T$ with $\mathbf{a}_1 = \eta_1$ and $M_1 = 1$. We need to show that for any vector $\mathbf{v} \in \mathbb{R}^{n+1}$ and any $n \geq 0$ the expression $\mathbf{v}^T M_{n+1}\mathbf{v} \geq 0$. Decomposing $\mathbf{v} = (\mathbf{w}^T, x)^T$ where $\mathbf{w} \in \mathbb{R}^n$ and $x \in \mathbb{R}$ we have

$$\begin{aligned}\mathbf{v}^T M_{n+1}\mathbf{v} &= \mathbf{w}^T M_n \mathbf{w} + 2x\mathbf{w}^T\mathbf{a}_n + x^2 \\ &= \mathbf{w}^T M_n \mathbf{w} - (\mathbf{w}^T\mathbf{a}_n)^2 + (x + \mathbf{w}^T\mathbf{a}_n)^2 \\ &\geq \mathbf{w}^T M_n \mathbf{w} - (\mathbf{w}^T\mathbf{a}_n)^2 \\ &= \mathbf{w}^T(M_n - \mathbf{a}_n\mathbf{a}_n^T)\mathbf{w}.\end{aligned}$$

It follows that $M_{n+1} \geq 0$ if $M_n \geq \mathbf{a}_n\mathbf{a}_n^T$. To show the latter we note that $\mathbf{a}_n\mathbf{a}_n^T = \eta_n^2\mathbf{b}_n\mathbf{b}_n^T \leq \mathbf{b}_n\mathbf{b}_n^T$ with $\mathbf{b}_n = (\mathbf{a}_{n-1}^T, 1)^T$. Since

$$M_n - \mathbf{b}_n\mathbf{b}_n^T = \left(\begin{array}{c|c} M_{n-1} - \mathbf{a}_{n-1}\mathbf{a}_{n-1}^T & \mathbf{0} \\ \hline \mathbf{0} & 0 \end{array}\right),$$

it follows that $M_n \geq \mathbf{a}_n \mathbf{a}_n^T$ if $M_{n-1} \geq \mathbf{a}_{n-1}\mathbf{a}_{n-1}^T$. Since $M_1 = 1 \geq \eta_1^2 = \mathbf{a}_1\mathbf{a}_1^T$ the proof follows by induction.

A.2 Master equation

This section aims to show how the master equation can be transformed into Lindblad form. Starting from the general master equation (1.11) we expand $A = \sum_{i,j} A_{ij} B_i^\dagger B_j$ and $\mathcal{J}\rho = \sum_{i,j} A_{ij} B_j \rho B_i^\dagger + A_{ij}^* B_i \rho B_j^\dagger$. Then,

$$\dot{\rho} = -\sum_{i,j} A_{ij} [B_i^\dagger, B_j \rho] + \text{h.c.} \tag{A.1}$$

We now identify Hamiltonian and dissipative part of A by the relations $R_{ij} = -\mathrm{i}\hbar(A_{ij} - A_{ji}^*)$ and $L_{ij} = A_{ij} + A_{ji}^*$ equivalent to Eqs. (1.17) and (1.18), respectively. In this basis the effective Hamiltonian and effective dissipation read $H_{\text{eff}} = \frac{1}{2}\sum_{i,j} R_{ij} B_i^\dagger B_j$ and $\Lambda_{\text{eff}} = \sum_{i,j} L_{ij} B_i^\dagger B_j$. Using this notation it follows that

$$\begin{aligned} \dot{\rho} &= -\frac{\mathrm{i}}{\hbar}\sum_{i,j} \frac{R_{ij}}{2} [B_i^\dagger B_j, \rho] && \text{(A.2)} \\ &\quad -\sum_{i,j} \frac{L_{ij}}{2} (B_i^\dagger B_j \rho + \rho B_i^\dagger B_j - 2 B_j \rho B_i^\dagger), && \text{(A.3)} \end{aligned}$$

because both $R_{ij}^* = R_{ji}$ and $L_{ij}^* = L_{ji}$. Provided that L is positive semidefinite the master equation is physical. By diagonalizing $L = \sum_k \gamma_k \mathbf{e}_k \mathbf{e}_k^\dagger$ with eigenvalues $\gamma_k \geq 0$ and orthonormal eigenvectors $\mathbf{e}_k$ we define the (unnormalized) jump operators $j_k = \sqrt{\gamma_k}\mathbf{e}_k^\dagger \mathbf{B}$. The eigenvalues are the corresponding dissipation rates. Using this procedure we obtain the Lindblad form (1.16).

A.3 Time delays

A.3.1 Master equation

Here, we model the effect of time delays on the master equation. We work in an interaction picture with respect to H_0 including local decoherence. For the ladder operators we have $\tilde{b}_j(t) = b_j e^{-\mathrm{i}\Omega_j t - \gamma_j t/2}$ where b_j is the corresponding operator in the Schrödinger picture. Thus,

$$\begin{aligned} \tilde{B}_j(t-\tau) &= (\mu_j \tilde{b}_j(t) e^{\mathrm{i}\Omega_j\tau} + \nu_j \tilde{b}_j^\dagger(t) e^{-\mathrm{i}\Omega_j\tau}) e^{\gamma_j\tau/2} \\ &= (\tilde{B}_j(t)\cos(\Omega_j\tau) + \mathrm{i}\tilde{B}_j^-(t)\sin(\Omega_j\tau)) e^{\gamma_j\tau/2}, \end{aligned}$$

where we defined $\tilde{B}_j^- = \mu_j \tilde{b}_j - \nu_j \tilde{b}_j^\dagger$. Typically, the decay rates γ_j are considered to be much smaller than the oscillation frequencies Ω_j. In this case, the approximation to neglect delays is based on the smallness of the parameter $\epsilon_j = \Omega_j\tau$. To first order and setting $e^{\gamma_j\tau/2}\approx 1$ we thus have $\tilde{B}_j(t-\tau)\approx\tilde{B}_j+\mathrm{i}\epsilon_j\tilde{B}_j^-$. Including these delays we find that the operator A of the general master equation becomes

$$\begin{aligned} A &= \sum_{k<j}\eta_{jk}g_jg_k\tilde{B}_j^\dagger(t)\tilde{B}_k(t-\tau_{jk})+\sum_j\frac{g_j^2}{2}\tilde{B}_j^\dagger(t)\tilde{B}_j(t) \\ &\approx \sum_{k<j}\eta_{jk}g_jg_k\tilde{B}_j^\dagger\tilde{B}_k+\sum_j\frac{g_j^2}{2}\tilde{B}_j^\dagger\tilde{B}_j \qquad (A.4)\\ &\quad +\mathrm{i}\sum_{k<j}\epsilon_{jk}\eta_{jk}g_jg_k\tilde{B}_j^\dagger\tilde{B}_k^-, \qquad (A.5)\end{aligned}$$

where we have defined $\tau_{jk}=\tau_j-\tau_k$ and $\epsilon_{jk}=\Omega_k\tau_{jk}$. The line (A.5) thus presents a correction to the master equation due to delays. In order to neglect it altogether we have to compare the associated rate $\eta_{jk}g_jg_k\epsilon_{jk}$ to all other rates in the system, in particular the smallest rates are the damping rates γ_j. Defining the quality factor $Q_j=\Omega_j/\gamma_j$ we obtain the condition $\eta_{jk}g_jg_k\ll Q_j^{-1}\tau_{jk}^{-1}$ which can be a fairly restrictive upper bound for the light-mediated coupling strengths if the damping rates are small and the delays are large. Instead of this heuristic argument a more rigorous stability criterion has to be applied in general [48] which however goes beyond the scope of this article.

A.3.2 Back-action cancellation

We derive here the equation of motion for the first oscillator in the looped scenario 1-2-1 in the presence of time delays

$$\begin{aligned}\dot{b}_1 &= (-\mathrm{i}\Omega-\gamma_1'/2)b_1+g_1\left(\mu_1f_{\mathrm{in},1}+\nu_1f_{\mathrm{in},1}^\dagger\right)\\ &\quad -\eta_2g_1g_2e^{-\mathrm{i}\phi}\left(\mu_1B_2(t-\tau_{12})-\nu_1B_2^\dagger(t-\tau_{12})\right),\end{aligned}$$

with optically modified damping rate γ_1' (cf. Appendix A.4) and optical back-action force

$$f_{\mathrm{in},1} = a_{\mathrm{in}}(\zeta_1)+e^{-\mathrm{i}\phi}\Big[\eta_2\eta_1a_{\mathrm{in}}(\zeta_3)+\sqrt{1-\eta_1^2\eta_2^2}h_{\mathrm{in}}(\zeta_3)\Big],$$

with combined noise input h_{in} due to losses. The back-action noise driving b_1 is filtered with its susceptibility $\chi_1(\omega)=[\gamma_1'/2-\mathrm{i}(\omega-\Omega_1)]^{-1}$. Within the small bandwidth $\gamma_1\ll\Omega_1$ one can then approximate

$$f_{\mathrm{in},1}\approx\int\frac{\mathrm{d}\omega}{\sqrt{2\pi}}a_{\mathrm{in}}(\omega)e^{\mathrm{i}\omega\tau_1}(1+\eta_1\eta_2e^{-\mathrm{i}\phi}e^{\mathrm{i}\Omega_1\tau_{13}})+\ldots,$$

omitting the noise term involving the uncorrelated input h_{in}. This leads to a suppression factor for $\phi=\pi$ of $1-\eta_1\eta_2e^{\mathrm{i}\Omega_1\tau_{13}}$ for both a_{in} and $a_{\mathrm{in}}^\dagger$. Significant delay introduces a phase shift that adds back-action from the orthogonal optical quadrature. Consequently, the total back-action force amounts to

$$\begin{aligned}\dot{b}_1 &\approx g_1(1-\eta_1\eta_2\cos(\Omega_1\tau_{13}))\left(\mu_1a_{\mathrm{in}}+\nu_1a_{\mathrm{in}}^\dagger\right)\\ &\quad -\mathrm{i}g_1\eta_1\eta_2\sin(\Omega_1\tau_{13}))\left(\mu_1a_{\mathrm{in}}-\nu_1a_{\mathrm{in}}^\dagger\right)\\ &\quad -g_1\sqrt{1-\eta_1^2\eta_2^2}\left(\mu_1h_{\mathrm{in}}+\nu_1h_{\mathrm{in}}^\dagger\right).\end{aligned}$$

We also see that changing the phase shift to $\phi = \pi + \Omega_1 \tau_{13}$ allows us to compensate for the delay and recover full back-action cancellation.

A.4 Gaussian Dynamics

Starting from the master equation (A.1) we can derive equations of motion for expectation values of any system operator. Assuming the system operators are linear, we first transform $B_i = \sum_j U_{ij} Q_j$ into a basis of canonical operators Q_i with U being the basis transformation matrix. The operators Q_i are Hermitian and satisfy the commutation relation $[Q_i, Q_j] = \mathrm{i} J_{ij}$ with J being a real skew-symmetric matrix as for standard harmonic oscillators. The matrix A transforms under U into $\tilde{A} = U^\dagger A U$. We then obtain the transformed master equation

$$\dot{\rho} = -\sum_{i,j} \tilde{A}_{ij} [Q_i, Q_j \rho] + \text{h.c.}$$

The time evolution of the expectation value of any system operator $\bar{Y} = \langle Y \rangle$ reads

$$\begin{aligned} \frac{\mathrm{d}}{\mathrm{d}t}\bar{Y} &= \mathrm{Tr}\{Y \dot{\rho}\} \\ &= -\sum_{i,j} \left(\tilde{A}_{ij} \langle [Y, Q_i] Q_j \rangle - \tilde{A}^*_{ij} \langle Q_j [Y, Q_i] \rangle \right). \end{aligned} \tag{A.6}$$

For first and second moments closed-form equations of motion can be derived. We define the symmetric covariance matrix as

$$\bar{C}_{kl} = \frac{1}{2} \langle Q_k Q_l + Q_l Q_k \rangle - \langle Q_k \rangle \langle Q_l \rangle. \tag{A.7}$$

The equations of motion read [203]

$$\frac{\mathrm{d}}{\mathrm{d}t} \bar{\mathbf{Q}} = F \bar{\mathbf{Q}}, \tag{A.8}$$

$$\frac{\mathrm{d}}{\mathrm{d}t} \bar{C} = F \bar{C} + \bar{C} F^T + N. \tag{A.9}$$

Here we defined the real-valued matrices F and N as

$$F = 2J\,\mathrm{Im}\{\tilde{A}\}, \tag{A.10}$$

$$N = J\,\mathrm{Re}\{\tilde{A} + \tilde{A}^T\} J^T, \tag{A.11}$$

which describe drift and diffusion, respectively, of the Gaussian state. In terms of the Hamiltonian and dissipative parts of A, R and L, respectively, these can be re-written as

$$F = J \left(\mathrm{Re}\{\tilde{R}\} + \mathrm{Im}\{\tilde{L}\} \right), \tag{A.12}$$

$$N = J\,\mathrm{Re}\{\tilde{L}\} J^T. \tag{A.13}$$

Equation (A.9) is used to calculate the entanglement dynamics in the looped schemes in Sec. 1.4.3.

In steady state $\dot{\mathbf{Q}} = 0$ and the covariances are obtained by solving the Lyapunov equation

$$F\bar{C} + \bar{C}F^T + N = 0. \tag{A.14}$$

This equation is solved in order to obtain the steady-state phonon occupations in Sec. 1.4.2 and the steady-state entanglement in the simple cascaded scenario 1-2 in Sec. 1.4.3.

In the following we assume two harmonic oscillators such that $Q = (X_1, P_1, X_2, P_2)$ with $[X_i, P_j] = \mathrm{i}\delta_{ij}$. For the purpose of illustration we first consider the looped geometry 1-2-1 for $\phi = \pi$, $\eta_1 = \eta_2 = \eta$ and local QND interactions with $B_1 = \mathrm{i}X_1$ and $B_2 = X_2$. This corresponds to a coupling Hamiltonian $H_{\text{eff}} \propto X_1X_2$. The drift matrix then evaluates as

$$F = \begin{pmatrix} -\gamma_1/2 & \Omega_1 & 0 & 0 \\ -\Omega_1 & -\gamma_1/2 & -g & 0 \\ 0 & 0 & -\gamma_2/2 & \Omega_2 \\ -g & 0 & -\Omega_2 & -\gamma_2/2 \end{pmatrix}, \tag{A.15}$$

and the diffusion matrix is

$$N = \begin{pmatrix} \gamma_{1,\text{th}} & 0 & 0 & 0 \\ 0 & \gamma_{1,\text{th}} + \Gamma_1 & 0 & 0 \\ 0 & 0 & \gamma_{2,\text{th}} & 0 \\ 0 & 0 & 0 & \gamma_{2,\text{th}} + \Gamma_2 \end{pmatrix}, \tag{A.16}$$

with $g = 2\eta g_1 g_2$, $\Gamma_1 = 2g_1^2(1-\eta^2)$ and $\Gamma_2 = g_2^2$.

In order to solve the equation of motion (A.9) of the covariance matrix we assume an initial thermal state $\bar{C}_0 = \text{diag}\left(\bar{n}_{\text{th},1} + \frac{1}{2}, \bar{n}_{\text{th},1} + \frac{1}{2}, \bar{n}_{\text{th},2} + \frac{1}{2}, \bar{n}_{\text{th},2} + \frac{1}{2}\right)$.

In Sec. 1.4.3 we consider more general light-matter interactions $B_i = \mu_i b_i + \nu_i b_i^\dagger$ with $\mu_i = \cos\theta_i$ and $\nu_i = \sin\theta_i$. We find modified damping rates $\gamma_i' = \gamma_i + \cos(2\theta_i)\Gamma_i$ and back-action rates $\Gamma_{i,X} = \frac{1-\sin(2\theta_i)}{2}\Gamma_i$ and $\Gamma_{i,P} = \frac{1+\sin(2\theta_i)}{2}\Gamma_i$. With these changes the drift matrix for the 1-2-1 scheme then reads

$$F = \begin{pmatrix} -\gamma_1'/2 & \Omega_1 & g(\alpha-\beta)/2 & 0 \\ -\Omega_1 & -\gamma_1'/2 & 0 & g(\alpha+\beta)/2 \\ -g(\alpha+\beta)/2 & 0 & -\gamma_2'/2 & \Omega_2 \\ 0 & -g(\alpha-\beta)/2 & -\Omega_2 & -\gamma_2'/2 \end{pmatrix}, \tag{A.17}$$

and the diffusion matrix is

$$N = \begin{pmatrix} \gamma_{1,\text{th}} + \Gamma_{1,X} & 0 & 0 & 0 \\ 0 & \gamma_{1,\text{th}} + \Gamma_{1,P} & 0 & 0 \\ 0 & 0 & \gamma_{2,\text{th}} + \Gamma_{2,X} & 0 \\ 0 & 0 & 0 & \gamma_{2,\text{th}} + \Gamma_{2,P} \end{pmatrix}. \tag{A.18}$$

In the double-loop scenario 1-2-1-2, back-action rates change to $\Gamma_2 = 2g_2^2(1-\eta^2)$ and coupling strengths in the lower triangle are multiplied by $2 - \eta^2$ for the additional pass through system 2. Moreover, the diffusion matrix acquires small off-diagonal entries for the covariances of X_1, X_2 and P_1, P_2 because of an increased uni-directionality for finite loss.

A.5 Gaussian state entanglement criteria

In order to quantify the degree of entanglement between two oscillators in Sec. 1.4.3 we evaluate two established non-separability criteria for Gaussian states. The first one is the logarithmic negativity [98, 99]

$$E_{\mathcal{N}} = \sum_{\pm} \max\left(0, -\log_2\left(2\tilde{c}_{\pm}\right)\right), \tag{A.19}$$

where $\tilde{c}_{\pm} = \sqrt{(p \pm \sqrt{p^2 - 4q})/2}$ are the symplectic eigenvalues of the partial transpose of the covariance matrix $\bar{C}^{T_1}$. Defining the block-matrix form of the 4×4 covariance matrix,

$$\bar{C} = \begin{pmatrix} v_1 & v_{12} \\ v_{12}^T & v_2 \end{pmatrix}, \tag{A.20}$$

the coefficients evaluate as $p = \det v_1 + \det v_2 - 2\det v_{12}$ and $q = \det \bar{C}$. The logarithmic negativity directly measures the two-mode squeezing parameter r as $E_{\mathcal{N}} \approx -\log_2(r)$ [87].

As a second entanglement criterion we evaluate the EPR variance [100, 101]

$$\Delta_{\mathrm{EPR}} = \frac{1}{2}\left[\mathrm{Var}(X_1 + X_2) + \mathrm{Var}(P_1 - P_2)\right], \tag{A.21}$$

which is conveniently expressed in terms of experimentally accessible variances. The EPR variance detects entanglement for $\Delta_{\mathrm{EPR}} < 1$ and even stronger EPR correlations for $\Delta_{\mathrm{EPR}} < 0.5$ [204]. We remark that further local unitary transformations of the quadratures X_i, P_i and a relative weighting between systems 1 and 2 would have to be included in Δ_{EPR} in order to obtain not only a sufficient, but also a necessary criterion for entanglement [100].

A.6 Master equation with delay

Non-Markovian master equation before eliminating the delays

$$\dot{\rho}(t) = -\sum_{j \geq k} 2\sqrt{\Gamma_j \Gamma_k}[B_j^\dagger(t), B_k(t - \tau_{jk})\rho(t)]\Theta(\tau_{jk}) + \text{H.c.} \tag{A.22}$$

with delays τ_{jk} from sites k to j. With delay, we expand $B_k(t - \tau) \approx B_k - \tau \dot{B}_k$ to first order and obtain

$$\dot{\rho} = -\sum_{j \geq k} 2\sqrt{\Gamma_j \Gamma_k}[B_j^\dagger, B_k \rho]\Theta(\tau_{jk}) + \text{H.c.} \tag{A.23}$$

$$+\sum_{j > k} 2\sqrt{\Gamma_j \Gamma_k}\tau_{jk}[B_j^\dagger, \dot{B}_k \rho] + \text{H.c.} \tag{A.24}$$

The first line describes the instantaneous dynamics, while the second line contains correction terms due to finite delay.

In the experiment, the operators B_j have the form $B_j = X_j e^{\mathrm{i}\phi_j}$. Then, $\dot{X}_j = \Omega_j P_j$. First consider the instantaneous dynamics ($\tau = 0$). We can separate the dynamics into Hamiltonian and dissipative parts. The effective Hamiltonian is given by

$$\begin{aligned} H_{\mathrm{eff}} &= -\mathrm{i}\hbar \sum_{j>k} \sqrt{\Gamma_j \Gamma_k} (B_j^\dagger B_k - B_k^\dagger B_j) && \text{(A.25)} \\ &= -\hbar \sum_{j>k} 2\sqrt{\Gamma_j \Gamma_k} \sin(\phi_{jk}) X_j X_k && \text{(A.26)} \end{aligned}$$

The dissipative part reads

$$\begin{aligned} \mathcal{L}_{\mathrm{eff}}\rho &= -\sum_{j\geq k} \sqrt{\Gamma_j \Gamma_k} \left([B_j^\dagger, B_k \rho] + [B_k^\dagger, B_j \rho] \right) \Theta(\tau_{jk}) + \mathrm{H.c.} && \text{(A.27)} \\ &= -\sum_{j} \sqrt{\Gamma_j \Gamma_k} [B_j^\dagger, B_k \rho] + \mathrm{H.c.} && \text{(A.28)} \\ &= -\frac{1}{2} \left(J^\dagger J \rho + \rho J^\dagger J \right) + J \rho J^\dagger && \text{(A.29)} \end{aligned}$$

with jump operator

$$J = \sum_j \sqrt{2\Gamma_j} B_j = \sum_j \sqrt{2\Gamma_j} X_j e^{\mathrm{i}\phi_j} \qquad \text{(A.30)}$$

In the experiment, $B_1 = iX_s$, $\phi_1 = \pi/2$; $B_2 = X_m$, $\phi_2 = 0$; $B_3 = ie^{\mathrm{i}\phi} X_s$, $\phi_3 = \phi + \pi/2$. Delay $\tau_{jk} = \tau(j-k)$. For the effective Hamiltonian we find

$$H_{\mathrm{eff}} = \hbar 2\sqrt{\Gamma_m \Gamma_s} [1 - \cos(\phi)] X_m X_s - \hbar 2\Gamma_s \sin(\phi) X_s^2 \qquad \text{(A.31)}$$

The collective jump operator is

$$J = \sqrt{2\Gamma_m} X_m + \mathrm{i}\sqrt{2\Gamma_s} (1 + e^{\mathrm{i}\phi}) X_s \qquad \text{(A.32)}$$

The delay introduces the following correction terms. For the Hamiltonian

$$\begin{aligned} \delta H_{\mathrm{eff}} &= \mathrm{i}\hbar \sum_{j>k} \sqrt{\Gamma_j \Gamma_k} \tau_{jk} (B_j^\dagger \dot{B}_k - \dot{B}_k^\dagger B_j) && \text{(A.33)} \\ &= \mathrm{i}\hbar \sum_{j>k} \Omega_k \tau_{jk} \sqrt{\Gamma_j \Gamma_k} (e^{-\mathrm{i}\phi_{jk}} X_j P_k - e^{\mathrm{i}\phi_{jk}} P_k X_j) && \text{(A.34)} \end{aligned}$$

and for the dissipation

$$\begin{aligned} \delta \mathcal{L}_{\mathrm{eff}}\rho &= \sum_{j>k} \sqrt{\Gamma_j \Gamma_k} \tau_{jk} \left([B_j^\dagger, \dot{B}_k \rho] + [\dot{B}_k^\dagger, B_j \rho] \right) + \mathrm{H.c.} && \text{(A.35)} \\ &= \sum_{j>k} \sqrt{\Gamma_j \Gamma_k} \Omega_k \tau_{jk} \left(e^{-\mathrm{i}\phi_{jk}} [X_j, P_k \rho] + e^{\mathrm{i}\phi_{jk}} [P_k, X_j \rho] \right) + \mathrm{H.c.} \end{aligned}$$

Explicitly, we have

$$\begin{aligned} \delta H_{\mathrm{eff}} &= \mathrm{i}\hbar \Gamma_s (2\Omega_s \tau)(e^{-\mathrm{i}\phi} X_s P_s - e^{\mathrm{i}\phi} P_s X_s) \\ &\quad -\hbar 2\sqrt{\Gamma_s \Gamma_m} \tau \left(\Omega_s X_m P_s - \cos(\phi) \Omega_m X_s P_m \right) \end{aligned}$$

and

$$\begin{aligned}
\delta\mathcal{L}_{\mathrm{eff}}\rho &= \sum_{j>k}\sqrt{\Gamma_j\Gamma_k}\tau_{jk}\left([B_j^\dagger,\dot{B}_k\rho]+[\dot{B}_k^\dagger,B_j\rho]\right)+\mathrm{H.c.}\\
&= \Gamma_s(2\Omega_s\tau)\left(e^{-\mathrm{i}\phi}[X_s,P_s\rho]+e^{\mathrm{i}\phi}[P_s,X_s\rho]\right)+\mathrm{H.c.}\\
&\quad +\mathrm{i}\sqrt{\Gamma_m\Gamma_s}\Omega_s\tau\left([X_m,P_s\rho]-[P_s,X_m\rho]\right)+\mathrm{H.c.}\\
&\quad -\mathrm{i}\sqrt{\Gamma_m\Gamma_s}\Omega_m\tau\left(e^{-\mathrm{i}\phi}[X_s,P_m\rho]-e^{\mathrm{i}\phi}[P_m,X_s\rho]\right)+\mathrm{H.c.}
\end{aligned}$$

These are complicated expressions. In the end, for a linear system it is more instructive to consider the Heisenberg-Langevin equations. The time evolution of the expectation value of an observable A is simply given by

$$\begin{aligned}
\frac{\mathrm{d}}{\mathrm{d}t}\langle A\rangle &= \frac{1}{\mathrm{i}\hbar}\langle[A,H_0]\rangle+\langle A\mathcal{L}_0\rangle \\
&\quad -\sum_{j\geq k}2\sqrt{\Gamma_j\Gamma_k}\Theta(\tau_{jk})\left\langle[A,B_j^\dagger]B_k(t-\tau_{jk})-B_k^\dagger(t-\tau_{jk})\langle[A,B_j]\right\rangle
\end{aligned} \tag{A.36}$$

A.7 Adiabatic elimination of the cavity

In this section we provide a treatment of the light-mediated spin-membrane dynamics without the non-resolved sideband approximation. This follows the approach of references [112, 205, 206]. The general light-matter Hamiltonian for cascaded interactions as in equation (1.4) reads

$$H_{\text{int}} = \sum_{i=1}^{n} \hbar\sqrt{2\Gamma_i}(B_i^\dagger a(\zeta_i) + a^\dagger(\zeta_i)B_i). \tag{A.37}$$

The light field $a(\zeta)$ propagates in positive ζ-direction and sequentially couples to N quantum systems at n different locations ζ_i. The local light-matter couplings are described by coupling strengths Γ_i (measurement rates) and general system operators B_i. For negligible optical propagation delays between the systems, a master equation can be derived which reads

$$\dot{\rho} = -\sum_{1\leq j<i\leq n} 2\eta_{ij}\sqrt{\Gamma_i\Gamma_j}[B_i^\dagger, B_j\rho] - \sum_{i=1}^{n}\Gamma_i[B_i^\dagger, B_i\rho] + \text{h.c.} \tag{A.38}$$

The first term describes couplings between the systems, while the second term contains decay of system into the light-field and ensuing back-action noise. Transmission coefficients for the light field between locations i and j are denoted η_{ij}

In the experiment, the spin couples to the light field at two locations ζ_1 and ζ_3 with coupling strength Γ_s as is evident from equation (4.15). The mechanical oscillator does not couple directly to the traveling field, but does so via the cavity mode at location ζ_2. In order to derive the effective spin-membrane interaction, we first derive the effective spin-cavity-membrane dynamics. Based on this result we eliminate the cavity to obtain a master-equation for the coupled spin-membrane system.

To eliminate the cavity we assume the following hierarchy of timescales $2\pi/\tau_{ij} > \kappa > \Gamma_i$, meaning that optical propagation delays τ_{ij} are much shorter than the photon life time in the cavity. The cavity decay rate κ must in turn be much larger than the optomechanical coupling strength g_{om} and the atomic spin read-out rate Γ_s. In this situation we first perform an adiabatic elimination of the traveling field a. The result is a coupling of all systems to the cavity. The time order is the following: system B_1, then cavity c coupling to system B_2 directly, then system B_3.

We use the following notation that allows us to keep the calculation general,

$$B_1 = iX_s \tag{A.39}$$

$$B_3 = ie^{i(\phi+\phi_r)}X_s \tag{A.40}$$

$$B_2 = ic/\sqrt{2} \tag{A.41}$$

$$B_4 = e^{i\phi_c}X_m \tag{A.42}$$

We define $\Gamma_1 = \Gamma_3 = \Gamma_s = \alpha_1^2|\bar{S}_x\bar{F}_x|/2$, $\Gamma_2 = \kappa$ and $\Gamma_4 = \Gamma_m = 4g_{\text{om}}^2/\kappa = (4g_0/\kappa)^2\Phi_m$. We have also defined the phase ϕ_r of the reflected cavity field, which is given by $\phi_r = \pi + 2\phi_c$. This accounts for the phase shift of the classical pump field upon reflection from the cavity. After elimination of the traveling field a, the resulting master equation

$$\dot{\rho} = \mathcal{L}_0\rho + \mathcal{L}_c\rho + \mathcal{L}_{\text{int}}\rho \tag{A.43}$$

is composed of three terms. The internal system dynamics are captured by

$$\mathcal{L}_0\rho = \frac{1}{i\hbar}[H_0,\rho] - \Big(\Gamma_1[B_1^\dagger,B_1\rho] + \Gamma_3[B_3^\dagger,B_3\rho] + \ \eta_{13}2\sqrt{\Gamma_1\Gamma_3}[B_3^\dagger,B_1\rho] + \text{h.c.}\Big)$$

The bare cavity dynamics are

$$\mathcal{L}_c\rho = i\Delta_c[c^\dagger c,\rho] + \kappa\mathcal{D}[c]\rho$$

The interaction of the cavity with the three systems is

$$\begin{aligned}\mathcal{L}_{\text{int}}\rho &= -i\eta_{12}\sqrt{2\Gamma_1\kappa}[c^\dagger,B_1\rho] + i\eta_{23}\sqrt{2\Gamma_3\kappa}[B_3^\dagger,c\rho] + \text{h.c.}\\ &\quad -i\sqrt{\frac{\Gamma_4\kappa}{2}}[B_4^\dagger c + c^\dagger B_4,\rho]\end{aligned}$$

We see that cavity decay in $\mathcal{L}_c$ scales with κ while the interaction scales with $\sqrt{\kappa}$. Provided that κ is much larger than any light-matter coupling strength Γ_i we can eliminate the cavity. We also assume that intrinsic decoherence on the individual systems is much slower than the cavity decay. These assumptions do not present severe restrictions in optomechanical or spin systems because decoherence in these systems is naturally much slower than typical cavity linewidths. The coupling strengths Γ_s and Γ_m both depend on the laser power and can thus easily be made smaller than the cavity decay rate κ by reducing the coherent pump flux Φ_L.

To ease notation we define the operators

$$B_{\text{in}} = \sqrt{\frac{\Gamma_4}{2}}B_4 + \eta_{12}\sqrt{2\Gamma_1}B_1 \tag{A.44}$$

$$B_{\text{out}} = \sqrt{\frac{\Gamma_4}{2}}B_4 - \eta_{23}\sqrt{2\Gamma_3}B_3 \tag{A.45}$$

for systems at the cavity input and output, respectively. This allows to write $\mathcal{L}_{\text{int}}$ in a compact form

$$\mathcal{L}_{\text{int}} = -i\sqrt{\kappa}[B_{\text{out}}^\dagger,c\rho] - i\sqrt{\kappa}[c^\dagger,B_{\text{in}}\rho] + \text{h.c.} \tag{A.46}$$

This is our starting point for deriving the effective master equation for the cavity-mediated interaction between subsystems 1,2 and 3 via the projection technique [73, 112, 205, 206]. To do so we go into the interaction picture of H_0, make a Born-Markov approximation and trace out the cavity mode. This gives

$$\dot\rho = \mathcal{L}_0\rho + \int_0^\infty \text{Tr}_c\left\{\mathcal{L}_{\text{int}}e^{(\mathcal{L}_0+\mathcal{L}_c)\tau}\left[\mathcal{L}_{\text{int}}\rho\otimes\rho_{c,0}\right]\right\}d\tau \tag{A.47}$$

We assume that the cavity remains in the vacuum state $\rho_{c,0}$. In expanding this expression we only keep terms with cavity field correlation functions of the form $\text{Tr}_c\left\{ce^{\mathcal{L}\tau}[c^\dagger\rho_{c,0}]\right\}$. These two-time vacuum correlation functions can be evaluated using the quantum regression theorem [73] yielding ($\tau > 0$)

$$\text{Tr}_c\left\{c\,e^{\mathcal{L}_c\tau}\left[c^\dagger\rho_{c,0}\right]\right\} = e^{(i\Delta_c-\kappa/2)\tau}$$

Using these relations we obtain

$$\dot{\rho} - \mathcal{L}_0\rho = \mathcal{L}_{\text{eff}}\rho = -\kappa \int_0^\infty [\tilde{B}^\dagger_{\text{out}}(t), \tilde{B}_{\text{in}}(t-\tau)\rho] e^{(i\Delta_c - \kappa/2)\tau} d\tau + \text{h.c.} \tag{A.48}$$

This expression contains integrals of the form

$$\int_0^\infty \tilde{B}^\dagger_i(t)\tilde{B}_j(t-\tau) e^{(i\Delta_c-\kappa/2)\tau} d\tau \tag{A.49}$$

which can be evaluated under the assumption that the operators can be written in the form $B_i = \mu_i b_i + \nu_i b_i^\dagger$ with spin/phonon annihilation and creation operators b_i and $b_i^\dagger$, respectively. Assuming that all dynamics are slower than the intrinsic oscillation at frequency Ω_i one finds $\tilde{b}_i(t-\tau) \approx e^{i\Omega_i\tau}\tilde{b}_i(t)$ such that the integrals yield

$$\int_0^\infty \tilde{B}_i(t-\tau)e^{(i\Delta_c-\kappa/2)\tau} d\tau \approx \mu_i \chi_c(\Omega_i)\tilde{b}_i(t) + \nu_i\chi_c(-\Omega_i)\tilde{b}_i^\dagger(t)$$

We define the complex rate coefficients

$$\lambda_{ij}^{\mp} \;=\; \sqrt{\Gamma_i\Gamma_j}\frac{\kappa}{2}\chi_c(\pm\Omega_j) \tag{A.50}$$

The real parts of these coefficients are decoherence rates while the imaginary parts correspond to frequency shifts or coupling constants. Here, we absorb the oscillator frequency shifts $\delta\Omega_i \propto \text{Im}\left[\lambda_{ii}^+ + \lambda_{ii}^-\right]$ by renormalizing the bare oscillator frequencies. The cavity-induced decoherence rates are defined as $\gamma_i^\pm = \text{Re}[\lambda_{ii}^\pm]$ and correspond to downward ($-$) and upward ($+$) jumps, respectively.

In the secular approximation we drop terms containing b_i^2 or $(b_i^\dagger)^2$. This allows us to write

$$\begin{aligned}
\mathcal{L}_{\text{eff}}\rho \;=\;& -\frac{\gamma_m^+}{2}[b_m^\dagger, b_m\rho] - \frac{\gamma_m^-}{2}[b_m, b_m^\dagger\rho] + \text{h.c.} && \text{(A.51)}\\
& -2\eta_{13}\gamma_s^+[b_s^\dagger, b_s\rho] - 2\eta_{12}\gamma_s^-[b_s, b_s^\dagger\rho] + \text{h.c.} && \text{(A.52)}\\
& -i\sqrt{2}\eta_{12}e^{-i\phi_c}(\lambda_{ms}^+[X_m, b_s\rho] + \lambda_{ms}^-[X_m, b_s^\dagger\rho]) + \text{h.c.} && \text{(A.53)}\\
& -i\sqrt{2}\eta_{12}e^{-i(\phi+\phi_r-\phi_c)}(\lambda_{sm}^+[X_s, b_m\rho] + \lambda_{sm}^-[X_s, b_m^\dagger\rho]) + \text{h.c.} && \text{(A.54)}
\end{aligned}$$

Together with $\mathcal{L}_0$ we get the full master equation for the spin-membrane dynamics

$$\begin{aligned}
\dot{\rho} \;=\;& \frac{1}{i\hbar}[H_0, \rho] + \sum_i \left\{ \left[\gamma_{i,0}(\bar{n}_i + 1) + \tilde{\gamma}_i^-\right]\mathcal{D}[b_i]\rho + \left(\gamma_{i,0}\bar{n}_i + \tilde{\gamma}_i^+\right)\mathcal{D}[b_i^\dagger]\rho \right\} && \text{(A.55)}\\
& -i\eta_{12}e^{-i\phi_c}(\lambda_{ms}^+[b_m + b_m^\dagger, b_s\rho] + \lambda_{ms}^-[b_m + b_m^\dagger, b_s^\dagger\rho]) + \text{h.c.}\\
& -i\eta_{23}e^{-i(\phi+\phi_r-\phi_c)}(\lambda_{sm}^+[b_s + b_s^\dagger, b_m\rho] + \lambda_{sm}^-[b_s + b_s^\dagger, b_m^\dagger\rho]) + \text{h.c.}
\end{aligned}$$

where the modified decoherence rates are

$$\begin{aligned}
\tilde{\gamma}_s^\pm \;&=\; 2\Gamma_s\,\text{Re}\left[1 + \eta_{13}e^{-i(\phi+\phi_r)}r_c(\pm\Omega_s)\right] && \text{(A.56)}\\
\tilde{\gamma}_m^\pm \;&=\; \Gamma_m\frac{\kappa}{2}\,\text{Re}\left[\chi_c(\pm\Omega_m)\right] && \text{(A.57)}
\end{aligned}$$

and cavity reflectivity is defined as $r_c(\omega) = 1 - \kappa\chi_c(\omega)$. The coupling strength of the coherent spin-membrane dynamics is

$$g = \frac{1}{2}\,\mathrm{Re}\left[\eta_{12}(\lambda_{ms}^{+} + \lambda_{ms}^{-})e^{-i\phi_c} + \eta_{23}(\lambda_{sm}^{+} + \lambda_{sm}^{-})e^{-i(\phi+\phi_r-\phi_c)}\right] \tag{A.58}$$

In practice we can assume identical oscillator frequencies $|\Omega_s| = \Omega_m = \Omega_0$ and transmission coefficients $\eta_{12} = \eta_{23} = \eta$.

$$g = \frac{\eta\sqrt{\Gamma_s\Gamma_m}}{2}\frac{\kappa}{2}\,\mathrm{Re}\left[e^{-i\phi_c}(\chi_c(\Omega_0) + \chi_c(-\Omega_0))(1 - e^{-i\phi})\right] \tag{A.59}$$

For zero cavity detuning $\Delta_c = 0$ and $\phi = \pi$ we obtain

$$g = \frac{2\eta\sqrt{\Gamma_s\Gamma_m}}{1 + 4\Omega_0^2/\kappa^2} \tag{A.60}$$

All dissipative spin-membrane couplings can be neglected in this case. Moreover, for $\Omega \ll \kappa$, the decoherence rates become

$$\tilde{\gamma}_m^{\pm} \approx \frac{\Gamma_m}{1 + 4\Delta_c^2/\kappa^2} \pm \frac{8\Gamma_m\kappa^2\Delta_c\Omega_m}{(\kappa^2 + 4\Delta_c^2)^2} + \mathcal{O}(\Omega_m^2) \tag{A.61}$$

$$\tilde{\gamma}_s^{\pm} \approx 2\Gamma_s[1 + \eta_{13}\cos(\phi)] \mp \eta_{13}\sin(\phi)\frac{8\Gamma_s\kappa\Delta_c\Omega_s}{\kappa^2 + 4\Delta_c^2} + \mathcal{O}(\Omega_s^2) \tag{A.62}$$

For the mechanical oscillator, these are the well known sideband scattering rates, whose difference accounts for the optomechanical damping rate. Interestingly, for $\phi = \pi/2$, analogous sideband cooling can be performed on the spin oscillator which is located outside the cavity.

In the resolved-sideband regime, the dissipative couplings cannot be neglected and will add considerable noise to the coherent coupling. This is due to the fact that red and blue sidebands experience different phase shifts upon input to and output from the cavity.

The master equation (A.55) covers the full effective dynamics of the spin-membrane system. The first line includes the Hamiltonian of the individual systems. Further, there is thermal noise acting on each system with bath occupation $\bar{n}_i$ and intrinsic damping rates $\gamma_{i,0}$. Dynamical back-action by the cavity as well as quantum noise from the input field add decoherence rates $\Gamma_i^{\pm}$. The quantum cooperativity of each system can simply be defined as the ratio between (single-pass) measurement rate and thermal decoherence rate $\gamma_{i,0}(\bar{n}_i + 1/2)$, i.e. $c_i = \Gamma_i/\gamma_{i,0}(\bar{n}_i + 1/2)$. For the spin oscillator, the actual double-pass back-action rate is strongly suppressed for $\phi = \pi$ due to destructive interference of quantum noise acting on the spin in the first and second pass. The residual back-action is due to losses and the cavity phase shift rotating the optical quadratures upon reflection.

Bibliography

[1] R. Blatt and D. Wineland, *Entangled states of trapped atomic ions*, Nature **453**, 1008 (2008), doi:10.1038/nature07125.

[2] R. Hanson and D. D. Awschalom, *Coherent manipulation of single spins in semiconductors*, Nature **453**, 1043 (2008), doi:10.1038/nature07129.

[3] J. Clarke and F. K. Wilhelm, *Superconducting quantum bits*, Nature **453**, 1031 (2008), doi:10.1038/nature07128.

[4] A. Browaeys, D. Barredo, and T. Lahaye, *Experimental investigations of dipole–dipole interactions between a few rydberg atoms*, J. Phys. B: At., Mol. Opt. Phys. **49**, 152001 (2016), doi:10.1088/0953-4075/49/15/152001.

[5] H. J. Kimble, *Strong interactions of single atoms and photons in cavity QED*, Phys. Scr. **T76**, 127 (1998), doi:10.1238/physica.topical.076a00127.

[6] E. Verhagen, S. Deleglise, S. Weis, A. Schliesser, and T. J. Kippenberg, *Quantum-coherent coupling of a mechanical oscillator to an optical cavity mode*, Nature **482**, 63 (2012), doi:10.1038/nature10787.

[7] L. F. Buchmann and D. M. Stamper-Kurn, *The quantum/classical transition in mediated interactions*, Ann. Phys. **527**, 156 (2015), doi:10.1002/andp.201400150.

[8] L. M. Duan, M. D. Lukin, J. I. Cirac, and P. Zoller, *Long-distance quantum communication with atomic ensembles and linear optics*, Nature **414**, 413 (2001), doi:10.1038/35106500.

[9] N. Gisin and R. Thew, *Quantum communication*, Nat. Photonics **1**, 165 (2007), doi:10.1038/nphoton.2007.22.

[10] H. J. Kimble, *The quantum internet*, Nature **453**, 1023 (2008), doi:10.1038/nature07127.

[11] A. Kuzmich, W. P. Bowen, A. D. Boozer, A. Boca, C. W. Chou, L. M. Duan, and H. J. Kimble, *Generation of nonclassical photon pairs for scalable quantum communication with atomic ensembles*, Nature **423**, 731 (2003), doi:10.1038/nature01714.

[12] S. Ritter, C. Nolleke, C. Hahn, A. Reiserer, A. Neuzner, M. Uphoff, M. Mucke, E. Figueroa, J. Bochmann, and G. Rempe, *An elementary quantum network of single atoms in optical cavities*, Nature **484**, 195 (2012), doi:10.1038/nature11023.

[13] P. C. Humphreys, N. Kalb, J. P. J. Morits, R. N. Schouten, R. F. L. Vermeulen, D. J. Twitchen, M. Markham, and R. Hanson, *Deterministic delivery of remote entanglement on a quantum network*, Nature **558**, 268 (2018), doi:10.1038/s41586-018-0200-5.

[14] R. Riedinger, A. Wallucks, I. Marinković, C. Löschnauer, M. Aspelmeyer, S. Hong, and S. Gröblacher, *Remote quantum entanglement between two micromechanical oscillators*, Nature **556**, 473 (2018), doi:10.1038/s41586-018-0036-z.

[15] J. I. Cirac, P. Zoller, H. J. Kimble, and H. Mabuchi, *Quantum state transfer and entanglement distribution among distant nodes in a quantum network*, Phys. Rev. Lett. **78**, 3221 (1997), doi:10.1103/PhysRevLett.78.3221.

[16] S. J. van Enk, J. I. Cirac, and P. Zoller, *Photonic channels for quantum communication*, Science **279**, 205 (1998), doi:10.1126/science.279.5348.205.

[17] D. P. DiVincenzo, *The physical implementation of quantum computation*, Fortschr. Phys. **48**, 771 (2000), doi:10.1002/1521-3978(200009)48:9/11<771::AID-PROP771>3.0.CO;2-E.

[18] C. W. Gardiner, *Driving a quantum system with the output field from another driven quantum system*, Phys. Rev. Lett. **70**, 2269 (1993), doi:10.1103/PhysRevLett.70.2269.

[19] H. J. Carmichael, *Quantum trajectory theory for cascaded open systems*, Phys. Rev. Lett. **70**, 2273 (1993), doi:10.1103/PhysRevLett.70.2273.

[20] P. Lodahl, S. Mahmoodian, S. Stobbe, A. Rauschenbeutel, P. Schneeweiss, J. Volz, H. Pichler, and P. Zoller, *Chiral quantum optics*, Nature **541**, 473 (2017), doi:10.1038/nature21037.

[21] D. E. Chang, J. S. Douglas, A. González-Tudela, C.-L. Hung, and H. J. Kimble, *Colloquium: Quantum matter built from nanoscopic lattices of atoms and photons*, Rev. Mod. Phys. **90**, 031002 (2018), doi:10.1103/RevModPhys.90.031002.

[22] A. F. van Loo, A. Fedorov, K. Lalumière, B. C. Sanders, A. Blais, and A. Wallraff, *Photon-mediated interactions between distant artificial atoms*, Science **342**, 1494 (2013), doi:10.1126/science.1244324.

[23] K. Lalumière, B. C. Sanders, A. F. van Loo, A. Fedorov, A. Wallraff, and A. Blais, *Input-output theory for waveguide qed with an ensemble of inhomogeneous atoms*, Phys. Rev. A **88**, 043806 (2013), doi:10.1103/PhysRevA.88.043806.

[24] C. A. Muschik, E. S. Polzik, and J. I. Cirac, *Dissipatively driven entanglement of two macroscopic atomic ensembles*, Phys. Rev. A **83**, 052312 (2011), doi:10.1103/PhysRevA.83.052312.

[25] H. Krauter, C. A. Muschik, K. Jensen, W. Wasilewski, J. M. Petersen, J. I. Cirac, and E. S. Polzik, *Entanglement generated by dissipation and steady state entanglement of two macroscopic objects*, Phys. Rev. Lett. **107**, 080503 (2011), doi:10.1103/PhysRevLett.107.080503.

[26] K. Stannigel, P. Rabl, and P. Zoller, *Driven-dissipative preparation of entangled states in cascaded quantum-optical networks*, New J. Phys. **14**, 063014 (2012), doi:10.1088/1367-2630/14/6/063014.

[27] H. Pichler, T. Ramos, A. J. Daley, and P. Zoller, *Quantum optics of chiral spin networks*, Phys. Rev. A **91**, 042116 (2015), doi:10.1103/PhysRevA.91.042116.

[28] B. Julsgaard, A. Kozhekin, and E. S. Polzik, *Experimental long-lived entanglement of two macroscopic objects*, Nature **413**, 400 (2001), doi:10.1038/35096524.

[29] J. Majer, J. M. Chow, J. M. Gambetta, J. Koch, B. R. Johnson, J. A. Schreier, L. Frunzio, D. I. Schuster, A. A. Houck, A. Wallraff, et al., *Coupling superconducting qubits via a cavity bus*, Nature **449**, 443 (2007), doi:10.1038/nature06184.

[30] K. Baumann, C. Guerlin, F. Brennecke, and T. Esslinger, *Dicke quantum phase transition with a superfluid gas in an optical cavity*, Nature **464**, 1301 (2010), doi:10.1038/nature09009.

[31] N. Spethmann, J. Kohler, S. Schreppler, L. Buchmann, and D. M. Stamper-Kurn, *Cavity-mediated coupling of mechanical oscillators limited by quantum back-action*, Nat. Phys. **12**, 27 (2015), doi:10.1038/nphys3515.

[32] M. Mirhosseini, E. Kim, X. Zhang, A. Sipahigil, P. B. Dieterle, A. J. Keller, A. Asenjo-Garcia, D. E. Chang, and O. Painter, *Cavity quantum electrodynamics with atom-like mirrors*, Nature **569**, 692 (2019), doi:10.1038/s41586-019-1196-1.

[33] S. Kato, N. Német, K. Senga, S. Mizukami, X. Huang, S. Parkins, and T. Aoki, *Observation of dressed states of distant atoms with delocalized photons in coupled-cavities quantum electrodynamics*, Nature Communications **10**, 1160 (2019), doi:10.1038/s41467-019-08975-8.

[34] N. Leung, Y. Lu, S. Chakram, R. K. Naik, N. Earnest, R. Ma, K. Jacobs, A. N. Cleland, and D. I. Schuster, *Deterministic bidirectional communication and remote entanglement generation between superconducting qubits*, npj Quantum Information **5**, 18 (2019), doi:10.1038/s41534-019-0128-0.

[35] I. D. Leroux, M. H. Schleier-Smith, H. Zhang, and V. Vuletić, *Unitary cavity spin squeezing by quantum erasure*, Phys. Rev. A **85**, 013803 (2012), doi:10.1103/PhysRevA.85.013803.

[36] T. M. Karg, B. Gouraud, P. Treutlein, and K. Hammerer, *Remote hamiltonian interactions mediated by light*, Phys. Rev. A **99**, 063829 (2019), doi:10.1103/PhysRevA.99.063829.

[37] R. Loudon, *The Quantum Theory of Light* (Oxford University Press, 2000).

[38] A. F. Kockum, G. Johansson, and F. Nori, *Decoherence-free interaction between giant atoms in waveguide quantum electrodynamics*, Phys. Rev. Lett. **120**, 140404 (2018), doi:10.1103/PhysRevLett.120.140404.

[39] K. Hammerer, A. S. Sørensen, and E. S. Polzik, *Quantum interface between light and atomic ensembles*, Rev. Mod. Phys. **82**, 1041 (2010), doi:10.1103/RevModPhys.82.1041.

[40] J. D. Thompson, B. M. Zwickl, A. M. Jayich, F. Marquardt, S. M. Girvin, and J. G. E. Harris, *Strong dispersive coupling of a high-finesse cavity to a micromechanical membrane*, Nature **452**, 72 (2008), doi:10.1038/nature06715.

[41] P.-L. Yu, K. Cicak, N. S. Kampel, Y. Tsaturyan, T. P. Purdy, R. W. Simmonds, and C. A. Regal, *A phononic bandgap shield for high-q membrane microresonators*, Appl. Phys. Lett. **104**, 023510 (2014), doi:10.1063/1.4862031.

[42] P. Treutlein, C. Genes, K. Hammerer, M. Poggio, and P. Rabl, in *Cavity Optomechanics: Nano- and Micromechanical Resonators Interacting with Light*, edited by M. Aspelmeyer, T. J. Kippenberg, and F. Marquardt (Springer Berlin Heidelberg, 2014), chap. Hybrid Mechanical Systems, pp. 327–351, ISBN 978-3-642-55312-7.

[43] V. Giovannetti, S. Lloyd, and L. Maccone, *Quantum-enhanced measurements: Beating the standard quantum limit*, Science **306**, 1330 (2004), doi:10.1126/science.1104149.

[44] L. Pezzè, A. Smerzi, M. K. Oberthaler, R. Schmied, and P. Treutlein, *Quantum metrology with nonclassical states of atomic ensembles*, Rev. Mod. Phys. **90**, 035005 (2018), doi:10.1103/RevModPhys.90.035005.

[45] G. Kurizki, P. Bertet, Y. Kubo, K. Mølmer, D. Petrosyan, P. Rabl, and J. Schmiedmayer, *Quantum technologies with hybrid systems*, Proc. Natl. Acad. Sci. **112**, 3866 (2015), doi:10.1073/pnas.1419326112.

[46] S. Camerer, M. Korppi, A. Jöckel, D. Hunger, T. W. Hänsch, and P. Treutlein, *Realization of an optomechanical interface between ultracold atoms and a membrane*, Phys. Rev. Lett. **107**, 223001 (2011), doi:10.1103/PhysRevLett.107.223001.

[47] A. Jöckel, A. Faber, T. Kampschulte, M. Korppi, M. T. Rakher, and P. Treutlein, *Sympathetic cooling of a membrane oscillator in a hybrid mechanical–atomic system*, Nat. Nanotechnol. **10**, 55 (2015), doi:10.1038/nnano.2014.278.

[48] A. Vochezer, T. Kampschulte, K. Hammerer, and P. Treutlein, *Light-mediated collective atomic motion in an optical lattice coupled to a membrane*, Phys. Rev. Lett. **120**, 073602 (2018), doi:10.1103/PhysRevLett.120.073602.

[49] B. Vogell, T. Kampschulte, M. T. Rakher, A. Faber, P. Treutlein, K. Hammerer, and P. Zoller, *Long distance coupling of a quantum mechanical oscillator to the internal states of an atomic ensemble*, New J. Phys. **17**, 043044 (2015), doi:10.1088/1367-2630/17/4/043044.

[50] P. Christoph, T. Wagner, H. Zhong, R. Wiesendanger, K. Sengstock, A. Schwarz, and C. Becker, *Combined feedback and sympathetic cooling of a mechanical oscillator coupled to ultracold atoms*, New J. Phys. **20**, 093020 (2018), doi:10.1088/1367-2630/aadf20.

[51] C. B. Møller, R. A. Thomas, G. Vasilakis, E. Zeuthen, Y. Tsaturyan, M. Balabas, K. Jensen, A. Schliesser, K. Hammerer, and E. S. Polzik, *Quantum back-action-evading measurement of motion in a negative mass reference frame*, Nature **547**, 191 (2017), doi:10.1038/nature22980.

[52] M. Fleischhauer and M. D. Lukin, *Quantum memory for photons: Dark-state polaritons*, Phys. Rev. A **65**, 022314 (2002), doi:10.1103/PhysRevA.65.022314.

[53] N. Sangouard, C. Simon, H. de Riedmatten, and N. Gisin, *Quantum repeaters based on atomic ensembles and linear optics*, Rev. Mod. Phys. **83**, 33 (2011), doi:10.1103/RevModPhys.83.33.

[54] A. D. Ludlow, M. M. Boyd, J. Ye, E. Peik, and P. O. Schmidt, *Optical atomic clocks*, Rev. Mod. Phys. **87**, 637 (2015), doi:10.1103/RevModPhys.87.637.

[55] C. Gross and I. Bloch, *Quantum simulations with ultracold atoms in optical lattices*, Science **357**, 995 (2017), doi:10.1126/science.aal3837.

[56] M. Aspelmeyer, T. J. Kippenberg, and F. Marquardt, *Cavity optomechanics*, Rev. Mod. Phys. **86**, 1391 (2014), doi:10.1103/revmodphys.86.1391.

[57] R. A. Norte, J. P. Moura, and S. Gröblacher, *Mechanical resonators for quantum optomechanics experiments at room temperature*, Phys. Rev. Lett. **116**, 147202 (2016), doi:10.1103/PhysRevLett.116.147202.

[58] C. Reinhardt, T. Müller, A. Bourassa, and J. C. Sankey, *Ultralow-noise sin trampoline resonators for sensing and optomechanics*, Phys. Rev. X **6**, 021001 (2016), doi:10.1103/PhysRevX.6.021001.

[59] Y. Tsaturyan, A. Barg, E. S. Polzik, and A. Schliesser, *Ultracoherent nanomechanical resonators via soft clamping and dissipation dilution*, Nat. Nanotechnol. **12**, 776 (2017), doi:10.1038/nnano.2017.101.

[60] A. H. Ghadimi, S. A. Fedorov, N. J. Engelsen, M. J. Bereyhi, R. Schilling, D. J. Wilson, and T. J. Kippenberg, *Elastic strain engineering for ultralow mechanical dissipation*, Science (2018), doi:10.1126/science.aar6939.

[61] J. Chan, T. P. M. Alegre, A. H. Safavi-Naeini, J. T. Hill, A. Krause, S. Gröblacher, M. Aspelmeyer, and O. Painter, *Laser cooling of a nanomechanical oscillator into its quantum ground state*, Nature **478**, 89 (2011), doi:10.1038/nature10461.

[62] J. D. Teufel, T. Donner, D. Li, J. W. Harlow, M. S. Allman, K. Cicak, A. J. Sirois, J. D. Whittaker, K. W. Lehnert, and R. W. Simmonds, *Sideband cooling of micromechanical motion to the quantum ground state*, Nature **475**, 359 (2011), doi:10.1038/nature10261.

[63] R. W. Peterson, T. P. Purdy, N. S. Kampel, R. W. Andrews, P.-L. Yu, K. W. Lehnert, and C. A. Regal, *Laser cooling of a micromechanical membrane to the quantum backaction limit*, Phys. Rev. Lett. **116**, 063601 (2016), doi:10.1103/PhysRevLett.116.063601.

[64] D. J. Wilson, V. Sudhir, N. Piro, R. Schilling, A. Ghadimi, and T. J. Kippenberg, *Measurement-based control of a mechanical oscillator at its thermal decoherence rate*, Nature **524**, 325 (2015), doi:10.1038/nature14672.

[65] M. Rossi, N. Kralj, S. Zippilli, R. Natali, A. Borrielli, G. Pandraud, E. Serra, G. Di Giuseppe, and D. Vitali, *Normal-mode splitting in a weakly coupled optomechanical system*, Phys. Rev. Lett. **120**, 073601 (2018), doi:10.1103/PhysRevLett.120.073601.

[66] R. W. Andrews, R. W. Peterson, T. P. Purdy, K. Cicak, R. W. Simmonds, C. A. Regal, and K. W. Lehnert, *Bidirectional and efficient conversion between microwave and optical light*, Nat. Phys. **10**, 321 (2014), doi:10.1038/nphys2911.

[67] M. Forsch, R. Stockill, A. Wallucks, I. Marinković, C. Gärtner, R. A. Norte, F. van Otten, A. Fiore, K. Srinivasan, and S. Gröblacher, *Microwave-to-optics conversion using a mechanical oscillator in its quantum ground state*, Nat. Phys. **16**, 69 (2020), doi:10.1038/s41567-019-0673-7.

[68] R. Riedinger, S. Hong, R. A. Norte, J. A. Slater, J. Shang, A. G. Krause, V. Anant, M. Aspelmeyer, and S. Gröblacher, *Non-classical correlations between single photons and phonons from a mechanical oscillator*, Nature **530**, 313 (2016), doi:10.1038/nature16536.

[69] E. S. Polzik and K. Hammerer, *Trajectories without quantum uncertainties*, Ann. Phys. **527**, A15 (2015), doi:10.1002/andp.201400099.

[70] J. Kohler, J. A. Gerber, E. Dowd, and D. M. Stamper-Kurn, *Negative-mass instability of the spin and motion of an atomic gas driven by optical cavity backaction*, Phys. Rev. Lett. **120**, 013601 (2018), doi:10.1103/PhysRevLett.120.013601.

[71] T. M. Karg, B. Gouraud, C. T. Ngai, G.-L. Schmid, K. Hammerer, and P. Treutlein, *Light-mediated strong coupling between a mechanical oscillator and atomic spins 1 meter apart*, Science **369**, 174 (2020), doi:10.1126/science.abb0328.

[72] M. Wallquist, K. Hammerer, P. Rabl, M. Lukin, and P. Zoller, *Hybrid quantum devices and quantum engineering*, Phys. Scr. **T137**, 014001 (2009), doi:10.1088/0031-8949/2009/t137/014001.

[73] C. Gardiner and P. Zoller, *Quantum Noise: A Handbook of Markovian and Non-Markovian Quantum Stochastic Methods with Applications to Quantum Optics*, Springer Series in Synergetics (Springer, 2004).

[74] M. J. Collett and C. W. Gardiner, *Squeezing of intracavity and traveling-wave light fields produced in parametric amplification*, Phys. Rev. A **30**, 1386 (1984), doi:10.1103/PhysRevA.30.1386.

[75] C. A. Muschik, K. Hammerer, E. S. Polzik, and I. J. Cirac, *Quantum teleportation of dynamics and effective interactions between remote systems*, Phys. Rev. Lett. **111**, 020501 (2013), doi:10.1103/PhysRevLett.111.020501.

[76] K. Stannigel, P. Rabl, A. S. Sørensen, P. Zoller, and M. D. Lukin, *Optomechanical transducers for long-distance quantum communication*, Phys. Rev. Lett. **105**, 220501 (2010), doi:10.1103/PhysRevLett.105.220501.

[77] T. P. Purdy, P.-L. Yu, R. W. Peterson, N. S. Kampel, and C. A. Regal, *Strong optomechanical squeezing of light*, Phys. Rev. X **3**, 031012 (2013), doi:10.1103/PhysRevX.3.031012.

[78] W. H. P. Nielsen, Y. Tsaturyan, C. B. Møller, E. S. Polzik, and A. Schliesser, *Multimode optomechanical system in the quantum regime*, Proceedings of the National Academy of Sciences **114**, 62 (2017), doi:10.1073/pnas.1608412114.

[79] A. H. Safavi-Naeini, J. T. Hill, S. Meenehan, J. Chan, S. Gröblacher, and O. Painter, *Two-dimensional phononic-photonic band gap optomechanical crystal cavity*, Phys. Rev. Lett. **112**, 153603 (2014), doi:10.1103/PhysRevLett.112.153603.

[80] C. Sayrin, C. Junge, R. Mitsch, B. Albrecht, D. O'Shea, P. Schneeweiss, J. Volz, and A. Rauschenbeutel, *Nanophotonic optical isolator controlled by the internal state of cold atoms*, Phys. Rev. X **5**, 041036 (2015), doi:10.1103/PhysRevX.5.041036.

[81] P. Solano, P. Barberis-Blostein, F. K. Fatemi, L. A. Orozco, and S. L. Rolston, *Super-radiance reveals infinite-range dipole interactions through a nanofiber*, Nat. Commun. **8**, 1857 (2017), doi:10.1038/s41467-017-01994-3.

[82] K. Hammerer, K. Stannigel, C. Genes, P. Zoller, P. Treutlein, S. Camerer, D. Hunger, and T. W. Hänsch, *Optical lattices with micromechanical mirrors*, Phys. Rev. A **82**, 021803 (2010), doi:10.1103/PhysRevA.82.021803.

[83] B. Vogell, K. Stannigel, P. Zoller, K. Hammerer, M. T. Rakher, M. Korppi, A. Jöckel, and P. Treutlein, *Cavity-enhanced long-distance coupling of an atomic ensemble to a micromechanical membrane*, Phys. Rev. A **87**, 023816 (2013), doi:10.1103/PhysRevA.87.023816.

[84] J. S. Bennett, L. S. Madsen, M. Baker, H. Rubinsztein-Dunlop, and W. P. Bowen, *Coherent control and feedback cooling in a remotely coupled hybrid atom–optomechanical system*, New J. Phys. **16**, 083036 (2014), doi:10.1088/1367-2630/16/8/083036.

[85] X. Huang, E. Zeuthen, D. V. Vasilyev, Q. He, K. Hammerer, and E. S. Polzik, *Unconditional steady-state entanglement in macroscopic hybrid systems by coherent noise cancellation*, Phys. Rev. Lett. **121**, 103602 (2018), doi:10.1103/PhysRevLett.121.103602.

[86] H. Ritsch, P. Domokos, F. Brennecke, and T. Esslinger, *Cold atoms in cavity-generated dynamical optical potentials*, Rev. Mod. Phys. **85**, 553 (2013), doi:10.1103/RevModPhys.85.553.

[87] B. Kraus, K. Hammerer, G. Giedke, and J. I. Cirac, *Entanglement generation and hamiltonian simulation in continuous-variable systems*, Phys. Rev. A **67**, 042314 (2003), doi:10.1103/PhysRevA.67.042314.

[88] C. A. Muschik, H. Krauter, K. Hammerer, and E. S. Polzik, *Quantum information at the interface of light with atomic ensembles and micromechanical oscillators*, Quantum Inf. Process. **10**, 839 (2011), doi:10.1007/s11128-011-0294-2.

[89] A. A. Clerk, M. H. Devoret, S. M. Girvin, F. Marquardt, and R. J. Schoelkopf, *Introduction to quantum noise, measurement, and amplification*, Rev. Mod. Phys. **82**, 1155 (2010), doi:10.1103/RevModPhys.82.1155.

[90] C. W. Gardiner and M. J. Collett, *Input and output in damped quantum systems: Quantum stochastic differential equations and the master equation*, Phys. Rev. A **31**, 3761 (1985), doi:10.1103/PhysRevA.31.3761.

[91] K. Hammerer, M. Aspelmeyer, E. S. Polzik, and P. Zoller, *Establishing einstein-poldosky-rosen channels between nanomechanics and atomic ensembles*, Phys. Rev. Lett. **102**, 020501 (2009), doi:10.1103/PhysRevLett.102.020501.

[92] I. de Vega and D. Alonso, *Dynamics of non-markovian open quantum systems*, Rev. Mod. Phys. **89**, 015001 (2017), doi:10.1103/RevModPhys.89.015001.

[93] D. V. Vasilyev, C. A. Muschik, and K. Hammerer, *Dissipative versus conditional generation of gaussian entanglement and spin squeezing*, Phys. Rev. A **87**, 053820 (2013), doi:10.1103/PhysRevA.87.053820.

[94] W. Bowen and G. Milburn, *Quantum Optomechanics* (Taylor & Francis, 2015).

[95] S. G. Hofer and K. Hammerer, *Entanglement-enhanced time-continuous quantum control in optomechanics*, Phys. Rev. A **91**, 033822 (2015), doi:10.1103/PhysRevA.91.033822.

[96] M. J. Woolley and A. A. Clerk, *Two-mode back-action-evading measurements in cavity optomechanics*, Phys. Rev. A **87**, 063846 (2013), doi:10.1103/PhysRevA.87.063846.

[97] C. F. Ockeloen-Korppi, E. Damskägg, J.-M. Pirkkalainen, A. A. Clerk, M. J. Woolley, and M. A. Sillanpää, *Quantum backaction evading measurement of collective mechanical modes*, Phys. Rev. Lett. **117**, 140401 (2016), doi:10.1103/PhysRevLett.117.140401.

[98] K. Życzkowski, P. Horodecki, A. Sanpera, and M. Lewenstein, *Volume of the set of separable states*, Phys. Rev. A **58**, 883 (1998), doi:10.1103/PhysRevA.58.883.

[99] G. Vidal and R. F. Werner, *Computable measure of entanglement*, Phys. Rev. A **65**, 032314 (2002), doi:10.1103/PhysRevA.65.032314.

[100] L.-M. Duan, G. Giedke, J. I. Cirac, and P. Zoller, *Inseparability criterion for continuous variable systems*, Phys. Rev. Lett. **84**, 2722 (2000), doi:10.1103/PhysRevLett.84.2722.

[101] R. Simon, *Peres-horodecki separability criterion for continuous variable systems*, Phys. Rev. Lett. **84**, 2726 (2000), doi:10.1103/PhysRevLett.84.2726.

[102] S. L. Braunstein and P. van Loock, *Quantum information with continuous variables*, Rev. Mod. Phys. **77**, 513 (2005), doi:10.1103/RevModPhys.77.513.

[103] C. A. Muschik, K. Hammerer, E. S. Polzik, and J. I. Cirac, *Efficient quantum memory and entanglement between light and an atomic ensemble using magnetic fields*, Phys. Rev. A **73**, 062329 (2006), doi:10.1103/PhysRevA.73.062329.

[104] C. M. Trail, P. S. Jessen, and I. H. Deutsch, *Strongly enhanced spin squeezing via quantum control*, Phys. Rev. Lett. **105**, 193602 (2010), doi:10.1103/PhysRevLett.105.193602.

[105] M. Wang, W. Qu, P. Li, H. Bao, V. Vuletić, and Y. Xiao, *Two-axis-twisting spin squeezing by multipass quantum erasure*, Phys. Rev. A **96**, 013823 (2017), doi:10.1103/PhysRevA.96.013823.

[106] P.-O. Guimond, M. Pletyukhov, H. Pichler, and P. Zoller, *Delayed coherent quantum feedback from a scattering theory and a matrix product state perspective*, Quantum Science and Technology **2**, 044012 (2017), doi:10.1088/2058-9565/aa7f03.

[107] J. Zhang, Y. xi Liu, R.-B. Wu, K. Jacobs, and F. Nori, *Quantum feedback: Theory, experiments, and applications*, Phys. Rep. **679**, 1 (2017), quantum feedback: theory, experiments, and applications, doi:https://doi.org/10.1016/j.physrep.2017.02.003.

[108] M. Kitagawa and M. Ueda, *Squeezed spin states*, Phys. Rev. A **47**, 5138 (1993), doi:10.1103/PhysRevA.47.5138.

[109] J. D. Teufel, T. Donner, M. A. Castellanos-Beltran, J. W. Harlow, and K. W. Lehnert, *Nanomechanical motion measured with an imprecision below that at the standard quantum limit*, Nat. Nanotechnol. **4**, 820 (2009), doi:10.1038/nnano.2009.343.

[110] K. W. Murch, K. L. Moore, S. Gupta, and D. M. Stamper-Kurn, *Observation of quantum-measurement backaction with an ultracold atomic gas*, Nat. Phys. **4**, 561 (2008), doi:10.1038/nphys965.

[111] F. Brennecke, S. Ritter, T. Donner, and T. Esslinger, *Cavity optomechanics with a bose-einstein condensate*, Science **322**, 235 (2008), doi:10.1126/science.1163218.

[112] I. Wilson-Rae, N. Nooshi, W. Zwerger, and T. J. Kippenberg, *Theory of ground state cooling of a mechanical oscillator using dynamical backaction*, Phys. Rev. Lett. **99**, 093901 (2007), doi:10.1103/PhysRevLett.99.093901.

[113] F. Marquardt, J. P. Chen, A. A. Clerk, and S. M. Girvin, *Quantum theory of cavity-assisted sideband cooling of mechanical motion*, Phys. Rev. Lett. **99**, 093902 (2007), doi:10.1103/PhysRevLett.99.093902.

[114] S. G. Hofer, W. Wieczorek, M. Aspelmeyer, and K. Hammerer, *Quantum entanglement and teleportation in pulsed cavity optomechanics*, Phys. Rev. A **84**, 052327 (2011), doi:10.1103/PhysRevA.84.052327.

[115] M. Rossi, D. Mason, J. Chen, and A. Schliesser, *Observing and verifying the quantum trajectory of a mechanical resonator*, Phys. Rev. Lett. **123**, 163601 (2019), doi:10.1103/PhysRevLett.123.163601.

[116] C. Galland, N. Sangouard, N. Piro, N. Gisin, and T. J. Kippenberg, *Heralded single-phonon preparation, storage, and readout in cavity optomechanics*, Phys. Rev. Lett. **112**, 143602 (2014), doi:10.1103/PhysRevLett.112.143602.

[117] M. L. Gorodetksy, A. Schliesser, G. Anetsberger, S. Deleglise, and T. J. Kippenberg, *Determination of the vacuum optomechanical coupling rate using frequency noise calibration*, Opt. Express **18**, 23236 (2010), doi:10.1364/OE.18.023236.

[118] S. Gröblacher, K. Hammerer, M. R. Vanner, and M. Aspelmeyer, *Observation of strong coupling between a micromechanical resonator and an optical cavity field*, Nature **460**, 724 (2009), doi:10.1038/nature08171.

[119] A. H. Safavi-Naeini and O. Painter, in *Cavity Optomechanics: Nano- and Micromechanical Resonators Interacting with Light*, edited by M. Aspelmeyer, T. J. Kippenberg, and F. Marquardt (Springer Berlin Heidelberg, 2014), chap. Optomechanical Crystal Devices, pp. 195–231, ISBN 978-3-642-55312-7.

[120] D. J. Wilson, C. A. Regal, S. B. Papp, and H. J. Kimble, *Cavity optomechanics with stoichiometric sin films*, Phys. Rev. Lett. **103**, 207204 (2009), doi:10.1103/PhysRevLett.103.207204.

[121] J. C. Sankey, C. Yang, B. M. Zwickl, A. M. Jayich, and J. G. E. Harris, *Strong and tunable nonlinear optomechanical coupling in a low-loss system*, Nat. Phys. **6**, 707 (2010), doi:10.1038/nphys1707.

[122] A. M. Jayich, J. C. Sankey, B. M. Zwickl, C. Yang, J. D. Thompson, S. M. Girvin, A. A. Clerk, F. Marquardt, and J. G. E. Harris, *Dispersive optomechanics: a membrane inside a cavity*, New J. Phys. **10**, 095008 (2008), doi:10.1088/1367-2630/10/9/095008.

[123] V. Dumont, S. Bernard, C. Reinhardt, A. Kato, M. Ruf, and J. C. Sankey, *Flexure-tuned membrane-at-the-edge optomechanical system*, Opt. Express **27**, 25731 (2019), doi:10.1364/OE.27.025731.

[124] T. P. Purdy, R. W. Peterson, P.-L. Yu, and C. A. Regal, *Cavity optomechanics with* $\mathrm{Si_3N_4}$ *membranes at cryogenic temperatures*, New Journal of Physics **14**, 115021 (2012), doi:10.1088/1367-2630/14/11/115021.

[125] T. Weiss, C. Bruder, and A. Nunnenkamp, *Strong-coupling effects in dissipatively coupled optomechanical systems*, New J. Phys. **15**, 045017 (2013), doi:10.1088/1367-2630/15/4/045017.

[126] C. Stambaugh, H. Xu, U. Kemiktarak, J. Taylor, and J. Lawall, *From membrane-in-the-middle to mirror-in-the-middle with a high-reflectivity sub-wavelength grating*, Ann. Phys. **527**, 81 (2015), doi:10.1002/andp.201400142.

[127] X. Chen, C. Chardin, K. Makles, C. Caër, S. Chua, R. Braive, I. Robert-Philip, T. Briant, P.-F. Cohadon, A. Heidmann, et al., *High-finesse fabry–perot cavities with bidimensional si3n4 photonic-crystal slabs*, Light: Science & Applications **6**, e16190 (2016), doi:10.1038/lsa.2016.190.

[128] J. P. Moura, R. A. Norte, J. Guo, C. Schäfermeier, and S. Gröblacher, *Centimeter-scale suspended photonic crystal mirrors*, Opt. Express **26**, 1895 (2018), doi:10.1364/OE.26.001895.

[129] P.-L. Yu, T. P. Purdy, and C. A. Regal, *Control of material damping in high-q membrane microresonators*, Phys. Rev. Lett. **108**, 083603 (2012), doi:10.1103/PhysRevLett.108.083603.

[130] Y. Tsaturyan, A. Barg, A. Simonsen, L. G. Villanueva, S. Schmid, A. Schliesser, and E. S. Polzik, *Demonstration of suppressed phonon tunneling losses in phononic bandgap shielded membrane resonators for high-q optomechanics*, Opt. Express **22**, 6810 (2014), doi:10.1364/oe.22.006810.

[131] M. Yuan, M. A. Cohen, and G. A. Steele, *Silicon nitride membrane resonators at millikelvin temperatures with quality factors exceeding 108*, Appl. Phys. Lett. **107**, 263501 (2015), doi:10.1063/1.4938747.

[132] D. Rugar, R. Budakian, H. J. Mamin, and B. W. Chui, *Single spin detection by magnetic resonance force microscopy*, Nature **430**, 329 (2004), doi:10.1038/nature02658.

[133] M. Poggio and C. L. Degen, *Force-detected nuclear magnetic resonance: recent advances and future challenges*, Nanotechnology **21**, 342001 (2010), doi:10.1088/0957-4484/21/34/342001.

[134] T. P. Purdy, R. W. Peterson, and C. A. Regal, *Observation of radiation pressure shot noise on a macroscopic object*, Science **339**, 801 (2013), doi:10.1126/science.1231282.

[135] M. Rossi, D. Mason, J. Chen, Y. Tsaturyan, and A. Schliesser, *Measurement-based quantum control of mechanical motion*, Nature **563**, 53 (2018), doi:10.1038/s41586-018-0643-8.

[136] L. G. Villanueva and S. Schmid, *Evidence of surface loss as ubiquitous limiting damping mechanism in sin micro- and nanomechanical resonators*, Phys. Rev. Lett. **113**, 227201 (2014), doi:10.1103/PhysRevLett.113.227201.

[137] A. Jöckel, M. T. Rakher, M. Korppi, S. Camerer, D. Hunger, M. Mader, and P. Treutlein, *Spectroscopy of mechanical dissipation in micro-mechanical membranes*, Appl. Phys. Lett. **99**, 143109 (2011), doi:http://dx.doi.org/10.1063/1.3646914.

[138] T. Faust, J. Rieger, M. J. Seitner, J. P. Kotthaus, and E. M. Weig, *Signatures of two-level defects in the temperature-dependent damping of nanomechanical silicon nitride resonators*, Phys. Rev. B **89**, 100102 (2014), doi:10.1103/PhysRevB.89.100102.

[139] R. Peterson, Ph.D. thesis, University of Colorado (2017).

[140] E. D. Black, *An introduction to pound-drever-hall laser frequency stabilization*, Am. J. Phys. **69**, 79 (2001), doi:10.1119/1.1286663.

[141] A. Ryou and J. Simon, *Active cancellation of acoustical resonances with an fpga fir filter*, Rev. Sci. Instrum. **88**, 013101 (2017), doi:10.1063/1.4973470.

[142] N. C. Pisenti, A. Restelli, B. J. Reschovsky, D. S. Barker, and G. K. Campbell, *An ultra-low noise, high-voltage piezo driver*, Rev. Sci. Instrum. **87**, 124702 (2016), doi:10.1063/1.4969059.

[143] S. Mancini, D. Vitali, and P. Tombesi, *Optomechanical cooling of a macroscopic oscillator by homodyne feedback*, Phys. Rev. Lett. **80**, 688 (1998), doi:10.1103/PhysRevLett.80.688.

[144] C. Genes, D. Vitali, P. Tombesi, S. Gigan, and M. Aspelmeyer, *Ground-state cooling of a micromechanical oscillator: Comparing cold damping and cavity-assisted cooling schemes*, Phys. Rev. A **77**, 033804 (2008), doi:10.1103/PhysRevA.77.033804.

[145] L. Neuhaus, R. Metzdorff, S. Chua, T. Jacqmin, T. Briant, A. Heidmann, P.-F. Cohadon, and S. Deléglise, in *2017 Conference on Lasers and Electro-Optics Europe European Quantum Electronics Conference (CLEO/Europe-EQEC)* (2017), pp. 1–1.

[146] T. Botter, D. W. C. Brooks, N. Brahms, S. Schreppler, and D. M. Stamper-Kurn, *Linear amplifier model for optomechanical systems*, Phys. Rev. A **85**, 013812 (2012), doi:10.1103/PhysRevA.85.013812.

[147] S. Weis, R. Rivière, S. Deléglise, E. Gavartin, O. Arcizet, A. Schliesser, and T. J. Kippenberg, *Optomechanically induced transparency*, Science **330**, 1520 (2010), doi:10.1126/science.1195596.

[148] R. H. Lehmberg, *Radiation from an n-atom system. i. general formalism*, Phys. Rev. A **2**, 883 (1970), doi:10.1103/PhysRevA.2.883.

[149] M. W. Sørensen and A. S. Sørensen, *Three-dimensional theory for light-matter interaction*, Phys. Rev. A **77**, 013826 (2008), doi:10.1103/PhysRevA.77.013826.

[150] L.-M. Duan, J. I. Cirac, P. Zoller, and E. S. Polzik, *Quantum communication between atomic ensembles using coherent light*, Phys. Rev. Lett. **85**, 5643 (2000), doi:10.1103/PhysRevLett.85.5643.

[151] J. M. Geremia, J. K. Stockton, and H. Mabuchi, *Tensor polarizability and dispersive quantum measurement of multilevel atoms*, Phys. Rev. A **73**, 042112 (2006), doi:10.1103/PhysRevA.73.042112.

[152] M. Kubasik, M. Koschorreck, M. Napolitano, S. R. de Echaniz, H. Crepaz, J. Eschner, E. S. Polzik, and M. W. Mitchell, *Polarization-based light-atom quantum interface with an all-optical trap*, Phys. Rev. A **79**, 043815 (2009), doi:10.1103/PhysRevA.79.043815.

[153] R. J. Sewell, M. Napolitano, N. Behbood, G. Colangelo, F. Martin Ciurana, and M. W. Mitchell, *Ultrasensitive atomic spin measurements with a nonlinear interferometer*, Phys. Rev. X **4**, 021045 (2014), doi:10.1103/PhysRevX.4.021045.

[154] J. H. Müller, P. Petrov, D. Oblak, C. L. Garrido Alzar, S. R. de Echaniz, and E. S. Polzik, *Diffraction effects on light–atomic-ensemble quantum interface*, Phys. Rev. A **71**, 033803 (2005), doi:10.1103/PhysRevA.71.033803.

[155] B. Q. Baragiola, L. M. Norris, E. Montaño, P. G. Mickelson, P. S. Jessen, and I. H. Deutsch, *Three-dimensional light-matter interface for collective spin squeezing in atomic ensembles*, Phys. Rev. A **89**, 033850 (2014), doi:10.1103/PhysRevA.89.033850.

[156] M. Gross and S. Haroche, *Superradiance: An essay on the theory of collective spontaneous emission*, Phys. Rep. **93**, 301 (1982), doi:https://doi.org/10.1016/0370-1573(82)90102-8.

[157] S. Inouye, A. P. Chikkatur, D. M. Stamper-Kurn, J. Stenger, D. E. Pritchard, and W. Ketterle, *Superradiant rayleigh scattering from a bose-einstein condensate*, Science **285**, 571 (1999), doi:10.1126/science.285.5427.571.

[158] J. G. Bohnet, Z. Chen, J. M. Weiner, D. Meiser, M. J. Holland, and J. K. Thompson, *A steady-state superradiant laser with less than one intracavity photon*, Nature **484**, 78 (2012), doi:10.1038/nature10920.

[159] G. K. Brennen, I. H. Deutsch, and P. S. Jessen, *Entangling dipole-dipole interactions for quantum logic with neutral atoms*, Phys. Rev. A **61**, 062309 (2000), doi:10.1103/PhysRevA.61.062309.

[160] S. L. Bromley, B. Zhu, M. Bishof, X. Zhang, T. Bothwell, J. Schachenmayer, T. L. Nicholson, R. Kaiser, S. F. Yelin, M. D. Lukin, et al., *Collective atomic scattering and motional effects in a dense coherent medium*, Nat. Commun. **7**, 11039 (2016), doi:10.1038/ncomms11039.

[161] H. Tanji-Suzuki, I. D. Leroux, M. H. Schleier-Smith, M. Cetina, A. T. Grier, J. Simon, and V. Vuletić, in *Advances in Atomic, Molecular, and Optical Physics*, edited by E. Arimondo, P. Berman, and C. Lin (Academic Press, 2011), vol. 60 of *Advances In Atomic, Molecular, and Optical Physics*, pp. 201 – 237.

[162] K. Hammerer, K. Mølmer, E. S. Polzik, and J. I. Cirac, *Light-matter quantum interface*, Phys. Rev. A **70**, 044304 (2004), doi:10.1103/PhysRevA.70.044304.

[163] D. A. Steck, *Rubidium 87 d line data*, available online at http://steck.us/alkalidata (revision 2.0.1) (2008).

[164] D. V. Kupriyanov, O. S. Mishina, I. M. Sokolov, B. Julsgaard, and E. S. Polzik, *Multimode entanglement of light and atomic ensembles via off-resonant coherent forward scattering*, Phys. Rev. A **71**, 032348 (2005), doi:10.1103/PhysRevA.71.032348.

[165] S. R. de Echaniz, M. Koschorreck, M. Napolitano, M. Kubasik, and M. W. Mitchell, *Hamiltonian design in atom-light interactions with rubidium ensembles: A quantum-information toolbox*, Phys. Rev. A **77**, 032316 (2008), doi:10.1103/PhysRevA.77.032316.

[166] I. H. Deutsch and P. S. Jessen, *Quantum control and measurement of atomic spins in polarization spectroscopy*, Opt. Commun. **283**, 681 (2010), quo vadis Quantum Optics?, doi:http://dx.doi.org/10.1016/j.optcom.2009.10.059.

[167] D. V. Vasilyev, K. Hammerer, N. Korolev, and A. S. Sørensen, *Quantum noise for faraday light–matter interfaces*, J. Phys. B: At., Mol. Opt. Phys. **45**, 124007 (2012), doi:10.1088/0953-4075/45/12/124007.

[168] J. Hu, W. Chen, Z. Vendeiro, H. Zhang, and V. Vuletić, *Entangled collective-spin states of atomic ensembles under nonuniform atom-light interaction*, Phys. Rev. A **92**, 063816 (2015), doi:10.1103/PhysRevA.92.063816.

[169] B. Julsgaard, Ph.D. thesis, University of Aarhus (2003).

[170] G. A. Smith, S. Chaudhury, A. Silberfarb, I. H. Deutsch, and P. S. Jessen, *Continuous weak measurement and nonlinear dynamics in a cold spin ensemble*, Phys. Rev. Lett. **93**, 163602 (2004), doi:10.1103/PhysRevLett.93.163602.

[171] A. Roth, Ph.D. thesis, Universität Hannover (2018).

[172] B. Zhu, J. Cooper, J. Ye, and A. M. Rey, *Light scattering from dense cold atomic media*, Phys. Rev. A **94**, 023612 (2016), doi:10.1103/PhysRevA.94.023612.

[173] P. T. Starkey, C. J. Billington, S. P. Johnstone, M. Jasperse, K. Helmerson, L. D. Turner, and R. P. Anderson, *A scripted control system for autonomous hardware-timed experiments*, Rev. Sci. Instrum. **84**, 085111 (2013), doi:10.1063/1.4817213.

[174] H. Metcalf and P. van der Straten, *Laser Cooling and Trapping*, Graduate Texts in Contemporary Physics (Springer New York, 2001).

[175] W. Ketterle, D. S. Durfee, and D. M. Stamper-Kurn, *Making, probing and understanding bose-einstein condensates*, arXiv:cond-mat/9904034 (1999).

[176] A. Faber, Ph.D. thesis, University of Basel (2016).

[177] R. Grimm, M. Weidemüller, and Y. B. Ovchinnikov, in *Advances In Atomic, Molecular, and Optical Physics*, edited by B. Bederson and H. Walther (Academic Press, 2000), vol. 42 of *Advances In Atomic, Molecular, and Optical Physics*, chap. Optical Dipole Traps for Neutral Atoms, pp. 95–170.

[178] G. Buser, Master's thesis, University of Basel (2016).

[179] J. Dalibard and C. Cohen-Tannoudji, *Laser cooling below the doppler limit by polarization gradients: simple theoretical models*, J. Opt. Soc. Am. B **6**, 2023 (1989), doi:10.1364/JOSAB.6.002023.

[180] J. Appel, P. J. Windpassinger, D. Oblak, U. B. Hoff, N. Kjærgaard, and E. S. Polzik, *Mesoscopic atomic entanglement for precision measurements beyond the standard quantum limit*, Proceedings of the National Academy of Sciences **106**, 10960 (2009), doi:10.1073/pnas.0901550106.

[181] F. Kaminski, N. S. Kampel, M. P. H. Steenstrup, A. Griesmaier, E. S. Polzik, and J. H. Müller, *In-situ dual-port polarization contrast imaging of faraday rotation in a high optical depth ultracold 87rb atomic ensemble*, Eur. Phys. J. D **66**, 1 (2012), doi:10.1140/epjd/e2012-30038-0.

[182] W. Happer, *Optical pumping*, Rev. Mod. Phys. **44**, 169 (1972), doi:10.1103/RevModPhys.44.169.

[183] A. Jöckel, Ph.D. thesis, University of Basel (2014).

[184] G. L. Schmid, Master's thesis, University of Basel (2019).

[185] F. M. Ciurana, Ph.D. thesis, ICFO Barcelona (2017).

[186] B. Julsgaard, J. Sherson, J. L. Sørensen, and E. S. Polzik, *Characterizing the spin state of an atomic ensemble using the magneto-optical resonance method*, J. Opt. B: Quantum Semiclassical Opt. **6**, 5 (2003), doi:10.1088/1464-4266/6/1/002.

[187] A. H. Safavi-Naeini, S. Gröblacher, J. T. Hill, J. Chan, M. Aspelmeyer, and O. Painter, *Squeezed light from a silicon micromechanical resonator*, Nature **500**, 185 (2013), doi:10.1038/nature12307.

[188] M. G. Moore and P. Meystre, *Theory of superradiant scattering of laser light from bose-einstein condensates*, Phys. Rev. Lett. **83**, 5202 (1999), doi:10.1103/PhysRevLett.83.5202.

[189] M. A. Norcia, M. N. Winchester, J. R. K. Cline, and J. K. Thompson, *Superradiance on the millihertz linewidth strontium clock transition*, Sci. Adv. **2** (2016), doi:10.1126/sciadv.1601231.

[190] T. Lahaye, C. Menotti, L. Santos, M. Lewenstein, and T. Pfau, *The physics of dipolar bosonic quantum gases*, Rep. Prog. Phys. **72**, 126401 (2009), doi:10.1088/0034-4885/72/12/126401.

[191] M. Takeuchi, S. Ichihara, T. Takano, M. Kumakura, T. Yabuzaki, and Y. Takahashi, *Spin squeezing via one-axis twisting with coherent light*, Phys. Rev. Lett. **94**, 023003 (2005), doi:10.1103/PhysRevLett.94.023003.

[192] F. Le Kien, P. Schneeweiss, and A. Rauschenbeutel, *Dynamical polarizability of atoms in arbitrary light fields: general theory and application to cesium*, Eur. Phys. J. D **67**, 92 (2013), doi:10.1140/epjd/e2013-30729-x.

[193] B. E. A. Saleh and M. C. Teich, *Fundamentals of Photonics* (John Wiley & Sons, Inc., 1991).

[194] T. D. Ladd, F. Jelezko, R. Laflamme, Y. Nakamura, C. Monroe, and J. L. O'Brien, *Quantum computers*, Nature **464**, 45 (2010), doi:10.1038/nature08812.

[195] P. Campagne-Ibarcq, E. Zalys-Geller, A. Narla, S. Shankar, P. Reinhold, L. Burkhart, C. Axline, W. Pfaff, L. Frunzio, R. J. Schoelkopf, et al., *Deterministic remote entanglement of superconducting circuits through microwave two-photon transitions*, Phys. Rev. Lett. **120**, 200501 (2018), doi:10.1103/PhysRevLett.120.200501.

[196] P. Kurpiers, P. Magnard, T. Walter, B. Royer, M. Pechal, J. Heinsoo, Y. Salathé, A. Akin, S. Storz, J. C. Besse, et al., *Deterministic quantum state transfer and remote entanglement using microwave photons*, Nature **558**, 264 (2018), doi:10.1038/s41586-018-0195-y.

[197] J. Hofmann, M. Krug, N. Ortegel, L. Gérard, M. Weber, W. Rosenfeld, and H. Weinfurter, *Heralded entanglement between widely separated atoms*, Science **337**, 72 (2012), doi:10.1126/science.1221856.

[198] R. A. Thomas, M. Parniak, C. Østfeldt, C. B. Møller, C. Bærentsen, Y. Tsaturyan, A. Schliesser, J. Appel, E. Zeuthen, and E. S. Polzik, *Entanglement between distant macroscopic mechanical and spin systems*, arXiv:2003.11310 (2020).

[199] H. Xu, D. Mason, L. Jiang, and J. G. E. Harris, *Topological energy transfer in an optomechanical system with exceptional points*, Nature **537**, 80 (2016), doi:10.1038/nature18604.

[200] N. R. Bernier, L. D. Tóth, A. K. Feofanov, and T. J. Kippenberg, *Level attraction in a microwave optomechanical circuit*, Phys. Rev. A **98**, 023841 (2018), doi:10.1103/PhysRevA.98.023841.

[201] G. Vasilakis, H. Shen, K. Jensen, M. Balabas, D. Salart, B. Chen, and E. S. Polzik, *Generation of a squeezed state of an oscillator by stroboscopic back-action-evading measurement*, Nat. Phys. **11**, 389 (2015), doi:10.1038/nphys3280.

[202] A. A. Clerk, F. Marquardt, and K. Jacobs, *Back-action evasion and squeezing of a mechanical resonator using a cavity detector*, New J. Phys. **10**, 095010 (2008), doi:10.1088/1367-2630/10/9/095010.

[203] S. C. Edwards and V. P. Belavkin, *Optimal quantum filtering and quantum feedback control*, arXiv:quant-ph/0506018 (2005).

[204] M. D. Reid, P. D. Drummond, W. P. Bowen, E. G. Cavalcanti, P. K. Lam, H. A. Bachor, U. L. Andersen, and G. Leuchs, *Colloquium: The einstein-podolsky-rosen paradox: From concepts to applications*, Rev. Mod. Phys. **81**, 1727 (2009), doi:10.1103/RevModPhys.81.1727.

[205] I. Wilson-Rae, N. Nooshi, J. Dobrindt, T. J. Kippenberg, and W. Zwerger, *Cavity-assisted backaction cooling of mechanical resonators*, New J. Phys. **10**, 095007 (2008), doi:10.1088/1367-2630/10/9/095007.

[206] M. Wallquist, K. Hammerer, P. Zoller, C. Genes, M. Ludwig, F. Marquardt, P. Treutlein, J. Ye, and H. J. Kimble, *Single-atom cavity qed and optomicromechanics*, Phys. Rev. A **81**, 023816 (2010), doi:10.1103/PhysRevA.81.023816.

Acknowledgements

A lot of people have supported me in the past years and contributed to the success of this thesis.

Philipp Treutlein has triggered my fascination for this field of research and kept inspiring and encouraging me throughout all this time. I feel very grateful for your trust and I am honored that you gave me so much independence and freedom in designing and building this complex experiment. Thank you!

I wish to thank Simon Gröblacher for reviewing my thesis. Beyond that, you were a great help to us in the beginning of my PhD, when we explored tethered photonic crystal membranes for use in our experiment.

I am indebted to Klemens Hammerer for numerous discussions about cascaded quantum systems and all other aspects of this experiment. Your vast knowledge of atomic ensemble physics and optomechanics was invaluable to this work.

It was a pleasure working together with Baptiste Gouraud on the design and implementation of this experiment! Thank you for carefully developing the theory together with me, sharing a lot of the work in the lab and always keeping calm when things did not work out the way they should.

I would like to thank Andreas Jöckel, Aline Vochezer, Lucas Béguin and Tobias Kampschulte for introducing me to this experiment. In particular, Andreas taught me everything I know about designing cavities.

Without the help of Michael Steinacher from the electronics workshop and Sascha Martin and colleagues from the mechanical workshop none of the experiments would have worked the way they did. Thank you!

I am grateful to Chun Tat Ngai and Gian-Luca Schmid for their help with the characterization and optimization of the atomic setup. I would like to thank Gianni Buser for his companionship in the lab and for heavy metal. Thank you to the rest of the group for their support and providing a good atmosphere!

Meinen Eltern Helga und Rudi und meinem Bruder Simon möchte ich von ganzem Herzen für Ihre konstante Unterstützung und Ermutigung danken.

Ardita, Danke für deine Liebe und Geduld, und dass du immer an meiner Seite stehst!